

Hierarchical Engineering of Microstructural Lengthscales in Fe-Si Based Alloys to Minimize
Thermal Conductivity for Thermoelectric Applications

A Dissertation

Presented to
the faculty of the School of Engineering and Applied Science
University of Virginia

In partial fulfillment
of the requirements for the degree

Doctor of Philosophy

By

Wade A. Jensen

November 2018

APPROVAL SHEET

The dissertation
is submitted in partial fulfillment of the requirements
for the degree of
Doctor of Philosophy

Author

The dissertation has been read and approved by the examining committee:

Jerrold A. Floro

Patrick Hopkins

James Fitz-Gerald

Bi-Cheng Zhou

Gary Shiflet

Accepted for the School of Engineering and Applied Science:

Craig H. Benson, Dean, School of Engineering and Applied Science

November 2018

Abstract

Semiconducting β -FeSi₂ is a candidate thermoelectric material whose constituents are abundant and eco-friendly, but significant improvements in thermoelectric properties are needed before it becomes viable in applications. Nanostructuring of the β matrix and Si_{1-x}Ge_x lamellae, via control of eutectic solidification and eutectoid decomposition, has been shown in the literature as an effective method to reduce thermal conductivity. This dissertation research investigated processing methods to engineer hierarchical structures, characterized the consequent microstructures, and related these features to thermal conductivity and independent thermal scattering contributions of heterointerfaces.

The binary Fe-Si system was first investigated as a means to understand the eutectoid decomposition (α -FeSi₂ \rightarrow β -FeSi₂ + Si). We characterized the nucleation modes of the binary system, showing that nucleation of eutectoid colonies occurs preferentially on cracks. Nucleation can also occur on eutectic Si microconstituents, but is only observed only at small undercoolings, when Si diffusion to the eutectic particles creates a large local chemical driving force for β nucleation. Low temperature aging of binary samples produced cooperatively-grown Si lamellae, which decomposed into nanowires and spheroids via Rayleigh instability upon further aging. The growth velocity (v) and interlamellar spacing (λ) of pearlitic colonies obeys a relation of the type $v\lambda^n = f(T)$. This bounds the activation energy for the diffusion, although the exact mechanism could not be specified from the data. We also found that the eutectoid Si are polycrystalline with interfaces primarily being twin boundaries on the $\{111\}$ planes.

We then alloyed small quantities of Ge to the system (now a ternary Fe-Si-Ge) to enhance thermoelectric properties and widen the design space. Eutectic solidification ($L \rightarrow \alpha$ -FeSi₂ + Si₁₋

$_z\text{Ge}_z$) was used to create meso-scale lamellae. Eutectic morphology and Ge disposition amongst the product phases can be controlled through the solidification rate. By increasing the rate from ambient cooling in a chilled hearth ($\sim 10^2$ °C/s), to melt-spinning, ($\sim 10^6$ °C/s), eutectic lengthscales can be reduced by over two orders of magnitude, while the Ge concentration in the lamellae and matrix roughly doubles. Subsequent aging produced eutectoid decomposition ($\alpha\text{-FeSi}_2 \rightarrow \beta\text{-FeSi}_2 + \text{Si}_{1-y}\text{Ge}_y$) where the additional diamond cubic product is interleaved with the eutectic lamellae, creating a hierarchical structure.

Preliminary work exploring ultra-rapid solidification rates, $\sim 10^9$ °C/s, was performed via pulse laser melting (PLM) with a high-power UV laser. Although this surface-melting technique raised the solidification rate vis-à-vis melt-spinning, there are numerous sample processing challenges to overcome before routine synthesis is possible. Furthermore, PLM artifacts such as the small depth of melting and surface cracking rendered characterization of thermal or electrical transport effectively impossible. Nonetheless, SEM micrographs of PLM samples show potential for developing an optimized microstructure for maximal thermal scattering.

The Si-rich region of the Fe-Si-Ge ternary phase diagram, which was previously unexplored, has been mapped through Rietveld analysis and differential scanning calorimetry. Compositional ranges for $\alpha\text{-FeSi}_2 + \varepsilon\text{-FeSi} + \text{Si}_{1-z}\text{Ge}_z$ and $\beta\text{-FeSi}_2 + \varepsilon\text{-FeSi} + \text{Si}_{1-y}\text{Ge}_y$ three-phase regions were experimentally determined for both 1000 °C and 900 °C sections. Ge additions were found to have a negligible effect on the lattice parameters of intermetallic phases, but have a moderate effect on phase transformation temperatures. Although our composition resolution was not fine enough for differential scanning calorimetry to resolve liquidus surface features, we were able to estimate the position of the ternary eutectic point and the $\varepsilon\text{-FeSi/SiGe}$ cotectic line.

Microstructural characterization was performed, in part, as a means to discover a relationship between hierarchical structuring and thermal conductivity. For the binary sample, process conditions were exploited to create morphological extremes (nanostructured versus coarse particles) and then compared them to investigate the degree of thermal scattering imposed by the β /Si heterointerface. Nanostructuring of the eutectoid Si increased the density of heterointerfaces by 40x vis-à-vis coarse Si equiaxed particles, with a concomitant reduction in thermal conductivity of only 2x. For ternary alloy specimens, melt-spinning and low temperature aging significantly lowered thermal conductivity, which decreased from $22.8 \text{ W m}^{-1} \text{ K}^{-1}$ down to $8.3 \text{ W m}^{-1} \text{ K}^{-1}$. We analyzed the thermal conductivity in terms of a series thermal resistance model, via Matthiessen's rule, and showed that Ge composition has a significant effect on phonon scattering at the β -FeSi₂/Si_{1-x}Ge_x heterointerface. By increasing Ge concentration from 0 to 30 at%, the thermal boundary conductance is reduced by an order of magnitude.

Acknowledgements

I would first like to extend my gratitude to my advisor, Professor Jerrold Floro. He has been an incredible mentor; his guidance has facilitated my development into a materials scientist. His support has helped me find my passion in metallurgy. I am also grateful for his infinite patience and understanding. The II-VI Foundation has generously funded this entire dissertation, and I appreciate their focus on my personal and career development. I would also like to thank Professor William Soffa for his advice and metallurgical insights.

The department and staff of the University of Virginia are amazing. I am grateful to Richard White, Michael Sabat, Helge Heinrich, Diane Dickie, and Joe Thompson for sharing their immense characterization expertise with me and training me on various equipment. Thanks to Tanner FitzGerald and Barry Baber for their assistance in making and fixing our broken equipment; they are both miracle workers. My gratitude to Kimberly Fitzhugh-Higgins for her kindness and care through the most trying times of grad school. To Dr. James A Thomson for helping me get my general anxiety under control. I would also like to thank my groupmates: Naiming Liu, Eric Vetter, Eli Sullivan, Priya Ghatwai, Jatin Amatya, Chris Duska, Eva Rosker, Marie Phillips, and David Joo.

I would also like to acknowledge the groups whose equipment has made my research possible. Thanks to Professor Beth Opila for allowing me to collect data from her ICP and DSC. To Dr. Bonnie McFarland and Lucas Herweyer for their help running ICP samples and Rebekah Webster for training me on the DSC. To Dr. Michael Melia and Professor James Fitz-Gerald for use of their Excimer laser, and Dr. Brian Donovan and Professor Patrick Hopkins for their expertise in time

domain thermal reflection and collecting our thermal conductivity data. And finally, to Professor Gary Shiflet, for allowing me to use his arc-melter during the renovation of MSB.

Finally, I would like to thank my parents, Bert and Gaye Jensen, for their love and support. And my dear friends, Jenny Rosner, Teressa Paulsen, George Ebunga, Chris Eby, Andrew Cheung for all they have done to keep me sane over the last 5 years.

List of Figures

- Figure 1.1:** Diagram from Zhao et al. [1], demonstrating that hierarchical optimization at several lengthscales could significantly improve thermoelectric efficiency. We investigated the following lengthscales with their corresponding features: meso-scale through eutectic solidification, nano-scale through eutectoid decomposition, and atomic scale through Ge disposition control.....28
- Figure 1.2:** Diagram of a thermoelectric generator, a solid-state device that utilizes the movement of charge carriers, both holes and electrons, along a thermal gradient to produce an electrical current.....30
- Figure 1.3:** A graph plotting efficiency vs heat source temperature for different values of zT . Data points denote efficiencies and operating temperatures of other energy production means. [2].....31
- Figure 1.4:** Graphs depicting the relationship between thermoelectric properties and charge carrier density. Ranges indicating typical values of S , σ , κ_e , and κ_l for insulators, semiconductors and metals are denoted as well [3].....32
- Figure 1.5:** Si-rich region of the binary Fe-Si phase diagram [4]. The eutectic solidification at 73.5 at% Si and the eutectoid decomposition at 70.5 at% Si are marked with a blue and red arrow respectively. The unit cell for pertinent phases (made in CrystalMaker) are displayed to the right of the diagram.....34
- Figure 1.6:** Matlab generated plot showing κ_l of bulk Si-Ge alloys as a function of Ge fraction; the reduction in κ_l is due to alloy scattering.....35
- Figure 1.7:** The effect of aging conditions on thermoelectric properties as a function of temperature: a) thermal conductivity, b) electrical conductivity, c) Seebeck coefficient, and d) the

figure of merit. Changes in properties are caused by lengthscale differences of the two-phase $\beta + \text{Si}$ microstructure. Data taken from [6].....39

Figure 1.8: Plots comparing thermoelectric properties of powder processed and P-doped $\beta\text{-FeSi}_2$ and $\beta\text{-FeSi}_2 + \text{SiGe}$ composites: a) electrical conductivity, b) Seebeck coefficient, c) thermal conductivity, d) power factor, and e) figure of merit. Data taken from [7].....41

Figure 1.9: Simplified diagram depicting phonon scattering mechanisms in a crystalline material: phonon-boundary scattering at interfaces, phonon-impurity scattering at impurity atoms, and phonon-phonon scattering caused by interactions between phonons.....45

Figure 1.10: Plot of thermal boundary conductances as a function of temperature for various heterointerfaces and bond types. Red lines indicate the highest and lowest values observed in the phonon-dominated regime of thermal boundary conductance. [8].....46

Figure 2.1: a) Schematic of the large-capacity arc-melting chamber and b) the layout of the Cu hearth.....50

Figure 2.2: a) Schematic of the small-capacity arc-melting chamber and b) the layout of the Cu hearth. The Red x's mark crucibles that cannot be used for melting.....51

Figure 2.3: Simplified diagram of the pulse laser set-up. Samples were either pulse laser melted with the laser following Path 1, or a mirror could be inserted to direct the laser along Path 2 onto the immersed sample.....53

Figure 2.4: a) XRD spectrum showing compositional change in the SiGe (111) peak position, lower 2θ equates to greater Ge concentration. b) Plot showing differences in experimental and theoretical lattice parameter as a function of composition.....57

Figure 2.5: Schematic of the SEM in transmission mode, depicting the setup required for TKD analysis.....60

Figure 3.1: **Figure 3.1:** As cast microstructure from $\text{Fe}_{28.4}\text{Si}_{71.6}$ alloy viewed perpendicular to the axis of growth; the red arrow denotes the direction of solidification. a) Optical micrograph showing single phase α - FeSi_2 and cracks caused by solidification. b) EBSD map showing the α grain size and columnar structure.....64

Figure 3.2: As-cast microstructure of the hypoeutectic $\text{Fe}_{27}\text{Si}_{73}$ alloy. SEM-BSE micrographs of a) the irregular eutectic $\alpha + \text{Si}$ microstructure and microstructural cross-sections showing the macrosegregation from b) top and c) bottom of the boule as evidenced by differences in the microconstituent fractions. All images are viewed along the solidification direction.....66

Figure 3.3: Time-temperature-transformation (TTT) diagram for the ($\alpha \rightarrow \beta + \text{Si}$) eutectoid decomposition for pure and Cu contaminated [21]. The red circle indicates the aging parameters for our $\text{Fe}_{28.4}\text{Si}_{71.6}$ sample.....67

Figure 3.4: BSE-SEM micrographs depicting our two suggested nucleation modes. Colony nucleation occurring on a) cracks at 680 °C, with blue arrows showing the growth direction, and b) an example of the proposed mechanism of eutectic Si assisted nucleation at 800 °C.....68

Figure 3.5: a) Schematic illustrations of the eutectoid region and the Gibb's free energy diagrams showing the evolution of Si depletion in the α phase and the resulting effect on chemical driving force for β nucleation. b) SEM micrograph indicating epitaxial growth of eutectoid Si growing on eutectic Si.....69

Figure 3.6: The reaction front of β -FeSi₂ + Si colonies for Fe₂₇Si₇₃ samples partially aged at: a) 567 °C, b) 680 °C, c) 800 °C, and d) 910 °C.....71

Figure 3.7: a) SEM and b) EBSD images of the same nascent β + Si nucleus. The color denotes orientation. The β matrix (light blue) has indications of strain caused by the spatial alignment of Si lamellae, and this is observed as color variations.....73

Figure 3.8: Two TKD-EBSD maps showing eutectoid morphology, with corresponding nanowire pole figures. These pole figures clearly show a 180 ° rotation around the plane normal for (111) and ($\bar{1}\bar{1}\bar{1}$) planes, which is characteristic of twinning in FCC lattices. Each plane is labeled; we assigned the plane most parallel to the surface sample as (111).....74

Figure 3.9: SEM micrographs of ion cross-section of a) underaged and b) overaged Fe₂₇Si₇₃ samples. The surface and milled edge surfaces are perpendicular.....75

Figure 3.10: SEM micrographs depicting the effects of Rayleigh instability on eutectoid Si close to (Lamellae), and far away (Nanowire and Spheroid), from the reaction front. These images come from the Fe_{28.4}Si_{71.6} samples.....76

Figure 3.11: Arrhenius plot of $\ln(v\lambda^n)$ vs $1/T$, where the activation energy for the eutectoid decomposition occurs via interface or volume diffusion mechanisms. Bounds for the activation

energy are defined by plotting both interface and volume limited growth kinetics ($n = 2$ or 3 , respectively).....78

Figure 3.12: SEM micrograph of the transient degenerate pearlite (fine spheroids) prior to achieving steady state lamellae propagation, in the $\text{Fe}_{27}\text{Si}_{73}$ sample aged at $910\text{ }^\circ\text{C}$80

Figure 3.13: $\text{Fe}_{28.4}\text{Si}_{71.6}$ samples aged at a) $567\text{ }^\circ\text{C}$ for 56 hours to produce high β/Si heterointerface density, and b) $910\text{ }^\circ\text{C}$ to produce low β/Si heterointerface density. The lighter phase in both images is the β matrix and the darker phase is the Si phase.....82

Figure 3.14: EBSD micrographs for $\text{Fe}_{28.4}\text{Si}_{71.6}$ sample aged at a) $567\text{ }^\circ\text{C}$ for 56 hours and c) $910\text{ }^\circ\text{C}$ for 120 hours, with respective colony diameter distributions b) and d).....83

Figure 4.1: Micrographs of $\text{Fe}_{28}\text{Si}_{68}\text{Ge}_4$ alloy. a) Optical micrograph of the coarse, slow-cool eutectic microstructure, and BSE-SEM micrographs of b) a single $\text{Si}_{1-x}\text{Ge}_x$ lamella with entrained $\epsilon\text{-FeSi}$. c) BSE-SEM micrograph showing the rapid-cool eutectic microstructure. In all three images, the darkest phase is $\alpha\text{-FeSi}_{2+x}$ while the lightest phase is DC.....90

Figure 4.2: EBSD maps of $\text{Fe}_{28}\text{Si}_{68}\text{Ge}_4$ alloys produced by a) slow-cool and b) rapid-cool techniques. Heavy black lines indicate grain orientations that differ more than 15° , light black lines are differences greater than 5° and also denote the location of eutectic SiGe lamella. Insets show respective Z axis pole figures.....91

Figure 4.3: EBSD Map of the rapid-cooled $\text{Fe}_{28}\text{Si}_{68}\text{Ge}_4$. Differences in color denote changes in the α orientation, and the dark striations mark the location of SiGe lamellae. Inlays of $\alpha\text{-FeSi}_2$ crystal orientations show that SiGe lamellae are found singularly along the α (001) habit plane....93

Figure 4.4: SEM-BSE micrographs showing a) the faceted eutectic ribbons of $\text{Fe}_{27}\text{Si}_{73}$ (black), and b) the eutectic lamellae of $\text{Fe}_{28}\text{Si}_{68}\text{Ge}_4$ (white) and the faceted α phase.....94

Figure 4.5: EBSD Euler orientation maps, with the colony diameter distributions shown inset, for the binary slow-cool + 567 °C/56Hr. Black lines between grains depict crystal misorientation of 15°, and white grains are eutectic SiGe lamellae.....96

Figure 4.6: TKD-EDS composition map illustrating large amounts of Ge partition into eutectoid nanowires, with limited Ge remaining in the β matrix. The overlay in the center shows the transmission micrograph of the same area.....98

Figure 4.7: Representative XRD spectrum of an aged rapid-cool sample with the highest intensity peaks labeled.....99

Figure 4.8: Diagram depicting the lattice parameters and composition of DC phases determined by Rietveld refinement. Liquid and solid state processing controls the Ge disposition of DC nanoconstituents.....100

Figure 4.9: BSE-SEM micrographs of β + DC pearlitic colonies in the interlamellar regions of samples aged at 567 °C: a) slow-cool and b) rapid-cool samples. c) Rapid-cool sample aged at 900 °C with homogeneous dispersion of spheroidized particles.....102

Figure 4.10: Thermal conductivity plotted as a function of mean interface spacing. The symbols circled in red were aged at 567 °C and are similar in terms of microstructure.....103

Figure 4.11: The thermal conductivity as a function of DC phase composition. The open symbols are values predicted by Mattheissen's rule by only accounting for bulk and alloy scattering. The

solid symbols are the measured values. We attribute this discrepancy to additional scattering at the heterointerfaces.....106

Figure 4.12: Thermal boundary conductance for the $\beta/\text{Si}_{1-x}\text{Ge}_x$ heterointerface, calculated from Mattheissen's rule, as a function of Si nanoconstituent composition.....108

Figure 4.13: Theoretical curve derived from Mattheissen's rule, showing the change in κ_{Total} , with $\text{Si}_{69}\text{Ge}_{33}$ nanoinclusions, as a function of volume fraction and interface density. The yellow dot denotes κ for 25 nm wide nanowire with a TBC of $49 \text{ MW m}^{-2} \text{ K}^{-1}$109

Figure 5.1: Splat-cooled $\text{Fe}_{28}\text{Si}_{68}\text{Ge}_4$ sample pulsed twice with 2.5 J/cm^3 fluence. The laser-pulsed region, which is noted as having a large number of cracks and diffuse DC microconstituents, is bounded by black lines.....114

Figure 5.2: BSE-SEM micrographs of rapid-cooled a) $\text{Fe}_{28.4}\text{Si}_{71.6}\text{Ge}_4$ aged at $567 \text{ }^\circ\text{C}$ for 56 hrs showing eutectic and eutectoid DC, b) $\text{Fe}_{22.5}\text{Si}_{67.5}\text{Ge}_{10}$ with eutectic DC + ϵ lamellae, and c) $\text{Fe}_{23.5}\text{Ge}_{71.5}\text{Ge}_5$ with Si-rich proeutectic and Ge-rich eutectic phases. PLM microstructure of a) $\text{Fe}_{28.4}\text{Si}_{71.6}\text{Ge}_4$, b) $\text{Fe}_{22.5}\text{Si}_{67.5}\text{Ge}_{10}$, and c) $\text{Fe}_{23.5}\text{Ge}_{71.5}\text{Ge}_5$ alloys showing complete DC solid solubility in $\alpha\text{-FeSi}_2$118

Figure 5.3: $\text{Fe}_{22.5}\text{Si}_{67.5}\text{Ge}_{10}$ ribbon after PLM (2 pulses at 2.5 J/cm^2), depicting the close proximity of different $\alpha + \text{DC}$ microstructures. The blue outlines highlight $\alpha + \text{DC}$ colonies and the yellow lines mark the spatial alignments of DC inclusions. The different microstructures are described in the text.....120

Figure 5.4: Micrographs depicting different $\alpha + DC$ microstructures commonly observed in PLM samples: a) nascent Si-rich dendrites, and b) two periodic eutectic micrographs showing variations on colony morphology. These micrographs were taken from $Fe_{28}Si_{68}Ge_4$ ribbons that were pulsed twice at $2.5 J/cm^2$121

Figure 5.5: Micrograph of $Fe_{28}Si_{68}Ge_4$ depicting the cloudy morphology. An overlay made from image processing with a bandpass filter shows the particles within the diffuse interface. Wavy DC inclusions and clouds are shown to align themselves along perpendicular directions.....123

Figure 5.6: SEM micrograph a large eutectic colony with ribbon morphology, ribbons are shown to align along two perpendicular directions.....124

Figure 5.7: Micrographs depicting different $\alpha + DC$ microstructures commonly observed in PLM samples and fast Fourier transforms quantifying eutectic spatial alignment: a) global eutectic microstructure, b) a single eutectic colony highlighted in blue, c) a single ribbon eutectic colony, and d) a single colony with cloudy morphology.....126

Figure 5.8: PLM $Fe_{28}Si_{68}Ge_4$ sample (SPS disk) aged at $567^\circ C$ for 56 hrs. a) and b) Depicting unknown decomposition that occurs in DC supersaturated α phase. The reaction front between the supersaturated α and the disilicide + DC region is clearly defined.....128

Figure 5.9: PLM sample aged at $567^\circ C$ for 56 hrs, with a range of decomposition morphologies: a) Ge-rich lamellae decorated by epitaxial Si-rich DC particles, inlay uses a bandpass filter to highlight composition contrasts, b) darkening contrast of lamellae as homogenization dilutes Ge concentration, and range of decomposition morphologies ranging from the supersaturated α (rightmost), to homogenizing lamellae, to c) the leftmost area where recent decomposition is still limited to epitaxial particles.....129-130

Figure 5.10: Powder processed $\text{Fe}_{28}\text{Si}_{68}\text{Ge}_4$ samples that were melted with an IR laser for ~600 pulses. a) Heterogeneous microstructure consisting of eutectic lamellae, spheroids, and DC phase forming an apparently continuous layer in the α grain boundaries. b) Higher mag image depicting the fine eutectic lamellae.....133

Figure 6.1: Fe-Si-Ge ternary phase diagram in the Si-rich region, with isothermal sections at a) 1000 °C and b) 900 °C. Red lines denote tie lines connecting the FeSi_2 and DC compositions for measured compositions (black dots).....138

Figure 6.2: DCS curves of samples, $\text{Fe}_{22.5}\text{Si}_{67.5}\text{Ge}_{10}$ (Red) and $\text{Fe}_{23.5}\text{Si}_{71.5}\text{Ge}_5$ (Black) which are the compositions with the largest and smallest change in enthalpy due to $\text{L} \leftrightarrow \alpha\text{-FeSi}_2 + \varepsilon\text{-FeSi} + \text{Si}_{1-x}$ eutectic solidification, respectively.....142

Figure 6.3: a) 3D and b) 2D ternary surface plots of liquidus temperatures. Data points were taken from experimental measurements and Fe-Si, Si-Ge, and Fe-Ge binary phase diagrams. The blue curves bound the location of the $\varepsilon + \text{DC}$ cotectic line, above the upper line proeutectic ε forms and proeutectic DC forms below the lower line. The white oval indicates our estimate for the ternary eutectic point.....145

Figure 6.4: SEM micrographs of as-cast microstructures of a) $\text{Fe}_{27}\text{Si}_{63}\text{Ge}_{10}$ showing the proeutectic ε and b) $\text{Fe}_{22.5}\text{Si}_{67.5}\text{Ge}_{10}$ showing the presence of proeutectic DC. Inset shows the eutectic $\alpha + \varepsilon$ microstructure found at the edge of the eutectic DC lamellae. The cross sections were taken from the top of each boule.....146

Figure 6.5: a) Truncated ternary surface diagram of the Tammann triangle, the color gradient relates to the change in enthalpy. b) 3D diagram depicting the measured liquidus surface (ranging

from red to purple) as it slopes towards lower temperatures in respect to the eutectic isotherm (yellow plane).....148

Figure 7.1: Micrographs depicting lengthscales of eutectic lamellae made by arc-melting, melt-spinning, and pulse laser melting techniques. The scale bars for the illuminated areas and the inlays are consistent.....151

Figure 7.2: Plot showing the decrease in TBC as a function of at% Ge. The data points are color coded to the micrographs and corresponding $\beta/\text{Si}_{1-x}\text{Ge}_x$ interface.....152

Figure 7.3: Combination of 900 and 1000 °C isothermal sections. ϵ is not stable at equilibrium in the blue region, only stable above the eutectoid isotherm in the purple region, and is stable above and to an unknown temperature below the eutectoid isotherm.....154

Figure A2.1: The HighScore Plus program, with important tabs and windows marked for reference.....168

Figure A2.2: Expanded “Refinement Control” and “Object Inspector” windows.....171

Figure A4.1: TEM images with an unknown scale bar, showing the sharp interface between the β matrix and a) the crystalline DC nanowire and b) the amorphous DC nanowire. The colored lines are oriented along atom rows.....177

Figure A4.2: TEM-EDS map depicting the disposition of constituent elements. Ge disposition is mostly inside the nanowires, because it was ejected during the eutectoid phase transformation. It should also be noted that Co substitutes Fe sites in the β matrix.....178

- Figure A5.1:** Plot using the Callaway-Debye model to show the effects on Ge fraction and lengthscale of SiGe nanowires on thermal conductivity.....181
- Figure A5.2:** Comparison of thermal conductivities predicted by the Callaway-Debye model and measurements taken via TDTR.....182
- Figure A6.1:** Simplified model to determine a) the perimeter to area ratio of a 2D system and b) the surface area to volume ratio for a 3D system. The dimensions of the Si inclusions and the β matrix are labeled.....183
- Figure A6.2:** Plot of 2D and 3D models showing the change in interface density as a function of inclusion thickness, ranging from large (lamellae) to small (nanowire). The geometric correction factor at $0.03 \mu\text{m}$ is 2.....185
- Figure A6.3:** Plot of 2D and 3D models showing the change in interface density as a function of spheroid radius. The geometric correction factor is consistently 1.5.....187
- Figure A7.1:** Surface plots using Matthiessen's equations to determine the theoretical κ_t as a function of interface density and volume fraction. κ_{DC} and h_k were obtained from a given at% Ge inclusion: a) 0 at% Ge, b) 6 at% Ge, c) 18 at% Ge, and d) 31 at% Ge. The yellow dots designate the interface density of $\sim 22 \text{ int}/\mu\text{m}$, and this falls around our measured thermal conductivity values.....189-191
- Figure A8.1:** Simplified diagram depicting the liquid pulse laser ablation process. First the incident laser pulse heats the sample surface, and creates a plasma plume. The liquid medium constrains the growth of the plume which then coalesces into nanoparticles.....193

Figure A8.2: SEM micrographs of ablated SPS disks, over-processing caused the surface to bead up. PLA was performed in a) ethanol immersion and b) Ar atmosphere. c) A cross-section of the beads reveals that only the outside layer was affected.....195

Figure A8.3: Micrographs showing a a) pre-PLA powder particle with rough edges and b) a powder particle covered in ablated nanoparticles.....197

List of Tables

Table 2.1: Wyckoff numbers for phases present in the Si-rich region of the Fe-Si-Ge ternary phase diagram.....56

Table 3.1: Aging parameters used with Fe₂₇Si₇₃ samples to produce intermediate stages of decomposition.....68

Table 3.2: Determined growth rate and interlamellar spacing found for each aging temperature found in Figure 3.6.....72

Table 4.1: Composition of microconstituents for slow-cool and rapid-cool samples.....97

Table 4.2: Summary of relevant data for and results of the Mattheissen's rule calculations.....107

Table 6.1: Rietveld Refinement data for all compositions and homogenization treatments. The “f” values are the volume fractions of the respective phases.....140

Table 6.2: Rietveld Refinement determined lattice parameters of iron silicides of all baseline and Ge alloyed compositions. Units are in Å.....141

Table 6.3: Compiled DSC data for all compositions.....143

List of Terms and Symbols

α : α -FeSi₂

BSE: Backscattered Electrons

β : β -FeSi₂

n: Carrier Concentration

K: Constant

ρ : Density

DC: Diamond Cubic

DSC: Differential Scanning Calorimetry

D: Diffusivity

EBSD: Electron Backscatter Diffraction

e⁻: Electrons

m^{*}: Effective Mass of Electron

σ : Electrical Conductivity

EDS: Energy Dispersive Spectroscopy

$\frac{\Delta S_f^b}{R}$: Entropy of Fusion

ϵ : ϵ -FeSi

FFT: Fast Fourier Transform

GOF: Goodness of Fit

∇ : Gradient

v_g : Group Velocity

V: Growth Rate

v: Growth Velocity

c_p: Heat Capacity at Constant Pressure

c_v: Heat Capacity at Constant Volume

q: Heat Flux

T_{Cold}: Heat Sink

T_{Hot}: Heat Source

h^+ : Holes

ICP-OES: Inductively Coupled Plasma – Optical Emission Spectroscopy

ρ_{int} : Interface Density

λ : Interlamellar Spacing

JMA: Johnson-Mehl-Avrami

∇^2 : Laplace Operator

a: Lattice Parameter

L: Liquid Phase

LPLA: Liquid Pulse Laser Ablation

λ_{MFP} : Mean Free Path

pO: Partial Pressure of Oxygen

$S^2\sigma$: Power Factor

PLM: Pulse Laser Melting

$\frac{\partial T}{\partial t}$: Rate of Change of Temperature with Respect to Time

SEM: Scanning Electron Microscopy

S: Seebeck Coefficient

S-K: Shapiro and Kirkaldy

T: Temperature

h_k : Thermal Boundary Conductance

κ : Thermal Conductivity

κ_e : Thermal Conductivity from Charge Carriers

κ_l : Thermal Conductivity from Lattice Vibrations

ΔT : Thermal Gradient

zT: Thermoelectric Figure of Merit

t: Time

TDTR: Time Domain Thermoreflectance

κ_{Total} : Total Thermal Conductivity

TEM: Transmission Electron Microscope

TKD: Transmission Kikuchi Diffraction

UV: Ultra-Violet

V: Volume

f : Volume Fraction

XRD: X-Ray Diffraction

Table of Contents

Abstract.....	1
Acknowledgements.....	4
List of Figures.....	6
List of Tables.....	17
List of Terms and Symbols.....	18
1 Introduction.....	28
1.1 Motivation.....	28
1.2 Background.....	29
1.2.1 Thermoelectrics.....	29
1.2.2 Modern Thermoelectric Research.....	33
1.2.3 Phases Present in the Fe-Si Based Thermoelectric.....	34
1.2.4 Eutectic and Eutectoid Processing.....	36
1.2.5 Prior Work on Binary Fe-Si Alloys.....	38
1.2.6 Prior Work on Ternary Fe-Si-Ge Alloys.....	40
1.2.7 Thermal Conductivity.....	43
1.3 Thesis Organization.....	47
2 Material Processing and Characterization Methods.....	49
2.1 Sample Fabrication.....	49

	22
2.1.1 Large-Capacity Arc-Melter/Melt-Spinner.....	49
2.1.2 Small-Capacity Arc-Melter.....	50
2.1.3 Oxide Surface Layer and Partial Pressure of Oxygen.....	51
2.1.4 Pulse Laser Ablation (PLA).....	52
2.1.5 Sample Encapsulation in Inert Atmosphere.....	53
2.1.6 Isothermal Heat Treatments in Tube Furnace.....	54
2.1.7 Sample Mounting in Epoxy.....	54
2.2 Characterization Techniques.....	55
2.2.1 X-Ray Diffraction (XRD).....	55
2.2.1.1 Rietveld Refinement.....	55
2.2.1.2 Lattice Parameter and Composition, Vegard's Law.....	56
2.2.2 Scanning Electron Microscope (SEM).....	57
2.2.2.1 Energy Dispersive Spectroscopy (EDS).....	58
2.2.2.2 Electron Backscatter Diffraction (EBSD).....	58
2.2.2.3 Linear Intercepts Method.....	59
2.2.2.4 Transmission Kikuchi Diffraction (TKD).....	59
2.2.3 Inductively Coupled Plasma – Optical Emission Spectroscopy (ICP-OES)..	61
2.2.4 Differential Scanning Calorimeter (DSC).....	61
2.2.5 Time Domain Thermoreflectance.....	62

3 Binary Fe-Si Alloys.....	63
3.1. Binary Fe-Si Alloys.....	63
3.1.1 Solidification of Molten $\text{Fe}_{27}\text{Si}_{73}$ and $\text{Fe}_{28.4}\text{Si}_{71.6}$ Boules.....	64
3.1.2 ICP Determined Compositions and the Effect of Cu Impurity on Decomposition Rate.....	65
3.2 Hypoeutectic $\text{Fe}_{27}\text{Si}_{73}$ - Mechanisms of Eutectoid Decomposition.....	68
3.2.1 Nucleation Mechanism for Eutectoid Decomposition.....	68
3.2.2 Eutectoid Microstructure of β/Si Colonies.....	71
3.2.3 Rayleigh Instability of Eutectoid Microstructure.....	74
3.2.4 Activation Energy of Eutectoid Decomposition.....	77
3.2.5 Divorced Eutectoid Decomposition in High-Temperature Conditions.....	79
3.3 $\text{Fe}_{28.4}\text{Si}_{71.6}$ - Effect of Eutectoid Structure on Thermal Transport.....	81
3.3.1 Density of Heterointerfaces.....	81
3.3.2 Thermal Conductivity.....	83
3.3.3 Thermal Boundary Conductance.....	84
3.4 Summary.....	86
4 Fe-Si-Ge Ternary Alloy.....	88
4.1 Microstructural Lengthscales Induced by Solidification.....	88

4.1.1 Eutectic Microstructure of Fe ₂₈ Si ₆₈ Ge ₄ alloy.....	89
4.1.2 Ternary Eutectic Microstructure.....	93
4.1.3 Eutectoid Microstructure.....	95
4.1.4 Size of β + Eutectoid SiGe Colonies.....	95
4.2 How Processing Determines Ge Disposition.....	97
4.2.1 Silicide Phase Compositions.....	97
4.2.2 Eutectic and Eutectoid SiGe Compositions.....	99
4.3 Thermal Transport.....	101
4.3.1 Thermal Conductivity of Hierarchically Processed Fe ₂₈ Si ₆₈ Ge ₄	101
4.3.2 Phonon Scattering of β /DC Heterointerface.....	104
4.4 Future Directions.....	108
4.5 Conclusions.....	110
5 Ultra-Rapid Solidification via Pulse Laser Processing.....	112
5.1 Processing Parameters for Base Materials.....	112
5.1.1 Additional Fe-Si-Ge Alloys.....	112
5.1.2 Challenges of Pulse Laser Melting.....	113
5.1.3 Excimer Parameters.....	115

5.1.4 Sample Processing Routes.....	116
5.2 Microstructure Resulting from PLM.....	117
5.2.1 Supersaturated α -FeSi ₂	117
5.2.2 α + DC Microstructures from PLM.....	119
5.2.3 Fast Fourier Transform of DC inclusions.....	125
5.3 Microstructures of PLM Samples After Aging.....	126
5.3.1 Decomposition in Supersaturated α Regions.....	127
5.3.2 Decomposition in Eutectic α + DC Regions.....	129
5.3.3 Transformation Rate.....	132
5.4 Future Directions.....	132
5.5 Summary.....	134
6 Fe-Si-Ge Ternary Phase Diagram.....	136
6.1 Key Isothermal Sections in the Si-rich Region.....	136
6.2 Lattice Parameters of Iron Silicides with Ge Incorporation.....	139
6.3 DSC Analysis.....	141
6.3.1 Temperature of Phase Transformations.....	141
6.3.2 Liquidus Surface and Microstructure of As-Cast Alloys.....	144

6.3.3 Tammann Triangle.....	147
6.4 Conclusion.....	147
7 Conclusion.....	150
7.1 Summary.....	150
7.2 Future Work.....	154
References.....	156
Appendix 1: Procedures for Mounting a Melt-Spun Ribbon in Epoxy.....	166
Appendix 2: Procedure for Rietveld Refinement.....	168
Appendix 3: Mirror-Shine Polish Procedures.....	175
Appendix 4: Preliminary TEM.....	177
Appendix 5: Callaway-Debye Model and Size Effect.....	180
Appendix 6: 2D to 3D Interface Density – Geometric Correction Factor.....	183
A.6.1 Nanowires to Lamellae.....	183
A.6.2 Spheroids.....	186
Appendix 7: Models for Predicting Thermal Conductivity.....	188

Appendix 8: Attempts at Liquid Pulse Laser Ablation.....	193
A8.1 LPLA of SPS Disks.....	194
A8.2 LPLA of Powder.....	196

1 Introduction

1.1 Motivation

Current means of energy production are highly inefficient. Research from the Lawrence Livermore National Laboratory estimates that ~68% of the energy the United States produced yearly, from 2015 to 2017, was rejected as waste heat [9]. The last decade has seen a societal push for technologies to increase power efficiency and seek renewable, sustainable, and eco-friendly energy production means. One such direction is direct energy conversion via thermoelectric materials. These materials are solid-state “generators” that convert a thermal gradient into an electrical

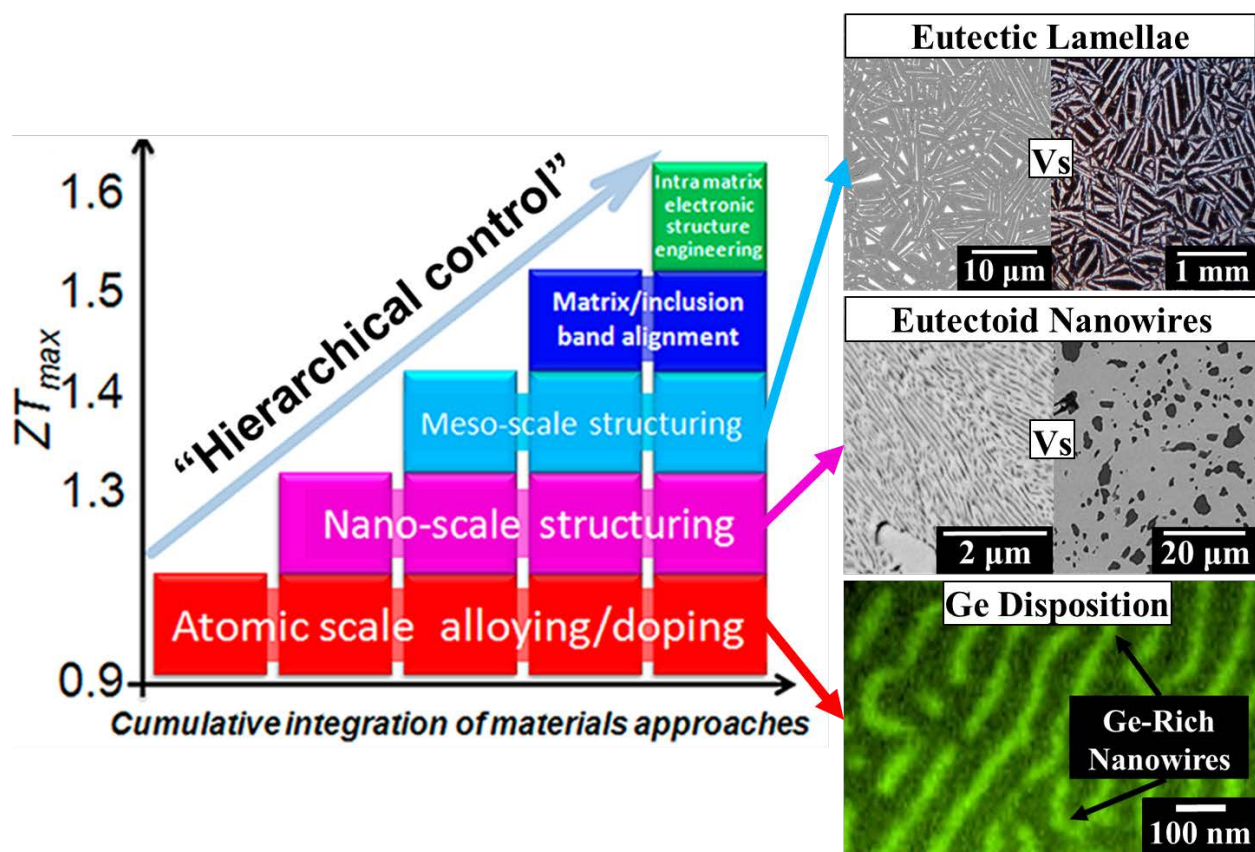


Figure 1.1: Diagram from Zhao et al. [1], demonstrating that hierarchical optimization at several lengthscales could significantly improve thermoelectric efficiency. We investigated the following lengthscales with their corresponding features: meso-scale through eutectic solidification, nano-scale through eutectoid decomposition, and atomic scale through Ge disposition control.

current without moving parts. If thermoelectric devices collected even 10% of the annual waste heat, it could provide enough electricity to power 180 million homes. However, modern thermoelectrics do not have the efficiency suitable for commercial use and are rarely used beyond niche applications such as satellite power generators and Peltier coolers [10].

To create a viable thermoelectric material, we sought to optimize the Fe-Si-Ge alloy system. We chose this alloy system because it is eco-friendly, and made from inexpensive and abundant constituents. In this work, we only investigated atomic-scale, nano-scale, and meso-scale structuring and their effects on thermal conductivity; these microstructural lengthscales can be seen in Figure 1.1. The Fe-Si-Ge alloy systems provide opportunities for hierarchical structuring by exploiting a strategy combining both liquid and solid-state processing. Eutectic solidification ($L \rightarrow \alpha\text{-FeSi}_{2+\delta} + \text{Si}_{1-z}\text{Ge}_z$) leads to meso-scale structuring of $\text{Si}_{1-y}\text{Ge}_y$ lamellae and the lamellar spacing further controls eutectoid colony grain size. Subsequent eutectoid decomposition ($\alpha\text{-FeSi}_{2+\delta} \rightarrow \beta\text{-FeSi}_2 + \text{Si}_{1-y}\text{Ge}_y$), results in a nanoscale structural inhomogeneity, interleaved within the eutectic lamellae. Atomic-scale structuring occurs through the control of Ge disposition inside nanoinclusions via eutectic and eutectoid processing, and will be shown to have the strongest effect on phonon scattering.

1.2 Background

1.2.1 Thermoelectrics

Thermoelectrics are solid-state materials that can convert a temperature gradient into an electrical current. Figure 1.2 depicts a diagram of a thermoelectric generator, which consists of a p-type (excess holes, h^+) and n-type (excess electrons, e^-) semiconductor connected to a heat source (T_{hot}) and a heat sink (T_{Cold}). Charge carriers behave like a diffuse gas and diffuse down the temperature

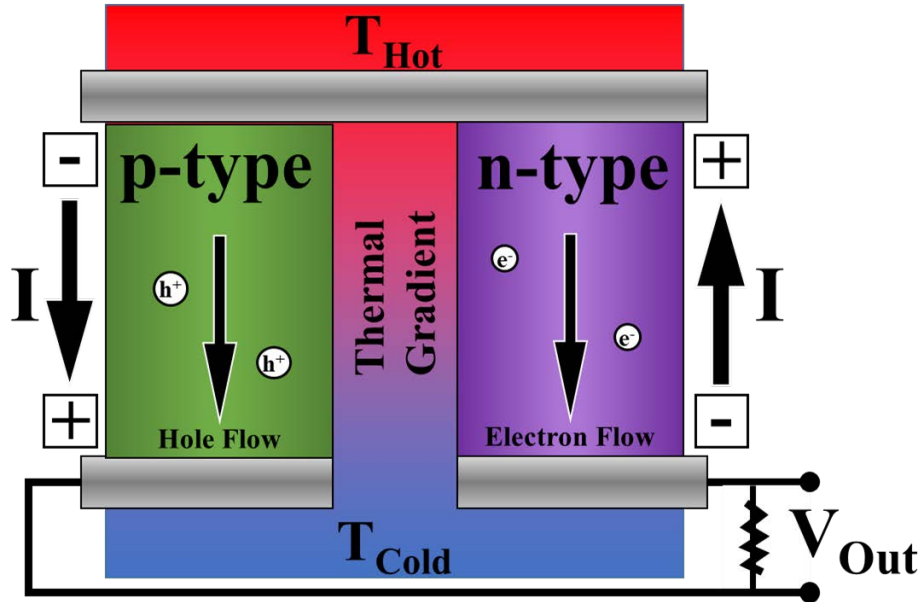


Figure 1.2: Diagram of a thermoelectric generator, a solid-state device that utilizes the movement of charge carriers, both holes and electrons, along a thermal gradient to produce an electrical current.

gradient; it is this coordinated movement of holes and electrons that creates an electrical current (I). For a thermoelectric to be efficient, it is necessary to have good charge carrier density and mobility. It is imperative that the material does not reach thermal equilibrium quickly, removing the driving force and terminating current production. One modern strategy for an ideal thermoelectric is described as the “phonon glass/electron crystal” [11]; where electrons flow unimpeded like in a periodic crystal lattice, but phonons are heavily scattered like in an amorphous glass. Simultaneously maximizing electrical conductivity while minimizing thermal conductivity is a nontrivial materials science challenge.

A material’s thermoelectric efficiency is quantified by a dimensionless figure of merit:

$$zT = \frac{S^2 \sigma T}{\kappa_e + \kappa_l} \quad 1-1$$

where S is the Seebeck coefficient – the magnitude of the induced voltage per temperature gradient and is related to the average energy of charge carriers, σ is the electrical conductivity, and together

$S^2\sigma$ is known as the power factor. There are two mechanisms by which thermal conduction occurs: heat can be carried by charge carriers (κ_e), and by lattice vibrations called “phonons” (κ_l). Phonons and heat transfer will be discussed in more detail later in this chapter. T is the temperature, noting that the materials properties are themselves temperature dependent. Figure 1.3 shows the efficiency of several zT values as a function of heat source temperature, as well as the efficiencies of other forms of energy production [2]. It is only been recently that a $zT > 2$ at 923 K has been achieved [12], but significant improvement must be made if they are to be as efficient as other energy production technologies.

Individual optimization of these parameters is nontrivial as they are inextricably connected. This dissertation specifically investigated how to reduce κ_l and is undoubtedly doing so at the expense of σ ; crystal defects, such as impurity atoms and interfaces, are scattering sites for electrons as well as phonons. With precise doping it is possible to improve $S^2\sigma$ [3], and mitigate and overcome the disadvantage caused by crystal defects. As shown in Figure 1.4, the increase in carrier density

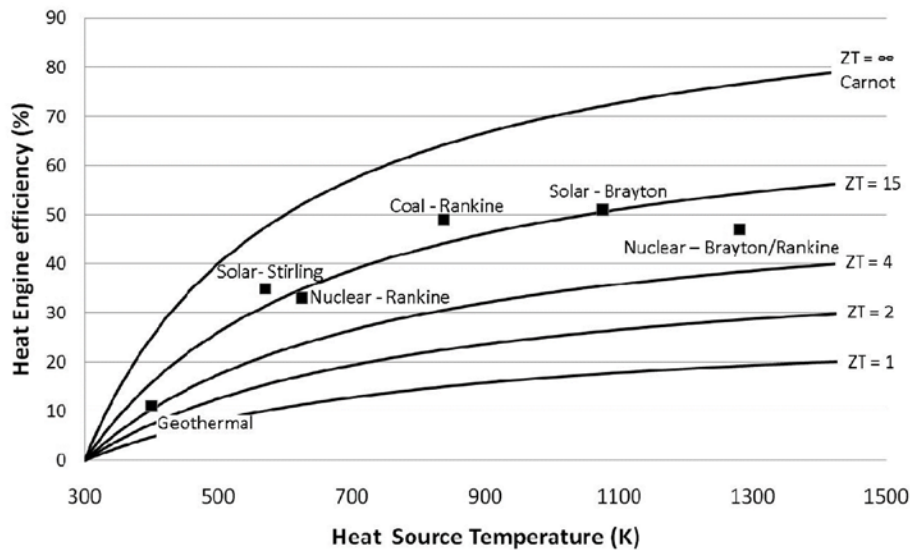


Figure 1.3: A graph plotting efficiency vs heat source temperature for different values of zT . Data points denote efficiencies and operating temperatures of other energy production means. [2]

improves electrical conduction due to the greater number of charge carriers, however, the new carriers also lower S . This is because the Seebeck coefficient is proportionally dependent on:

$$S \sim \frac{m^*}{n^{2/3}} \quad 1-2$$

where m^* is the effective mass and n is the carrier concentration. Heavy carriers have lower mobilities and thus low electrical conductivities. The increase in σ is caused by an increase in

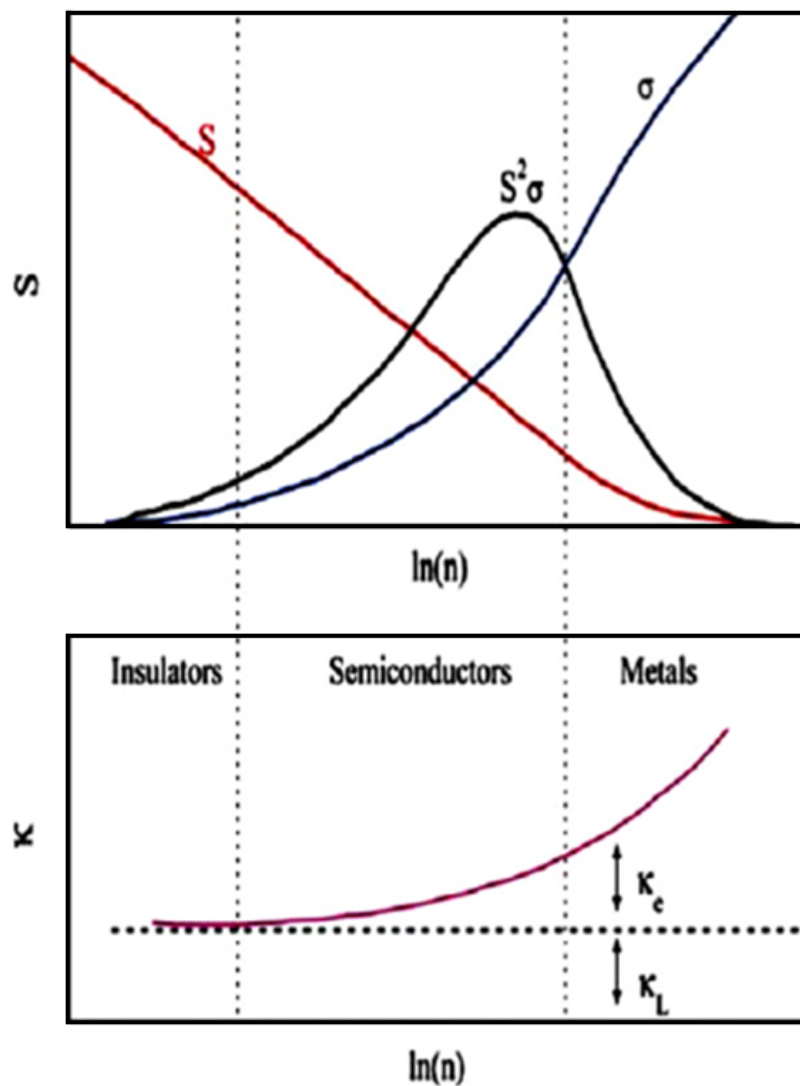


Figure 1.4: Graphs depicting the relationship between thermoelectric properties and charge carrier density. Ranges indicating typical values of S , σ , κ_e , and κ_l for insulators, semiconductors and metals are denoted as well [3].

lighter, lower energy carriers [11]. Maximization of $S^2\sigma$ can be achieved by careful doping; however, this is beyond the scope of this dissertation.

1.2.2 Modern Thermoelectric Research

Most modern, high efficiency thermoelectric materials seek to increase thermoelectric efficiency by pursuing the phonon glass-electron crystal model. A review from Snyder et al. [13] describes some of the strategies to obtain a phonon glass-electron crystal material: 1) create disorder within the unit cell via alloying with isoelectric cation and anions, which does not reduce σ but does reduce κ ; 2) exploit materials with large, complex crystal structures [11][3], such as PbTe [14][15] and Bi₂Te₃ [16][17]-based alloys, which have inherently low κ_l and high S; and 3) synthesize nanostructured two-phase materials, for example, made by either eutectoid decomposition or powder processing, which creates large heterointerface densities [18] and small grain sizes [11]. Other approaches are possible; for example, Zebarjadi et al. show improvement $S^2\sigma$ via “electron screening” caused by metallic nanoparticles donating electrons and acting as scattering sites for low energy electrons [19][20][21].

Our approach to improve thermoelectric efficiency was inspired by Zhao *et al.* [1], which suggests that hierarchical control and careful optimization across multiple lengthscales could significantly improve thermoelectric efficiency, Figure 1.1. This paper is also the inspiration for our hierarchical approach. Recent work performed by the Kanatzidis group on PbTe-SrTe alloys demonstrates the potential of the hierarchical structuring approach [1]. They employed nonequilibrium solidification techniques to supersaturate PbTe with Sr. This allowed for hierarchical structuring along the following lengthscales: 1) atomic-scale: utilizing doping and alloy scattering from Na doping and Sr; 2) nano-scale: through precipitation of copious nanoscale SrTe precipitates; 3) meso-scale: fine grains via powder processing; and 4) bandgap engineering: valence band

convergence of PbTe due to Sr alloying and valence band alignment between the precipitate and matrix. This emphasis on hierarchical structuring has successfully increased zT to an unprecedented 2.5 at 923 K [12].

1.2.3 Phases Present in the Fe-Si Based Thermoelectric

Figure 1.5 [4] shows the Si-rich region of the ternary phase diagram, along with the crystal structures of the four phases encountered over the course of this project: α -FeSi₂, β -FeSi₂, ϵ -FeSi, and Si_{1-x}Ge_x which we also refer to as diamond cubic (DC).

α -FeSi₂ is the metallic, high temperature iron disilicide phase. It has a tetragonal lattice, P4/mmm space group, and 1 formula unit per unit cell. α -FeSi₂ is a nonstoichiometric phase; with a Fe

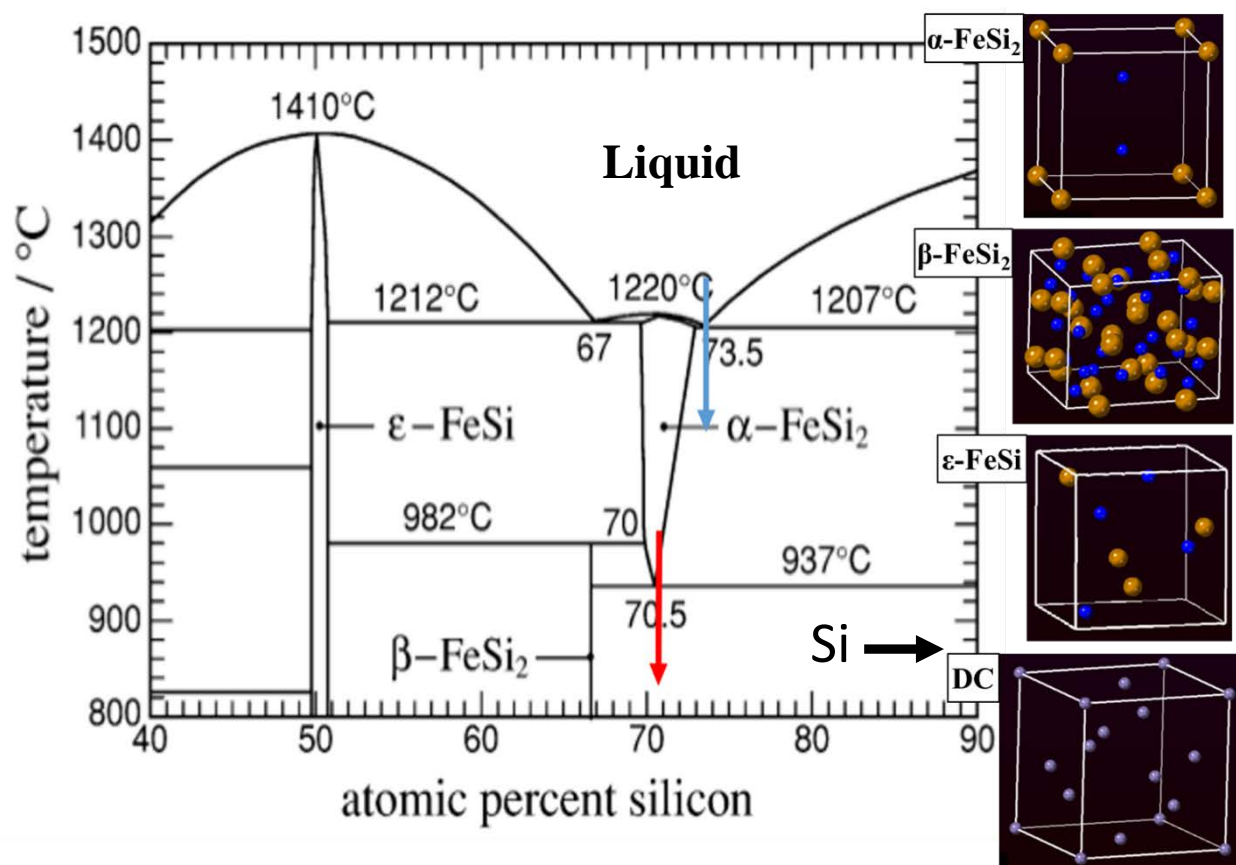


Figure 1.5: Si-rich region of the binary Fe-Si phase diagram [4]. The eutectic solidification at 73.5 at% Si and the eutectoid decomposition at 70.5 at% Si are marked with a blue and red arrow respectively. The unit cell for pertinent phases (made in CrystalMaker) are displayed to the right of the diagram.

vacancy concentration that can be as large as 13-18% [22][23], and is stable over a wide compositional range. The α phase is often referred to as α -FeSi₂ or α -Fe₂Si₅ [24][25]. However, it would be more accurately expressed as α -FeSi_{2+ δ} , where δ is the “excess” Si caused by Fe vacancies. The reason we do not refer to the phase as α -Fe₂Si₅ is because the ideal unit cell has 1 Fe and 2 Si atoms. This phase is stable at high temperatures, but decomposes through a eutectoid isotherm at 937 °C to stoichiometric β -FeSi₂ and Si [4].

β -FeSi₂ has many appealing properties for a potential thermoelectric material. It is one of the few semiconducting transition metal silicides with an indirect bandgap of $E_{\text{gap}} = 0.78$ eV [26]. β is a stoichiometric line compound that occurs at low temperatures. The complex orthorhombic crystal structure, Cmca space group with 16 formula units per unit cell, contributes to a naturally high Seebeck coefficient and low thermal conductivity [27]. It is oxidation resistant up to 900 K, made from inexpensive constituents, and is easily synthesized. However, the thermoelectric performance is limited by poor electrical conductivity [24].

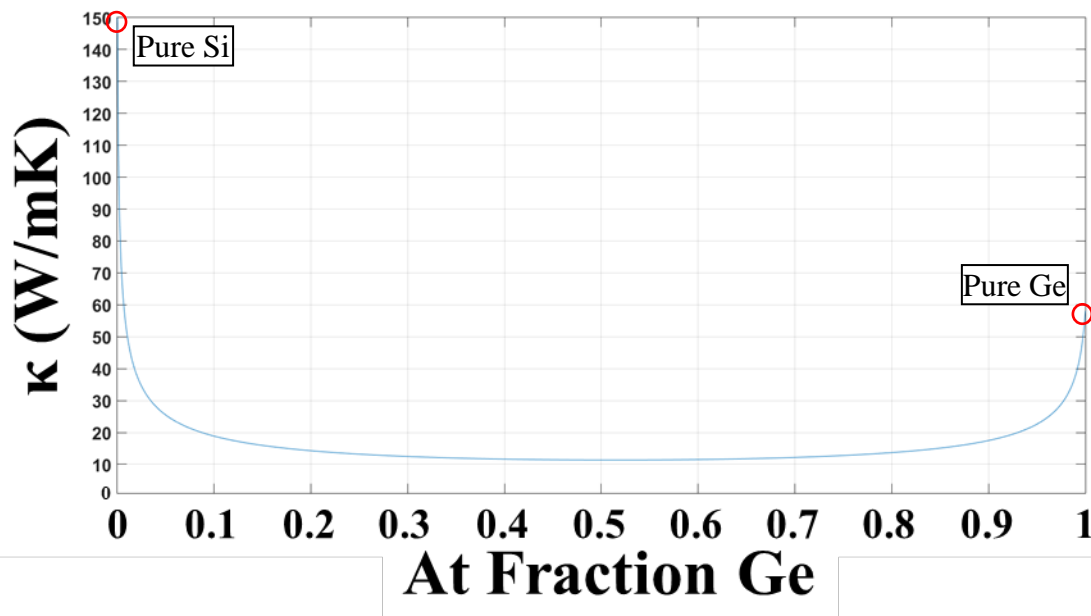


Figure 1.6: Matlab generated plot showing κ_l of bulk Si-Ge alloys as a function of Ge fraction; the reduction in κ_l is due to alloy scattering.

The ϵ -FeSi phase has a B20 crystal structure and P2₁3 space group with 4 formula units per unit cell [28]. It is often referred to as a metallic phase [29] but is actually a narrow bandgap semiconductor (~ 0.1 eV) [28][30] and only exhibits semiconductor properties at low temperatures. Since it acts like a poor metal at elevated temperatures, copious nucleation of ϵ inclusions were avoided whenever possible as it can have deleterious effects on thermoelectric properties. The ϵ phase is predominantly a concern in our ternary Fe-Si-Ge experiments, where it occurs over a broad compositional range along with the disilicide and DC phases.

Any Si (Fe-Si binary alloys) or Si_{1-x}Ge_x (Fe-Si-Ge ternary alloys) rejected by the intermetallic phases form a completely miscible Si_{1-x}Ge_x alloy as a diamond cubic microconstituent. It should be noted that Fe also has negligible solubility in Si and Ge. The literature establishes SiGe as an efficient thermoelectric material; an n-type Si₈₀Ge₂₀ can have a zT of 1 with maximum efficiency at 900 °C [11]. There are two immediate benefits to compositing this alloy into the β -FeSi₂ matrix. Ge alloying can reduce thermal conductivity via alloy scattering of phonons [5]. As seen in Figure 1.6, alloy scattering has a profound effect on thermal conductivity; even small concentrations of Ge efficiently minimize thermal conductivity to ~ 12 W/mK, as opposed to 149 W/mK and 58 W/mK for pure Si and Ge respectively. The DC bandgap can also be tuned by Ge concentration [31][32], however band-gap engineering as a hierarchical structuring approach was beyond the scope of this project.

1.2.4 Eutectic and Eutectoid Processing

As shown in Figure 1.5, the Si-rich region has liquid and solid-state phase transformations that aid in the hierarchical structuring of Fe-Si based alloys. Eutectic solidification occurs when two solid phases with different crystal structures grow simultaneously from an undercooled liquid. This growth often occurs cooperatively and creates periodic and alternating lamellae/lathes/rods when

the liquid/solid interface is quasi-planar. Lamellar spacing (λ) is determined by the diffusion length of solute, and temperature, at the solidification front. Faster cooling rates result in a smaller diffusion distances that in turn result in finer eutectic lengthscales. It can also be viewed in thermodynamic terms, where the undercooling provides the energy to create heterointerfaces [33][34]. If the reaction front moves faster than the diffusion of solute in the liquid phase then it is possible for phases to become supersaturated beyond the normal solubility limit, which is called solute trapping [35]. This is caused by extreme solidification rates like those achieved by melt-spinning and pulse laser melting. Both meso-scale and atomic-scale structuring are also dependent upon solidification rate. We explored a range of solidification rates ranging from 10^2 °C/s (ambient cooling) to 10^6 °C/s (melt-spinning) to 10^9 °C/s (pulse laser melting).

The eutectoid decomposition is analogous to eutectic solidification except it is an entirely solid-state transformation. Like the eutectic, the fine lamellar morphology can result from the cooperative growth of product phases. As will be discussed in Chapter 3, uncoupled or “divorced” eutectoid is also possible, and occurs when the matrix phase grows faster than the other; this typically forms finely dispersed spheroids in a continuous matrix phase. Lamellar spacing is governed by the degree of undercooling, and can also be viewed as caused by either temperature-limited diffusion lengths or the undercooling providing energy to create additional heterointerfaces [33].

Eutectoid decomposition results in a pearlitic microstructure consisting of DC lamellae in a β -FeSi₂ matrix. Manipulation of the pearlitic microstructure provides a route for hierarchical structural control determined by composition, processing methodology, and aging parameters. By controlling the eutectoid decomposition kinetics, we can vary lengthscales and morphology of the

Si phase. This allows for the modification of phonon scattering by tailoring the β -FeSi₂/Si heterointerface density and the β -FeSi₂/Si grain size distribution.

1.2.5 Prior Work on Binary Fe-Si Alloys

The β -FeSi₂ phase is a well-studied semiconductor, and its thermoelectric properties have been well documented. Single-phase β has only a modest zT , with the best reported value being $zT = 0.4$ for Co-doped β -FeSi₂ [36]. Several effective dopants have been identified for p-type and n-type doping on substitutional Fe [27][37] and Si [38] sites. Alloying with isoelectric and isostructural elements such as Ru, Os, and Ge has also been shown to improve properties [39][26]. Several methods have been explored for synthesizing single-phase β material. The previous references synthesized their samples by powder processing, from either previously arc-melted material or stoichiometrically weighed powders of Fe and Si, via high-energy ball milling and spark plasma sintering (SPS). There are benefits to powder processing as opposed to casting: the SPS process can circumvent densification issues which will be discussed in the follow chapters, and creates fine α grains which in turn refine the β grain size [40]. Yamauchi et al. [41] used suction casting of stoichiometric β -FeSi₂. β is a line compound and achieving a single-phase material is nontrivial, as often times slight compositional variations give rise to ϵ or Si inclusions. They sought to minimize the ϵ nucleation upon solidification by alloying with Cu. From this work, they have shown that ϵ provides low-energy nucleation sites for β grains and enhances the nucleation rate; however, it was also shown that the peritectoid transformation ($\epsilon + \alpha \rightarrow \beta$) is sluggish and they were not able to solutionize the ϵ particles. Other papers attempting to utilize the peritectoid reaction (α -FeSi₂ + ϵ -FeSi \rightarrow β -FeSi₂) to reduce β grain size [41][41][41][41][37][40][42] also found that complete transformation cannot be achieved in reasonable timescales. Cu was shown to suppress primary ϵ nucleation during the synthesis

process. A Johnson-Mehl-Avrami (JMA) analysis revealed that Cu accelerates the eutectoid decomposition., speeding up phase transformation by Cu.

Another route to enhance β -FeSi₂ is to introduce an additional phase by exploiting the eutectoid decomposition (α -FeSi₂ \rightarrow β -FeSi₂ + Si) found at 70.5 at% Si in Fe-Si binary system, Figure 1.5.

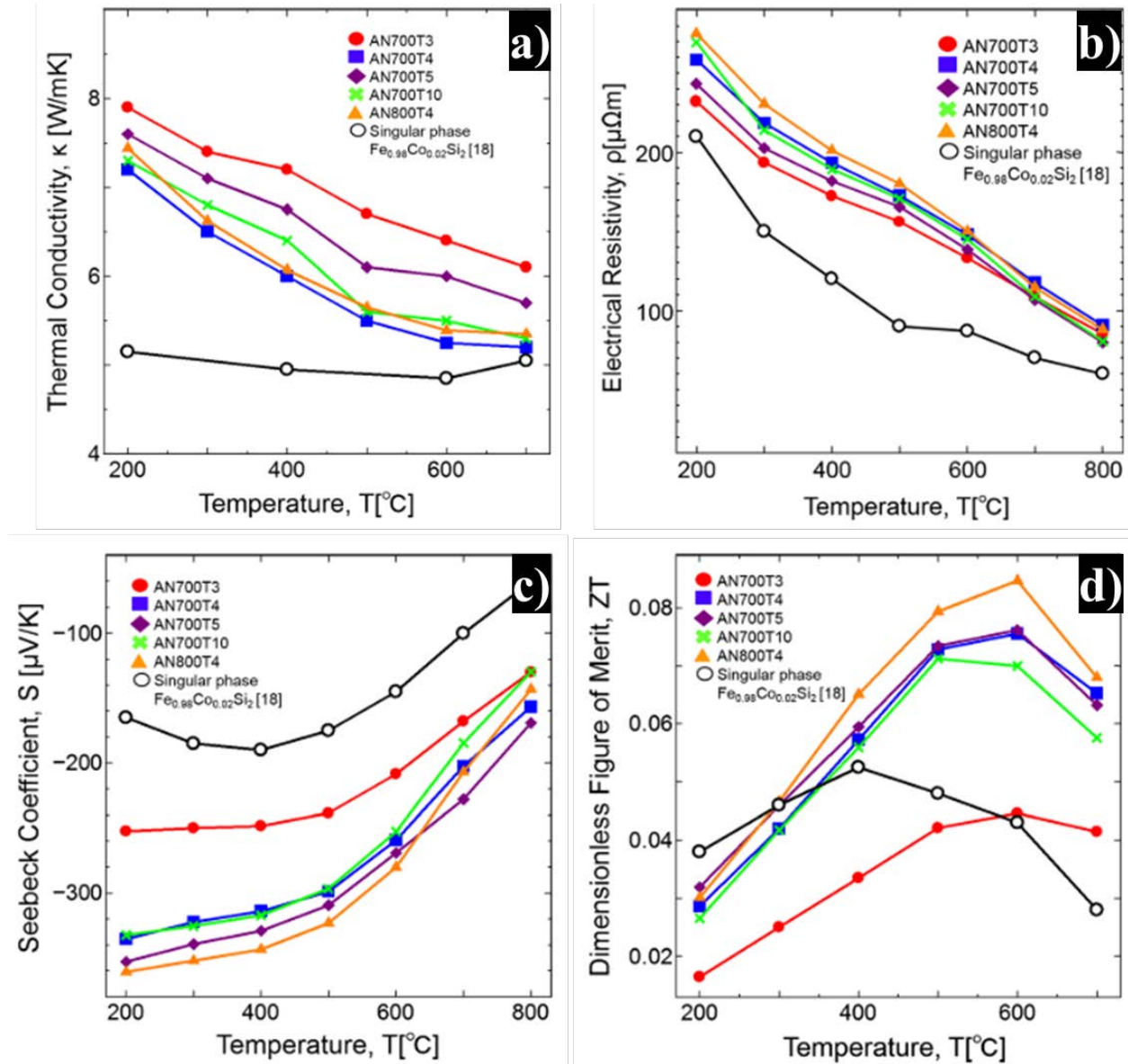


Figure 1.7: The effect of aging conditions on thermoelectric properties as a function of temperature: a) thermal conductivity, b) electrical conductivity, c) Seebeck coefficient, and d) the figure of merit. Changes in properties are caused by lengthscale differences of the two-phase β + Si microstructure. Data taken from [6].

The addition of the Si phase increases the power $S^2\sigma$ and reduces κ_l through interface density. Ail et al., measured thermoelectric properties of α -FeSi₂ samples aged at 600-850 °C for prolonged times; this produced coarsened Si quasi-equiaxed particles varying lengthscales. They demonstrated that the Si morphology is dependent on aging conditions and that κ decreases with diminished lengthscales [43]. In another paper, Redzuan et al. measured the thermoelectric properties of a sample, made by powder processing, and decomposed at 700 and 800 °C. The resulting β /Si composites showed that the presence of Si greatly improves the figure of merit. However, their aging parameters were problematic, as at least one data point was only partially transformed and the others produced coarsened Si particles. From Figure 1.7 [6], we can see that the presence of Si increased κ . This is caused by the high Si volume fraction, coarseness of Si inclusions, and facile heat transfer through Si ($\kappa_{Si} = 149$ W/mK). However, the figure of merit was still greatly enhanced and was most likely due to the major improvement in the Seebeck coefficient [6]. These papers suggest that the $\beta +$ Si composite can have superior thermoelectric properties and that properly nanostructuring Si through low temperature aging can enhance thermoelectric efficiency.

Nagase et al. [44] performed melt-spinning on Fe-Si compositions of the eutectoid (70.5 at% Si) and eutectic (73.5 at% Si). They found that rapid solidification of Fe_{29.5}Si_{70.5} and Fe_{26.5}Si_{73.5} engendered eutectic microstructures of $\epsilon + \alpha$ and $\alpha +$ Si, respectively. They used JMA analysis to show that the fine eutectic lamellae and Si-rich α phase accelerated the eutectoid decomposition. Aging produced fine eutectoid lamellae between the eutectic structures, but neither composition was analyzed for their thermoelectric properties.

1.2.6 Prior Work on Ternary Fe-Si-Ge Alloys

As previously mentioned, alloying the Fe-Si system with Ge provides an additional degree of freedom to enhance thermoelectric properties. However, research into $\beta/\text{Si}_{1-x}\text{Ge}_x$ composites is sorely lacking in the literature, with only three reports of which we are aware. Mohebbali *et al.* showed that spark plasma sintering P-doped SiGe with Co-doped $\beta\text{-FeSi}_2$ (consists of 75 at% of sample) yields a sharp increase in power factor and zT , as shown in Figure 1.8 [7]. It should be noted that the increase in κ_l is once again attributed to the larger bulk thermal conductivity of the

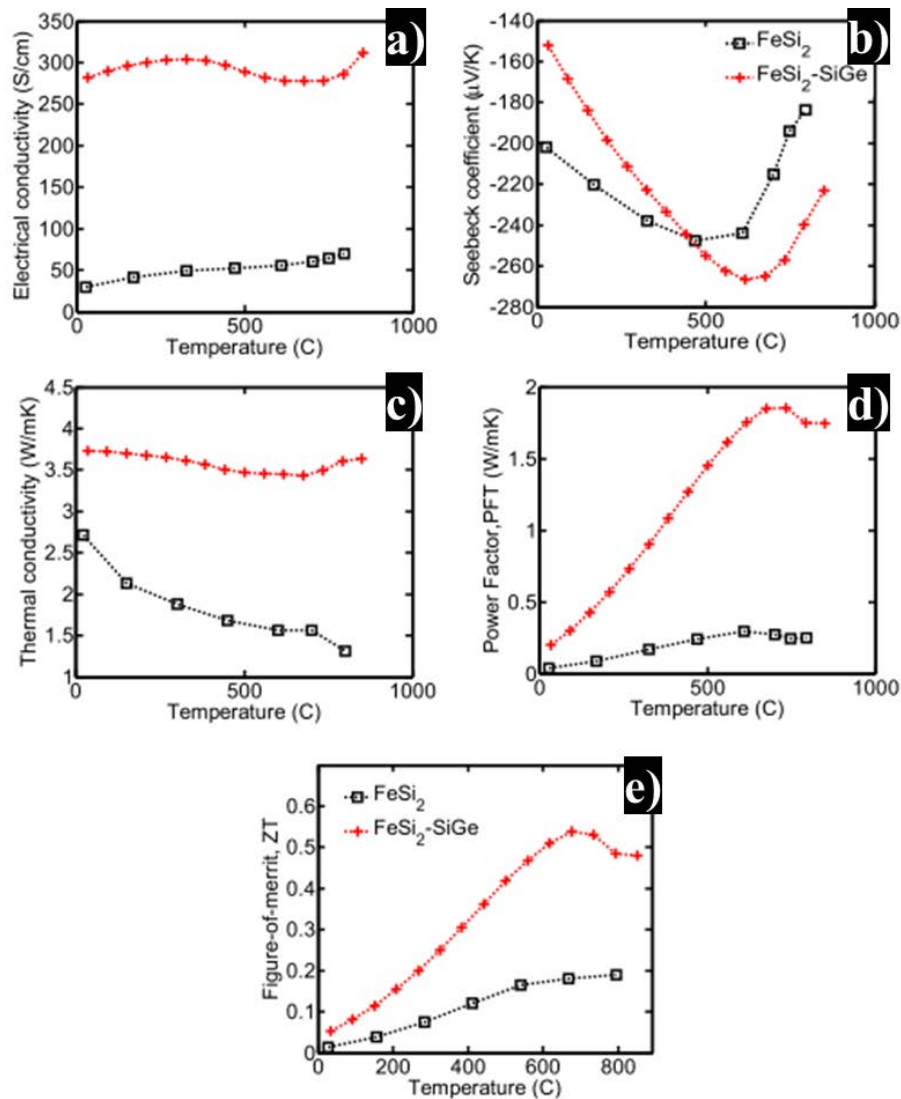


Figure 1.8: Plots comparing thermoelectric properties of powder processed and P-doped $\beta\text{-FeSi}_2$ and $\beta\text{-FeSi}_2 + \text{SiGe}$ composites: a) electrical conductivity, b) Seebeck coefficient, c) thermal conductivity, d) power factor, and e) figure of merit. Data taken from [7].

coarse SiGe particles. When compared to the control sample, the Ge additions increased zT by nearly 2x with a final value of 0.54 [7]. Abudakka et al. synthesized a P-doped $\text{Si}_{80}\text{Ge}_{20}$ matrix (consisting of 95 at% of the sample) with $\beta\text{-FeSi}_2$ particles. These samples were made with low-grade Fe, Si, and GeO_2 powders that were reduced with C during successive induction melts. This material achieved a zT of 0.8 at 950 °C which is comparable to high-purity SiGe materials [45]. A similar approach was taken by Nozariasbmarz et al [46] with the addition of an Ag impurity (sintering aid) and achieved a zT of 1.2. This is due partly to the high-volume fraction of SiGe, which is already an efficient thermoelectric; it has been shown in the binary Fe-Si system that Si volume fraction greatly controls properties of the bulk materials [47]. However, these papers did not compare properties against a similarly made single-phase SiGe control, so the benefits of the β inclusions were not defined.

The papers from Redzuan et al. and Mohebbali et al. reported significantly lower thermal conductivities from their base Fe-Si materials than we obtained through our hierarchical structuring, and the reason is not immediately clear. Both groups used lower grade elements (3N), Co doping, and powder processing techniques, which should result in additional thermal scattering. However, these components alone might not account for their exceptional thermal conductivities. Si-rich Fe-Si-Ge ternary alloys are potential materials for future semiconductor technologies; nanocomposites of semiconducting $\beta\text{-Fe}(\text{Si},\text{Ge})_2$ and $\text{Si}_{1-x}\text{Ge}_x$ have been explored for use as thermoelectrics [7][45], solar cells [48], and optoelectronics [49][50]. Even so, the ternary phase diagram of Fe-Si-Ge components is still largely unknown. Precise engineering of compositions and volume fractions are hampered without this information. Previous work has mapped the Fe-rich region [51], but the Si-rich region, which is important for semiconductors, has not been explored. Scarce thermodynamic data, especially for the Fe-Ge binary system, frustrates modeling

programs such as FactSage and Thermocalc from creating ternary phase diagrams that agree with experimental data.

1.2.7 Thermal Conductivity

Heat transfer through a solid material behaves analogously to atomistic diffusion; heat carriers diffuse along a temperature gradient from hot to cold. When a heat source is placed next to the material, a change in temperature from one side to the other can be modeled by the differential equation;

$$\frac{\partial T}{\partial t} = \frac{\kappa}{c_p \rho} \nabla^2 T \quad 1-3$$

where $\frac{\kappa}{c_p \rho}$ is the thermal diffusivity, which represents the ability of the material to conduct heat per its ability to store heat. Note that κ is the thermal conductivity (typical units of W/m-k), ρ is the density and C_p is the heat capacity (J/g-K). In analogy to the mass diffusivity, the thermal diffusivity has units of m²/s. This is the thermal analog (Newton's Law of Cooling) of Fick's 2nd law. Fourier's law describes the flow of heat in this system;

$$q = -\kappa \nabla T \quad 1-4$$

where q is the heat flux and ∇T is the thermal gradient. This is the thermal analog to Fick's 1st law and is the constitutive equation that defines the thermal conductivity.

According to the kinetic theory of energy transport, thermal conductivity (κ) is proportional to

$$\kappa \sim c_v v \lambda \quad 1-5$$

where c_v is the volumetric heat capacity, v the group velocity of the heat carrier, and λ is the mean free path between (phonon) scattering sites. While c_v and v are intrinsic material properties that are

specific to each material, λ is dictated by microstructure and the spacing between crystal defects such as alloy impurities and interfaces.

Heat transfer through solid matter occurs through two mechanisms: charge carriers and lattice vibrations. Due to the naturally low carrier concentration of semiconductors, κ_l is the major contributor to thermal conductivity. Many different vibration modes can be permitted along a crystallographic direction simultaneously, this superposition of waveforms creates a quantized wave packet or “phonon”. These vibrations are transmitted through crystalline matter via transverse or longitudinal waves, and depending on whether neighboring atoms move in-phase or out-of-phase are referred to as acoustic or optical phonons respectively [52].

As phonons travel through the crystal lattice, any break in periodicity, i.e., any crystal defect, can result in phonon scattering, Figure 1.9. In this work, two principle scattering mechanisms are of interest: 1) phonon-impurity (alloy) scattering where high frequency phonons with mean free paths on the order of lattice spacings are scattered by a solute element, 2) and phonon-boundary (boundary or interface) scattering where low frequency phonons scatter off interfaces such as grain boundaries and heterointerfaces. High frequency phonons scatter more readily due to their shorter mean free path, which leaves low frequency phonons to carry the majority of heat [53].

Heat transfer across a solid material creates a continuous thermal gradient; however, when heat flows across an interface there is a discontinuous drop in temperature on either side of the interface.

We attribute this temperature drop to the thermal boundary conductance (TBC); which relates to heat flux by the equation;

$$q = h_k \Delta T \quad 1-6$$

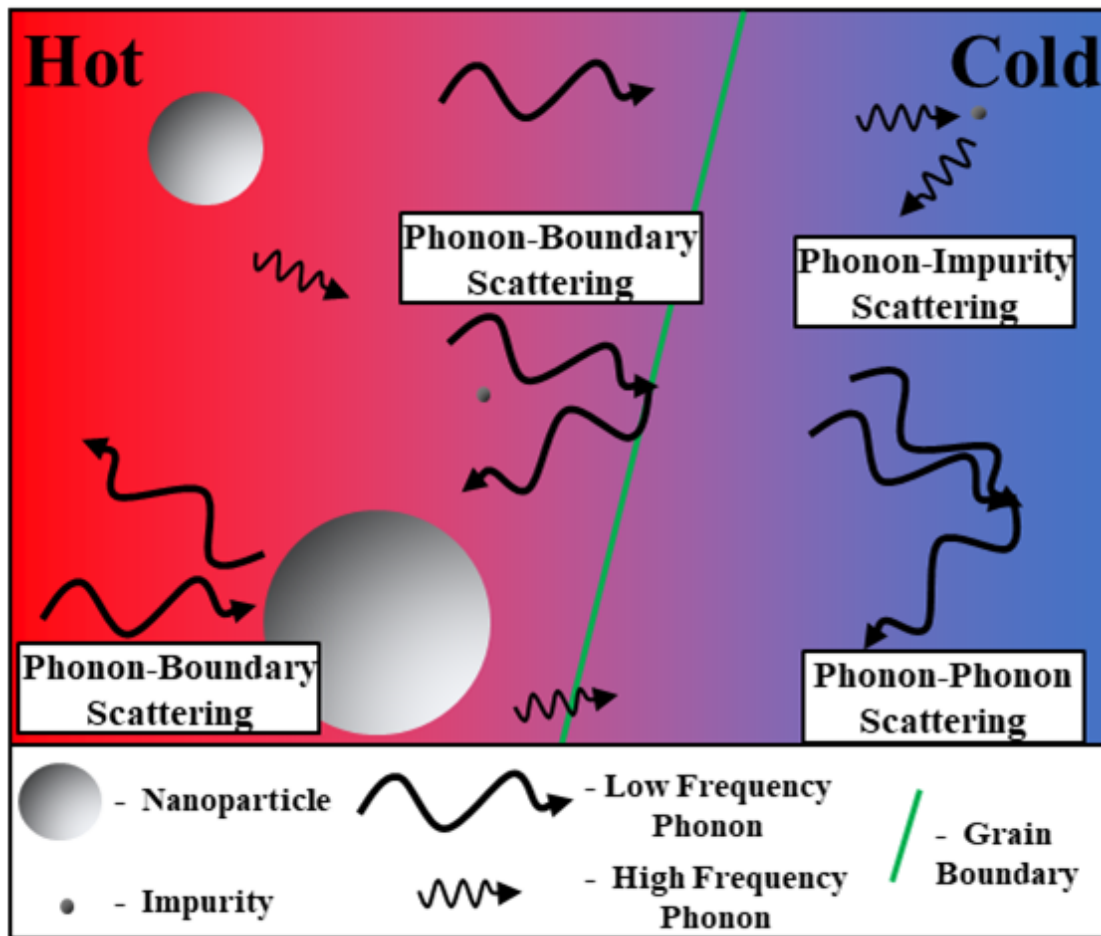


Figure 1.9: Simplified diagram depicting phonon scattering mechanisms in a crystalline material: phonon-boundary scattering at interfaces, phonon-impurity scattering at impurity atoms, and phonon-phonon scattering caused by interactions between phonons.

where h_k is the TBC and ΔT is the change in temperature on either side of the interface. Significant thermal scattering occurs due to the high interface density of nanostructured composites, and it is crucial to understand the phonon scattering contribution caused by each $\beta\text{-FeSi}_2/\text{Si}_{1-x}\text{Ge}_x$ heterointerface for further optimization. Boundary scattering is caused by differences in vibrational properties on both sides of the interface, due to different bonding strengths, atomic configurations, and Debye temperature. We used thermal boundary conductance (TBC) to describe the scattering contributions of the heterointerface. We used Matthiessen's rule,

$$\frac{1}{\kappa_{Total}} = \frac{f_A}{\kappa_A} + \frac{f_B}{\kappa_B} + \frac{\rho_{A/B}}{h_{k,A/B}} \quad 1-7$$

where κ_{Total} is the total thermal conductivity of the system, $f_{A,B}$ is the volume fraction of phase A or B, $\kappa_{A,B}$ is the thermal conductivity of phase A or B, $\rho_{A/B}$ is the interface density, and $h_{k,A/B}$ is the thermal boundary conductance of the A/B interface. This rule states that the total resistivity

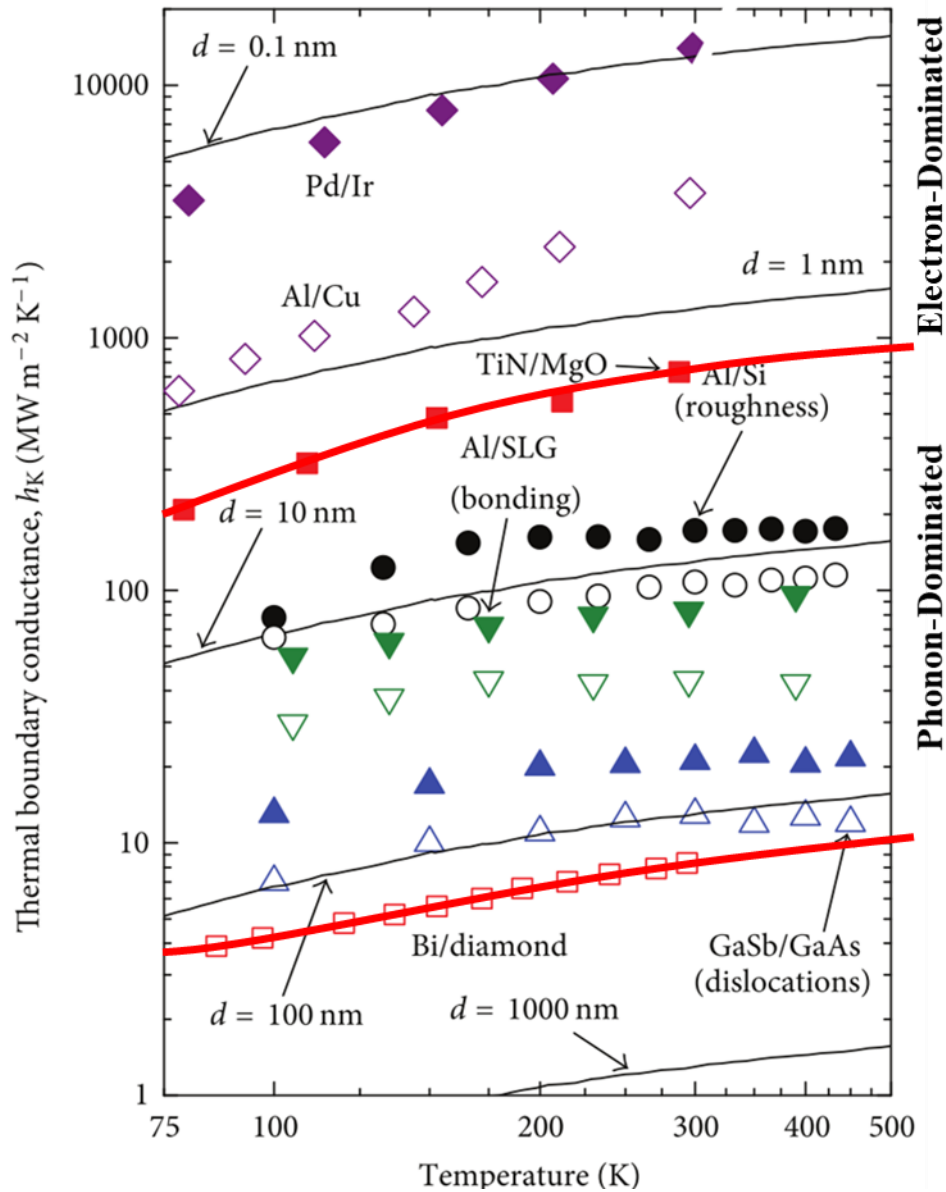


Figure 1.10: Plot of thermal boundary conductances as a function of temperature for various heterointerfaces and bond types. Red lines indicate the highest and lowest values observed in the phonon-dominated regime of thermal boundary conductance. [8]

of a material is a sum of all resistive elements [54]. Figure 1.10 [8] compares TBC values for various metallic/metallic, semiconductor/semiconductor, and metallic/semiconductor interfaces with black lines indicating the thickness of SiO₂ needed to have an equivalent conductance. The lowest TBC was measured from the Bi/diamond interface and is caused by the differences in heat transport carriers (electrons vs phonons, respectively), poor phonon coupling caused by mismatched Debye temperatures (low-frequency phonons vs high-frequency phonons, respectively), and mass mismatch [55]. Ideally the TBC should be as low as possible, and we will show in Chapter 4 that atomic-scale structuring, specifically of the DC nanowires, significantly increases boundary scattering.

Thermal boundary conductance is not the only model that can describe the reduction in thermal conductivity caused by nanostructured materials. The Callaway-Debye model ascribes the lower thermal conductivity to a “size effect”, caused by the phonon mean-free-path being longer than the width of the nanowire. We did not explore this model deeply, but more information about it is discussed in Chapter 3.3.3.

1.3 Thesis Organization

This dissertation is organized in the following way. Chapter 2 details the synthesis and characterization techniques used over the course of this project. Chapter 3 discusses investigations of the binary Fe-Si alloy system, focusing on understanding the eutectoid decomposition ($\alpha \rightarrow \beta + \text{Si}$) and resultant microstructure, and relating thermal conductivity measurements to the observed morphology. Chapter 4 expands the work done by the previous chapter by exploring the engineering space of the ternary Fe-Si-Ge alloy, emphasizing the determination of how Ge distributes in the structure, dependent of the processing conditions and microstructural lengthscales. Thermal conductivity and thermal boundary conductance are directly related to DC

nanowire composition and eutectoid interface density. Chapter 5 shows results from exploratory experiments into ultra-rapid solidification of ternary alloys. We successfully reduced the microstructural lengthscales below that obtained by melt-spinning, but due to inherent challenges with laser processing we were unable to collect thermal conductivity or microstructural data. The conclusion of my work on this project, Chapter 6 assesses part of the ternary Fe-Si-Ge phase diagram, using various sample compositions made throughout my dissertation. Key results and the directions of future research are summarized in Chapter 7.

2 Material Processing and Characterization Methods

2.1 Sample Fabrication

Alloy synthesis took place in either a large-capacity arc-melter/melt-spinner or a small-capacity arc-melter. Although the design and capabilities for each arc-melter is different, the overall process is similar. A charge of high purity elements was carefully weighed to ± 1 mg of the predetermined weight, and cleaned by a 15-minute sonication in acetone followed by an ethanol and DI water rinse. The charge is partitioned so that small lightweight pieces, and low melting temperature elements, are beneath larger pieces, and conducting elements are separated from insulating elements. A high-current electrical arc discharges from the tip of a sharpened tungsten stinger. The W stinger is “stirred” about 2-4 cm above the charge until it is fully melted and a sessile drop is formed. Another crucible is devoted to ~ 20 g of Ti to act as an O-getter. Both arc-melters are capable of achieving at least ~ 1500 °C, as Fe is easily melted, without pushing the power output. The power can safely go as high as to melt surface oxide (SiO_2) at ~ 1700 °C, but for safety reasons the power should not be kept that high for prolonged times and could be dangerous above this point.

2.1.1 Large-Capacity Arc-Melter/Melt-Spinner

The first stage of pumping was performed by a roughing pump and evacuates the chamber to ~ 50 mTorr followed by a diffusion pump evacuating to $\sim 1 \times 10^{-5}$ Torr. The chamber is backfilled to ~ 500 Torr Ar atmosphere, but Ar is not cycled again due to chamber size. The arc is initially struck on the Ti O-getter and kept there until the Ti has fully melted to further minimize the partial pressure of Oxygen (pO). A ~ 50 g charge was melted consecutively via a high-current arc until a liquid boule forms; to ensure complete homogenization the boules were flipped (after solidification

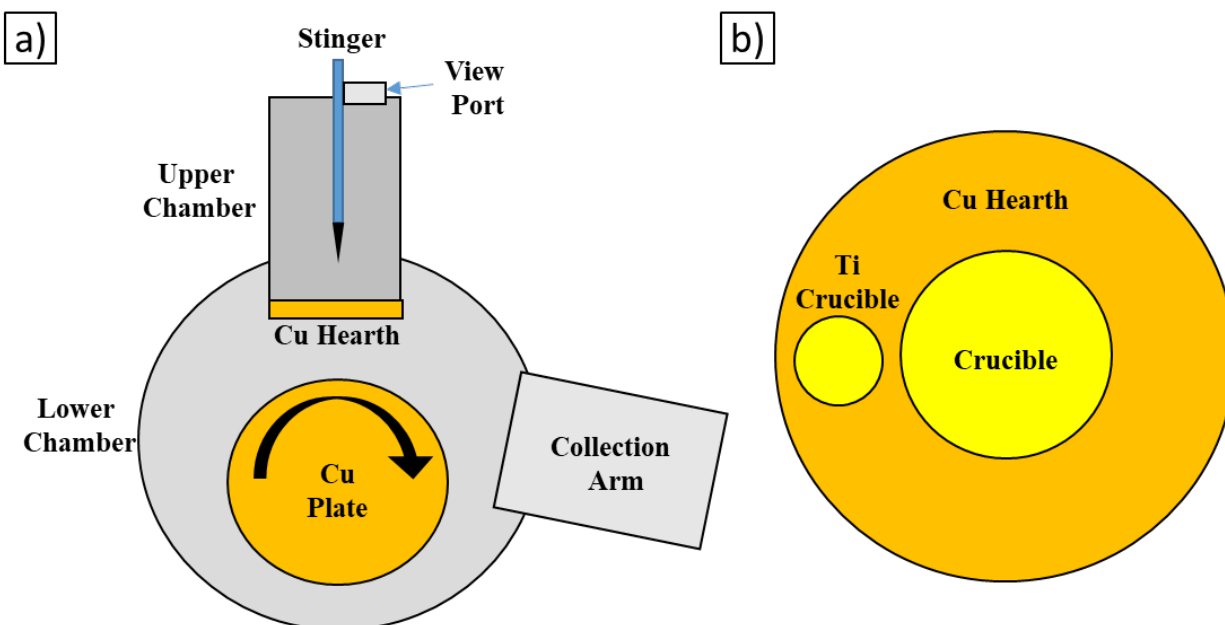


Figure 2.1: a) Schematic of the large-capacity arc-melting chamber and b) the layout of the Cu hearth.

and cooling) and the underside was remelted. A large boule could require 1-2 remelts to reach homogenization. Afterward, the melt was then allowed to ambiently cool (cooling rate of order 10^2 °C/sec) to room temperature on the water chilled Cu crucible.

In order to evaluate the effects of cooling rate on microstructure, ~15-25g of a boule would be sectioned off for melt-spinning. Re-melting was performed in the same chamber under the same initial conditions, but with a Cu crucible that was fitted with a 2 mm diameter BN aperture leading to a rotating Cu plate, Figure 2.1. The boule was re-melted and capillary forces contain the melt in place, sealing the aperture and effectively dividing the chamber in two. Ar gas was backfilled into the upper chamber until a pressure differential of ~380 Torr was reached, forcing the melt through the aperture onto the Cu plate, rotating at 1200 rpm, and the solidified ribbon was thrown into a collection arm. The resulting ribbons are ~50 μm thick and are extremely brittle; fine microstructures are caused by the rapid solidification rate, estimated to be on the order 10^6 °C/sec,

2.1.2 Small-Capacity Arc-Melter

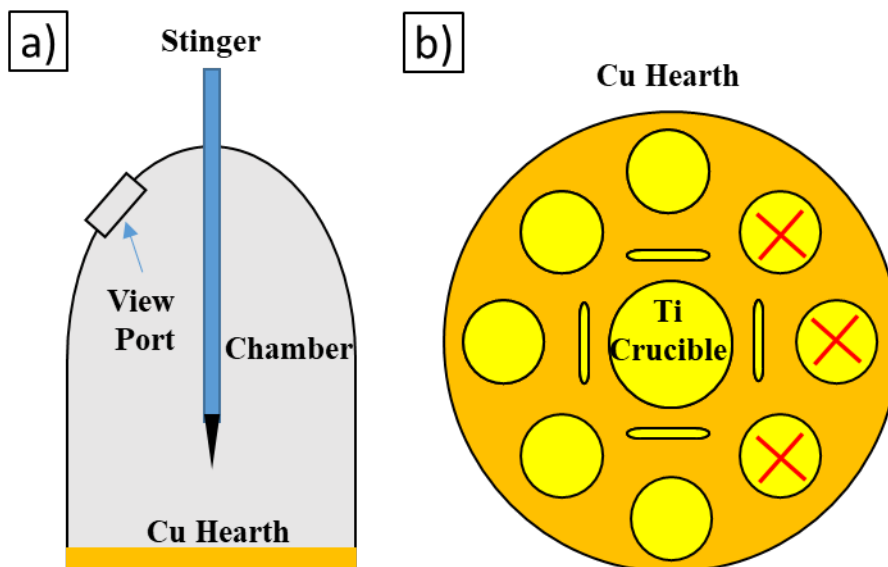


Figure 2.2: a) Schematic of the small-capacity arc-melting chamber and b) the layout of the Cu hearth. The Red x's mark crucibles that cannot be used for melting.

The small-capacity arc-melter has a smaller chamber, Figure 2.2.a, and a single crucible can only hold ~12g of a Si-rich charge. As shown in Figure 2.2.b, the hearth has multiple crucibles, and four cigar shaped crucibles that were not used, and can melt successive charges of identical or varying composition. Crucibles marked with a red x are directly below the Ar inlet valve and cannot be used due to the influx of gas blowing the smaller constituents of the charge away. The single roughing pump evacuates this chamber to ~70 mTorr. To remedy this relatively high pressure, two cycles of pumping and Ar backfilling was performed before a final backfill to ~500 Torr. The arc is quickly struck on the Cu hearth before being moved to melt the Ti O-getter and charges.

2.1.3 Oxide Surface Layer and Partial Pressure of Oxygen

According to the Ellingham diagram [56], Fe will not oxidize at pO below $\sim 10^{-6}$ Torr assuming that the melt is kept around 1600 °C. Both arc-melters are shown to be able to melt 99.99% pure Fe without producing a noticeable oxide surface layer, however there is observable oxide on the

surface of Si-rich alloys and is more prominent with small-capacity arc-melter produced samples. The estimated pO of the large-capacity arc-melter is below $\sim 2 \times 10^{-6}$ Torr, taking into account that air is $\sim 21\%$ O, with the Ti O-getter further reduces the pO below $\sim 10^{-6}$. The small capacity chamber can only pump to pO of $\sim 15 \times 10^{-3}$ Torr, but the multiple Ar backfills and Ti O-getter result in a comparable pO as the large-capacity chamber. It should be noted that boules in the smaller chamber can only be remelted once before the oxide layer becomes too thick and requires higher power to melt. The surface oxide layer can be easily polished off, and generally does not pose a major concern.

2.1.4 Pulse Laser Ablation (PLA)

Pulse laser ablation was explored as a technique to further reduce eutectic lengthscales; this technique sought to utilize a high-powered, UV laser (KrF, 248 nm wavelength, 25 ns pulse) to quickly melt and resolidify a Fe-Si-Ge sample. This produces a solidification rate between 10^9 - 10^{12} °C/s. Figure 2.3 shows a simplified diagram depicting the apparatus. The excimer laser first passes through an aperture, to limit the beam size, and then it is focused so that the sample surface is the focal point. The incident beam was ~ 1 mm thick by ~ 1 cm and would span the beyond length of the sample. Depending on the experiment, the excimer laser was used for pulse laser melting (PLM) of a sample surface or for liquid pulse laser ablation (LPLA) of powders; these are labeled Path1 and Path 2 respectively. The samples rested on a programmable surface stage that was capable of movement, so that even though the laser was stationary the sample surface could be rastered. The stage was programmed to raster the sample at small increments so each location would be melted multiple times. It was found that two pulses per area at 2.5 J/cm^2 fluence produced optimal microstructures.

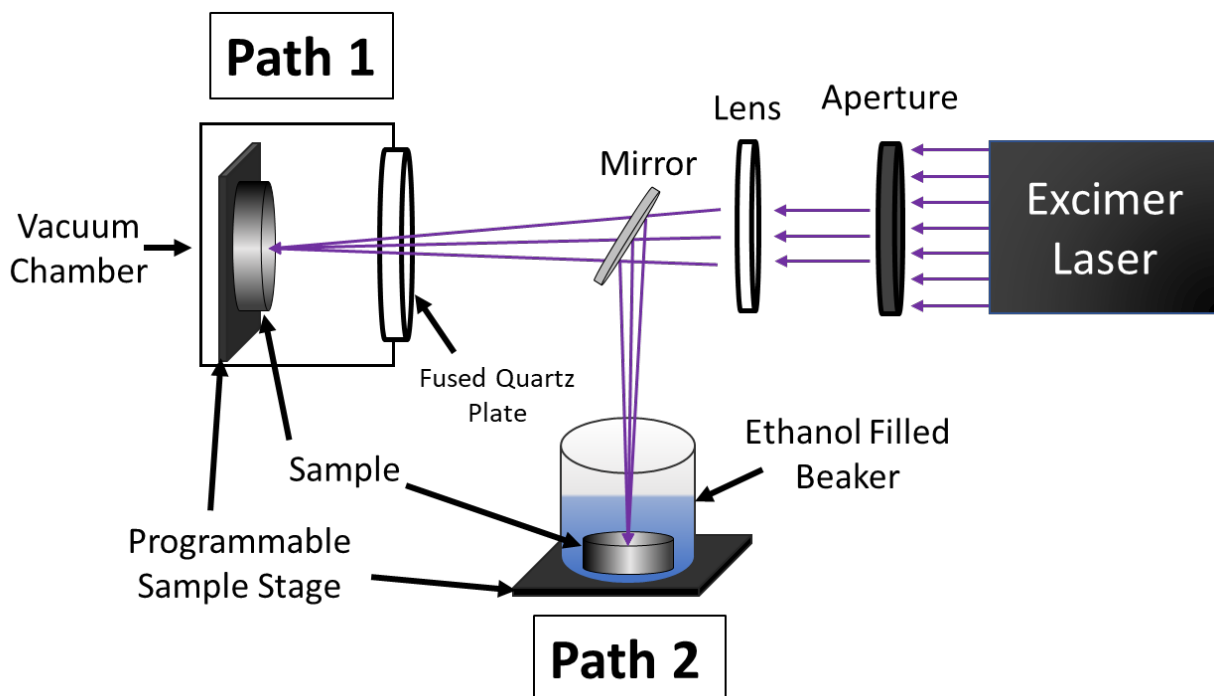


Figure 2.3: Simplified diagram of the pulse laser set-up. Samples were either pulse laser melted with the laser following Path 1, or a mirror could be inserted to direct the laser along Path 2 onto the immersed sample.

A fine (sub 25 μm), homogeneous microstructure was required as a starting sample, as limited diffusion lengthscales make homogenization of large DC grains difficult. Ideal samples were made via high-energy ball milling or melt-spinning and were polished and cleaned before processing. Artifacts from the laser pulse make subsequent characterization difficult.

2.1.5 Sample Encapsulation in Inert Atmosphere

Each sample was encapsulated in a fused quartz ampoule to avoid oxidation and contamination. Fused quartz tubes 4 ft long with an inner diameter of 10.5 mm were first “cut” in half using an oxyhydrogen torch. An appropriately sized sample is carefully slid into the tube until it reaches the bottom. Then the tube is heated again around the circumference ~ 10 cm from the tip. Once the tube had sufficiently softened, it is pulled until the heated section stretched into a narrow “neck”. A folded strip of Zr foil (~ 3 cm x 3 mm) was inserted into the tube and another neck was

made ~ 3 cm from the previous one. This forms an ampoule with two chambers, one for the sample and another for the Zr O-getter. This keeps the materials physically separated while sharing the same atmosphere and pO. The ampoules are evacuated to ~5 mTorr and then backfilled with desiccated Ar to ~300 mTorr. This is cycled three times, with the second to last including a slight heating of the quartz tube, in order to remove residual water vapor. The final Ar backfill was to a pressure of ~180 Torr; lower pressures are possible but when the tube is broken the sudden pressure change obliterates melt-spun ribbons. The second neck is then heated by the torch again and then sealed and separated from the rest of the tube. Water submersion can be used for leak checks, but the tubes must be completely dry before placed into a furnace. Water trapped in cavities at the tips can quickly vaporize and expand; cracking the cavities and exposing the ampoule interior to atmosphere.

2.1.6 Isothermal Heat Treatments in Tube Furnace

The ampoules were fed into the hot-zone of tube furnaces for isothermal aging. Heat treatments for Fe-Si and Fe-Si-Ge samples were isothermal as dynamic aging caused additional cracking due to differences in thermal expansion between the β matrix and DC inclusions. Temperatures were set according to an external thermocouple at the sample location, and were checked daily and adjusted as needed. The ampoules were pulled out of the furnace and immediately quenched in water. The neck of the ampoule could be quickly broken for bulk samples, but the ribbon containing ampoules were not broken as the influx of water would disintegrate the ribbons.

2.1.7 Sample Mounting in Epoxy

Samples meant for SEM or TDTR required mounting in epoxy. Epoxy was made with Buehler epoxy and hardener mixed in a 2:5 ratio. Due to the samples being semiconducting, a Ni

conducting filler was added, equal to the weight of epoxy, to reduce electron charging. Samples were placed into a 1” diameter cylindrical mold and covered with ~ 1 cm of the mixture. Due to their brittle nature and low weight, ribbons required a specific mounting process. Specific details can be found in the Appendix 1.

2.2 Characterization Techniques

2.2.1 X-Ray Diffraction (XRD)

XRD data was obtained from a PANalytical X'Pert Pro MPD and PANalytical Empyrean, using a Cu K α source, for phase identification and crystallographic characterization. Powder samples were prepared via mortar and pestle; powders were then sieved and reground until powder size was below 40 μm in diameter. Due to the limited availability of ribbon samples, only ~4 cm length of ribbon was devoted to any heat treatment. This amount produced enough powder for clear XRD peaks, but sieving for a homogenous particle size was not possible. The resultant powder was carefully collected on a clean ~1 cm by ~1 cm strip of double-sided tape. The strip was then fixed to a quartz zero diffraction plate and then placed in the sample holder. High-resolution data was obtained by scanning from 15 - 100°, encompassing a large breadth of peaks, and taken at the smallest step size (0.008° 2 θ). The PANalytical HighScore Plus program along with the PDF4 catalog was used for spectrum analysis.

2.2.1.1 Rietveld Refinement

The Rietveld refinement function of the PANalytical HighScore Plus program takes crystal structure data, in this case Wyckoff positions (Table 2.1) which denote the element and position in the crystal lattice, for each phase to create a theoretical spectrum. Variables related to background, peak position, peak intensity and peak width are varied and refined to actual data by

Table 2.1: Wyckoff numbers for phases present in the Si-rich region of the Fe-Si-Ge ternary phase diagram.

Phase	Element	X	Y	Z	sof	Wyckoff
α -FeSi ₂	Fe	0.0000	0.0000	0.0000	1	1a
	Si	0.5000	0.5000	0.2500	1	2h
β -FeSi ₂	Fe	0.2146	0.0000	0.0000	1	8d
	Fe	0.5000	0.3086	0.1851	1	8f
	Si	0.1282	0.2746	0.0512	1	16g
	Si	0.3727	0.0450	0.2261	1	16g
ϵ -FeSi	Fe	0.3865	0.3865	0.3865	1	4a
	Si	0.0926	0.0926	0.0926	1	4a
DC	Si	0.0000	0.0000	0.0000	X	8a
	Ge	0.0000	0.0000	0.0000	1-X	8a

the least squares method. The procedure for Rietveld Refinement can be found in the Appendix 2.

The goodness of fit (GOF) describes how well the theoretical spectrum fits the measured data and must be watched carefully, along with the fit line, to ensure that each refined variable is improving the agreement between spectra. Data was considered accurate if the GOF under a value of 4 [57].

The order of refinement was based on the procedures found in the literature [57][58]; variables such as peak position, peak intensity, and then peak shape are refined separately and sequentially to reduce the GOF value to its minimum. Data was taken from 15-100 °2 θ for 2 hours to ensure a broad spectrum with high signal-to-noise ratio. There were no significant differences in data between the 2 hr, 8 hr, and 10 hr scan times, so it was concluded that 2 hours was sufficient for Rietveld analysis of Fe-Si-Ge alloys.

2.2.1.2 Lattice Parameter and Composition, Vegard's Law

Ge composition of eutectic and eutectoid lamellae (diamond cubic solution phase, Si_{1-x}Ge_x) can be determined by Vegard's law, which states that the lattice parameter of an alloy increases as a function of the solute concentration. Figure 2.4.a shows the evolution of the SiGe peak position

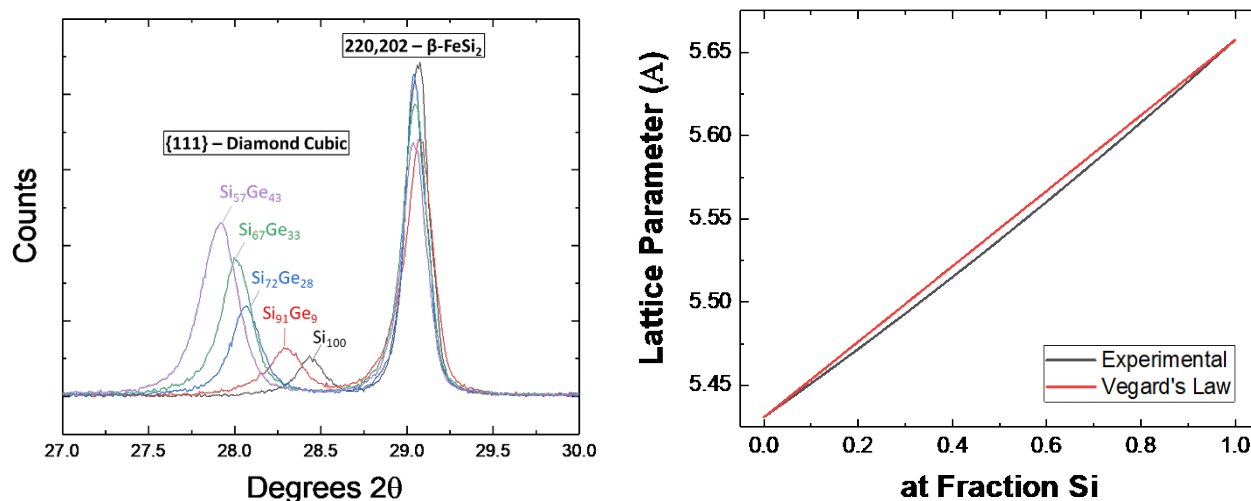


Figure 2.4: a) XRD spectrum showing compositional change in the SiGe (111) peak position, lower 2θ equates to greater Ge concentration. b) Plot showing differences in experimental and theoretical lattice parameter as a function of composition.

towards lower 2θ (increasing lattice parameter) as Ge concentration increases. SiGe lattice parameters do not behave as an ideal linear function; it has been shown experimentally that the line has negative curvature (Figure 2.4.b). This bowing has been well explored and the function is described by [31]

$$a_{\text{SiGe}} = 0.02733x^2 + 0.01992x + 0.5431 \text{ (nm)} \quad 2-1$$

and plotted along with Vegard's law in Figure 2.4.b. The experimental relationship between lattice parameter and composition was used in our Rietveld analysis.

2.2.2 Scanning Electron Microscope (SEM)

Prior to scanning electron microscopy (SEM), all samples were polished to mirror finish; the process can be found in the Appendix 3. Over the course of polishing, ~1-2 mm of material was removed from the bulk samples and ~10-20 μm for ribbons. This distance eliminates possible oxide contaminants and possible surface effects on microstructure. SEM was performed in a FEI

Quanta 650 operated at 10 KV and spot size 4, primarily in backscatter detection mode (BSE) for enhanced compositional contrast.

2.2.2.1 Energy Dispersive Spectroscopy (EDS)

EDS was used to chemically characterize individual microconstituents, however resolution was insufficient to directly distinguish between nanoscale eutectoid β and DC lamella. Chemical composition of a single phase was determined by areal sampling, and integrating composition over that area; these measurements were then averaged with measurements from the same phase in different areas of the same sample. This provides a much broader dataset than would be achieved by point analysis, and is more indicative of the actual composition. Complete maps of the microstructure were often scanned and then the compositions of areas of interest were later analyzed in Oxford Instrument's AZtec program. EDS measurements were taken at 15 keV and spot size 6 which was provided sufficient signal and gave bulk results similar to those of ICP (see below).

2.2.2.2 Electron Backscatter Diffraction (EBSD)

Select samples were further examined using electron backscatter diffraction (EBSD) to obtain eutectoid colony size and crystallographic orientation. To remove surface deformation prior to EBSD scans, these samples were finished with a vibratory polish with 5 μm colloidal silica. This was done for 2 hours and the frequency was tuned for the sample to make ~ 10 complete rotation per minute. Colloidal silica sticks to the surface, so it is important to gently clean the surface with a clean polishing cloth for several minutes under flowing water.

Crystal structure data must be manually created for each phase, and utilized the Wyckoff positions found in Table 2.1. Scans were taken at 30 keV and spot size 5 which provided the best diffraction

pattern and a reasonable scan time. Individually identifying the fine $\beta + \text{Si}$ eutectoid microstructure was not possible due to the fine DC nanowire lengthscale. The high heterointerface density contributed to a degraded signal, although the FEI software was generally able to detect the Kikuchi patterns of the dominant $\beta\text{-FeSi}_2$ phase. No such difficulties existed with coarsened or as-cast samples.

EBSD maps were processed with TANGO to remove false signals and fill in null points. Abnormal spikes were removed and null points were “filled in” by the surrounding grain orientation. The a and b axes of the β grain were often confused by TANGO making each grain identified as a patchwork of areas 90° rotated from each other; the software can be programmed to recognize rotations in grain orientations, such as twinning, and group them as a single grain if the degree and direction of rotation is known. For this case, a single β grain consisted of all 90° rotations along the a and b.

2.2.2.3 Linear Intercepts Method

SEM and EBSD images were used to determine the lengthscales of microconstituents, grain size, and interface density by the method of linear intercepts. Representative micrographs from each microstructure were drawn with 45 randomly oriented lines. The length of the lines and the number of heterointerfaces or homointerfaces were recorded and averaged. Lengthscale analysis was performed in ImageJ.

2.2.2.4 Transmission Kikuchi Diffraction (TKD)

Transmission Kikuchi diffraction (TKD) [59] is a technique that uses an SEM to perform transmission microscopy. As shown in Figure 2.4, the electrons pass through the thinned, electron transparent sample and the electrons that scatter 70° are collected by the EBSD forescatter detector.

TKD probes thicker regions (optimum patterns are collected from 75-200 nm [59]) than TEM and it is the bottom sample surface that are imaged. Because the detector is 70° off from the sample plane, a larger interaction volume is needed for electrons to scatter into the detector and these scattering events typically occur near the bottom surface, Figure 2.5. Like TEM, it is able to capture high magnification images and can also determine the composition and orientation of microconstituent phases, at lengthscales much finer and at a faster rate than SEM-EDS and SEM-EBSD.

Melt-spun ribbons were used, as their $50\ \mu\text{m}$ thickness, and lack of cracks, made sample preparation possible, whereas bulk samples did not have the integrity to reach electron transparency. A sufficiently large, aged ribbon was fixed onto a Cu specimen mount with a 2 mm aperture, and ion milled (Gatan, Precision Ion Polishing System) for ~ 3 hours with guns at 10° (top) and 5° (bottom). After a hole pierced the sample, the angles were reduced to 5° and 2°

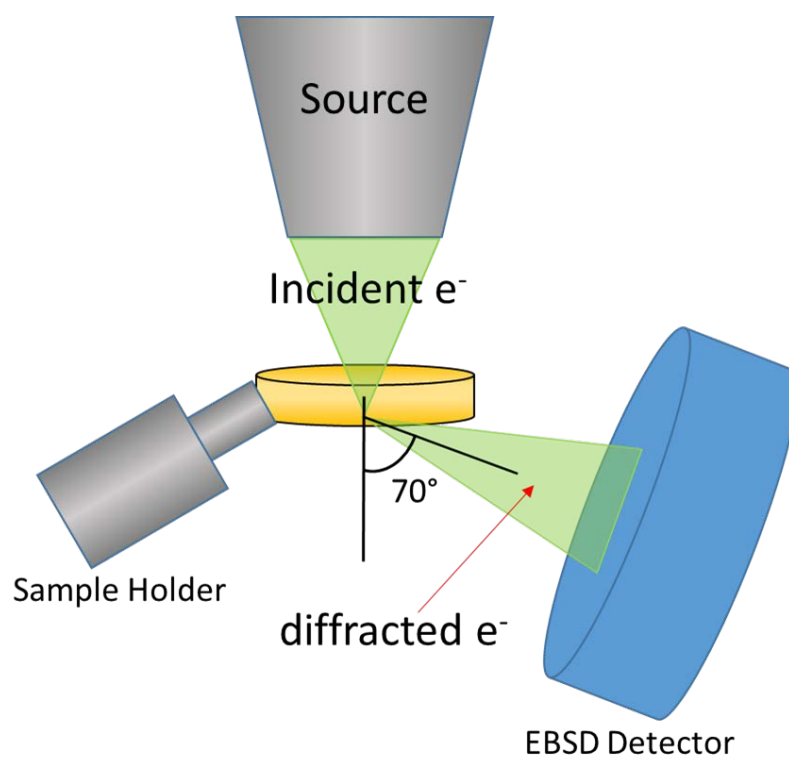


Figure 2.5: Schematic of the SEM in transmission mode, depicting the set-up required for TKD analysis.

respectively, and the sample was milled for another hour. The stage was cooled with liquid nitrogen to suppress beam-induced phase transformations.

2.2.3 Inductively Coupled Plasma – Optical Emission Spectroscopy (ICP-OES)

Bulk compositional analysis was performed on as-cast samples by Inductively Coupled Plasma – Optical Emission Spectroscopy (Thermo Scientific iCap 6200). A piece from a sample of interest, typically about 40 mg, was digested in a 3:2 solution of HNO₃ and HF for 24 hours. The solution was then diluted to 200-400 ppm with DI water. Three solutions were made from each and analyzed three times in order to determine error. The bulk composition for binary alloys were found to be Fe_{28.4}Si_{71.6} and Fe₂₇Si₇₃ and ternary alloys were Fe₂₈Si₆₈Ge₄, FeSiGe₅ and FeSiGe₁₀. The solutions were compared against Fe, Si, Cu, Ti, and W standards, where Cu, Ti, and W are possible contaminants from arc-melting. The error from this method was found to be ~1 at% for all components.

2.2.4 Differential Scanning Calorimetry (DSC)

A differential scanning calorimetry (DSC) determined the temperature of solid/solid and solid/liquid phase transformations [60][61][62]. The DSC goes through a preprogrammed thermal treatment and measures the heat flux between a sample and control. The machine was calibrated using Zn, Sn, Ag, In, and Al in Al₂O₃ cups, and background scans were run weekly to ensure high quality data.

Roughly 60 mg was taken from the center of each boule and was loaded into Al₂O₃ cups and loaded into a Netzsch STA 499 F1 Jupiter. For each scan, the temperature was initially ramped up to 1250 °C to melt the sample, then the sample was cooled by 5 °C/min to 800 °C and held there for 2.5 hours, in order to decompose the α phase. Then the sample was heated at 5 °C/min to 1250 °C.

The machine continually flowed 10 mL/min of Ar to reduce oxidation. Three heating and cooling cycles were performed on each sample and the phase transformation values were averaged for each composition. Analysis of the heating curves were performed in Proteus Analysis, the Netzsch analysis software.

2.2.5 Time Domain Thermoreflectance (TDTR)

Thermal conductivity was measured via (TDTR) [63][64][65] at room temperature. TDTR is an optical pump-probe measurement technique that utilizes a train of ultra-fast laser pulses to induce a modulated heating event and measure the temperature dependent change in reflectance of the sample surface between pulses. The heat capacity of the two-phase material was determined by a weighted sum of β -FeSi₂ [66] and Si [67], according to their volume fractions. The heat capacities of Si and Ge are nearly equivalent, so the Si value was used for thermal conductivity calculations for all Si_{1-x}Ge_x. The small spot size and shallow penetration depth of the incident beam make it an ideal technique for thermal conductivity measurements of challenging samples, such as epoxy mounted ribbons, where the beam can be positioned to avoid fractures in the slow-cool sample, which would otherwise bias the measured thermal conductivity.

3 Binary Fe-Si Alloy

3.1. Binary Fe-Si Alloys

The goal of this chapter is to investigate the eutectoid decomposition, $\alpha\text{-FeSi}_2 \rightarrow \beta\text{-FeSi}_2 + \text{Si}$, as a means to modify microstructure and control thermal transport. The eutectoid phase transformation is analogous to the pearlite transformation in Fe-C alloy systems, in terms of also being a eutectoid decomposition, but the kinetic processes by which $\alpha \rightarrow \beta + \text{Si}$ phase transformation occur are not as well-known. Understanding the eutectoid decomposition is imperative to optimize $\beta\text{-FeSi}_2 + \text{Si}$ for thermoelectric applications.

Two binary Fe-Si alloys were characterized with different intents. A $\text{Fe}_{27}\text{Si}_{73}$ composition was used to characterize the eutectoid phase transformation. Incomplete aging experiments show that nucleation of eutectoid colonies occurs preferentially on cracks, while at smaller undercooling, nucleation also could also nucleate on eutectic Si particles. Initially eutectoid Si grows as lamellae, but later coarsen into nanowires via the Rayleigh instability. Aging samples at various temperatures found that the growth velocity (v) and interlamellar spacing (λ) of the pearlitic colonies obey a relation of the type $v \lambda^n = f(T)$. While this sets bounds on the activation energy for the specific diffusion mechanism, the exact mechanism cannot be identified from our data. Further similarities to pearlite, such as divorced eutectic, were found to occur at high temperatures.

A hypereutectoid, $\text{Fe}_{28.4}\text{Si}_{71.6}$, alloy was used to explore the relationship between microstructure and thermal conductivity. Fine eutectoid Si increases the density of heterointerfaces by 40x as compared to highly coarsened (analogous to spheroidite) samples, and resulted in a 2x reduction in thermal conductivity. The thermal boundary conductance was determined for the $\beta\text{-FeSi}_2/\text{Si}$ heterointerface, which shows that the interface is a weak scatterer of phonons.

3.1.1 Solidification of Molten $\text{Fe}_{27}\text{Si}_{73}$ and $\text{Fe}_{28.4}\text{Si}_{71.6}$ Boules

After the arc-melting process, the melted boules were cooled to room temperature in a water-chilled crucible. Solidification begins at the chill zone where the boule contacts the Cu hearth. The α nuclei phase grows unabated in the columnar zone and form plates that can grow the entire height of the boule. It is not uncommon to observe shrinkage porosity in a solid boule, caused by the decrease in density from solidification. Both $\text{Fe}_{28.4}\text{Si}_{71.6}$ and $\text{Fe}_{27}\text{Si}_{73}$ compositions exhibit extensive cracking due to stresses associated with thermal gradients during cooldown; an example of this in $\text{Fe}_{28.4}\text{Si}_{71.6}$ can be seen in Figure 3.1. This hypereutectoid composition ($\text{Fe}_{28.4}\text{Si}_{71.6}$) had no evidence of as-cast eutectic microconstituents and was a single $\alpha\text{-FeSi}_2$ phase. The α phase solidifies congruently, and as such, micro and macro-segregation was not found to be an issue for the $\text{Fe}_{28.4}\text{Si}_{71.6}$ sample. EDS corroborates insignificant compositional variation from top to bottom of the boule or within a single grain. To avoid Si precipitation in a possibly supersaturated α phase, a high temperature homogenization of as-cast material was not performed before aging.

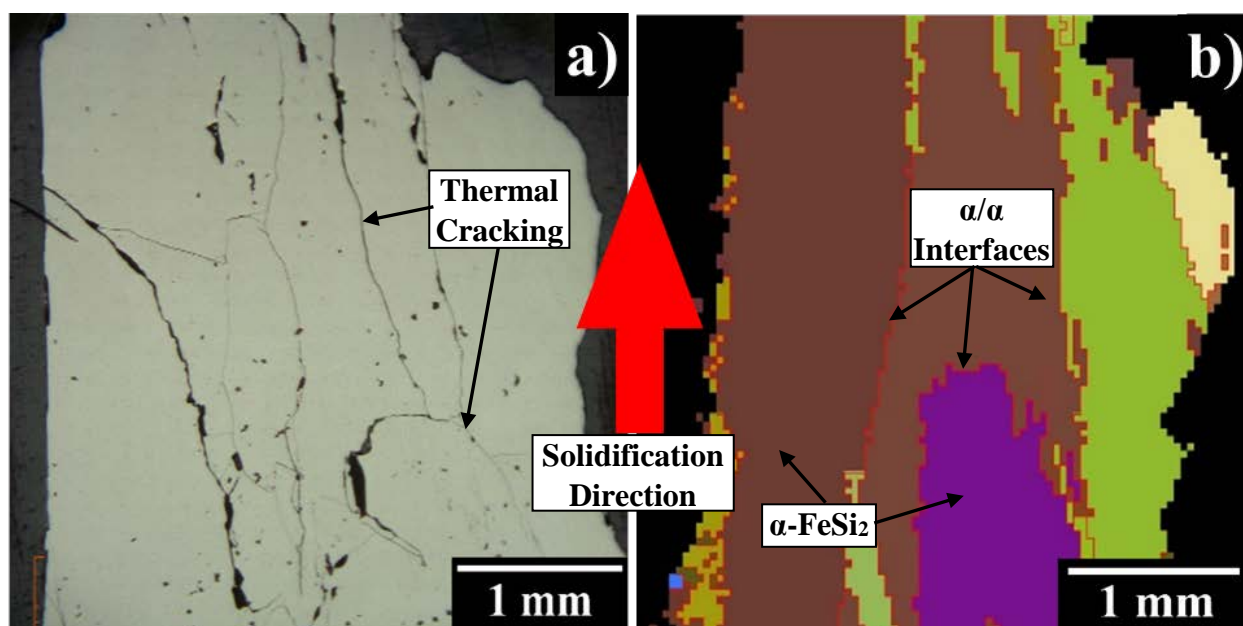


Figure 3.1: As cast microstructure from $\text{Fe}_{28.4}\text{Si}_{71.6}$ alloy viewed perpendicular to the axis of growth; the red arrow denotes the direction of solidification. a) Optical micrograph showing single phase $\alpha\text{-FeSi}_2$ and cracks caused by solidification. b) EBSD map showing the α grain size and columnar structure.

As-cast, the hypoeutectic sample contains coarse bands of proeutectic α interleaved with eutectic $\alpha + \text{Si}$. The hypoeutectic $\text{Fe}_{27}\text{Si}_{73}$ alloy has a striking, irregular (faceted) eutectic morphology, Figure 3.2.a, and will be discussed in the following chapter. Significant macro-segregation is present in hypoeutectic $\text{Fe}_{27}\text{Si}_{73}$; the eutectic $\alpha + \text{Si}$ volume fraction increases and proeutectic α decreases as a function of boule height as shown in Figures 3.2.b and Figure 3.2.c. The initial molten boule is Fe-rich. As proeutectic α nucleates and grows the melt depletes in Fe and the liquid phase evolves towards the eutectic composition. This results in larger $\alpha + \text{Si}$ volume fraction as solidification continues.

3.1.2 ICP Determined Compositions and the Effect of Cu Impurity on Decomposition Rate

Aging the $\text{Fe}_{28.4}\text{Si}_{71.6}$ and $\text{Fe}_{27}\text{Si}_{73}$ compositions with the same thermal treatment, 567 °C for 56 hours, does not result in a similar fraction of transformation despite having ostensibly the same α - FeSi_2 compositions. Where the former composition completely decomposed and coarsened to $\beta + \text{Si}$, the latter composition only had 3.4% decomposition. Since both compositions produce α phases of similar compositions, we expected that the decompositions would proceed at similar rates. The hypoeutectic sample, despite having copious α/Si heterogeneous nucleation sites, had a significantly slower transformation rate than the $\text{Fe}_{28.4}\text{Si}_{71.6}$ sample.

ICP analysis of both binary compositions show that the $\text{Fe}_{28.4}\text{Si}_{71.6}$ sample has trace amounts of Cu, W, and Ti contaminants not present in the $\text{Fe}_{27}\text{Si}_{73}$ sample. These contaminants are the consequence of improper arc-melting. $\text{Fe}_{28.4}\text{Si}_{71.6}$ was found to contain 0.07 at% Cu impurity, and prior work has shown trace Cu to have a profound effect on accelerating the eutectoid decomposition process [68][41]. The ageing parameters and transformation rate agrees with the 0.2 at% Cu samples explored by Yamauchi, et al., albeit to a lesser degree, and is designated in

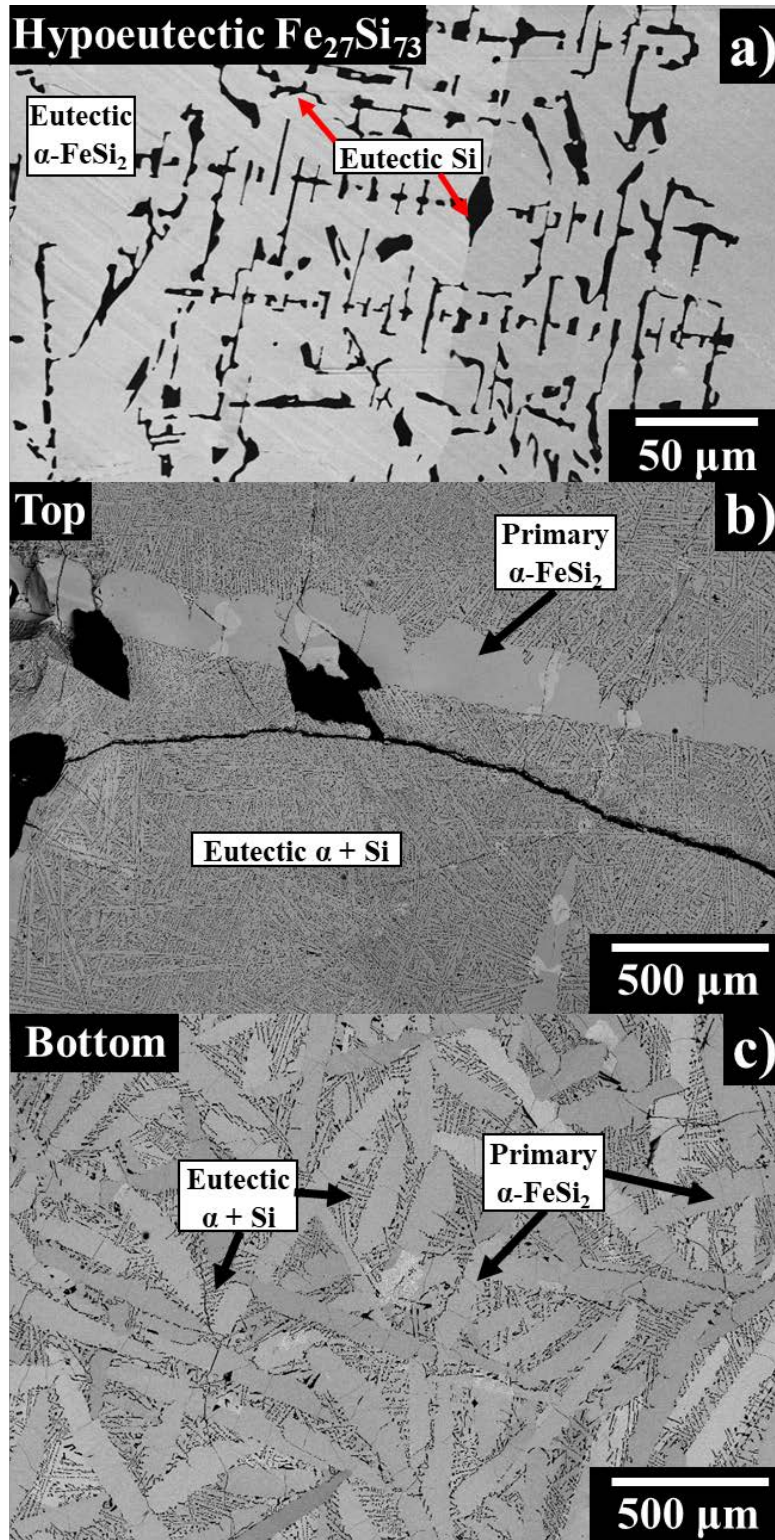


Figure 3.2: As-cast microstructure of the hypoeutectic $\text{Fe}_{27}\text{Si}_{73}$ alloy. SEM-BSE micrographs of a) the irregular eutectic $\alpha + \text{Si}$ microstructure and microstructural cross-sections showing the macrosegregation from b) top and c) bottom of the boule as evidenced by differences in the microconstituent fractions. All images are viewed along the solidification direction.

Figure 3.3 as a red circle. There is also a small amount of W in this sample, but the effect of W on decomposition has not been explored in the literature.

The detailed mechanism of Cu in enhancing the eutectoid transformation is not well understood. However, in comparing the β grain size of our samples with and without Cu, the grain size in $\text{Fe}_{27}\text{Si}_{73}$ is much larger, even in early stages of transformation, since the nucleation density is low. This suggests that Cu has a potent effect on activating nucleation of pearlitic colonies. Furthermore, Cu appears to effect lamellae spacing and size on samples aged at $800\text{ }^\circ\text{C}$; as will be shown later, the $\text{Fe}_{27}\text{Si}_{73}$ samples have thicker truncated lamellae, and the $\text{Fe}_{28.4}\text{Si}_{71.6}$ sample produces finer Si lamellae. This was not explored in-depth, but it appears that Cu also equalizes β and Si growth rates and promotes cooperative growth.

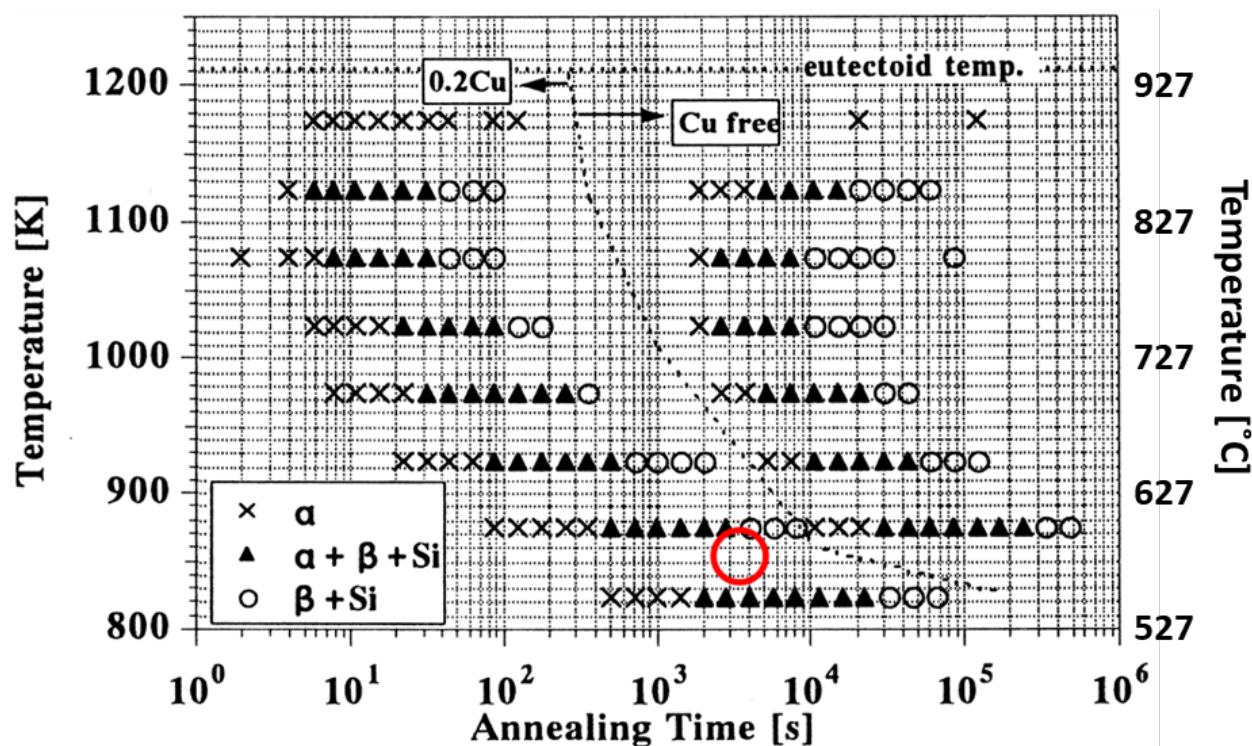


Figure 3.3: Time-temperature-transformation (TTT) diagram for the ($\alpha \rightarrow \beta + \text{Si}$) eutectoid decomposition for pure and Cu contaminated [21]. The red circle indicates the aging parameters for the $\text{Fe}_{28.4}\text{Si}_{71.6}$ sample.

These observations have serious implications for eutectoid processing, suggesting that eutectoid decomposition proceeds too slowly at large undercoolings and complete decomposition would not be achieved in a reasonable timeframe. The α/Si interface is not a facile nucleation site. In order to produce fine eutectoid, decomposition must be instigated by either: 1) impurities such as Cu to act as an accelerant, 2) powder processing which has high free surface densities, or 3) or as will be discussed later in Chapter 4, $\text{Si}_{1-x}\text{Ge}_x$ lamellae.

3.2 Hypoeutectic $\text{Fe}_{27}\text{Si}_{73}$ – Mechanism of Eutectoid Decomposition

3.2.1 Nucleation Mechanisms for Eutectoid Decomposition

Specimens from the $\text{Fe}_{27}\text{Si}_{73}$ composition were aged at four different temperatures (Table 3.1), with aging times adjusted so that the nascent stages of transformation could be characterized. Two preferred nucleation sites for pearlitic colonies were observed. Colonies were easily identified by their contrast difference in SEM-BSE. At 587 and 680 °C, β/Si colonies were found to only nucleate on cracks, while at 800 and 910 °C, nucleation occurred on both cracks and eutectic Si particles. Extensive areal surveys in the SEM confirm the nucleation mechanism for each case; Figure 3.4 shows examples. In many eutectoid reactions, colony nucleation is found to occur at

Table 3.1: Aging parameters used with $\text{Fe}_{27}\text{Si}_{73}$ samples to produce intermediate stages of decomposition.

Temperature (°C)	Time (hr)
567	56
680	2
800	1
910	10

grain boundaries, e.g., in austenite for the Fe-C archetypal system. In the current specimens, however, the grain size (on the order of 1 mm) is much larger than either the mean crack spacing ($\approx 17 \mu\text{m}$), or the spacing between eutectic Si particles ($\approx 5 \mu\text{m}$). Hence it is not surprising that internal free surfaces due to cracks act as alternative potent nucleation sites. Despite the higher

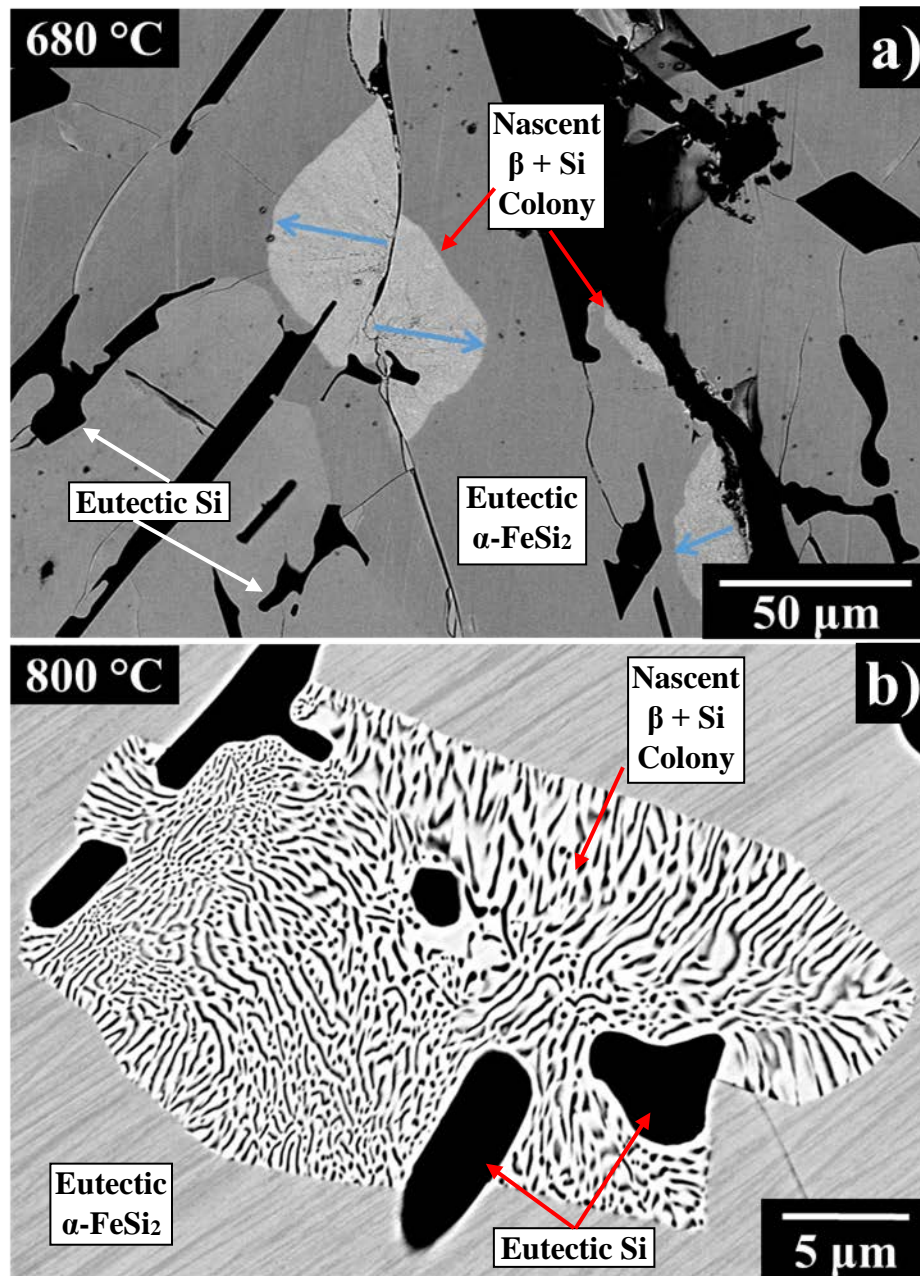


Figure 3.4: BSE-SEM micrographs depicting our two suggested nucleation modes. Colony nucleation occurring on a) cracks at 680 °C, with blue arrows showing the growth direction, and b) an example of the proposed mechanism of eutectic Si assisted nucleation at 800 °C.

α /Si interface density, no colonies were found to nucleate on the eutectic Si at lower aging temperatures. At temperatures closer to the eutectoid isotherm, aging occurs in the regime where, according to simple linear extensions of the solvi (Figure 3.5.a), diamond cubic Si has the larger driving force to form. High temperatures allow Si atoms in the metastable α -matrix to rapidly diffuse to nearby eutectic Si particles and attach epitaxially: Si growth on eutectic Si can be clearly seen at the α , β , and Si interface in Figure 3.5.b. The local Si composition of the adjoining α phase is reduced, as indicated in Figure 3.5.a). While the overall energy gain in transforming to the

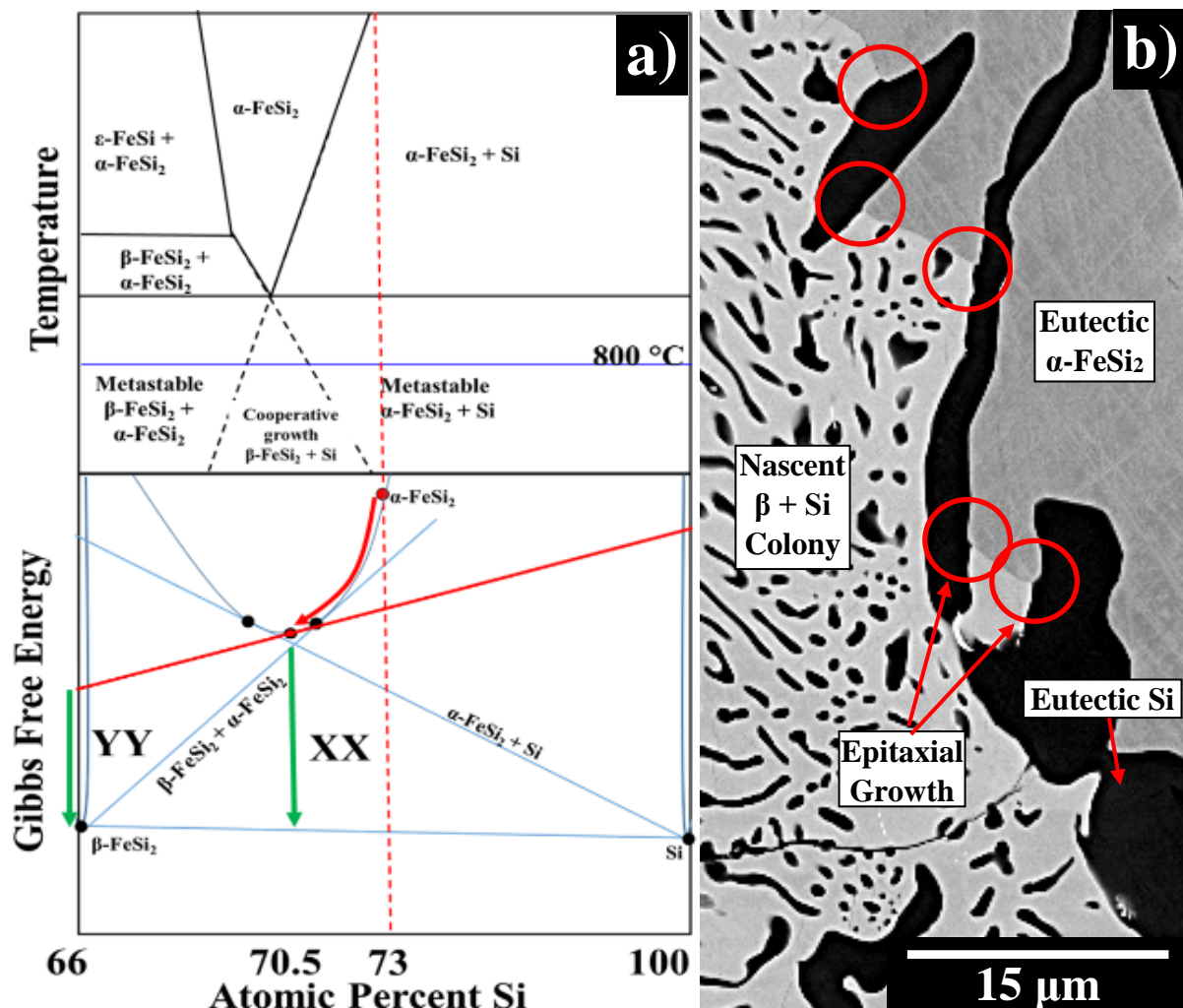


Figure 3.5: a) Schematic illustrations of the eutectoid region and the Gibbs free energy diagrams showing the evolution of Si depletion in the α phase and the resulting effect on chemical driving force for β nucleation. b) SEM micrograph indicating epitaxial growth of eutectoid Si growing on eutectic Si.

equilibrium $\beta + \text{Si}$ is given by the distance XX (for any particular composition), the driving force to nucleate the first β particles is actually given by the distance YY [69]. As the composition of α becomes more Fe-rich, the driving force rapidly increases, causing homogeneous nucleation of β -phase. Cooperative growth of Si lamellae in the β -matrix then ensues in a fashion similar to that discussed for Fe-C pearlitites [69].

3.2.2 Eutectoid Microstructure of β/Si Colonies

Pearlitic colonies are composed of Si wire-like features embedded in the β -matrix, as shown in the images of the growth fronts in Figure 3.6. Isothermal aging at lower temperatures produces lamellae that are extended in length vis-à-vis their thickness, and locally parallel. With increasing aging temperature, the lamellae become more compact and assume a wider range of local

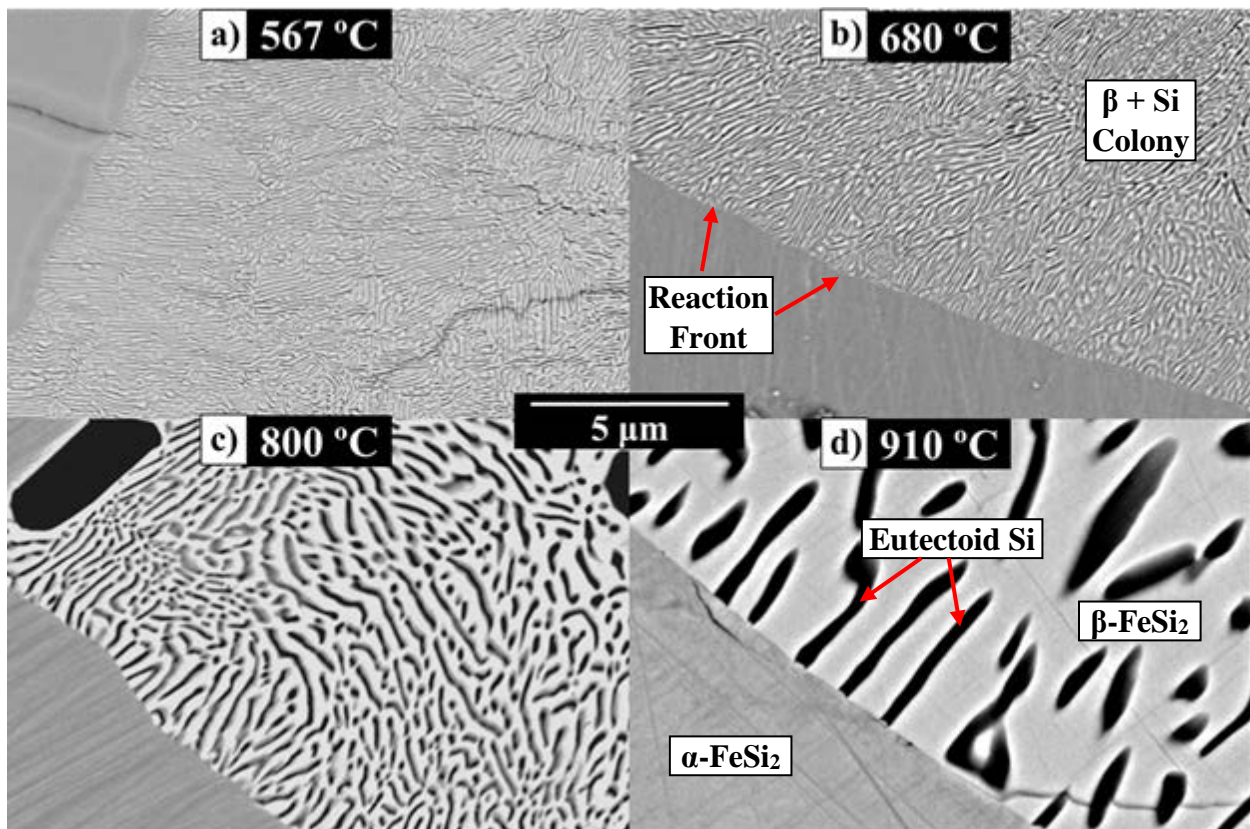


Figure 3.6: The reaction front of $\beta\text{-FeSi}_2 + \text{Si}$ colonies for $\text{Fe}_{27}\text{Si}_{73}$ samples partially aged at: a) 567 °C, b) 680 °C, c) 800 °C, and d) 910 °C.

Table 3.2: Determined growth rate and interlamellar spacing found for each aging temperature found in Figure 3.6.

T (°C)	λ (nm)	ν (nm/min)
567	54 ± 4	18 ± 1
680	107 ± 22	433 ± 22
800	157 ± 12	2217 ± 130
910	1246 ± 80	115 ± 61

orientations. Both the lamellar thickness and the interlamellar spacing (λ) increase with increasing aging temperature; the latter was measured for each temperature at the boundaries of growing colonies (e.g., Figure 3.6), using the method of linear intercepts. This was specifically done for regions at the transformation boundaries where the interlamellar spacing was smallest, to crudely account for the orientation of the lamellae relative to the 2D section. Growth rate (ν) was measured for each sample by measuring the diameter of the five largest β colonies in each sample, assuming that they nucleated near the beginning of the heat treatment, (e.g., see the blue arrows in Figure 3.4.a) and dividing by the total aging time. This will clearly underestimate the true interfacial velocity, since we do not account for any incubation time and we ignore growth in the third dimension. Results of these measurements are summarized in Table 3.2. As expected, the lamellar spacing and colony growth increases with increasing temperature; however, the growth rate of the 910 °C does not fully follow the trend and will be discussed later.

Resolving Si orientation through EBSD was a nontrivial challenge, caused by fine lengthscales, signal degradation from the high interface density, and difficult sample preparation. In Figure 3.7, we can clearly observe that lamellar spatial alignment and spacings are not indicative of colony boundaries: however, they do engender strain in the nascent β matrix, Figure 3.7.b. Matrix strain

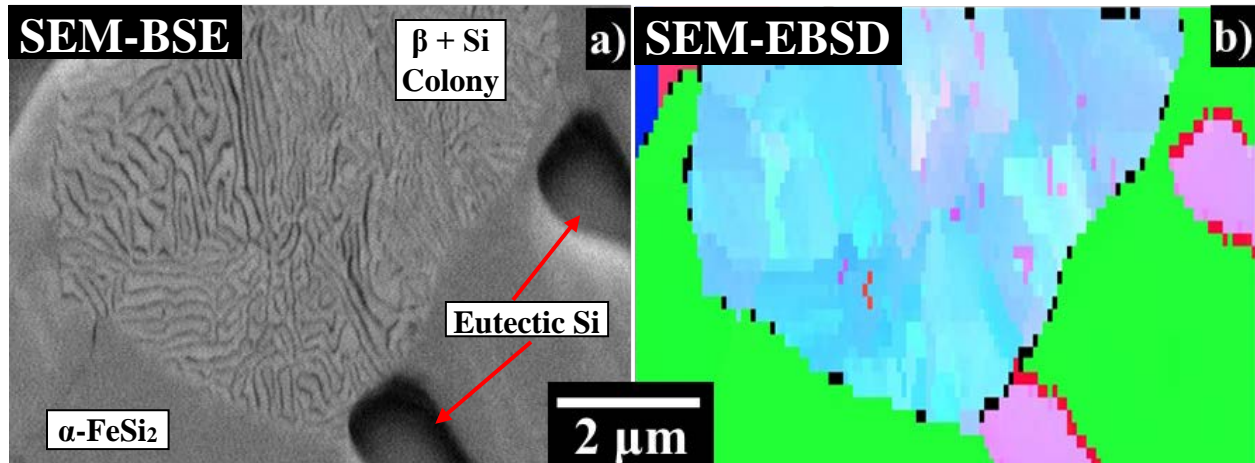


Figure 3.7: a) SEM and b) EBSD images of the same nascent $\beta + \text{Si}$ nucleus. The color denotes orientation. The β matrix (light blue) has indications of strain caused by the spatial alignment of Si lamellae, and this is observed as color variations.

was not observed in fully aged samples, where the strain could have been relaxed through annealing and the migration of defects to interfaces.

TKD-EBSD was performed on melt-spun $\text{Fe}_{28}\text{Si}_{68}\text{Ge}_4$ ribbons from Chapter 4: the orientation of the SiGe nanowire will be discussed here as it pertains to this investigation into eutectoid microstructure. The TKD-EBSD was not able to index the entirety of a nanowire (the indexed parts are colored and the unindexed parts are dark grey and black) but enough was indexed to identify several abrupt changes in orientation, Figure 3.8. Preliminary TEM, Appendix 4, suggests that these unindexed areas could be the result of amorphization during ion milling. Pole figures of these nanowire sections show that the change in orientation is caused by twinning of the $\{111\}$ planes, specifically we have observed twinning of (111) and $(\bar{1}\bar{1}\bar{1})$ planes with 180° rotations about the $[111]$ and $[\bar{1}\bar{1}\bar{1}]$ directions respectively. It is clear that a single nanowire is polycrystalline, but we were unable to ascertain the Si grain size. Our limited survey discovered four such events, so it is likely that Si/Si twin interfaces are quite common; however, since we were unable to determine their interface density, they were excluded from our thermal boundary conduction calculations. It

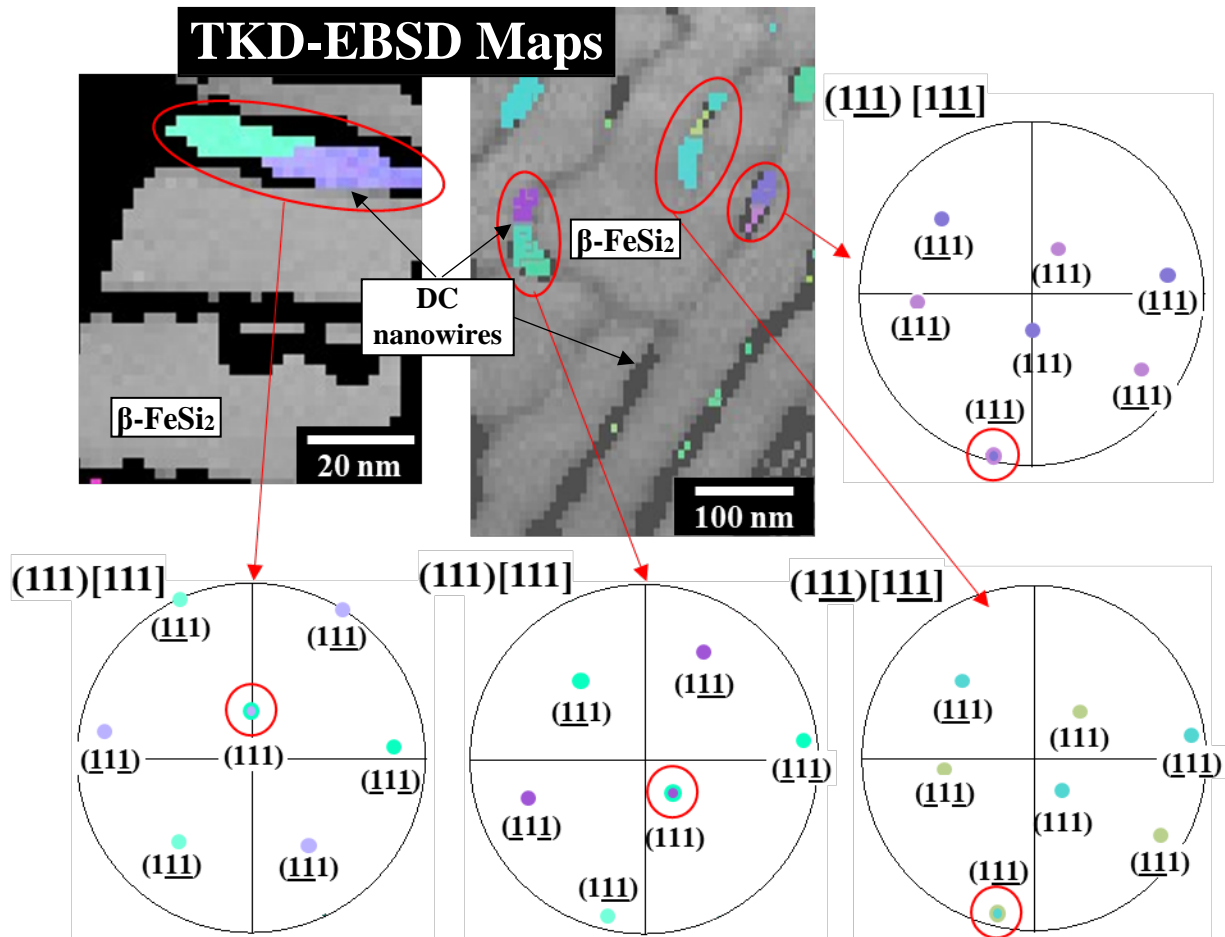


Figure 3.8: Two TKD-EBSD maps showing eutectoid morphology, with corresponding nanowire pole figures. These pole figures clearly show a 180° rotation around the plane normal for (111) and (111) planes, which is characteristic of twinning in FCC lattices. Each plane is labeled; we assigned the plane most parallel to the surface sample as (111).

should be mentioned that a sample prepared for TKD can also be used in a transmission scanning microscopy (TEM); this technique was not used for general characterization but the preliminary data can be found in Appendix 4.

3.2.3 Rayleigh Instability of Eutectoid Microstructure

Interpreting the morphology of eutectoid Si from 2D SEM cross-sections is nontrivial. The existing literature often refers to eutectoid Si as “nanowires”, and fully decomposed samples do exhibit both length-wise and edge-on nanowires. However, incompletely aged samples never exhibit

colonies with edge-on nanowires, instead they always appear as continuous lamellae. Confirmation of Si morphology was obtained by examining ion-milled cross-sections on under and overaged samples. 90° cross-sections clearly show that the eutectoid Si initially form as long, irregularly

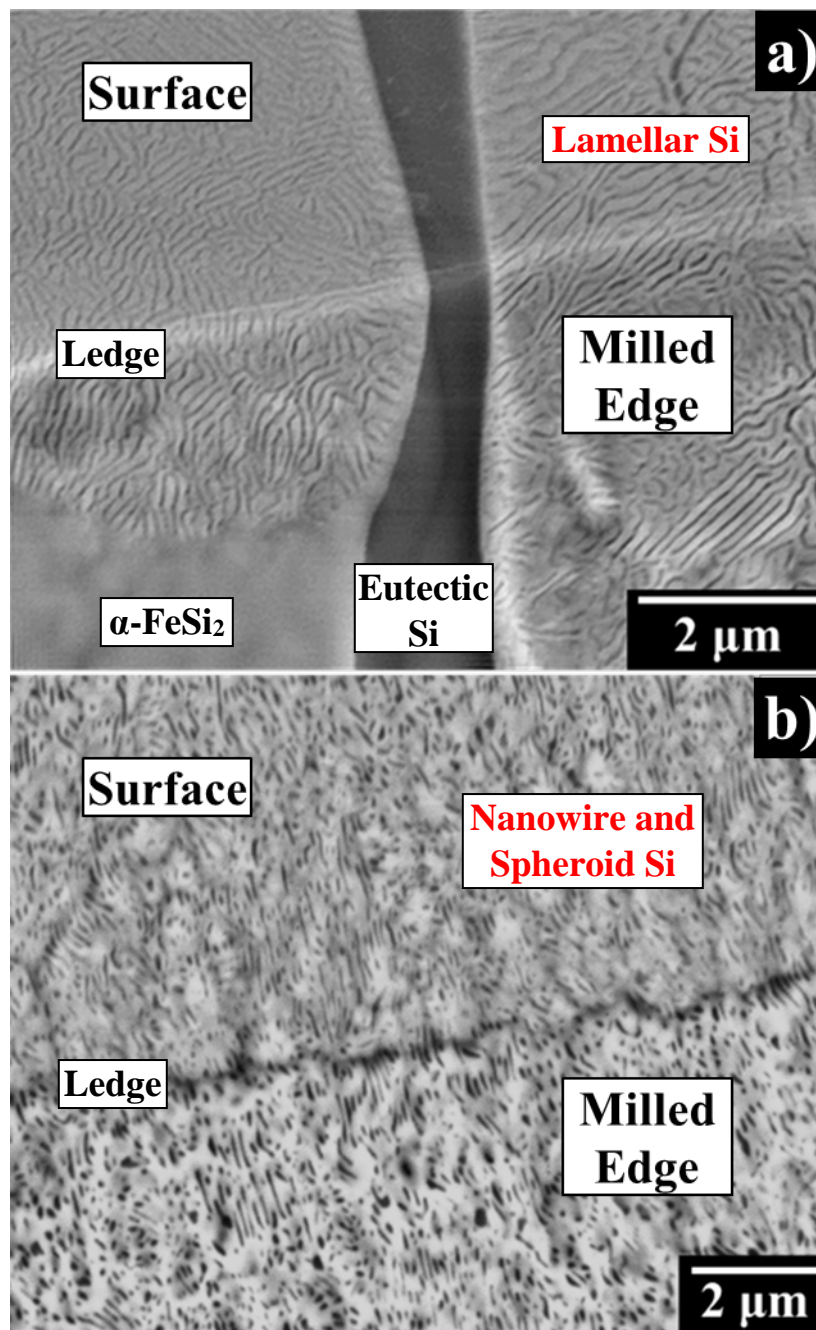


Figure 3.9: SEM micrographs of ion cross-section of a) underaged and b) overaged Fe₂₇Si₇₃ samples. The surface and milled edge surfaces are perpendicular.

shaped lamellae that are continuous in all orientations, Figure 3.9.a. As aging continues, the lamellae decompose to ribbons, nanowires, and culminating as spheroids, as shown in Figure 3.9.b. Figure 3.10 shows micrographs obtained from $\text{Fe}_{28.4}\text{Si}_{71.6}$ both at the growth interface and far behind the interface. The lamellae break up into wire-like structures behind the propagating interface, and eventually spheroidize. We emphasize that this must occur after the growth front has passed and is not the result of a divorced eutectoid. The fragmented lamellae are thicker than those at the growth front, and measurements of the eutectoid Si microconstituent show a decrease in the area fraction. In an extension of Lord Rayleigh's instability theory for wires [70], Werner showed that surface area can decrease when finite and semi-infinite lamellae disintegrate into

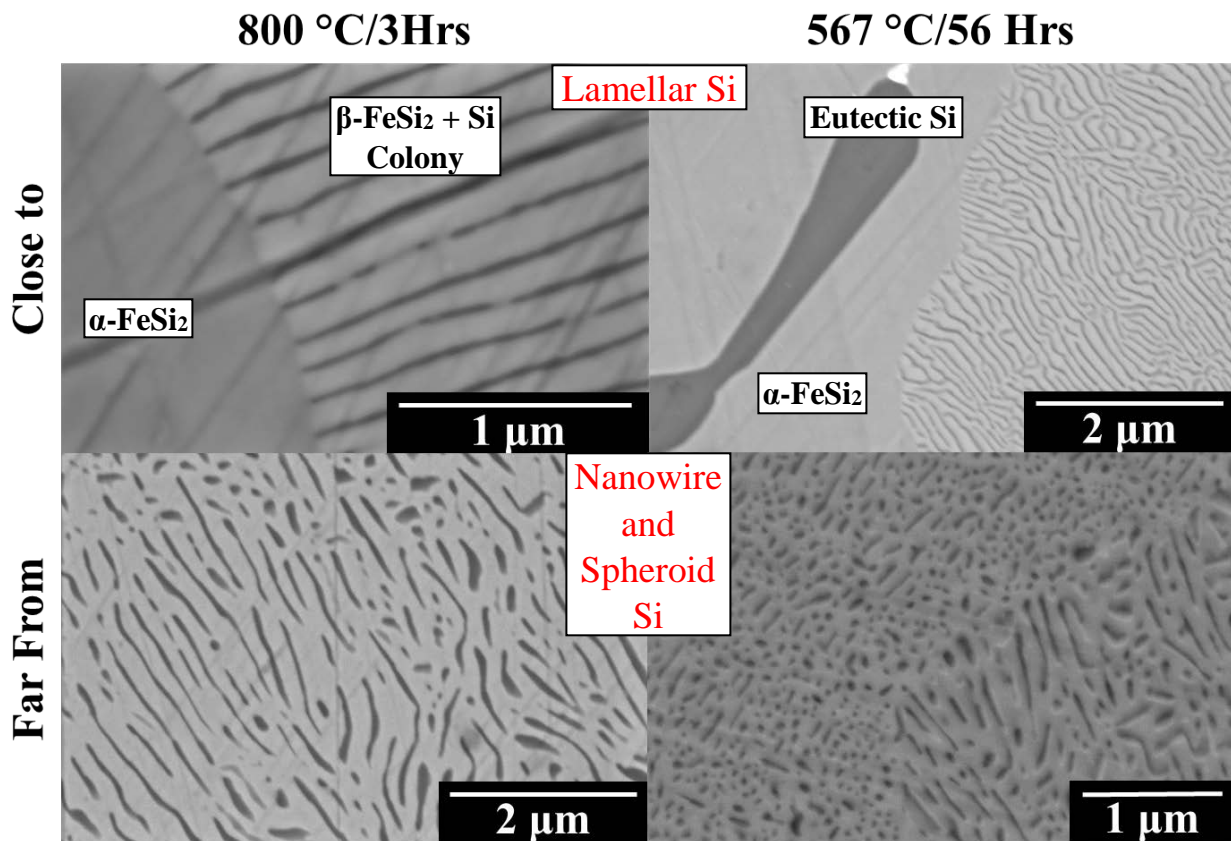


Figure 3.10: SEM micrographs depicting the effects of Rayleigh instability on eutectoid Si close to (Lamellae), and far away (Nanowire and Spheroid), from the reaction front. These images come from the $\text{Fe}_{28.4}\text{Si}_{71.6}$ samples.

narrow ribbons [71]. SEM inspection shows that this process occurs across the range of investigated temperatures on the same timescale as the eutectoid decomposition itself. At shorter timescales, there does not appear to be Ostwald ripening, i.e., there is no decrease in the number density of features via competitive coarsening. This implies that Si diffusion along the β /Si interface is faster than diffusion through the β -matrix, which would foster ripening.

3.2.4 Activation Energy of Eutectoid Decomposition

Eutectoid decomposition can be controlled by different kinetic processes including volume diffusion in either the parent or parent + product phases [72][73][74][75], or it can be controlled by diffusion in the advancing interphase interface [76][77]. Many treatments of eutectoid decomposition arrive at a relation between the interface velocity and interlamellar spacing of the form $v\lambda^2 = QD$, v and λ values are found in Table 3.2. It is usually necessary in deriving this to assume an “optimization condition” such as a relation to the minimum spacing or to maximum entropy production. Shapiro and Kirkaldy (S-K) [78] argued for a relation of the form:

$$v\lambda^3 = A(T)D(T)(K - 1) \quad 3-1$$

The coefficient A will in general contain terms related to the driving force (or undercooling), the relevant solidi in the binary phase diagram, local concentrations, phase volume fractions and interfacial energies. D is the effective diffusivity and K is a constant > 1 related to the choice of optimization condition. S-K gave specific form to eqn. (1) for kinetics controlled by diffusion in the growth interface, and assuming a simple symmetric eutectoid. S-K suggested that the temperature dependence of the diffusion kinetics could be obtained from Arrhenius plot of $\ln(v\lambda^3)$ vs. $1/T$, but that the resulting value would overestimate the real activation energy if the temperature dependence of A is ignored. As such, Figure 3.11 shows Arrhenius plots for $v\lambda^3$ and $v\lambda^2$ which

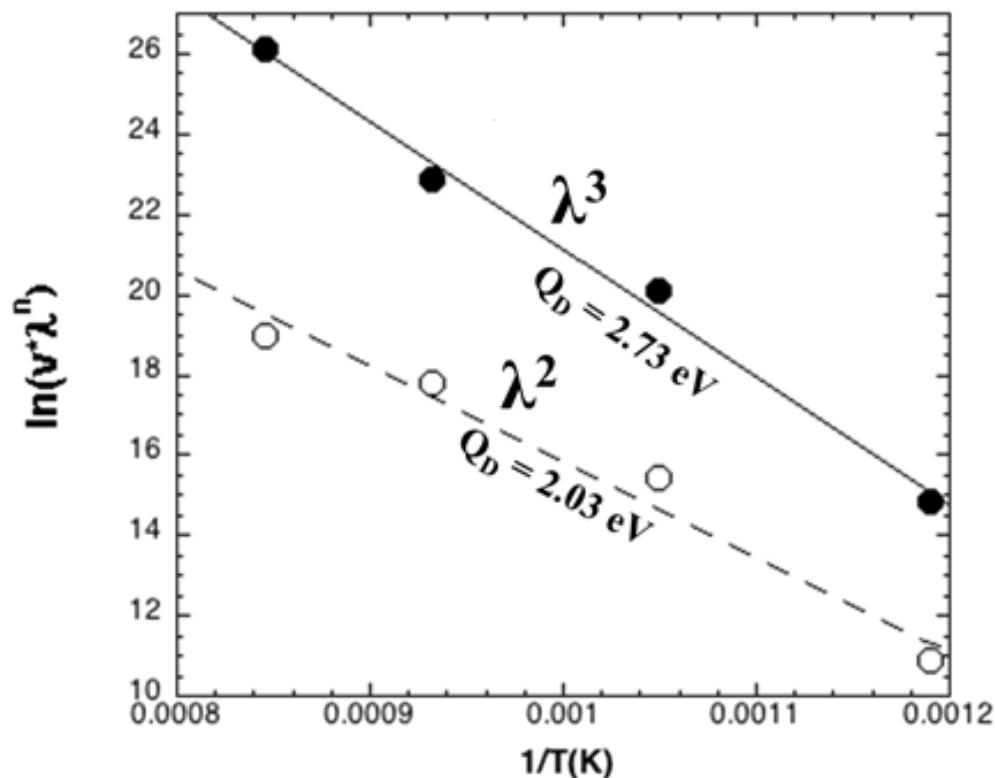


Figure 3.11: Arrhenius plot of $\ln(v\lambda^n)$ vs $1/T$, where the activation energy for the eutectoid decomposition occurs via interface or volume diffusion mechanisms. Bounds for the activation energy are defined by plotting both interface and volume limited growth kinetics ($n = 2$ or 3 , respectively).

should effectively bound the activation energy of the dominant kinetic mechanism. The result gives an activation energy bounded by 2.03 – 2.73 eV.

These values do not definitively identify the dominant kinetic mechanism, but are reasonable in magnitude. The observation discussed above that Si diffuses through the α -phase to grow on the eutectic Si indicates that volume diffusion can occur at these temperatures. Diffusivities of Si in the α and β phases are not known. d’Heurle and Gas noted in a review that Si diffusion in metal silicides has relatively low activation energy compared to metal self-diffusion of similar homologous temperature. This may result either from grain boundary diffusion or due to intrinsically large vacancy concentrations associated with structure or stoichiometry [79]. For example, silicon diffusion in MoSi_2 ($T_m = 2600$ K) has an activation energy of only 2.2 eV, whereas

the activation energy for self-diffusion of Mo in Mo ($T_m = 2900\text{K}$) is 4.4 eV. Furthermore, the α -FeSi₂ phase has a very high level of intrinsic vacancies (~14%) attributed to the Fe sublattice, associated with the off-stoichiometry composition [23][22]. However, we cannot rule out boundary diffusion. Taking the activation energy of grain boundary self-diffusion in Si as a proxy, this has been reported as 2.4 eV [80], also within the bounded range from Figure 3.11. In Figure 3.11, potential systematic errors in the measurement of v and λ will affect the activation energies as follows. The most likely systematic error in measuring λ would be to overestimate the spacing, but this is not likely to be an error much larger than the random error noted in Table 2, hence we do not consider this further. The most likely systematic error in measuring v is to underestimate the velocity, as described above. This is not likely to be significant at large undercooling, but could be significant in the sample aged at 910 °C, where the uncertainty in the start time is largest. For example, if we arbitrarily increase v by an order of magnitude at 910 °C, the resulting bounds on activation energy change to 2.51 – 3.2 eV. These bounds on activation energies are larger than what seems likely given the mechanisms described above, hence we believe our error in the velocity is not nearly as large as an order of magnitude.

3.2.5 Divorced Eutectoid Decomposition in High-Temperature Conditions

Examining the data in Table 3.2, it is apparent that the sample aged at 910 °C behaves quantitatively different from samples aged at lower temperatures. The velocity increases with aging temperature until 910 °C, where there is a marked decrease. At the same time, the interlamellar spacing increases by an order of magnitude compared with aging at 800 °C. The lamellae at this temperature tend to be very coarse and rather short. Furthermore, inspection of colonies at this temperature, unlike those formed at lower temperatures, shows significant heterogeneity. As shown in Figure 3.12, near the center of the colony, where nucleation is

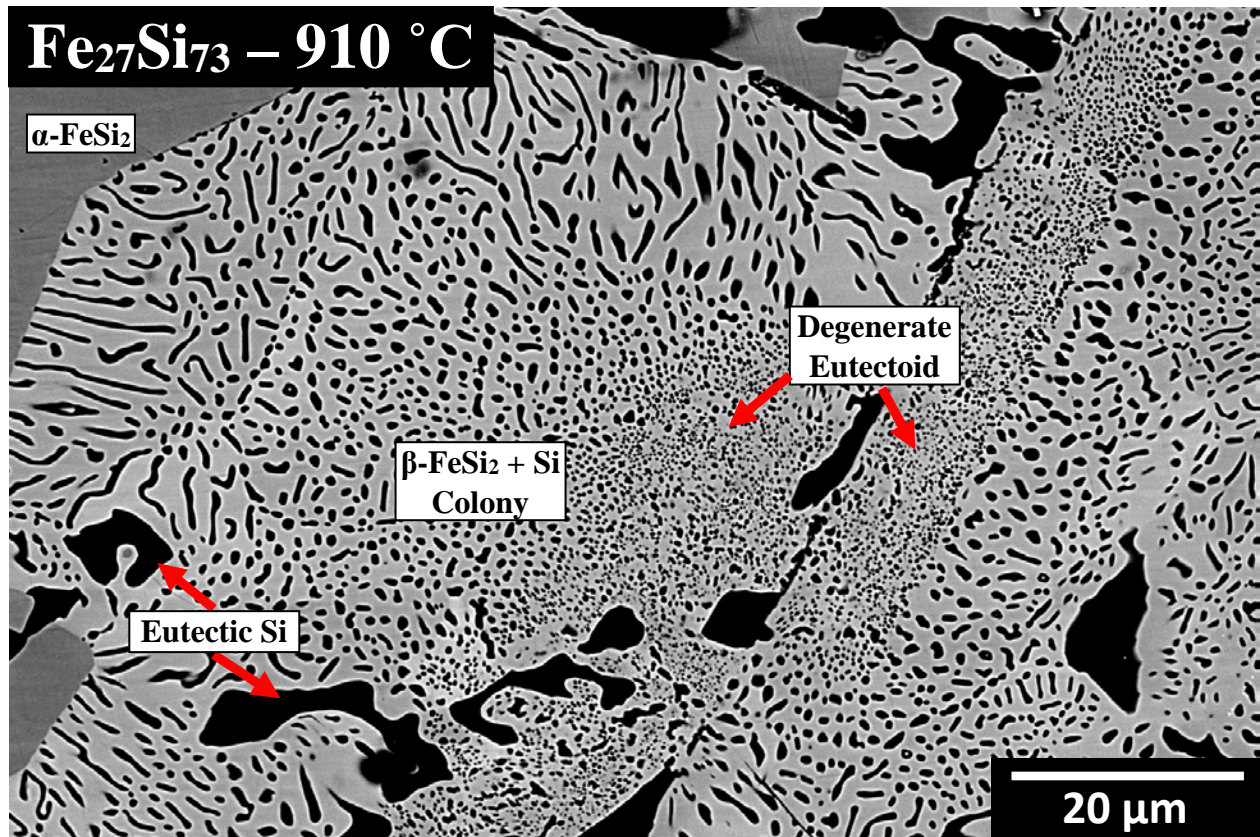


Figure 3.12: SEM micrograph of the transient degenerate pearlite (fine spheroids) prior to achieving steady state lamellae propagation, in the $\text{Fe}_{27}\text{Si}_{73}$ sample aged at $910\text{ }^{\circ}\text{C}$.

presumed to have occurred, the microstructure is much finer and more equiaxed. This is not due to breakup of lamellae due to an instability, as is discussed previously, which leads to coarser structures.

This fine-scale, spheroidal microstructure is attributed to transient degenerate pearlite, arising from initially uncoupled, competitive growth of microconstituents in the early stage of colony development [81][82][83]. Si spheroids nucleate with small spacings and are occluded by faster β phase growth. Screening the particles from the α phase initially limits the transformation lengthscales [84], and requires Si to repeatedly nucleate at the reaction front. This may explain the apparent decrease in colony growth rate observed at $910\text{ }^{\circ}\text{C}$, as the growth rate is only a maximum when cooperative growth is achieved. The degenerate microstructure depends on the ratio of the

growth rate of β and Si, V^β and V^{Si} respectively. When V^β/V^{Si} is much greater than unity, the decomposition produces fine spheroids whose spacing can be an order of magnitude smaller than that arising from lamellar growth [84]. Uncoupled growth is a transient mode, and as the interlamellar spacing increases and V^β decreases, the microstructure evolves from spheroid to truncated lamellae to lamellae (cooperative growth). The change from fine lamellae at high undercooling to ribbons at low undercooling suggests either V^β is inherently greater at high temperatures or the colonies had yet to reach steady state.

3.3 Fe_{28.4}Si_{71.6} - Effect of Eutectoid Structure on Thermal Transport

3.3.1 Density of Heterointerfaces

The Fe_{28.4}Si_{71.6} sample was used to observe microstructural and thermal conductivity differences caused by thermal processing extremes. One sample was aged at 567 °C for 56 hours and produce fine lamellar eutectic. Ageing at 910 °C for 120 hours deeply overaged the sample, resulting in heavily spheroidized and coarsened Si. Figure 3.13 compares the two samples; the low-temperature aging produced Si nanowires with mean diameter of 29 ± 5 nm and mean spacing 106 ± 20 nm, and the high-temperature aging produced highly coarsened particles 984 ± 883 nm diameter quasi-equiaxed particles that were spaced 2429 ± 1697 nm apart. The 2D β /Si interface density for both samples was determined by the linear intercepts method and was found to be $\rho_{\text{int}} = 11.0$ and 0.3 interfaces/ μm for the 567 °C and 910 °C samples, respectively.

The mean colony size was obtained using EBSD and the method of linear intercepts. The low-temperature grain size was 16 ± 15.3 μm while the sample overaged at high-temperatures had grain size of 29.7 ± 25.1 μm , Figure 3.14.a and Figure 3.14.c. In both samples, the grain size distributions show a large positive skew, almost tending towards bimodality, Figure 3.14.b and Figure 3.14.d.

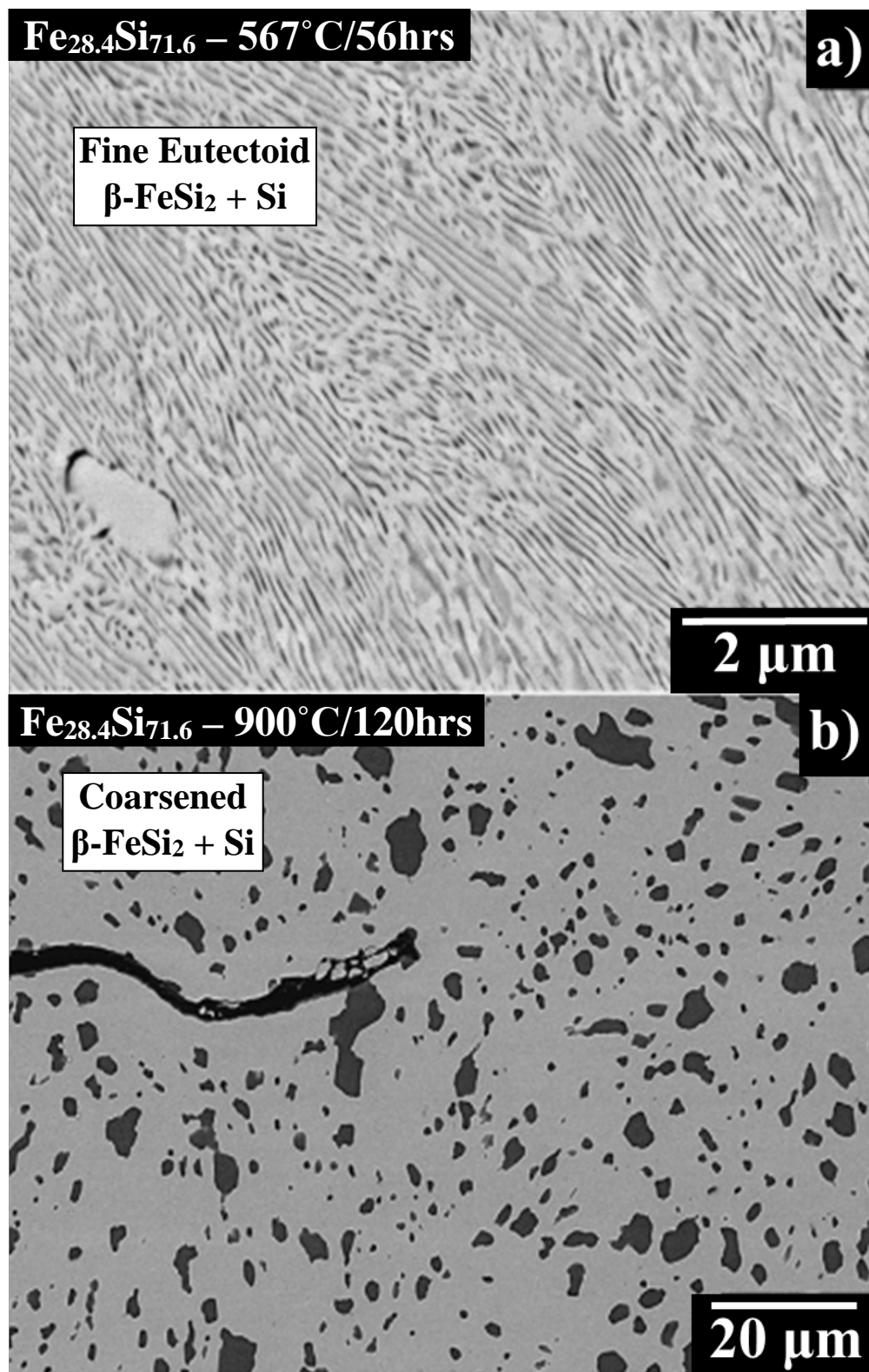


Figure 3.13: $\text{Fe}_{28.4}\text{Si}_{71.6}$ samples aged at a) 567°C for 56 hours to produce high β/Si heterointerface density, and b) 910°C for 120 hours to produce low β/Si heterointerface density. The lighter phase in both images is the β matrix and the darker phase is the Si phase.

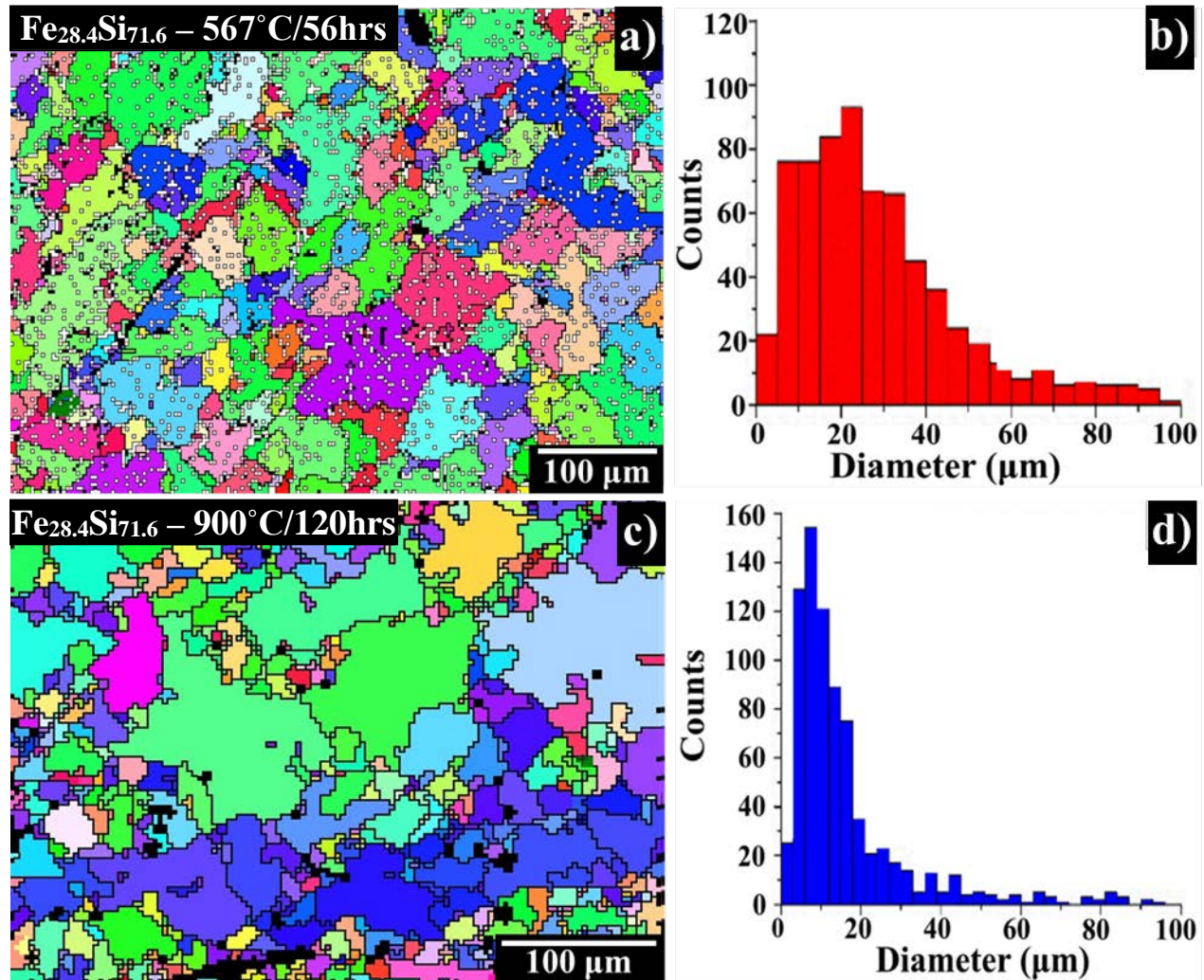


Figure 3.14: EBSD micrographs for Fe_{28.4}Si_{71.6} sample aged at a) 567 °C for 56 hours and c) 910 °C for 120 hours, with respective colony diameter distributions b) and d).

Higher-resolution EBSD from the 910 °C sample shows that, within a single large b grain, multiple equiaxed Si particles have similar orientations.

3.3.2 Thermal Conductivity

Given the large differences in the lengthscales and morphology of the microstructures, these two samples were subjected to time domain thermoreflectance (TDTR) measurements for thermal conductivity. The Fe_{28.4}Si_{71.6} sample aged at 910 °C for 120 hours had a thermal conductivity of 23 ± 5 W/m/K. For the sample aged at 567 °C for 56 hours, the thermal conductivity decreased to

12 ± 1 W/m/K. The fractures observed in the sample have a sufficiently low density that they are widely spaced compared to the volume probed by the TDTR pulse. Hence the cracks have no influence on the results for thermal conductivity. The absolute thermal conductivities measured here agree with those reported in references [43].

3.3.3 Thermal Boundary Conductance

We consider two general methods that can be employed to account for the effects of interfacial phonon scattering on the thermal conductivity. The first is rooted in the Callaway-Debye model for thermal conductivity [85], an approach that specifically considers how phonon transport depends on the size of a structure, such as the diameter of free-standing SiGe nanowires, relative to the phonon mean free path. When the phonon bulk mean free path (MFP) is longer than nanowire diameter, low frequency phonons are additionally scattered by the boundary and become a significant factor in thermal conductivity of SiGe nanowires [86][87]. This lowers the SiGe nanowire thermal conductivity below the alloy limit [88]. We also note this approach has been well studied for polycrystalline/nano-grained materials [89][90][91][52], and has demonstrated reasonable agreement in describing reductions in thermal conductivity due to grain boundaries in a chemically homogeneous material [92][93]. Thermal conductivity predictions made from this model can be found in the Appendix 5.

However, the application of this phonon-interface scattering rate approach towards predicting heterogeneous composites, including those that contain internal interfaces that separate heterogeneous materials, or even different phases of the same material, is questionable. This, in part, is due to the finite temperature drop that can exist across an interface or interfacial region that separates two different materials. This temperature drop, which is quantitatively related to the TBC

across the interface [94], is driven by the differing phonon energies, group velocities, and dispersions in the different materials, along with localized defects and impurities [8][95].

Thus, a conceptually simpler model to account for additional phonon thermal resistances due to the presence of internal interfaces directly considers this boundary as an additional resistance [95]. Having determined the thermal conductivity for each sample, it is clear that the β /Si interface contributes significantly to phonon scattering; however, we can assume from the order of magnitude increase in interface density and modest reduction in thermal conductivity that the β /Si interface is not efficient at scattering phonons. The β/β interface was deemed to be an insignificant contributor to thermal scattering in our samples, since the grain size is very large and hence the interface density is orders of magnitude smaller. Trace Cu contamination was also considered to have insignificant alloy scattering due to its low concentration.

Additional insight into the individual thermal scattering contributions can be obtained from modeling the system as a simple thermal circuit in series (Matthiessen's rule [52]),

$$\frac{1}{\kappa_T} = \frac{f_\beta}{\kappa_\beta} + \frac{f_{Si}}{\kappa_{Si}} + \frac{\rho_{\beta/Si}}{h_{k,\beta/Si}} \quad 3-2$$

where κ_T , κ_β , κ_{Si} , f_β , f_{Si} , $h_{k,\beta/Si}$, and $\rho_{\beta/Si}$ are the total measured thermal conductivity, the thermal conductivities of β and Si, the volume fraction of β and Si, the β /Si thermal boundary conductance, and β /Si interface density respectively. The bulk value of κ_{Si} is well documented and is used here, while f_β and f_{Si} were taken directly from Rietveld analysis. There are, however, differences between interface densities measured using linear intercepts from a 2D micrograph, and the actual interface density in 3D. As a first-order approximation, a simple geometric model is used here to compare the length of interface per area from micrographs and the 3D surface area per volume, at constant volume fraction of β and DC phases. The aspect ratios of planar lamellae were varied

such that the geometry evolved from sheet to lath to wires. A 2D to 3D correction factor was determined from the model that estimates the interface density is a factor of 2 larger for idealized nanowires vs. planar lamellae. A similar model was made for equiaxed particles approximated by spheres in 3D vs. projected circles in 2D. These geometry correction factor models can be found in the Appendix 6.

The only unknowns in this equation are κ_β and $h_{k,\beta/Si}$. Using data acquired from both 910 °C and 567 °C samples, we were able to simultaneously solve the two equations/two unknowns problem. The result gives $\kappa_\beta = 19.8 \pm 4$ W/m-K and $h_k = 571 \pm 51$ MW/m²-K. The thermal conductivity of β is larger than other reported values, 12.8 [37] and 14.2 [47] W/m-K. These prior investigations used powder processing and created significantly smaller β grain sizes compared to our samples that may reduce the overall thermal conductivity. The thermal boundary conductance is near the upper limit of the phonon-dominated thermal conductance regime [8], implying that the β/Si interface is an inefficient scatterer of phonons. This high TBC corroborates with values observed in other transition metal silicide/silicon interfaces, such as CoSi₂, TiSi₂, and NiSi [96][97].

3.4 Summary

We examined the mechanisms for the $\alpha\text{-FeSi}_2 \rightarrow \beta\text{-FeSi}_2 + \text{Si}$ eutectoid transformation with a hypoeutectic sample. Nucleation of pearlitic colonies occurred only on cracks at high undercoolings. At low undercoolings colonies also appear to nucleate on eutectic Si, and we suggest that facile diffusion of Si creates a large chemical driving force for β nucleation. However, we cannot be certain that unseen cracks are not responsible for colony nucleation, and tomography experiments are required to determine whether the α/Si interface is a distinct nucleation mode. Regardless, coaxing nucleation at high undercoolings is nontrivial and requires a facile heterogeneous nucleation sites, and will be further discussed in the following chapter. The

temperature-dependence of the interlamellar spacing and colony growth rate were obtained, setting bounds on the activation energy for Si diffusion. Since these bounds are consistent with either (anticipated) volume diffusion of Si in α , or boundary diffusion, we cannot be more specific on mechanism without further information. At temperatures well below the eutectoid isotherm, the transformation proceeds cooperatively producing parallel wavy lamellae of Si in the β matrix. At small undercooling there is indication that growth is close to becoming decoupled. Facile diffusion of Si at the β /Si interface leads to coarsening of Si lamellar into rods and spheroids behind the growing decomposition front.

The $\text{Fe}_{28.4}\text{Si}_{71.6}$ sample was used to create extremes in heterointerface density through low-temperature and prolonged high-temperature agings. A 2x reduction in thermal conductivity was associated with a 40x increase in β /Si heterointerface density; and we have shown that the β /Si interface is an inefficient phonon scatterer. Aging at greater undercoolings could promote higher β /Si interface density, but the transformation rate becomes unreasonable at lower temperatures. Hierarchical structuring of eutectoid and eutectic Si could be favorable due to the increased volume fraction of Si, but would not be desirable for thermal scattering. Ultimately, the binary Fe-Si alloy does not offer enough degrees of freedom to optimize thermoelectric properties. In order to continue reduce the thermal conductivity of the nanocomposite, and perhaps to tailor the electronic properties as well, the addition of isostructural elements such as Ge will be explored in the next chapter.

4 Fe-Si-Ge Ternary Alloy

As discussed in Chapter 3, the β -FeSi₂/Si semiconducting nanocomposite is a promising thermoelectric system with eco-friendly materials, but improvement of the properties requires additional flexibility to further increase phonon scattering, ideally without significant degradation of the power factor. Here we will explore how relatively small additions of Ge to the system can enhance the thermoelectric properties and widen the design space, if Ge content and spatial disposition can be controlled. We investigated the use of solidification combined with solid-state transformations to reduce the thermal conductivity via hierarchical modification of microstructure, specifically of the meso-scale eutectic. Solidification of Fe₂₈Si₆₈Ge₄ alloys leads to a eutectic lamellar microstructure comprised of hyperstoichiometric α -FeSi_{2+ δ} phase and diamond cubic (DC) Si_{1-x}Ge_x. The eutectic lengthscales can be varied over two orders of magnitude depending on solidification rate. Subsequent aging of the eutectic produces eutectoid decomposition, α -FeSi₂ \rightarrow β -FeSi₂ + Si_{1-y}Ge_y, where the nano-scale DC product is interleaved with the eutectic DC lamellae. By controlling both the frequency of β -FeSi₂/diamond cubic heterointerfaces, as well as the degree of Ge segregation into the eutectoid microconstituent, the thermal conductivity of the composite was varied from 22.8 W m⁻¹ K⁻¹ down to 8.3 W m⁻¹ K⁻¹. We analyze the thermal conductivity in terms of a series thermal resistance model, including thermal boundary conductances at heterointerfaces, and show that the thermal boundary conductance is reduced by at least an order of magnitude when the diamond cubic microconstituent is enriched from 0 to 30 at% Ge (atomic-scale structuring). Avenues for additional microstructural improvements towards thermoelectric applications are discussed.

4.1 Microstructural Lengthscales Induced by Solidification

4.1.1 Eutectic Microstructure of Fe₂₈Si₆₈Ge₄ alloy

In this chapter, the Fe₂₈Si₆₈Ge₄ alloys will be referred to by their processing methodology: we will refer to samples made by direct arc-melting as “slow-cool” and those produced from melt-spinning as “rapid-cool”. The mean cooling rate of the melt-spun material is estimated as 10⁶ °C/s, vs. 10² °C/s from the ambient cooling arc-melt. There are also two different DC phases arising from solidification and solid-state transformations, and will be referred to as eutectic and eutectoid SiGe, respectively.

As-cast, the slow-cool sample exhibits eutectic microstructure with an α -FeSi_{2+x} matrix containing eutectic SiGe lamellae (Figure 4.1.a). Close examination of the lamellae show that copious amounts of ϵ -FeSi are entrained within them (Figure 4.1.b). Like the binary alloys, fractures are present throughout the sample, but the intralamellar regions have a lower crack density than the surrounding α phase. Fracture is likely caused by large thermal gradient stresses generated during cooling of the boule. The relatively slow cooling rate promoted growth of coarse eutectic microstructures, where the interlamellar spacing is equivalent to α grain size: eutectic SiGe lamellae exhibit thicknesses of 44±11 μm and interlamellar spacing of 131±44 μm , based on linear intercept analysis. This results in an effective density of DC/ α -FeSi_{2+x} interfaces of 0.01 interfaces/ μm . The low interface density, presence of metallic ϵ -FeSi, and high crack density are deleterious to the thermoelectric properties.

Melt-spun, or rapid-cool, ribbons solve most of these issues. The 50 μm thick, melt-spun, although brittle, do not exhibit cracking. Formation of the ϵ phase was suppressed, only appearing in small amounts on the ribbon surface. The melt-spun sample increased the solidification rate four orders of magnitude vis-à-vis the slow-cooled sample. As can be seen in Figure 4.1.c, the faster rate significantly reduced eutectic lengthscale: the average lamella thickness was 129 ± 60 nm with an

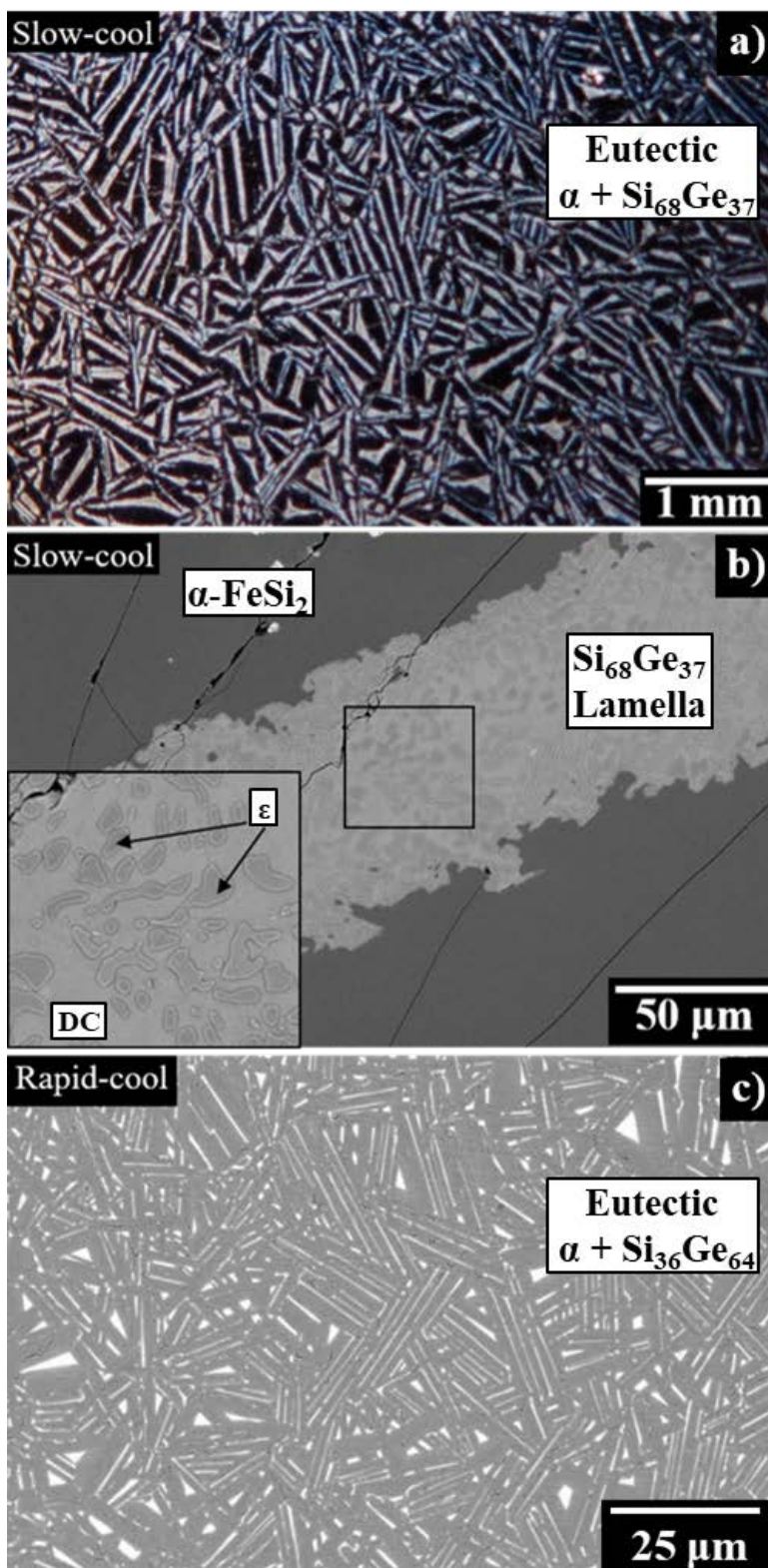


Figure 4.1: Micrographs of $\text{Fe}_{28}\text{Si}_{68}\text{Ge}_4$ alloy. a) Optical micrograph of the coarse, slow-cool eutectic microstructure, and BSE-SEM micrographs of b) a single $\text{Si}_{1-x}\text{Ge}_x$ lamella with entrained $\epsilon\text{-FeSi}$. c) BSE-SEM micrograph showing the rapid-cool eutectic microstructure. In all three images, the darkest phase is $\alpha\text{-FeSi}_{2+x}$ while the lightest phase is DC.

interlamellar spacing of $1.5 \pm 0.5 \mu\text{m}$. The morphology appears more ordered due to the interlamellar lengthscales now being smaller than the α grain. As a result of the finer lengthscales, the DC/ α interface density increased fifty-fold, to 0.54 interfaces/ μm . However, the ribbons pose their own set of challenges. Characterization is nontrivial as their diminutive size, brittle nature,

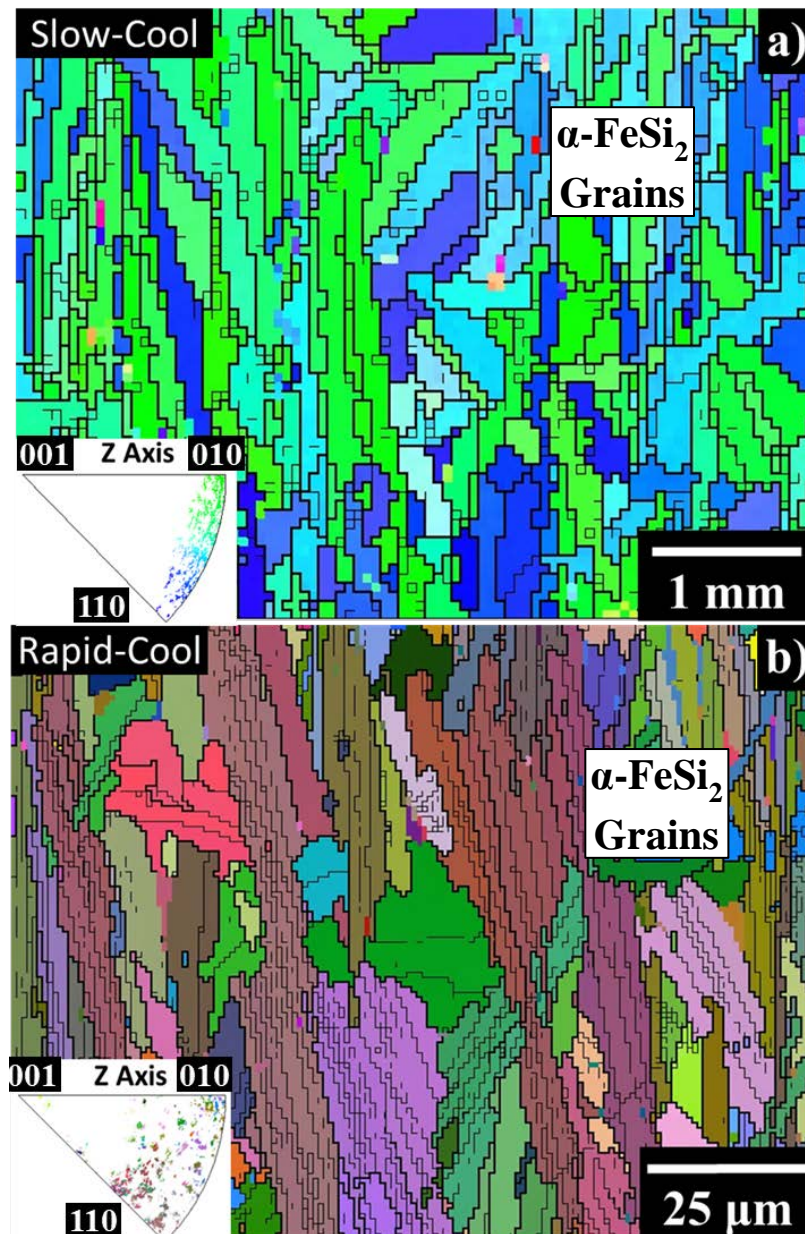


Figure 4.2: EBSD maps of $\text{Fe}_{28}\text{Si}_{68}\text{Ge}_4$ alloys produced by a) slow-cool and b) rapid-cool techniques. Heavy black lines indicate grain orientations that differ more than 15° , light black lines are differences greater than 5° and also denote the location of eutectic SiGe lamella. Insets show respective Z axis pole figures.

and sample curvature (an artifact of melt-spinning, the ribbon is curved both lengthwise and widthwise) preclude techniques that require large sample areas or physical contact, such as electrical conductivity measurements.

As-cast microstructures from the rapid-cool and slow-cool samples were analyzed with EBSD, and are shown in Figure 4.2. The slow-cool sample has a fairly tight distribution of α grain orientations ranging from (110) to (010) planes and are rotated around the surface normal. During solidification, nascent nuclei are randomly oriented across the casting surface; however, competitive growth between the erratically oriented nuclei ensures that only the fast-growing directions parallel to the heat flux dominate. This suggests that $\langle 100 \rangle$ and $\langle 110 \rangle$, and those directions in between, are the fast growth directions since they have oriented themselves along the thermal gradient. The (001) plane can only run parallel, and the [001] direction perpendicular, to the thermal flux. This results in the texture observed in Figure 4.2. The rapid-cool sample shows that the grains have a broader distribution and are rotated out of the surface plane; this is most likely caused by the cross-section not being perpendicular to the axis of growth and fast growth directions did not fully assert themselves.

We also observed that the eutectic SiGe lamellae only grow along the (001) habit plane of tetragonal α -FeSi_{2+x}, Figure 4.3. This EBSD map shows α colony orientations, denoted by color and marked with the orientation of the unit cell. The resolution was too poor to accurately image SiGe lamellae, but their position was detected by signal degradation (caused by the heterointerface) which are the dark lines in the α grain. This clearly demonstrates that the SiGe lamellae grow only along (001) habit plane; however, no specific in-plane orientation relation between the DC and α phases could be identified.

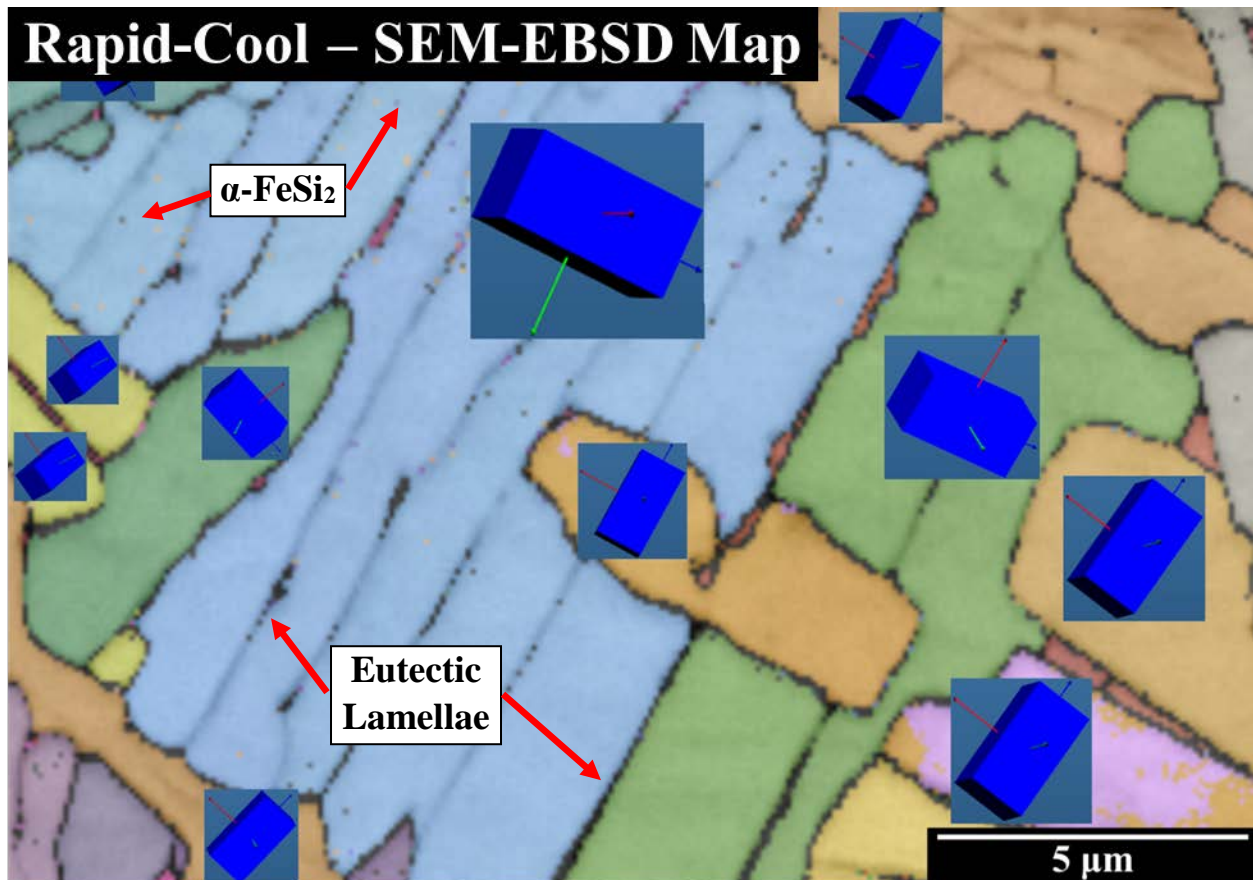


Figure 4.3: EBSD Map of the rapid-cooled $\text{Fe}_{28}\text{Si}_{68}\text{Ge}_4$. Differences in color denote changes in the α orientation, and the dark striations mark the location of SiGe lamellae. Inlays of α -FeSi₂ crystal orientations show that SiGe lamellae are found singularly along the α (001) habit plane.

4.1.2 Ternary Eutectic Microstructure

Surprisingly, the addition of Ge changes eutectic morphology from what was previously observed in the Fe-Si system, Figure 4.4. Croker et al [98], suggested that the different eutectic morphologies can be described by volume fraction (f) and the nondimensional entropy of fusion ($\frac{\Delta S_f}{R}$, where R is the gas constant). The volume fraction, in part, influences whether a eutectic grows in a cooperative mode; when the volume fractions are roughly equal, the two phases grow as interweaved lamellae, otherwise divorced eutectic (ribbons, rods, or spheroids) can form. The enthalpy of fusion is a good predictor of crystallization behavior: low values tend to be non-faceted, as isotropic growth occurs favorably; and high values tend to form facets due to anisotropic growth occurs favorably

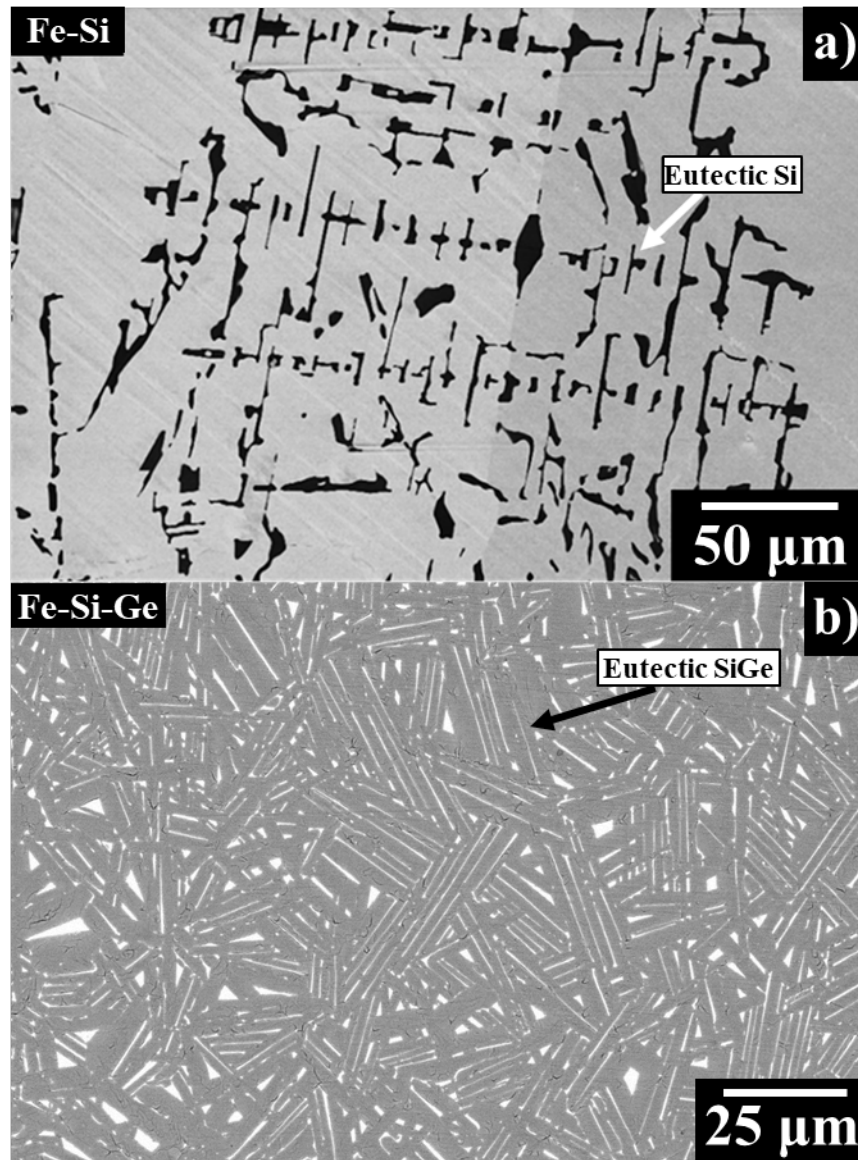


Figure 4.4: SEM-BSE micrographs showing a) the faceted eutectic ribbons of $\text{Fe}_{27}\text{Si}_{73}$ (black), and b) the eutectic lamellae of $\text{Fe}_{28}\text{Si}_{68}\text{Ge}_4$ (white) and the faceted α phase.

along certain directions [99]. If there is a low entropy of fusion phase and a high entropy of fusion

phase, $\frac{\Delta S_f^b}{R} < 2 < \frac{\Delta S_f^a}{R}$, then faceted eutectic is formed; if the entropies of fusion are low and

equivalent, $\frac{\Delta S_f^b}{R} \approx \frac{\Delta S_f^a}{R} < 2$, then non-faceted eutectic forms [98][100].

The Fe-Si alloy has a striking faceted eutectic morphology, Figure 4.4.a, where it is clear that the eutectic Si is faceted within the α matrix. The Fe-Si-Ge alloy has what appears to be non-faceted eutectic morphology, Figure 4.4.b; however, if it was truly non-faceted then there would not be a consistent (001) bounding plane for the $\text{Si}_{1-x}\text{Ge}_x$ lamellae. This suggests that that Si is the high entropy of fusion, faceted phase for the Fe-Si system, and that α is the high entropy of fusion phase for the Fe-Si-Ge phase. The exact reason for the reversal in entropy of fusion magnitudes is not fully understood. It is possible that as Ge is principally incorporated into the DC phase, the entropy must increase through entropy of mixing and effects a lower total change in entropy upon melting. This information, while not providing concrete values for entropy of fusion, illuminates the differences resulting in these two microstructures.

4.1.3 Eutectoid Microstructure

Subsequent isothermal aging caused eutectoid decomposition of the α phase into pearlitic colonies of $\beta + \text{Si}_{1-x}\text{Ge}_x$. This decomposition appears to proceed similarly to that observed in the Fe-Si binary system under similar aging conditions, resulting in eutectoid lamellae with comparable dimensions, interface density, and morphologies. Alloying with Ge does not noticeably change the eutectoid transformation rate, beyond creating heterogeneous nucleation sites at the interfaces with eutectic SiGe. Aging the slow-cool sample at 567 °C does not result in full decomposition; however, the rapid-cool sample does completely decompose in that amount of time. The eutectic SiGe provides potent nucleation sites and, as will be shown later, constrains colony size.

4.1.4 Size of $\beta +$ Eutectoid SiGe Colonies

The coarse eutectic structures in the slow-cool sample do not constrain pearlitic colony size, and they provide a negligible area fraction for heterogeneous nucleation sites; hence a longer time is

required to obtain complete transformation, ~ 120 hours at 567°C . While the average colony diameter was not measured for the slow-cooled sample, it is likely that the value is similar to a binary (Fe-Si) sample aged at 567°C for 56 hours, with an average diameter on the order of $16.0\ \mu\text{m}$. However, the melt-spun samples have a significantly higher nucleation rate for pearlitic colonies, where the fine eutectic lamellae provide facile and abundant nucleation sites (Figure 4.5). When aging is initiated below the eutectoid isotherm in this sample, Si locally diffuses to epitaxially grow on the eutectic lamellae, which leaves Si-depleted regions adjacent to the eutectic lamellae. These regions have a higher chemical driving force for β nucleation, which initiates cooperative lamellar growth [69]. This is similar to the eutectic Si nucleation mechanism discussed in Chapter 3.2.1, but here it occurs at lower temperature due to the increased heterointerface density. As a result, the eutectoid transformation reaches near complete decomposition at 567°C

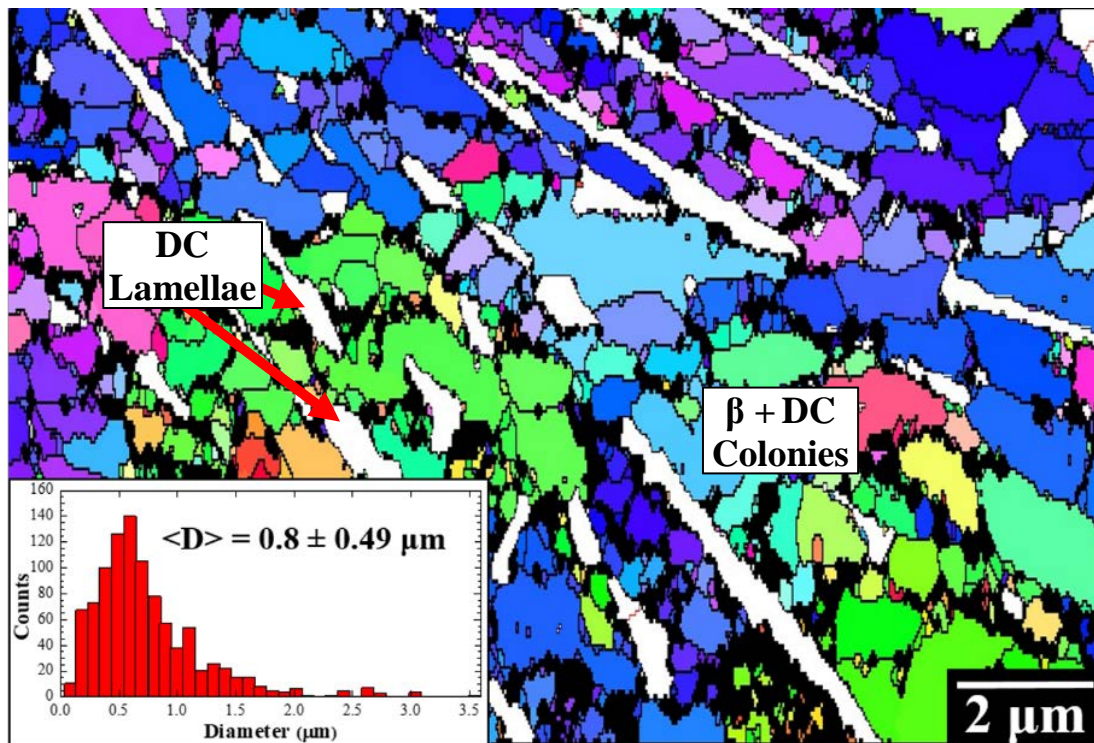


Figure 4.5: EBSD Euler orientation maps, with the colony diameter distributions shown inset, for the binary slow-cool + $567^\circ\text{C}/56\text{Hr}$. Black lines between grains depict crystal misorientation of 15° , and white grains are eutectic SiGe lamellae.

for 56 hours, without requiring a Cu accelerant [25]. The mean pearlitic colony size is only 800 ± 490 nm, due to both the higher nucleation density and to steric restrictions on growth due to the fine eutectic lamellae.

4.2 How Processing Determines Ge Disposition

4.2.1 Silicide Phase Compositions

The disposition of Ge through the hierarchical eutectic/eutectoid decomposition process is of great interest as the interplay between phases and their composition is important for thermal and electronic transport. When the velocity of the solidification front is comparable to solute diffusion, as it is for rapid solidification, solute uptake into the solid can exceed equilibrium concentrations [35][101]. Melt-spinning not only reduces eutectic length scales, but also changes the composition of the microconstituents, as shown in Table 4.1. EDS-SEM shows that the composition of the as-cast, slow-cool α phase was on average $\text{Fe}_{24.6}\text{Si}_{73.8}\text{Ge}_{1.6}$. By comparison, the Ge content of the rapid-cool ribbon nearly doubled to $\text{Fe}_{24.8}\text{Si}_{72.2}\text{Ge}_{3.0}$. Prolonged aging above 1000 °C (above the eutectoid isotherm) caused the α composition to evolve to ~1.6 at% Ge as determined by EDS; the combined results suggest that the solid solubility limit of Ge in the α -phase is 1.6 at% near 1000

Table 4.1: Composition of microconstituents for slow-cool and rapid-cool samples.

Phase	Slow-Cool	Rapid-Cool
$\alpha\text{-FeSi}_{2+x}$	$\text{Fe}_{24.6}\text{Si}_{73.8}\text{Ge}_{1.6}$	$\text{Fe}_{24.8}\text{Si}_{72.2}\text{Ge}_{3.0}$
$\beta\text{-FeSi}_2$	-	$\text{Fe}_{35.0}\text{Si}_{64.4}\text{Ge}_{0.6}$
Eutectic Lamellae	$\text{Si}_{63}\text{Ge}_{37}$	$\text{Si}_{36}\text{Ge}_{64}$
Eutectoid Nanowire	$\text{Si}_{94}\text{Ge}_6$	$\text{Si}_{82}\text{Ge}_{18}$

°C. The composition of the α phase is important because the β phase has a lower Ge solubility and the amount of entrained Ge governs the composition of the DC lamellae after eutectoid decomposition. Chemical analysis of the β phase was performed on the rapid-cool + 567 °C/56 hr sample by TKD-EDS. This technique maps composition with finer spatial resolution than is possible with standard SEM-EDS. Figure 4.6 illustrates the disposition of Ge after the eutectoid decomposition. As the α phase transforms to β , both the entrained Ge and excess Si were ejected along into the eutectoid DC nanowires, leaving the composition of the β phase as $\text{Fe}_{35.0}\text{Si}_{64.4}\text{Ge}_{0.6}$ as determined by EDS. Preliminary TEM-EDS map data, Appendix 4, corroborates that the eutectoid microstructure consists of Ge-rich nanowires and Ge poor $\beta\text{-FeSi}_2$. SEM-EDS was also performed on the much larger β grains of the rapid-cool + 900 °C/216 hr sample, and composition was found to be $\text{Fe}_{34.7}\text{Si}_{64.8}\text{Ge}_{0.6}$. Both of these values agree with other measurements of Ge solid solubility in β [39].

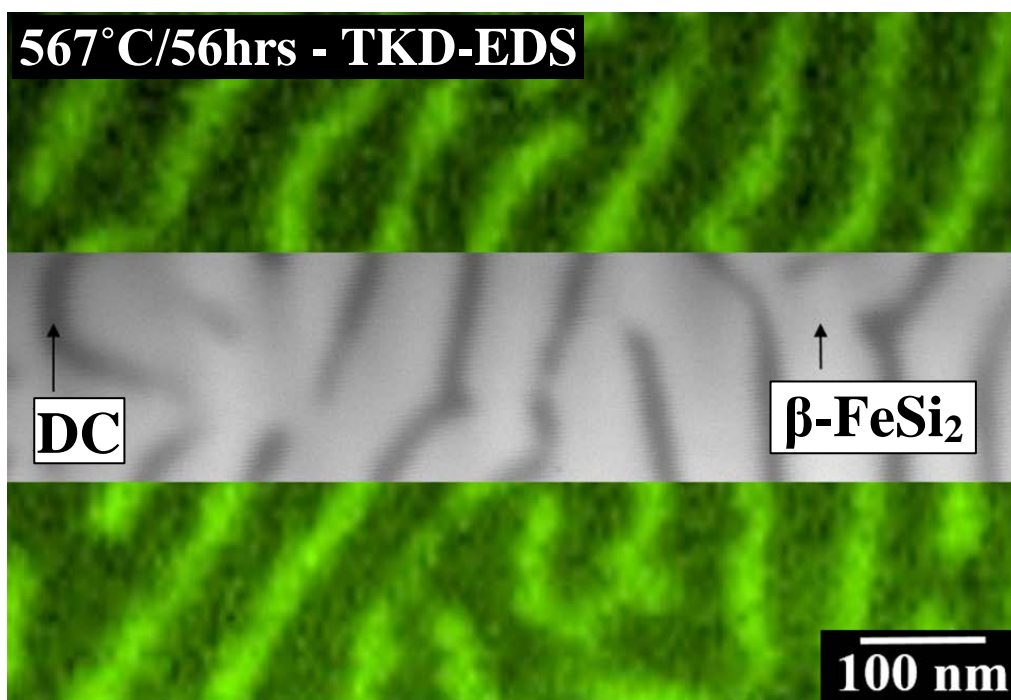


Figure 4.6: TKD-EDS composition map illustrating large amounts of Ge partition into eutectoid nanowires, with limited Ge remaining in the β matrix. The overlay in the center shows the transmission micrograph of the same area.

4.2.2 Eutectic and Eutectoid SiGe Compositions

Local chemical analysis of individual DC *eutectoid* lamella by EDS is nontrivial, owing to their small lengthscales and the enveloping β matrix, which invariably contributes a Si signal that confounds the measurement. Instead, we performed Rietveld refinement of high resolution XRD data to calculate the distinct lattice parameters from the eutectoid and eutectic microconstituents. Since the dependence of the $\text{Si}_{1-x}\text{Ge}_x$ lattice parameter on composition is well known [102], DC composition can be readily extracted from these data. A representative XRD spectrum for the aged samples can be found in Figure 4.7, which shows the major peak positions of constituent phases and clearly distinguishes between eutectic and eutectoid SiGe compositions. Rietveld refinement of these spectra shows that the specimens aged at 567 °C entrain a significant fraction of the total Ge present within the eutectoid lamellae, increasing from 6 at% Ge in the slow-cool + 567 °C/120 hr sample to about 18 at% for the rapid-cool + 567 °C/56 hr sample. The reduced Ge content in

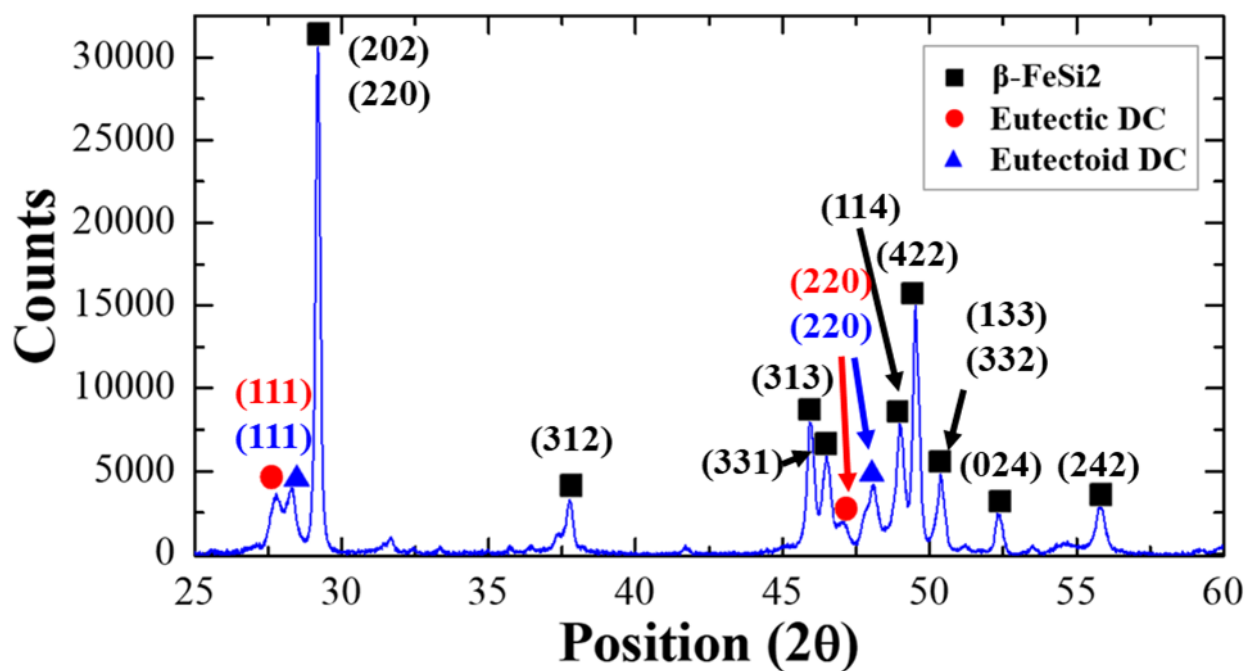


Figure 4.7: Representative XRD spectrum of an aged rapid-cool sample with the highest intensity peaks labeled.

the eutectoid DC of the slow-cool + 567 °C/120 hr sample is consistent with the lower Ge content in the as-cast α phase of this specimen. As seen in Figure 4.8, melt-spinning is effective at increasing the Ge content in both the eutectic and eutectoid lamellae. These values are significant. For example, it has been shown that as little as 10% Ge in Si reduces the thermal conductivity by an order of magnitude via alloy scattering of phonons [87] [103] [91]. At the same time, the bandgap is reduced by about 100 meV [104], and more closely aligns with the 0.78 bandgap of β [26]. The DC phase in the rapid-cool + 900 °C/216 hr sample had a composition of $\text{Si}_{69}\text{Ge}_{31}$, which is close to the equilibrium composition and will be discussed later.

There is also a small difference in the lattice parameter of pure Si and the Si produced via eutectoid decomposition. A 0.009 Å decrease in Si lattice parameter was consistently measured in aged samples and the pure Si had the accepted lattice parameter of 4.431 Å. Both samples underwent the same powder processing (hand-milled and sieved to have particle sizes below 40 μm) and mounting, and this suggests that the issue is not due to measurement errors or Rietveld refinement

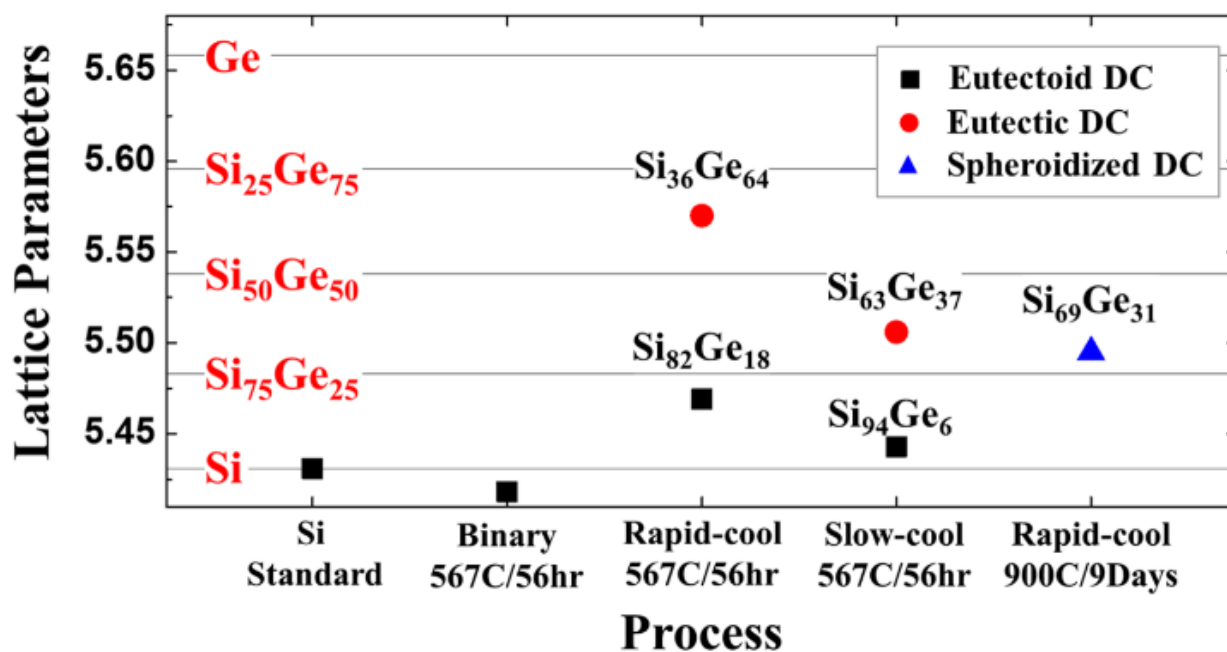


Figure 4.8: Diagram depicting the lattice parameters and composition of DC phases determined by Rietveld refinement. Liquid and solid state processing controls the Ge disposition of DC nanoconstituents.

but is an actual change in lattice parameter. It is possible that this is due to trace incorporation of Fe into the Si crystal structure, and the Fe concentration is too low for EDS to detect. Another explanation could be hydrostatic stain caused by the Si nanowire being entombed by the β matrix. However, the cause of the lattice parameter reduction was not pursued.

In order to convert DC lattice parameter to Ge concentration, experimentally measured data [102] for $\text{Si}_{1-x}\text{Ge}_x$ lattice parameters were used. By performing XRD scans and refinement on different samples of the same processed material, it was determined that the measurement variance is ± 1.5 at% Ge and $\pm 2.5\%$ for the volume fractions of the phases. We can compare Rietveld refinement with EDS areal measurements of the composition of the eutectic DC lamellae, which are large enough that EDS measurements are not significantly affected by spurious signals from the surrounding silicide. As measured by Rietveld refinement, the compositions of the eutectic lamellae were found to be $\text{Si}_{67}\text{Ge}_{33}$ for slow-cool and $\text{Si}_{36}\text{Ge}_{64}$ for rapid-cool, while by EDS they were determined to be $\text{Si}_{70}\text{Ge}_{30}$ and $\text{Si}_{28}\text{Ge}_{72}$, respectively. EDS and Rietveld refinement values for composition of the eutectic lamella do not agree perfectly due to systematic error of both techniques, but do indicate significant Ge uptake by the eutectoid lamellae, especially at high cooling rates.

4.3 Thermal Transport

4.3.1 Thermal Conductivity of Hierarchically Processed $\text{Fe}_{28}\text{Si}_{68}\text{Ge}_4$

Three samples with different eutectic + eutectoid processing regimens were used to explore the effects of hierarchical structuring and Ge on thermal conductivity. The slow-cool (Figure 4.9.a) and the rapid-cool (Figure 4.9.b) samples were aged at 567 °C for 120 hours (“slow-cool + 567 °C/120 hr”) and 56 hours (“rapid-cool + 567 °C/56 hr”) respectively, to fully decompose the α

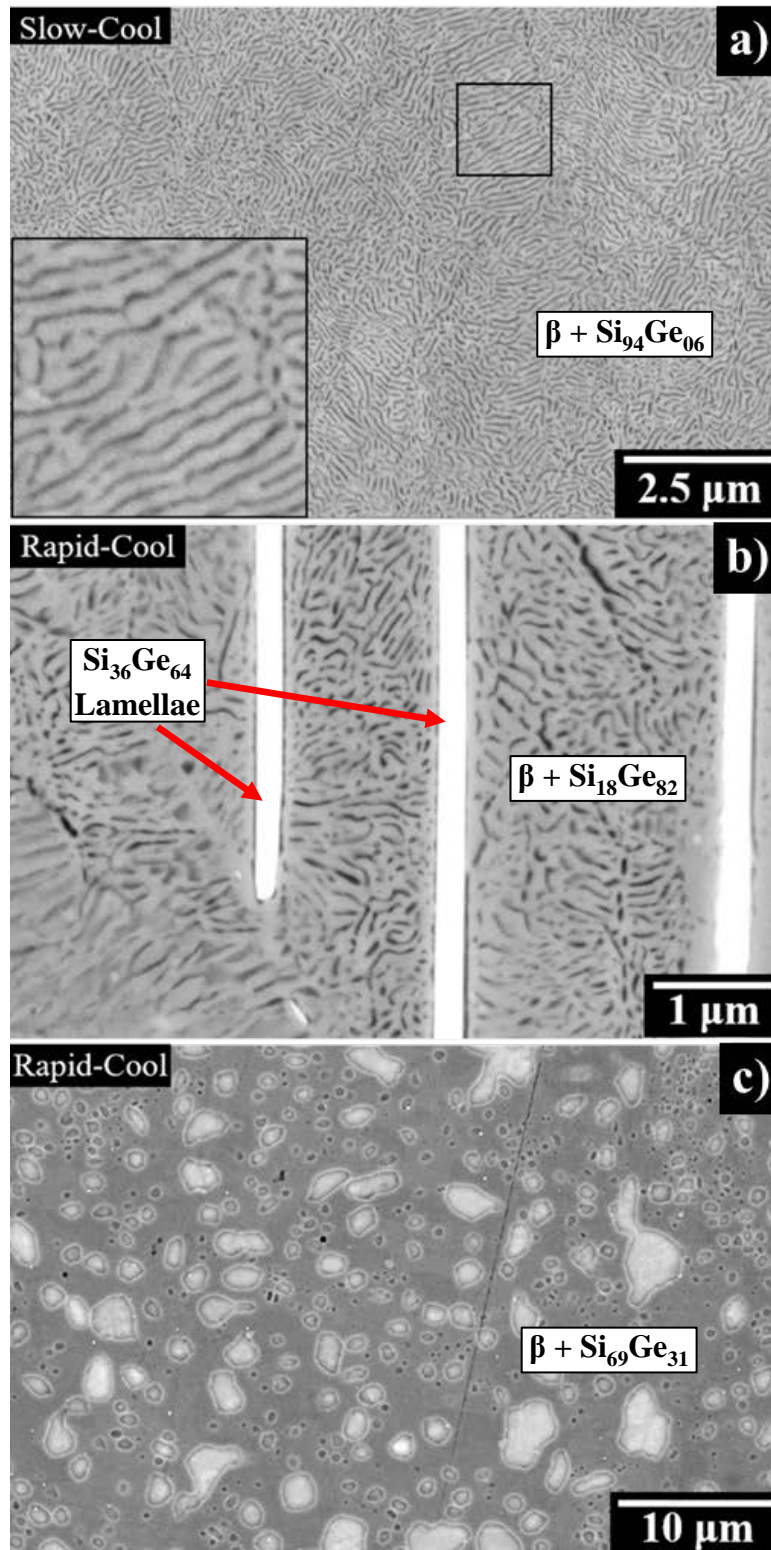


Figure 4.9: BSE-SEM micrographs of β + DC pearlitic colonies in the interlamellar regions of samples aged at 567 °C: a) slow-cool and b) rapid-cool samples. c) Rapid-cool sample aged at 900 °C with homogeneous dispersion of spheroidized particles.

phase into pearlitic $\beta + \text{Si}$. At these aging temperatures the eutectic lamellae do not significantly coarsen or evolve. This results in a local, 2D interface density of ~ 11.0 β/DC interfaces/ μm for each sample; however, the composition of eutectoid SiGe differs between the samples. An additional melt-spun ribbon was aged at 900°C for 9 days (rapid-cool + $900^\circ\text{C}/216$ hr) to produce a coarsened, spheroidized microstructure (Fig. 4.10.c) with the microconstituents ostensibly at their equilibrium compositions. For temperatures above $\sim 700^\circ\text{C}$ [105] the eutectoid interlamellar spacing exceeds the eutectic interlamellar spacing; hence the Si and Ge atoms released by eutectoid decomposition diffuse directly into the pre-existing eutectic lamellae. Simultaneously, the lamellae also break up into quasi-equiaxed particles. The DC particles have average 1.0 ± 0.9 μm diameter and are spaced 2.4 ± 1.7 μm apart. The coarsened particles present a 2D interface density of 0.86 ± 0.33 int/ μm . Room temperature characterization of thermal conductivity by TDTR was

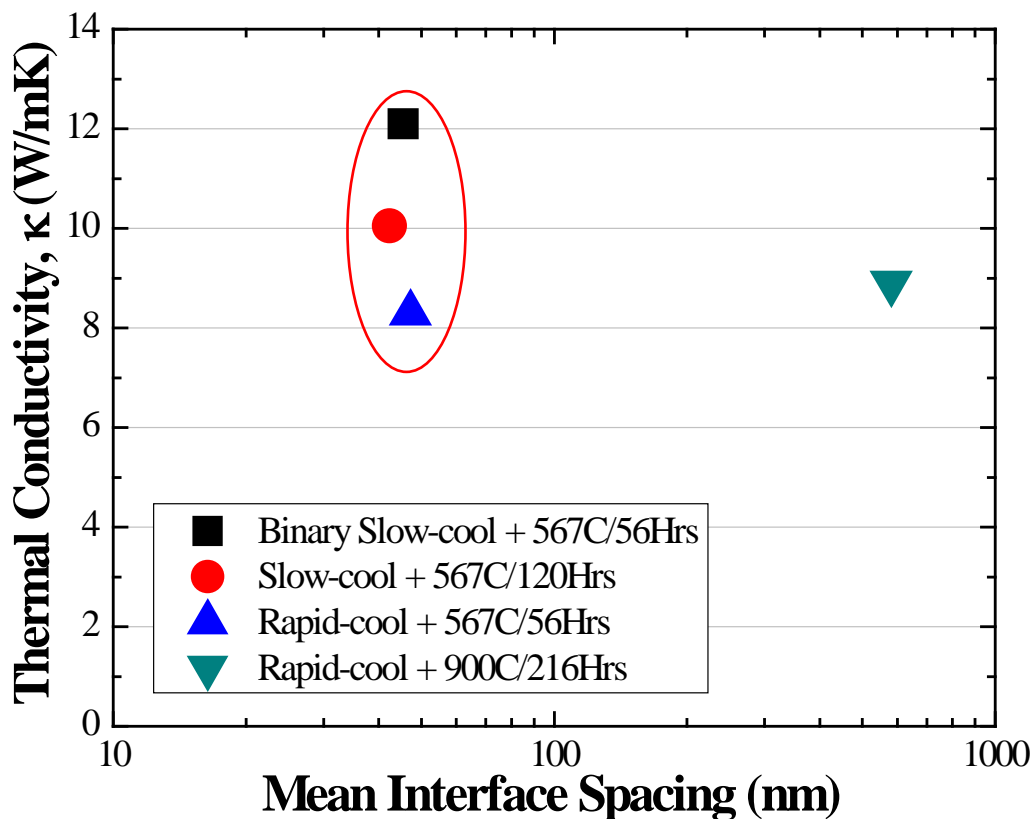


Figure 4.10: Thermal conductivity plotted as a function of mean interface spacing. The symbols circled in red were aged at 567°C and are similar in terms of microstructure.

performed for each of the three aged samples: slow-cool + 567 °C/120 hr, rapid-cool + 567 °C/56 hr, and rapid-cool + 900 °C/216 hr, each having a DC microconstituent with at% Ge of 6, 18, and 31 respectively. The data for the binary $\text{Fe}_{28.4}\text{Si}_{71.6}$ samples obtained in the previous chapter are also shown. Figure 4.10 depicts the four samples plotted according to their thermal conductivity vs. the β /DC heterointerface spacing *in the eutectoid structure only*. The samples aged at 567 °C, which are circled in the figure, have similar lengthscales for the eutectoid $\text{Si}_{1-x}\text{Ge}_x$ nanowires in the β matrix, irrespective of the different eutectic $\text{Si}_{1-y}\text{Ge}_y$ lamellae arising from the casting conditions. Despite the similar lengthscales, the thermal conductivity of the eutectoid microstructure decreases by almost 2x, associated with the increasing at% Ge in the DC phase. The phonon scattering efficiency of Ge-rich DC inclusions is further demonstrated by examining the rapid-cool + 900 °C/216 hr sample: despite having an order of magnitude higher interface spacing, the thermal conductivity is approximately the same as the rapid-cool + 567 °C/56 hr sample, 8.9 ± 0.6 and $8.3 \pm 0.7 \text{ W m}^{-1} \text{ K}^{-1}$, respectively. This reduction cannot be fully attributed to enhanced alloy scattering [88], and will be discussed later. In order to understand these effects, we analyze the role of the Ge content on the thermal boundary conductance (TBC) associated with the eutectoid $\beta\text{-FeSi}_2/\text{Si}_{1-x}\text{Ge}_x$ heterointerfaces.

4.3.2 Phonon Scattering of β /DC Heterointerface

Here, we will use the TBC-based thermal conductivity approach (Chapter 3.3.3) to analyze the phonon thermal transport in our samples; thus, in this context, we examine how TBC varies with Ge content in the diamond cubic phase, yielding insight into the role of alloy composition on TBC. This alloy composition effect on TBC has only been observed previously for interfaces in metallic alloys [106]. In metallic systems, thermal transport is dominated by electrons, and thus, electron effects (such as electron-phonon coupling in interfacial regions) may not be easily dismissed [107]

[108][109][110]. Therefore, our present analysis on alloy composition on non-metal/non-metal interfaces offers more direct, unique insight into the role of alloy composition on phonon-dominated TBC.

Similar to our TBC calculations in Chapter 3, it is assumed that scattering events in the bulk and at the interfaces of each phase are independent, and the system can be modeled as a thermal circuit with series resistances (via Matthiessen's rule [52]), given by

$$\frac{1}{\kappa_T} = \frac{f_\beta}{\kappa_\beta} + \frac{f_{DC}}{\kappa_{DC}} + \frac{\rho_{int,\beta/\beta}}{h_{k,\beta/\beta}} + \frac{\rho_{\beta/DC}}{h_{k,\beta/DC}} \quad 4-1$$

where the f 's and κ 's are the volume fractions and thermal conductivities for the β and DC ($\text{Si}_{1-x}\text{Ge}_x$) phases, respectively. Two interface types were considered: β/β grain boundaries and β/DC heterointerfaces which each have an accompanying 3D interface density (ρ_{int}) and thermal boundary conductance (h_k).

The phase volume fractions f_i were obtained from Rietveld analysis of the XRD data. The thermal conductivity of the β -FeSi₂ phase is taken as 19.8 W/m-K; this value was determined in the previous chapter [105]. The thermal conductivities of $\text{Si}_{1-y}\text{Ge}_y$ alloys as a function of Ge content were taken from ref [88]. Figure 4.11 shows the thermal conductivities measured by TDTR at room temperature, and compares these with the bulk thermal conductivities only (i.e., the sum of the first two terms on the right side of Eq. (1)). Clearly, the bulk resistances alone, even with alloy scattering in the diamond cubic microconstituent, cannot account for the observed reductions in thermal conductivity. This again indicates the importance of considering the TBC at the β -FeSi₂/ $\text{Si}_{1-x}\text{Ge}_x$ interfaces, as we discussed above.

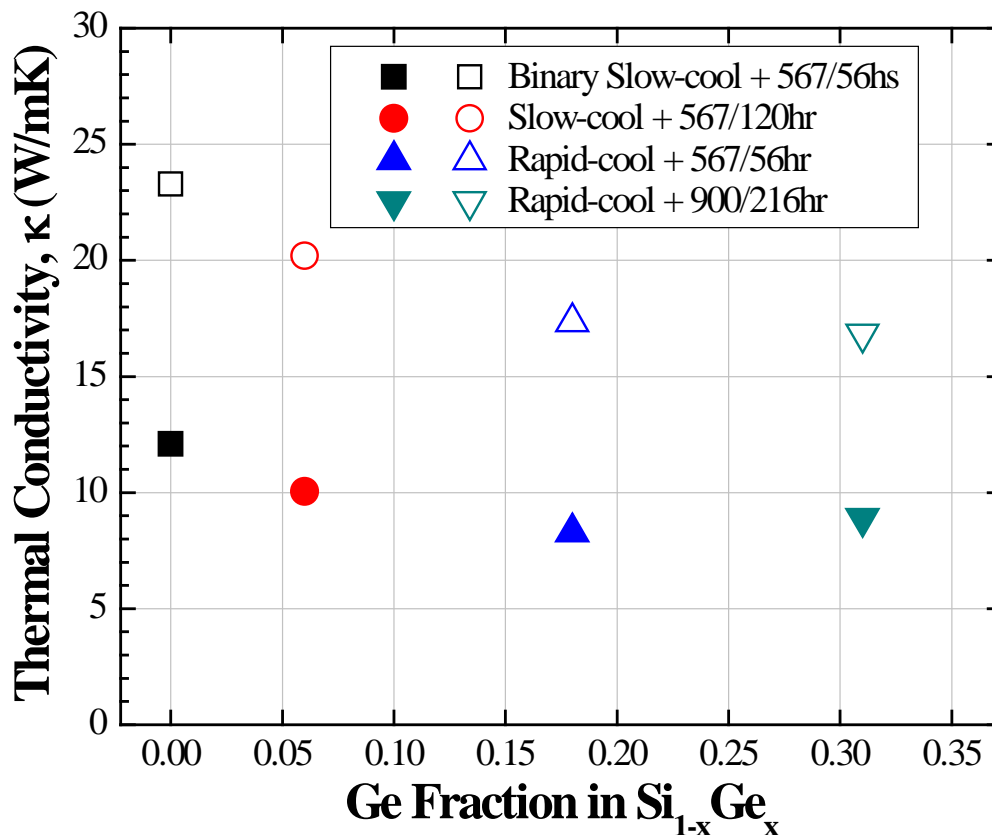


Figure 4.11: The thermal conductivity as a function of DC phase composition. The open symbols are values predicted by Matthiessen's rule by only accounting for bulk and alloy scattering. The solid symbols are the measured values. We attribute this discrepancy to additional scattering at the heterointerfaces.

Table 4.2 summarizes relevant data and calculation results for the samples of interest. The following assumptions were made in order to determine how thermal boundary conductance of the β /DC interface depends on Ge content from eqn. 1. For all the samples, the grain size, manifested in the $\rho_{int,\beta\beta}$ term of eqn. 1, was ignored. In most of the samples this is justified by the relatively large grain size, such that grain boundary scattering contributes negligibly to the measured thermal conductivity. However, for the rapid-cool + 567 °C/56 hr sample, ignoring the 800 nm grain size implies there will be some grain boundary scattering contributions to κ_l that will not be accounted for. In all samples, the eutectic lamellae are also ignored. In the samples with coarse lamellae, the TDTR probe was positioned between the lamellae and only measured the eutectoid structure anyway, so the resistance analysis must also exclude the lamellae. However, the fine scale lamellae

Table 4.2: Summary of relevant data for and results of the Mattheissen's rule calculations.

Sample	Solidification	Process	Interface	DC Composition	f_{β}	f_{DC}	3D $\rho_{\beta/DC}$ (int/ μ m)	3D $\lambda_{\beta/DC}$ (nm/int)	K_{SiGe} (W/mK)	K_T (W/mK)	H_k (MW/m ² K)
$Fe_{28.4}Si_{71.6}$	Slow-Cool	567C56hr	Eutectoid/ β	Si_{100}	0.825	0.175	22.66 \pm 3.45	45.5	149.0	12.1 \pm 1.0	571 \pm 51
		900C120hr		Si_{100}	0.828	0.172	0.44 \pm 0.11	2272.7		22.8 \pm 5.0	
$Fe_{28}Si_{68}Ge_4$	Slow-Cool	567C120hr	Eutectoid/ β	$Si_{94}Ge_{06}$	0.862	0.138	23.70 \pm 2.85	42.3	23.51	10.1 \pm 1.5	518 \pm 48
			Eutectic/ β	$Si_{63}Ge_{37}$		-	0.01 \pm 0.00	100000.0		-	
	Rapid-Cool	567C56hr	Eutectoid/ β	$Si_{82}Ge_{18}$	0.678	0.232	21.48 \pm 5.78	47.2	14.85	8.3 \pm 0.7	341 \pm 49
			Eutectic/ β	$Si_{36}Ge_{64}$		0.090	1.80 \pm 0.13	555.6			
		900C216hr	SiGe/ β	$Si_{69}Ge_{31}$	0.710	0.290	1.29 \pm 0.50	387.6	12.36	8.9 \pm 0.6	49 \pm 10

(cf. Figure 4.1.c) are included in the TDTR measurement. Their exclusion from the analysis of eqn. 1, via both interfacial and bulk effects, is justified by (1) their small interface density and thus small contribution to TBC and (2) the relatively small variation of the bulk thermal conductivity of $Si_{1-x}Ge_x$ alloys in the range $x = 0.23 - 0.81$ [88]. For the rapid-cool + 900 °C/216 hr ternary alloy, the sample has two distinct particle sizes, so all measurements are an average of the two. With these simplifications, the last column of Table 4.2 summarizes the resultant h_k 's, which are plotted vs. Ge content in Figure 4.12. The largest source of error in this calculation comes from the uncertainty of the interface density and in the measured thermal conductivities.

By using Matthiesen's rule, the β /Si interface was calculated to have a TBC of 554 ± 22 MW m⁻² K⁻¹. Compared to the TBC of other semiconductor/semiconductor interfaces, this value is close to the upper limit of measured TBC's in the phonon-dominated regime [8]. However, the Ge content of the DC phase has a significant effect on the TBC at this heterointerface, as seen in Figure 4.12. It is interesting to consider the rapid-cool + 900 °C sample. The extended high-temperature anneal coarsened and spheroidized the DC phase, producing $Si_{69}Ge_{31}$ particles with diameters ranging from 1-10 μ m. As such, the application of Mattheissen's Rule, Eq. (1), seems particularly

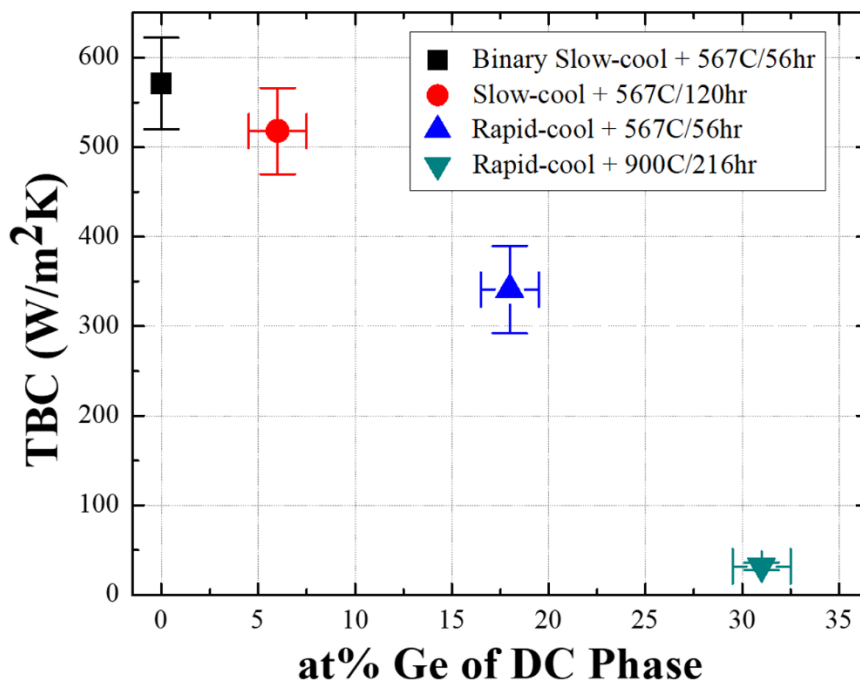


Figure 4.12: Thermal boundary conductance for the $\beta/\text{Si}_{1-x}\text{Ge}_x$ heterointerface, calculated from Mattheissen's rule, as a function of Si nanoconstituent composition.

reasonable. For example, the TBC across the $\beta/\text{Si}_{69}\text{Ge}_{31}$ yields a TBC of $49 \pm 16 \text{ MW m}^{-2} \text{ K}^{-1}$, an order of magnitude lower than that across the β/Si interface. Even with the potential uncertainties in the interface density, the presence of 31% Ge in the DC phase appears to significantly reduce the thermal boundary conductance of the β/DC heterointerface.

4.4 Future Directions

It should be recognized that a series resistance model wherein bulk thermal conductivities and a single-valued thermal boundary conductance are taken as independent is clearly an oversimplification. Future work should compare these predictions with diffuse-mismatch modeling, and with re-interpretation of the data in terms of the Callaway-Debye picture. This more rigorous modeling approach is beyond the scope of this current work. However, our experimental results, and the simple series resistance model, do point to a clear and important role of atomic-

scale structuring of Ge content in both bulk alloy scattering, and in enhancing boundary scattering effects associated with the heterophase structure.

These results suggest that minimum thermal conductivity in the β -FeSi₂/DC composite requires a *nanostructured* DC phase with ~30 at% Ge to take full advantage of alloy scattering and TBC effects, as well as potential benefits of reduced bandgap in the DC phase. Figure 4.13 uses Mattheissen's rule and the data collected for the β /Si₆₉G₃₁ heterointerface to model the change in thermal conductivity as a function of volume fraction and interface density. Assuming that the DC lengthscale is comparable to nanowires produced at 567 °C, the predicted thermal conductivity is ~2 W/mK and results in nearly a 4-fold reduction from the nanostructured Si₈₂Ge₁₈, and may have advantages in the thermoelectric power factor. Thermal conductivity steeply declines before leveling off at high interface densities, and suggests that ultra-fine lengthscales might not be

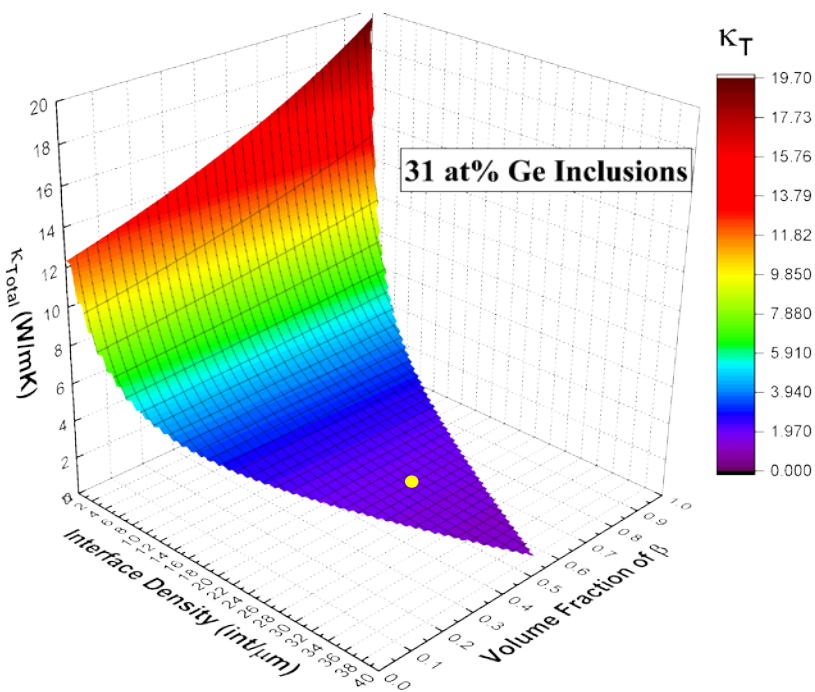


Figure 4.13: Theoretical curve derived from Mattheissen's rule, showing the change in κ_{Total} , with Si₆₉G₃₃ nanoinclusions, as a function of volume fraction and interface density. The yellow dot denotes κ for 25 nm wide nanowire with a TBC of 49 MW m⁻² K⁻¹.

required to produce a large decrease in thermal conductivity. Similar graphs for other measured compositions can be found in the Appendix 6.

Eutectoid decomposition efficiently creates nanowires and large heterointerface densities, but Ge entrainment in eutectic lamellae impedes our ability to segregate Ge into the finer-scale eutectoid nanowires. It is not likely that we can bypass the eutectic by choice of ternary composition. However, finer eutectic lengthscales and greater solute trapping are possible with even faster solidification rates. As will be shown in the subsequent chapter, pulse laser melting is capable of achieving these rates. Subsequent low temperature conversion promotes eutectoid decomposition, $\alpha \rightarrow \beta + \text{Si}$, and if the eutectic interlamellar spacings can be retained on the nanoscale, the eutectoid Si would simply diffuse to the lamellae, but without significant coarsening.

4.5 Conclusions

Ge additions to the Fe-Si system provide significant flexibility for modifying the structure and properties of Fe-Si-based thermoelectrics. Hierarchical microstructure was produced by combining eutectic and eutectoid decomposition in $\text{Fe}_{28}\text{Si}_{68}\text{Ge}_4$ alloys, ultimately producing a nanocomposite structure of $\beta\text{-FeSi}_2$ with embedded SiGe alloys of varying alloy composition. Rapid solidification of Fe-Si-Ge was shown to (1) reduce the lengthscales of eutectic lamella by two orders of magnitude, (2) eliminate the unwanted $\epsilon\text{-FeSi}$ phase, and (3) increase the final Ge content in the nano-scale eutectoid nanowires. Meso-scale structuring caused by eutectic solidification did not have a significant effect on thermal conductivity. The Ge concentration of DC inclusions (atomic-scale structuring) may be the most important, in this system, for reducing overall thermal conductivities; since we found that the hierarchical eutectoid + eutectic structure did not significantly reduce thermal conductivity vis-à-vis the coarser Ge-rich particles. It should

be noted that that the $\text{Si}_{69}\text{Ge}_{31}$ inclusions were possible due to solute trapping caused by rapid solidification.

We analyzed the thermal conductivity of the composite structure in terms of the effects of a Ge-dependent thermal boundary conductance associate with the $\beta\text{-FeSi}_2/\text{Si}_{1-y}\text{Ge}_y$ heterointerfaces. While the $\beta\text{-FeSi}_2/\text{Si}$ interface exhibits a relatively high thermal boundary conductance of $554 \pm 22 \text{ MW m}^{-2} \text{ K}^{-1}$, this value drops markedly with the inclusion of Ge into the diamond cubic, eutectoid microconstituent. By incorporating 30 at% Ge into DC particles by taking advantage of rapidly-solidified eutectic combined with eutectoid decomposition, the thermal conductivity of the system is reduced to $8.3 \pm 0.6 \text{ MW m}^{-1} \text{ K}^{-1}$, which we quantify as a reduction in thermal boundary conductance across the $\beta\text{-FeSi}_2/\text{Si}_{69}\text{Ge}_{31}$ interface. This thermal boundary conductance was determined to be $49 \pm 29 \text{ MW m}^{-2} \text{ K}^{-1}$, an order of magnitude lower than that across the $\beta\text{-FeSi}_2/\text{Si}$ interfaces, which we ascribe to the change in phononic properties of the Si-Ge alloy due to the varying alloy composition. Noting that the overall Ge content is still only 4 at%, the abundance and low toxicity of the primary components, Fe and Si, suggest that further pursuit of thermoelectric optimization through microstructure control in the dilute ternaries is warranted.

5 Ultra-Rapid Solidification via Pulse Laser Processing

Chapter 4 showed that rapid thermal processing by melt-spinning dramatically reduced lengthscales and increased Ge solute trapping in α -FeSi₂. This ultimately led to a beneficial (for thermoelectrics) reduction in thermal conductivity through reduction of the thermal boundary conductance (TBC) by increasing the Ge concentration of diamond cubic (DC) nanoinclusions. In order to further increase solidification rates, we explored laser-based melting and resolidification; in particular we used an Excimer UV laser for pulse laser melting (PLM). Due to the rapid pulse duration and high energy concentration, PLM achieves a faster solidification rate vis-à-vis melt-spinning, and is on the order of $10^9 - 10^{12}$ °C/s [111][112]. The enticing resultant microstructures, high interface density, and supersaturated phases suggest that further pursuit could yield a promising thermoelectric material. While a comprehensive investigation is beyond the scope of this dissertation, the goal of this chapter is to establish the potential for PLM as an avenue for future research and development in this materials system.

5.1 Processing Parameters for Base Materials

5.1.1 Additional Fe-Si-Ge Alloys

Two new Fe-Si-Ge alloy compositions, Fe_{22.5}Si_{67.5}Ge₁₀ and Fe_{23.5}Ge_{71.5}Ge₁₀, in addition to pre-existing samples of Fe₂₈Si₆₈Ge₄, were synthesized by melt-spinning (“rapid-cooling”). These new compositions were not used for thermal conductivity measurements, but were important for PLM and assessing the ternary phase diagram, which will be discussed in the following chapter. All the rapid-cool samples have Ge-rich eutectic SiGe (as will be seen later in Figures 5.2.a,b,c) but the Fe_{22.5}Si_{67.5}Ge₁₀ composition also has copious amounts of ϵ -FeSi. Unfortunately, due to difficulties

with the melt-spinning of these new samples, only small amounts of material were produced, limiting the scope of experimental iterations

5.1.2 Challenges of Pulse Laser Melting

A major aspect of this part of the project was to develop processing techniques to synthesize viable starting materials suitable for PLM. There are three main process challenges that must be overcome to produce samples that are amenable to subsequent aging (to produce eutectoid decomposition) and characterization of thermal conductivity. The first challenge is that the excimer laser is unable to homogenize coarse eutectic structures, due to the short pulse duration and ultra-rapid solidification rate. To exemplify this, Figure 5.1 shows a “splat-cooled” $\text{Fe}_{28}\text{Si}_{68}\text{Ge}_4$ sample, where the melt dripped onto the bottom of the arc-melter chamber and cooled at an intermediate rate. This sample was pulsed twice with a fluence of 2.5 J/cm^2 . The original microstructure is still apparent, although the morphologies are smeared as the interfaces became more diffuse. This suggests that at least partial melting occurred, but with insufficient extent (or time) to permit proper mixing in the liquid. In the splat-cool sample, DC lamellae with widths $\sim 5 \text{ }\mu\text{m}$ wide did not homogenize during PLM. However, a rapid-cool $\text{Fe}_{22.5}\text{Si}_{67.5}\text{Ge}_{10}$ sample with lamellae $\sim 1 \text{ }\mu\text{m}$ wide did homogenize during melting. In addition to the smaller lengthscales for intermixing the more facile homogenization could be caused by the larger DC volume fraction in this sample. SiGe [113] could have a higher UV absorption coefficient than $\alpha\text{-FeSi}_2$ (it has never been explored) and might absorb more energy per pulse, raising the overall sample temperature. The key point, however, is that the initial DC microconstituent lengthscales should be $\leq 1 \text{ }\mu\text{m}$ for excimer-based PLM to effectively intermix in the liquid state, so that subsequent solidification structure is not biased by the pre-existing structure from melt-spinning.

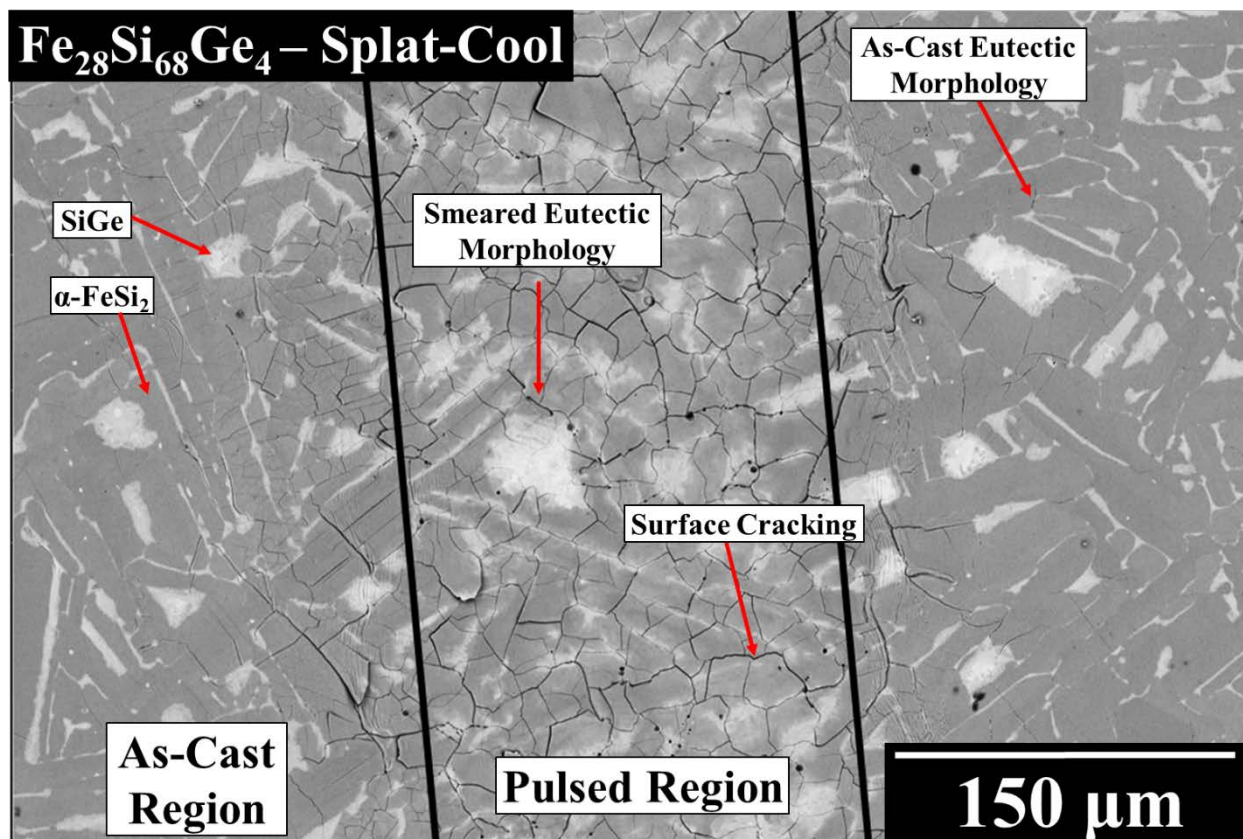


Figure 5.1: Splat-cooled $\text{Fe}_{28}\text{Si}_{68}\text{Ge}_4$ sample pulsed twice with 2.5 J/cm^3 fluence. The laser-pulsed region, which is noted as having a large number of cracks and diffuse DC microconstituents, is bounded by black lines.

The second challenge is that the melt-depth associated with excimer PLM is shallow. An ion-milled cross-section shows that the melt-depth created by two excimer pulses is on the order of $1 \mu\text{m}$ deep, which agrees with depths measured for Si [114]. Chemical and/or phase identification of the melted region via XRD or SEM-EBSD is not possible as the signal is overwhelmed by the underlying, unmodified material. SEM-EDS (at 5 kV) was performed for these samples and shows a significant amount of Ge entrained within the α phase, but was not able to resolve individual phase compositions.

The third challenge is that the re-solidified material is too damaged for TDTR measurements of thermal conductivity. The laser melted and re-solidified regions exhibit extensive fracturing, see

Fig. 5.1. The inter-crack “islands” of α phase ranged in diameter of 5 – 40 μm . Unfortunately, increasing the number of laser pulses only further damages the surface. One experiment was performed to observe the effects of over-melting by rastering a sample multiple times with 2.5 J/cm^2 fluence at 10 Hz for 30 minutes; A large pulse count ($\sim 18,000$ distributed over the entire sample) caused the surface to actually bead up; this is most likely caused by the melt not wetting the substrate and the influence of surface tension causing spheroidization; the literature suggests that lowering the pulse frequency could mitigate this effect [115].

Despite these challenges, we were able to examine aspects of how laser-based, or other pulse-optical processing techniques, might be used to effectively reduce structural lengthscales and increase Ge incorporation in the DC phase.

5.1.3 Excimer Laser Parameters

Laser fluence was calculated from the integration of energy across multiple pulses and the area of the incident beam. A range of fluences were initially tested from 0.5 to 2.5 J/cm^2 , as well as the number of pulses per area. It was found that higher fluences, from 1.5 to 2.5 J/cm^2 , efficiently melted the sample surface. The incident laser does not have a uniform energy density throughout the width of the beam, and a range of temperature gradients and distinct morphologies can be identified from the center to the edge. In order to produce a homogeneously *treated* sample, we rastered the laser across a region so that each area effectively received two pulses. From optical microscopy, the macrostructure appeared homogenous; however, there are diverse nano-scale $\alpha + \text{DC}$ morphologies observed within even a single “island” (localized region defined by surrounding cracks). This will be discussed with greater detail in the following sections. All experiments in the following sections were performed with two pulses at 2.5 J/cm^2 fluence in an Ar atmosphere.

5.1.4 Sample Processing Routes

Synthesizing a viable sample was nontrivial due to the challenges discussed earlier, and several attempts were made with varying levels of success. The large and sudden temperature gradient caused by the laser creates sufficient internal stresses to shatter a brittle ribbon unless it is firmly mounted into epoxy. Mounting is actually beneficial as the ribbons can then be easily polished to expose a homogenous microstructure. However, once the ribbon is mounted it cannot be removed or aged for eutectoid decomposition; heating the mount destroys both the epoxy and the ribbon. Samples made using this method were analyzed by SEM to characterize the PLM microstructure. We attempted mounting in a dissolvable material, Crystalbond, which allowed for ribbons to be polished, laser-pulsed, and extracted; however, the 10-30 μm thick ribbons were extremely brittle and disintegrated before they could finish the aging process. A method for aging an intact, single ribbon was not successfully developed, and will have to be the subject of future work. However, the need for pre-mounting could be eliminated if a large-area optical source was used.

Another approach to create mechanically robust samples was to use spark plasma sintering (SPS) to create a semi-dense disk. Ribbons were hand-powdered in a mortar and pestle and sieved to retain particle diameters below 40 μm . The powders were then spark plasma sintered by my groupmate, Naiming Liu, using the Poon group's SPS setup. Thermal budgets in SPS were limited to avoid structural coarsening. As a result, fully dense disks were not produced. Nonetheless, the disks were sufficiently robust to survive subsequent polishing and thermal treatments. The SPS samples were aged before PLM to establish a clear distinction between the base vs. melted material.

Yet another approach was considered and attempted in limited fashion. We considered PLM of powders themselves, which if successful, could then be spark plasma sintered. The motivation was

the consideration that ultra-rapid solidification of micron-sized powder would avoid fracture due to reduced mechanical constraint. We attempted liquid pulse laser ablation (LPLA) [116][117] on powders and SPS disks; with about 5g of aged powders were submerged (the suspension was given a day so that the powder could settle) in ~30 mL of ethanol (DI water oxidized the sample surface). Unlike in PLA, the plasma plume is constrained by the liquid medium (see Appendix 8), as the plume cools and condensates a part of it will condense and deposit on the sample surface and the other part condenses and forms ultra-fine nanoparticles suspended, and oftentimes floating on the medium [117]. After the ethanol evaporates, this powder was collected. However, neither approach produced sufficient material to obtain a detectable XRD signal. Data gathered from LPLA can be found in Appendix 8.

5.2 Microstructure Resulting from PLM

5.2.1 Supersaturated α -FeSi₂

Ribbons from the three compositions ($\text{Fe}_{28}\text{Si}_{68}\text{Ge}_4$, $\text{Fe}_{22.5}\text{Si}_{67.5}\text{Ge}_{10}$ and $\text{Fe}_{23.5}\text{Ge}_{71.5}\text{Ge}_5$) were mounted in epoxy, polished, and pulsed twice at 2.5 J/cm^2 fluence. The initial rapid-cool microstructure produced by melt-spinning can be seen in Figures 5.2.a,b,c. After PLM, we observed several distinct microstructures, including both single-phase α regions, and regions with two-phase $\alpha + \text{DC}$ having different morphologies. The two-phase microstructure will be discussed in the following section. Solute trapping [35] caused by the rapid solidification front engendered a homogeneous Si/Ge-supersaturated α -FeSi₂ phase, and is shown in Figures 5.2.d,e,f next to their corresponding pre-PLM counterparts. SEM-EDS indicated that Ge were concentrations near that

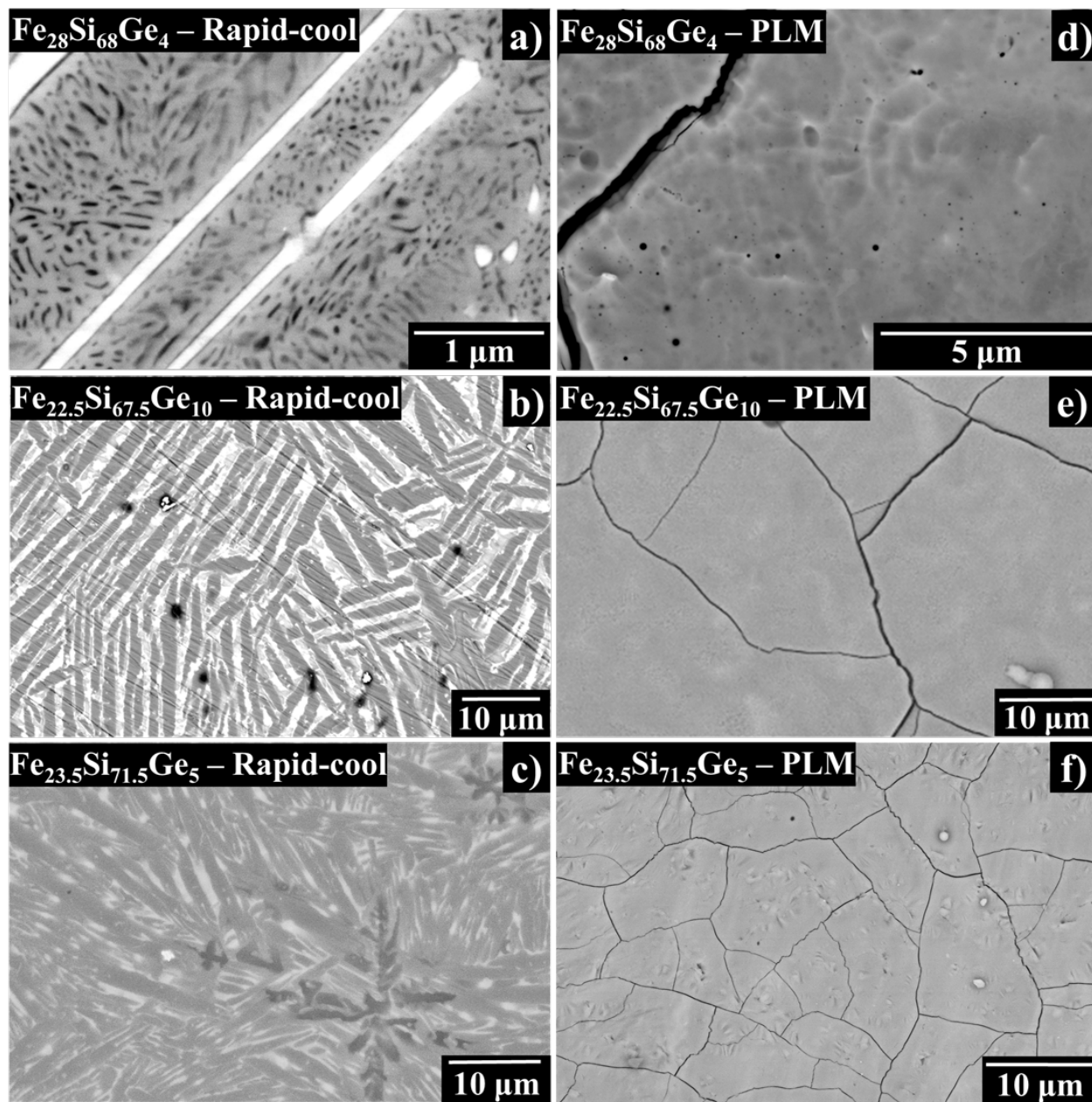


Figure 5.2: BSE-SEM micrographs of rapid-cooled a) $\text{Fe}_{28.4}\text{Si}_{71.6}\text{Ge}_4$ aged at 567°C for 56 hrs showing eutectic and eutectoid DC, b) $\text{Fe}_{22.5}\text{Si}_{67.5}\text{Ge}_{10}$ with eutectic DC + ϵ lamellae, and c) $\text{Fe}_{23.5}\text{Si}_{71.5}\text{Ge}_5$ with Si-rich proeutectic and Ge-rich eutectic phases. PLM microstructure of a) $\text{Fe}_{28.4}\text{Si}_{71.6}\text{Ge}_4$, b) $\text{Fe}_{22.5}\text{Si}_{67.5}\text{Ge}_{10}$, and c) $\text{Fe}_{23.5}\text{Si}_{71.5}\text{Ge}_5$ alloys showing complete DC solid solubility in $\alpha\text{-FeSi}_2$.

of the overall system composition, which is a far larger supersaturation than what was achieved by melt-spinning. The Si,Ge/Fe ratio of $\alpha\text{-FeSi}_2$ phases, with compositions of $\text{Fe}_{28.4}\text{Si}_{71.6}$ ($\text{Fe}_{28.4}\text{Si}_{71.6}$ – Slow-cool) and $\text{Fe}_{24.8}\text{Si}_{72.2}\text{Ge}_{3.0}$ ($\text{Fe}_{28}\text{Si}_{68}\text{Ge}_4$ – Rapid-cool), have increased from ~ 2.5 to ~ 3.5 vis-à-vis the $\text{Fe}_{22.5}\text{Si}_{67.5}\text{Ge}_{10}$ ($\text{Fe}_{22.5}\text{Si}_{67.5}\text{Ge}_{10}$ – PLM) α composition. If we assume that the $\alpha\text{-FeSi}_2$

crystal structure is conserved, and that the nonstoichiometric nature is facilitated by Fe vacancies, then there would have to be an increase in Fe vacancy from ~22% up to ~41%, respectively. However, maintaining a stable crystal structure with nearly half of the Fe atoms missing does not seem likely. There is a clear relationship that Fe at% decreases with increasing Ge concentration; it is possible that Ge is partially substituting on Fe sites. The covalent radii of Fe and Ge (132 and 120 pm, respectively) are more similar in size than Si (111 pm) [118]. Ge is lower in the Group IV column and has decreased electron affinity and a more metallic character, so it is possible that Ge preferentially fills Fe vacancies. Further experiments on lattice parameter deviations from Rietveld refinement and density measurements are required to better understand the atomic disposition of supersaturated α -phases.

The supersaturated α phase has many interesting implications for our thermoelectric research. Based on the results in Chapter 4, we anticipate that appropriate low-temperature aging should produce fine, Ge-rich eutectoid nanowires. For a system composition of $\text{Fe}_{22.5}\text{Si}_{67.5}\text{Ge}_{10}$, the equilibrium phases at 900 °C are $\beta + \text{Si}_{60}\text{Ge}_{40}$ (see Chapter 6); the $\beta/\text{Si}_{60}\text{Ge}_{40}$ interface (the highest achievable in the $\beta + \text{DC}$ two-phase existence region) would take advantage of low TBC and high density, and could have exceptional phonon scattering efficiency. Unfortunately, due to insufficient material for powder processing, only the $\text{Fe}_{28}\text{Si}_{68}\text{Ge}_4$ sample was aged and characterized. Ge-rich compositions should be explored for future PLM experiments.

5.2.2 $\alpha + \text{DC}$ Microstructures from PLM

Along with the supersaturated single-phase α regions, two-phase $\alpha + \text{DC}$ microstructures were also observed. It is currently unclear what causes the significant microstructural inhomogeneity occurring on 5-10 μm lengthscales, shown in Figure 5.3. Although the eutectic microstructures

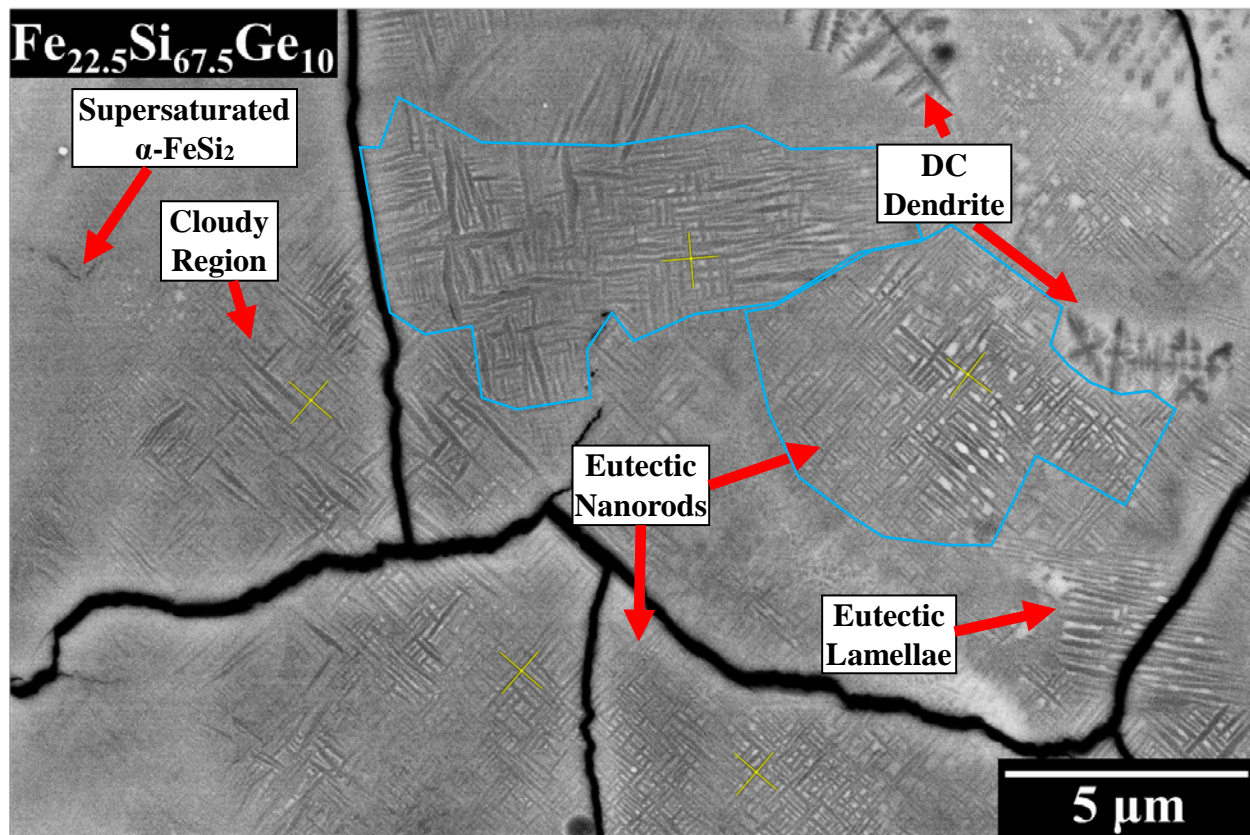


Figure 5.3: $\text{Fe}_{22.5}\text{Si}_{67.5}\text{Ge}_{10}$ ribbon after PLM (2 pulses at 2.5 J/cm^2), depicting the close proximity of different $\alpha + \text{DC}$ microstructures. The blue outlines highlight $\alpha + \text{DC}$ colonies and the yellow lines mark the spatial alignments of DC inclusions. The different microstructures are described in the text.

typically are found along the island edges, it is clear from spatial alignment of DC lamellae that the cracks formed after solidification and are therefore not directly responsible for eutectic nucleation. The blue outlines emphasize regions where DC inclusions have formed an ordered “criss-cross” pattern; inclusion run along one of two perpendicular directions which are marked by the yellow perpendicular lines. Clearly, these regions have the same inclusion alignment because the α matrix has the crystallographic orientation; these regions are $\alpha + \text{DC}$ colonies. Considering the ultra-fast solidification rate, these colonies are fairly large and can range from $5\text{-}10 \mu\text{m}$ in diameter. In this micrograph, there are three similarly marked alignments, not outlined in blue, that also contain different morphologies (what we are calling ribbon and cloudy). It is not clear if these are

the same colony or a coincidence of orientation; it is possible that their morphologies are connected by similar mechanisms. The relationship between microstructural variations and composition, initial surface morphology, substrate morphology, or solidification rate is not understood. A more

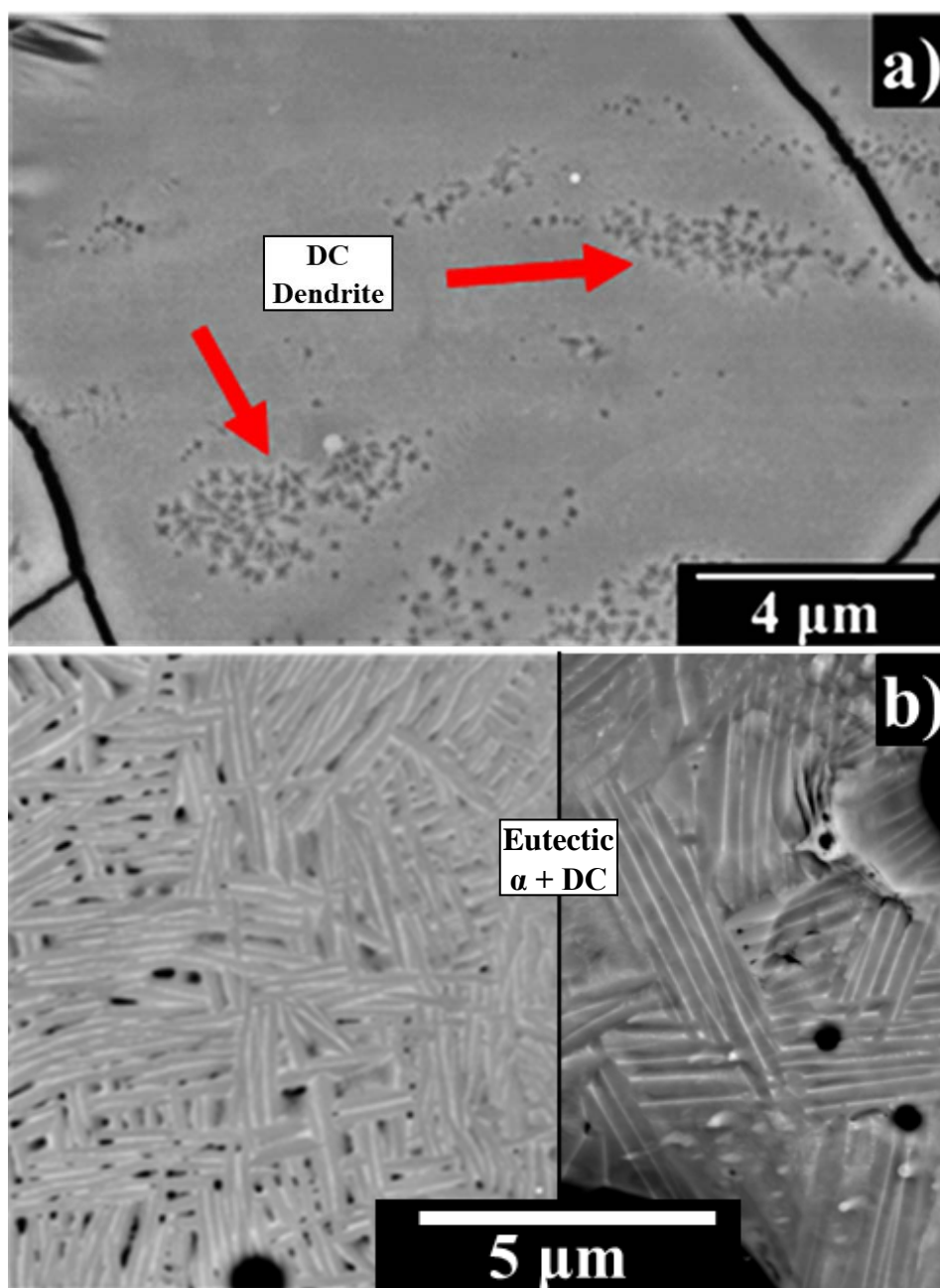


Figure 5.4: Micrographs depicting different $\alpha + DC$ microstructures commonly observed in PLM samples: a) nascent Si-rich dendrites, and b) two periodic eutectic micrographs showing variations on colony morphology. These micrographs were taken from $Fe_{28}Si_{68}Ge_4$ ribbons that were pulsed twice at $2.5 J/cm^2$.

systematic approach to characterizing fluence and solidification rate (preferably on homogenized base samples) is required before a proper connection can be determined.

There are four types of $\alpha + DC$ microstructures that appear throughout the different compositions and sample process histories, however the mechanisms of their formation are not well understood. The DC phase in Figure 5.4.a are clusters of nascent Si-rich dendrites that solidified initially from the melt. Figure 5.4.b has microconstituents that appear to have formed cooperatively, and indicates that ultra-rapid solidification has pushed lamellar lengthscales to the nano-scale. Two different images are shown here so to encompass the entirety of observed eutectic colony lengthscales. The linear intercepts method was used to characterize these lamellae; the 2D interface density of the eutectic structure is 6.6 ± 1.2 interfaces/ μm , average lamellar width is 51.9 ± 8.4 nm, and an interlamellar spacing of 175.1 ± 26.9 nm.

The $\alpha + DC$ two-phase region in Figure 5.5 has an odd morphology – which is notable for its highly diffuse interfaces vis-à-vis the sharp α/DC interfaces we typically observe. It has long “wavy” inclusions and cloudy diffuse regions, and for a lack of a better term, we will refer to this as cloudy morphology. The Ge-rich, diffuse interface is similar to what was observed in Figure 5.1; the PLM processing caused partial mixing of coarse DC structures. The Ge atoms rapidly diffused through the melt and froze before unmixed structure could form, suggesting the diffuse interface here is also caused by large amounts of Ge frozen in the matrix. The overlay in Figure 5.5 shows the same location that was processed by a Fourier bandpass filter (filters high frequencies to suppress contrast differences and low frequencies to enhance edges, processed in ImageJ) to remove contrast caused by the diffuse interface. This image processing revealed that the “cloudy” regions actually consist of DC spheroids (~ 30 nm wide and spaced ~ 50 nm apart) in a Group IV-rich diffuse interface. Although these regions have “wavy lamellae” it does not appear

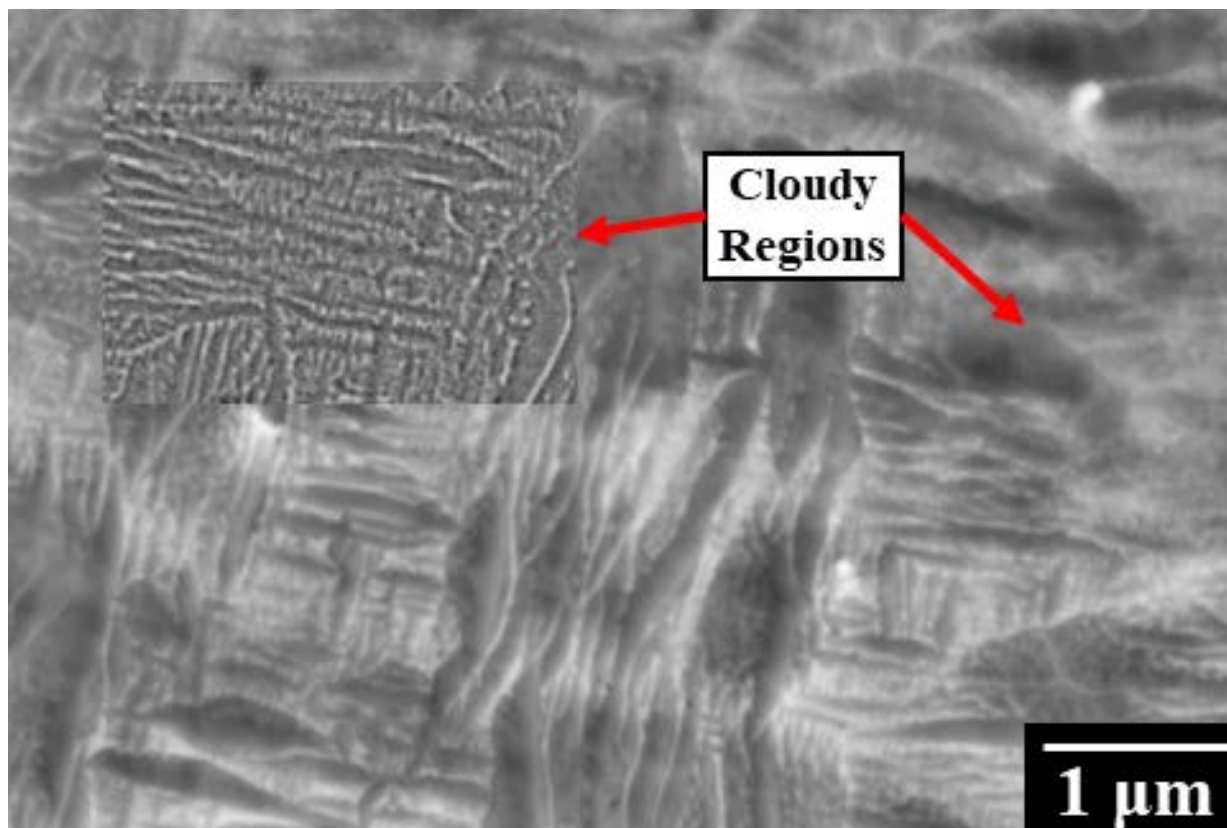


Figure 5.5: Micrograph of $\text{Fe}_{28}\text{Si}_{68}\text{Ge}_4$ depicting the cloudy morphology. An overlay made from image processing via bandpass filter shows the particles within the diffuse interface. Wavy DC inclusions and clouds are shown to align themselves along perpendicular directions.

to be the result of cooperative growth or by classical nucleation. It is odd that in this Group IV-rich diffuse regions Group IV elements have diffused up the concentration gradient into DC particles, and didn't nucleate $\alpha\text{-FeSi}_2$ particles in a DC matrix instead. Could these Group IV-rich regions be continuously ordering along the manner of a pseudospinodal decomposition, and the froze before unmixing reached completion? As shown in the next section, the cloudy morphology is also aligned along two perpendicular directions, granted that the inclusions are wavy and not as periodic as those seen in Figure 5.6

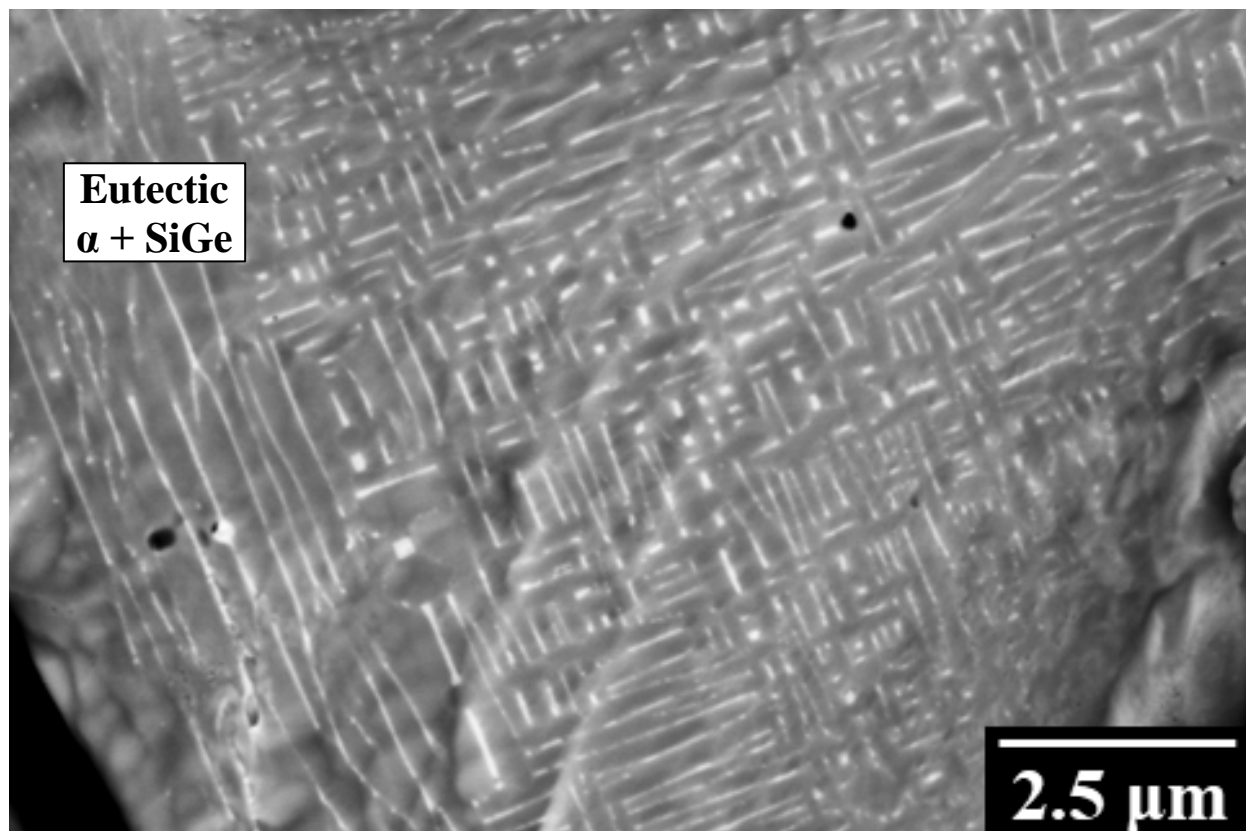


Figure 5.6: SEM micrograph a single, large eutectic colony with ribbon morphology, ribbons are shown to align along two perpendicular directions.

The DC phase in Figure 5.6 will be referred to as “ribbons”, as they would appear as ribbons (truncated lamellae) if extended into the 3rd dimension. These ribbons are believed to be eutectic in origin as : 1) heat would not have been retained long enough to cause solid-state precipitation and 2) primary DC solidifies out of the melt as dendrites. It is clear that the ribbons are aligned along one of two perpendicular directions and are encapsulated by a single orientation of α . It is unlikely that the DC inclusions are bounded by the α (001) habit plane as they are in other eutectic morphologies. This is clearly the case, as the two spatial alignments are not possible with the single habit plane. We have ruled out the possibility of ultra-fine α grains oriented so that the habit plane is facing a ribbon, as it is unlikely that periodicity would be maintained for over 10 μm .

It is possible that the faceting has changed, perhaps due to lattice parameter changes or in entropy of fusion caused by supersaturation. The micrograph suggests against eutectic DC nanorods growing along perpendicular planes, (100), (010), and (001), with the short rods being viewed end on and the long rods view lengthwise. If this morphology is truly caused by a eutectic solidification, then all the rods should be growing along the thermal gradient and long horizontal rod growth perpendicular to the gradient would not be feasible. If α is still the faceted phase, then perhaps the plane normal is the (001) plane and the ribbons are bounded by the {100} habit planes. It is also possible that the α phase is no longer faceted (see Chapter 4.1.2), and the DC ribbons have become the faceted phase. Like the eutectic Si in the Fe₂₇Si₇₃ sample, this would produce periodic, orderly inclusion inside of a single colony. In order to resolve this microstructure we need to: 1) know the orientation of the α grain and DC inclusions if possible, and 2) how the microstructure evolves in 3D via focused ion beam (FIB) microscopy. It should be noted, that the Figures 5.5 and Figure 5.6 have similar lengthscales: 1) 2D interface densities of 6.3 ± 1.6 interfaces/ μm , 2) average lamellar widths of 71.6 ± 7.1 nm, and 3) interlamellar spacing of 180.0 ± 35.4 nm. Both of these microstructures are approaching the eutectoid lamellar lengthscale.

5.2.3 Fast Fourier Transform of DC inclusions

A fast Fourier transform (FFT) takes repetitive elements from the initial micrograph, in our case the periodic Ge-rich lamellae, and converts them into the frequency domain. This allows for quantification of spatial alignments. Figures 5.7.a and b both show microstructures that arose from eutectic solidification albeit with different solidification rates. Unsurprisingly, PLM engendered a much finer lengthscale and has similar morphology to slow-cool and rapid-cool eutectics. The FFT graph of global morphology (Figure 5.7.a) shows that there is no global preferred alignment, and each colony is randomly oriented from nucleation. The FFT graph from a single eutectic colony

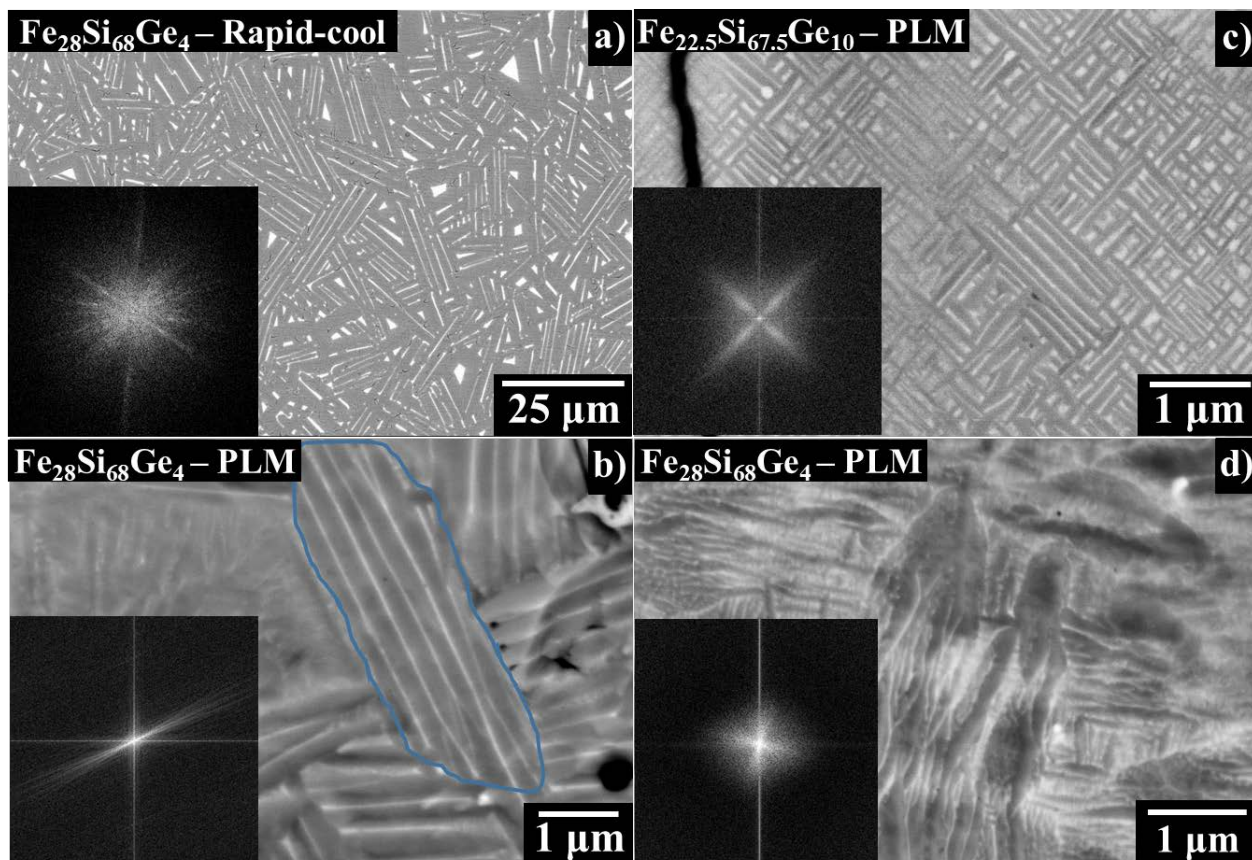


Figure 5.7: Micrographs depicting different $\alpha + DC$ microstructures commonly observed in PLM samples and fast Fourier transforms quantifying eutectic spatial alignment: a) global eutectic microstructure, b) a single eutectic colony highlighted in blue, c) a single ribbon eutectic colony, and d) a single colony with cloudy morphology.

clearly shows a single spatial alignment per colony. Figure 5.7.c and d both have four cloved pattern in FFT, and suggest that the DC inclusions from both morphologies are aligned crystallographically along two perpendicular directions within their α matrix. This suggests that both morphologies are ordered by the same mechanism and that they are inherently different from the lamellar microstructures we have previously observed. In should be noted that FFT graph of Figure 5.7.d does not have sharp peaks due to the “wavy” and “cloudy” nature of the DC inclusions.

5.3 Microstructures of PLM Samples After Aging

The solidification structures just described were observed in both ribbon and SPS samples, but only the powdered processed SPS samples could be aged. Aging the PLM $\text{Fe}_{28}\text{Si}_{68}\text{Ge}_4$ SPS samples at $567\text{ }^\circ\text{C}$ produced a divorced phase transformation, see Fig. 5.8. Without phase identification, it may not be prudent to assume that the microstructure is results from a divorced *eutectoid* ($\alpha \rightarrow \beta + \text{DC}$) transformation. The α phase is supersaturated well beyond the equilibrium composition and it is possible that Si,Ge must be ejected before eutectoid decomposition is to proceed. This could mean that the lamellar features shown in Figure 5.8 might actually result from a *discontinuous precipitation* process, $\alpha_{\text{ss}} \rightarrow \alpha_{\text{eq}} + \text{DC}$. Both transformations produce similar lamellar microstructures, nucleate and grow in similar manors, and can be nontrivial to differentiate [34]. Typically, when imaged with BSE-SEM the β phase has a much lighter contrast than the surrounding α phase, but the contrast difference is not easy to identify in these micrographs (Figure 5.5). For the sake of this chapter this transformation will be referred to simply as a “decomposition”. Even if this was a discontinuous precipitation, the small lengthscales and Ge-rich nanoinclusions would be conserved after the proper eutectoid decomposition, and should not be detrimental to thermal properties. We also do not believe that these transformations result in any metastable iron silicide or germanide phases. If a process scheme can be devised to produce samples of sufficient volume to perform XRD, then phase identification will be straightforward.

5.3.1 Decomposition in Supersaturated α Regions

In Figure 5.8, we can see the reaction front as it moves into the supersaturated α phase; the DC microconstituent appear as spheroids and truncated nanowires close to the reaction front, which suggests that the reaction is a divorced transformation rather than by Rayleigh coarsening of nanowires. The resulting nanoinclusions are finer than eutectoid nanowires engendered in the $\text{Fe}_{28.4}\text{Si}_{71.6}$ and $\text{Fe}_{28}\text{Si}_{68}\text{Ge}_4$ compositions via melt-spinning (rapid-cool), even when aged under

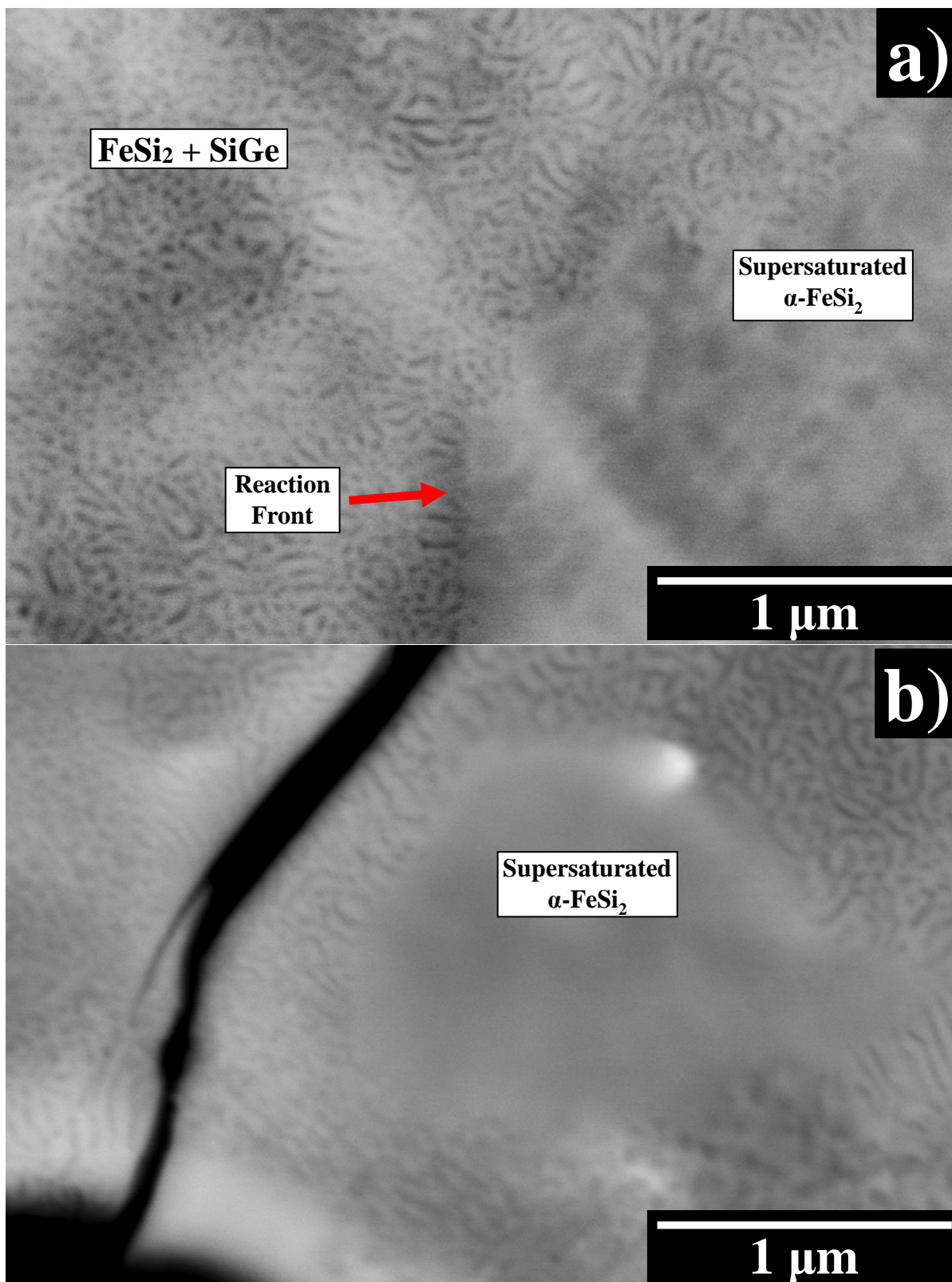
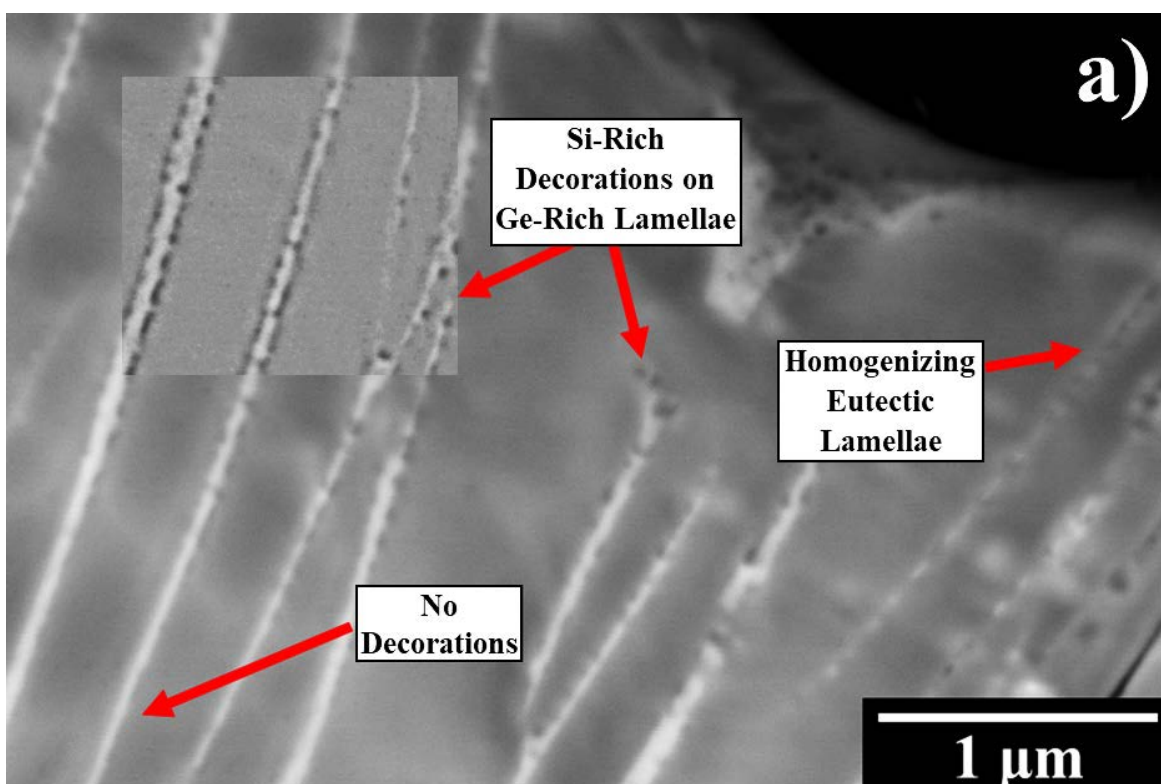


Figure 5.8: PLM $\text{Fe}_{28}\text{Si}_{68}\text{Ge}_4$ sample (SPS disk) aged at 567°C for 56 hrs. a) and b) Depicting unknown decomposition that occurs in DC supersaturated α phase. The reaction front between the supersaturated α and the disilicide + DC region is clearly defined.

identical conditions. The 2D silicide/SiGe interface density was increased to 29.8 ± 3.2 interfaces/ μm , almost 3x the 2D interface density obtained in the previous chapters; this due to finer particle widths, 24.2 ± 1.9 nm, higher interface per volume ratio of spheroid nanoinclusions, and finer interparticle spacings (48.5 ± 3.9 nm). This fine microstructure coupled with Ge-rich nanoinclusions would be ideal for thermal scattering.

5.3.2 Decomposition in Eutectic α + DC Regions

In the eutectic lamellae regions, the phase transformation proceeds in a different manner. As mentioned in Chapter 3.1.4, when the eutectoid lamellar spacing is on the same order of magnitude as the eutectic lamellar spacing, Si,Ge atoms diffuse directly to the α /DC interface and eventually homogenize into the lamellae. Figure 5.9.a shows Ge-rich eutectic lamellae decorated by numerous dark dot-like features; the overlay uses a Fourier bandpass filter to highlight compositional contrasts. These dots are not believed to be SiO_2 from O solutionized during PLM, as they



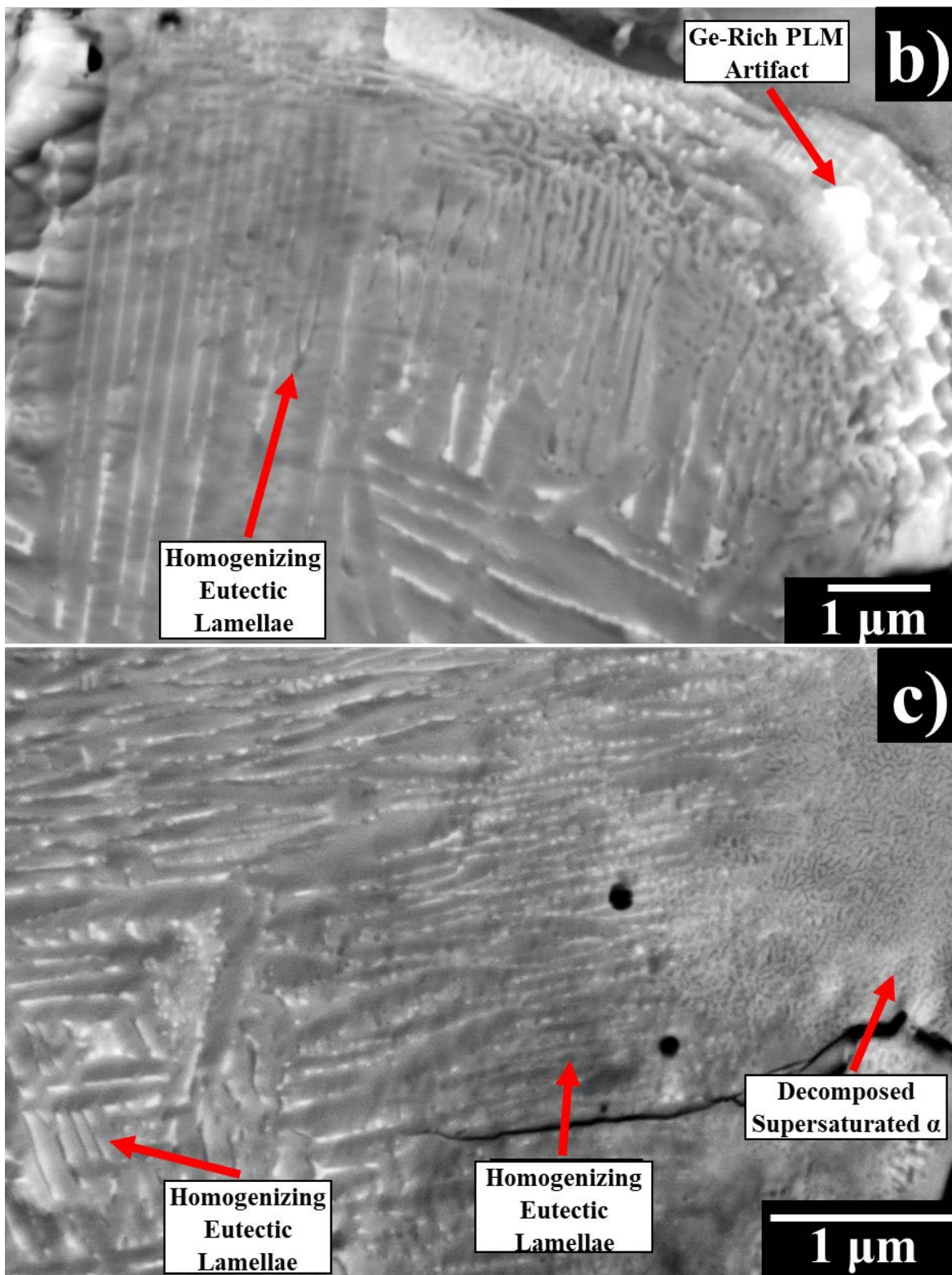


Figure 5.9: PLM sample aged at 567 °C for 56 hrs, with a range of decomposition morphologies: a) Ge-rich lamellae decorated by epitaxial Si-rich DC particles, inlay uses a bandpass filter to highlight composition contrasts, b) darkening contrast of lamellae as homogenization dilutes Ge concentration, and c) range of decomposition morphologies ranging from the supersaturated α (rightmost), to homogenizing lamellae, to the leftmost area where recent decomposition is still limited to epitaxial particles.

homogenize into the lamellae as shown by Figure 5.9.b but they do not form globally as would be expected from classical precipitation. These decorations are believed to result from the Si and Ge atoms, darker because they are Si-rich, diffusing out of the α phase to grow epitaxially on eutectic DC lamellae.

There are a few hypotheses as to why spherical particles are decorating eutectic interfaces, if we treat this as a solid-state analog of epitaxial thin film growth. Perhaps because of the lattice mismatch caused from Ge-rich “substrate” and the Si-rich epitaxial growth, quantum dots (QD) form to relieve lattice strain and minimize interfacial energy. This would be analogous to Volmer-Weber growth, as Si-rich “QD” form directly without an obvious wetting layer [119]. The QD appear to be situated in concavities. It is possible these concavities are the result of sinusoidal perturbations inherent to the lamellar surface and are artifacts of solidification. Or Rayleigh instability, during the aging process, could be exacerbating surface oscillations. The interface diffusion of Ge-rich Group IV elements could be moving toward local maxima, while creating a large number of steps for facile growth. Although why the Si-rich Group IV adatoms would diffuse against the flow of Rayleigh instability is not understood. After continued aging, these QD homogenize with the Ge-rich lamellae, lowering the Ge concentration. This is observed as a darkening of lamellar contrast, Figure 5.9.b.

The progression of aged microstructures can be seen in Figure 5.9.c as the transformation front began in the supersaturated α region (DC nanowires) on the right and moved towards the left of the micrograph. Once the reaction front moved into the $\alpha + DC$ region, and Si-rich particles start decorating the eutectic lamellae. As time progresses, they began to homogenize with eutectic lamellae, and precipitation of QD appear in recently transformed areas. No clear reaction front was observed in the $\alpha + DC$ regions; this might be more evidence for discontinuous precipitation. As

we do not see a contrast change in the disilicide despite the clear ejection of Group IV elements. The homogenized lamellar microstructure might not be as visually appealing as the hierarchical eutectic/eutectoid microstructure of the melt-spun ribbons, but the small lengthscales and high Ge concentrations could be as ideal as the supersaturated α phase in terms of reduced thermal conductivity.

5.3.3 Transformation Rate

Aging the laser-pulsed microstructure at 567 °C for 56 hrs did not result in complete decomposition as it did with the melt-spun ribbons. Like the hypoeutectic $\text{Fe}_{27}\text{Si}_{73}$ sample, colonies did not nucleate on the copious DC eutectic microconstituents during low temperature aging, and decomposition here was chiefly facilitated by cracks. Despite observing in Chapter 4.1.4 that eutectic lamellae provided facile heterogeneous nucleation sites, the two-phase regions here did not exhibit a higher colony nucleation density. It appears that the supersaturation slows Si and Ge diffusion into the DC nanoinclusions: this divorced transformation precedes slower than cooperative growth and could explain part of the sluggish transformation rate.

5.4 Future Directions

A possible solution to the cracked surface could be through composition control. My own exploratory experiments into PLM of a melt-spun $\text{Si}_{90}\text{Al}_{10}$ alloy, has shown that Si-rich alloys are not necessarily predisposed to surface cracking. It may be possible to minimize surface cracking by increasing the DC volume fraction.

Aging laser-pulsed samples has shown a cooperative phase transformation with lengthscales finer than what was achieved in the previous chapters and have, and presumably, a higher Ge concentration. Although the α /DC heterointerface did not seem to accelerating the decomposition

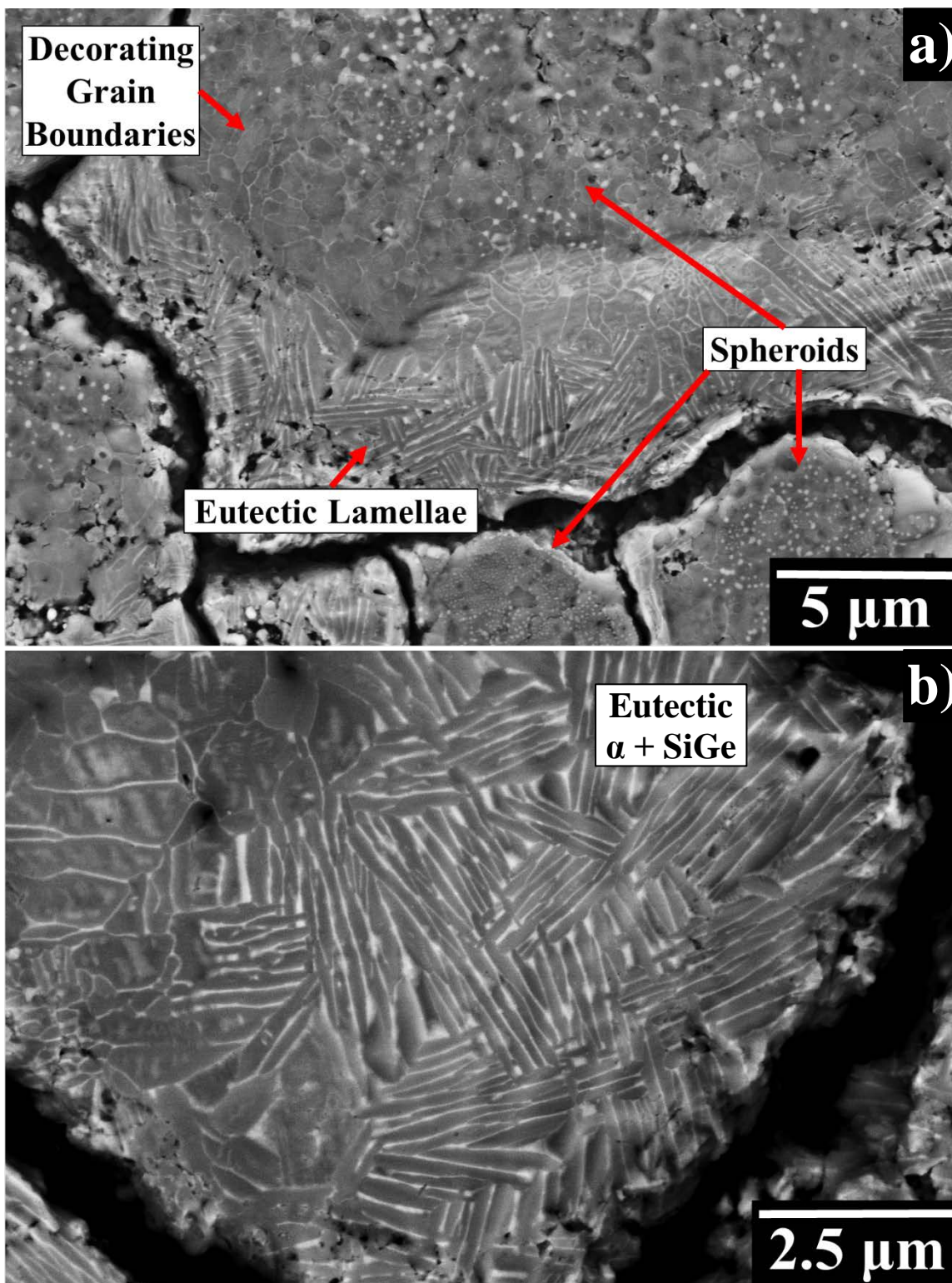


Figure 5.10: Powder processed $\text{Fe}_{28}\text{Si}_{68}\text{Ge}_4$ samples that were melted with an IR laser for ~ 600 pulses. a) Heterogeneous microstructure consisting of eutectic lamellae, spheroids, and DC phase forming an apparently continuous layer in the α grain boundaries. b) Higher mag image depicting the fine eutectic lamellae.

at 567 °C, it could be worthwhile to age at greater undercoolings to determine whether finer eutectoid nanowires could be grown between eutectic lamellae.

There are still, however, several challenges that need to be overcome in order to make pulse laser processing a viable technique for producing bulk thermoelectric materials. The excimer laser is not the ideal tool to achieve this, it is not able to produce a melt volume required to perform proper characterization. My groupmate, Naiming Liu, performed similar experiments with an IR fiber laser using much longer (100 μ sec) pulses (~600 pulses, 20Hz over ~30s), Figure 5.10. Although the surface was still highly damaged, this shows that a 25 nsec pulse duration is not necessary to achieve finer microstructures. This suggests that alternative optical sources such as flash lamps, could be used. Flashlamps also can produce sub-msec pulses, but can illuminate areas up to square meters. Longer pulse durations might be more favorable, as the melt will have more time for homogenization and greater absorption creates a larger melt volume. Once processing has been developed, the material should be fully characterized by XRD and thermal characterization.

5.5 Summary

The preliminary exploration of using PLM has shown that this technique is capable of producing microstructures not obtainable by melt-spinning. The resultant laser-pulsed microstructure produced ultra-fine $\alpha + \text{DC}$ two-phase regions and, in some cases, completely homogenized α phase. This demonstrates that the α phase is able to support a metastable composition up to at least $\text{Fe}_{22.5}\text{Si}_{67.5}\text{Ge}_{10}$. This is exciting, as this composition would yield fine two-phase $\beta + \text{Si}_{60}\text{Ge}_{40}$ microstructure and could have exceptional thermal scattering properties. Aging caused a divorced transformation, either eutectoid decomposition or discontinuous precipitation, with fine lengthscales and Si-rich nanoinclusions that are optimal for thermal scattering properties. However, we were unable to find a viable processing method and were unable to fully characterize

the PLM microstructure. We have shown that PLM is a promising processing route for future research into Fe-Si-Ge thermoelectrics, but still requires significant development.

6 Fe-Si-Ge Ternary Phase Diagram

Although nanocomposites of semiconducting β -Fe(Si,Ge)₂ and Si_{1-x}Ge_x diamond cubic (DC) phases have been explored for use as thermoelectrics [7][45][120][121], solar cells [48], and optoelectronics [49][50][122][123], the Si-rich region of the Fe-Si-Ge ternary phase diagram has not been investigated. Previous work only mapped the Fe-rich region relevant to transformer core materials [51]. The use of modeling programs such as FactSage and Thermocalc is frustrated by scarce thermodynamic data, especially for the Fe-Ge binary system. We found that both programs were unable to produce theoretical phase diagrams that agreed with our experimental data. Samples made in the previous chapter, as well as powder processed samples made by lab-member Naiming Liu, and new compositions melted and melt-spun by Naiming and myself, were repurposed to investigate the Fe-Si-Ge ternary phase diagram. The nonequilibrium processing techniques were required to produce fine microstructures, and to avoid formation of ϵ -FeSi, so as to reach equilibrium in a reasonable amount of time.

6.1 Key Isothermal Sections in the Si-rich Region

Understanding the extent of the phase coexistence regions, and the phase compositions, is critical for controlling Fe-Si-Ge alloy properties. Chapter 4 has shown that, through bulk composition and processing, the composition of Si_{1-x}Ge_x nanoinclusions can be systematically varied. This imparts greater flexibility in controlling and optimizing the thermoelectric properties. In this chapter, two key isothermal sections, above and below the $\alpha \rightarrow \beta + \text{Si}$ eutectoid isotherm, were investigated due to their importance towards microstructural engineering of the thermoelectric alloys.

A subset of our compositions was found to be in the three-phase coexistence region, where each phase has an invariant composition with only a change in volume fraction to maintain system

stoichiometry. These data points are of particular interest because their phase compositions at equilibrium fix the invariant points of the three-phase triangle, and can be easily used to map the ternary phase diagram. The compositions of the α , β , and ε phases were obtained by EDS and were found to be $\text{Fe}_{24.6}\text{Si}_{73.8}\text{Ge}_{1.6}$, $\text{Fe}_{35.0}\text{Si}_{64.4}\text{Ge}_{0.6}$, and $\text{Fe}_{49}\text{Si}_{51}$ respectively. Systematic error for the Quanta 650 EDX detector is about ± 1 at% when checked against a compositional standard, and is the main source of error in these measurements. As with our prior work, we found Rietveld refinement to be an indispensable technique for compositional analysis of DC inclusions. Through this technique we are also able to observe lattice parameters and volume fractions over a broader volume fraction vis-à-vis EDS to ensure equilibrium has been achieved. As we will discuss later in this chapter, the silicide phases do not follow Vegard's law and compositional analysis through XRD is not possible. Details of the refinement process are given in Appendix 2.

In order to establish whether our samples were truly at equilibrium, we utilized volume fractions and DC composition computed via Rietveld Refinement. Equilibrium was reached when the XRD spectrum showed that various DC compositions (proeutectic, eutectic, eutectoid, etc.) merged into a singular, sharp peak, and DC lattice parameters and volume fractions no longer shift as a function of aging time. Of the slow-cool compositions, only $\text{Fe}_{23.5}\text{Si}_{71.5}\text{Ge}_5$ reached equilibrium within the longest aging times used here -- 9 days. The slow approach to equilibrium in the unequilibrated specimens is due to the presence of the ε phase; aging in the $\beta + \text{DC}$ two-phase region for 30 days was not able to dissolve ε particles. The powder processed and ribbon samples, due to their fine microstructures, reached equilibrium before this time, but all samples were over aged to ensure equilibrium was met.

At 1000 °C the invariant composition for SiGe inclusions were found to be 32.3 ± 0.6 at% Ge when in equilibrium with α and ε phases, summarized in Figure 6.1.a. Achieving equilibrium at

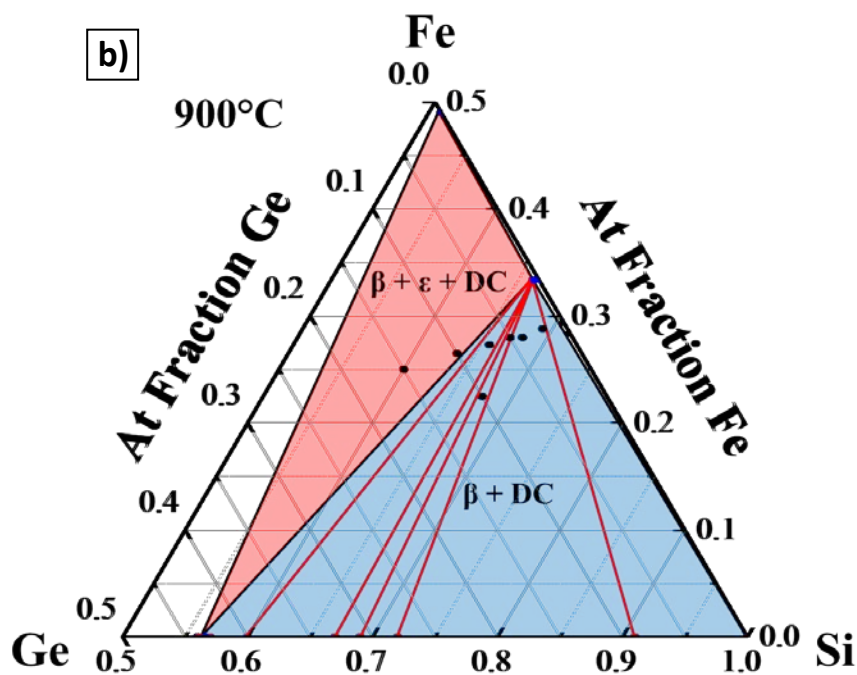
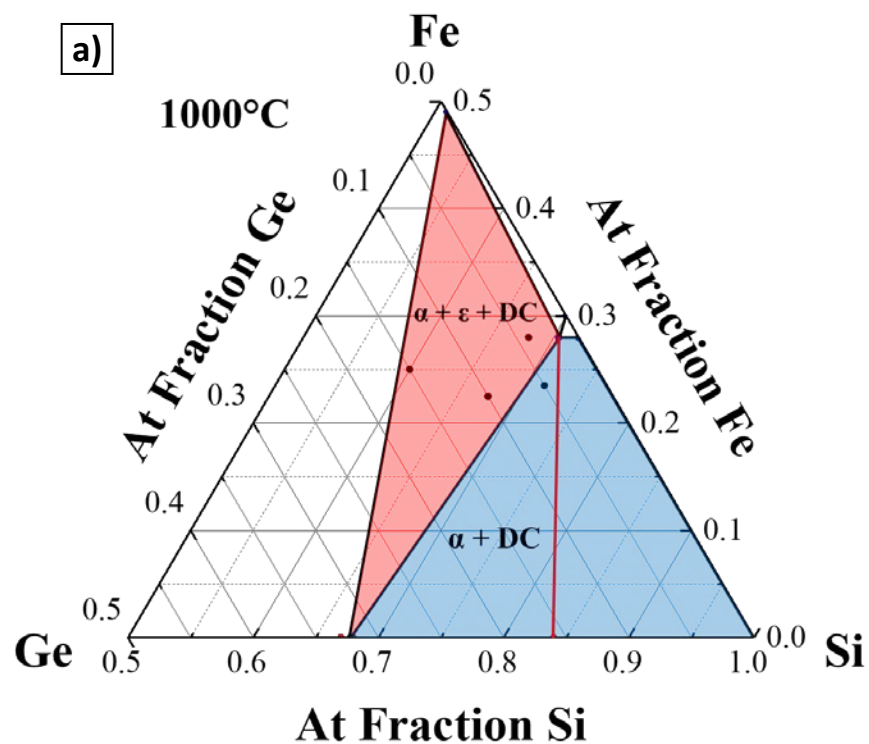


Figure 6.1: Fe-Si-Ge ternary phase diagram in the Si-rich region, with isothermal sections at a) 1000 °C and b) 900 °C. Red lines denote tie lines connecting the FeSi_2 and DC compositions for measured compositions (black dots).

900 °C was difficult due to the significantly slower kinetics. This necessitated the use of melt-spun ribbons and/or powder-SPS samples that produced fine-scale microstructures, and facile equilibration in a reasonable time frame. It was particularly important that base materials were initially free of ϵ . As previously mentioned, the ϵ -FeSi \rightarrow β -FeSi₂ is a time-consuming transformation, but the β -FeSi₂ \rightarrow ϵ -FeSi is not; reaching equilibrium is easier to allow ϵ to form than to age it out. The equilibrium SiGe inclusion composition in the $\beta + \epsilon + DC$ coexistence region increased to 43.5 ± 0.5 at% Ge at 900 °C, summarized in Figure 6.1.b. As discussed in the previous chapter, the 900 °C value has implications for $\beta + Si_{1-x}Ge_x$ nanocomposites as this sets the maximum attainable Ge incorporation in the DC phase, for the $\beta + DC$ two-phase region. The red lines on Figures 6.1.a and 6.1.b are tie lines of measured compositions for data points in the two-phase region. There is a reasonable agreement between the measured and calculated fractions and the mole fractions predicted from tie lines. This suggests that our approach correctly characterizes the ternary phase diagram; the principal error in these measurements are due to uncertainties in ICP bulk sample composition, the Rietveld-derived SiGe composition, and the silicide composition determined by SEM-EDS. A complete index of all compositions and volume fractions are shown in Table 6.1.

6.2 Lattice Parameters of Iron Silicides with Ge Incorporation

Lattice parameters of the diamond cubic phase were determined using Rietveld analysis on the nominally equilibrated samples from the previous section, which in turn determines the composition of the diamond cubic solution phase. We also examined whether Ge incorporated in the silicide parent phases (α , β , and ϵ) affected the nominal lattice parameters. The low solubility of Ge in the intermetallic phases prevents analysis by Rietveld refinement. Ge is isoelectronic with

Table 6.1: Rietveld Refinement data for all compositions and homogenization treatments. The “f” values are the volume fractions of the respective phases.

Sample Composition	Processing	Aging Temp. (°C)	DC Composition	f β	f α	fDC	f ϵ
Fe _{28.4} Si _{71.6}	Slow-Cool	900	Si ₁₀₀	0.83	-	0.17	-
Fe _{29.4} Si _{70.6}	Powder		Si ₁₀₀	0.84	-	0.16	-
Fe _{28.8} Si _{69.2} Ge ₂	Powder		Si ₉₁ Ge ₀₉	0.82	-	0.18	-
Fe ₂₈ Si ₆₇ Ge ₅	Powder		Si ₇₂ Ge ₂₈	0.79	-	0.21	-
Fe ₂₈ Si ₆₈ Ge ₄	Rapid-Cool		Si ₆₉ Ge ₃₁	0.71	-	0.29	-
Fe _{27.3} Si _{65.7} Ge ₇	Powder		Si ₆₇ Ge ₃₃	0.72	-	0.28	-
Fe _{22.5} Si _{67.5} Ge ₁₀	Rapid-Cool		Si ₆₀ Ge ₄₀	0.53	-	0.46	0.02
Fe _{26.5} Si _{63.5} Ge ₁₀	Powder		Si ₅₇ Ge ₄₃	0.60	-	0.36	0.04
Fe ₂₅ Si ₆₀ Ge ₁₅	Powder		Si ₅₆ Ge ₄₄	0.41	-	0.37	0.22
Fe _{23.5} Si _{71.5} Ge ₅	Slow-Cool	1000	Si ₈₄ Ge ₁₆	-	0.68	0.32	-
Fe ₂₈ Si ₆₈ Ge ₄	Rapid-Cool		Si ₆₈ Ge ₃₂	-	0.69	0.23	0.09
Fe _{22.5} Si _{67.5} Ge ₁₀	Rapid-Cool		Si ₆₈ Ge ₃₂	-	0.21	0.64	0.16
Fe ₂₅ Si ₆₀ Ge ₁₅	Powder		Si ₆₈ Ge ₃₂	-	0.02	0.65	0.33

Si and presumably substitutes on Si sites in the α , β , and ϵ crystal structures. We find that dilute incorporation of Ge has little effect on the averaged lattice parameters of the intermetallic phases, see Table 6.2. This table includes our results for binary Fe-Si alloys, which serve as an internal calibration for Ge substitution of Si. The tetragonal α phase was found to entrain the largest amount of Ge, up to ~3.0 at% for rapidly-solidified melt-spun samples [120][35], changing the composition from Fe_{28.4}Si_{71.6} to Fe_{24.8}Si_{72.2}Ge₃. The Group IV:Fe ratio shows that for every Fe atom there are 2.5 Group IV atoms in the binary system, and 3.0 Group IV atoms in the ternary system. It is possible that rather than the Fe vacancy % changing with added Ge, it could be possible that Ge is substituting on Fe sites. Despite this larger quantity of The Group IV element, the α phase did not show a significant increase in lattice parameter. On average there is a 0.008 Å expansion of the c-axis relative to the Ge-free α phase, however this difference barely exceeds the

Table 6.2: Rietveld Refinement determined lattice parameters of iron silicides of all baseline and Ge alloyed compositions. Units are in Å.

System	α		β			ϵ
	a,b	c	a	b	c	a
Fe-Si	2.693 ± 0.003	5.132 ± 0.003	9.879 ± 0.005	7.807 ± 0.003	7.836 ± 0.005	-
Fe-Si-Ge	2.696 ± 0.002	5.140 ± 0.003	9.875 ± 0.007	7.800 ± 0.013	7.837 ± 0.012	4.486 ± 0.002

error. The orthorhombic β phase has a limited solubility of ~ 0.6 at % Ge [120][39], and the solute does not have a noticeable effect on lattice parameter. Note that Rietveld analysis does show a wider variation across the various Fe-Si-Ge samples, as embodied in the standard deviations shown in Table 6.2. Nonetheless, the average lattice parameter is within error of Fe-Si values. The ϵ -phase, which has B20 crystal structure, is present in both Fe-Si and Fe-Ge equilibrium phase diagrams: ϵ -FeSi is stable up to 1410 °C where it congruently melts, while ϵ -FeGe undergoes peritectoid decomposition at 748 °C. It is possible to form miscible solutions ϵ -Fe(Si_{1-x}Ge_x) at temperatures below 748 °C, with at least one report showing Ge incorporation of up to $x=0.23$ [124]. However, we found no evidence of Ge incorporation in ϵ at 900 °C or 1000 °C. Our lattice parameter agrees with existing data for the ϵ phase as reported in the latest PDF-4 datasets from the International Center for Diffraction Data (<http://www.icdd.com>) such as PDF4 04-004-3037.

6.3 DSC Analysis

6.3.1 Temperature of Phase Transformations

We mapped two isothermal sections of the Si-rich region of the Fe-Si-Ge system by finding the chemical composition of equilibrium phases via Rietveld refinement. However, this information did not illuminate the effects of Ge on eutectic and eutectoid phase transformation. To complete crucial information about the ternary phase diagram, we utilized differential scanning calorimetry

(DSC) to identify the temperature of key phase transformations. Several new compositions were made so that more information about the liquidus surface could be obtained.

Figure 6.2 shows the DSC heating curves (see Chapter 2 for descriptions of the measurements) for compositions both close to, and far away from, the $L \Leftrightarrow \alpha\text{-FeSi}_2 + \varepsilon\text{-FeSi} + \text{Si}_{1-x}\text{Ge}_x$ eutectic point. The peaks are endothermic (heat absorption). The peaks in the heating curves for the two compositions show a clear difference in liquidus temperatures as well as an increase in volume undergoing eutectic solidification. It should be noted that the DSC indicates, via heat release or absorption, what temperature phase transformations occur, but is cannot itself indicate the nature of the transformation, hence additional information is used to determine the transformations. We used Proteus Analysis, the Nietzch DSC analysis software, to derive the temperatures of the

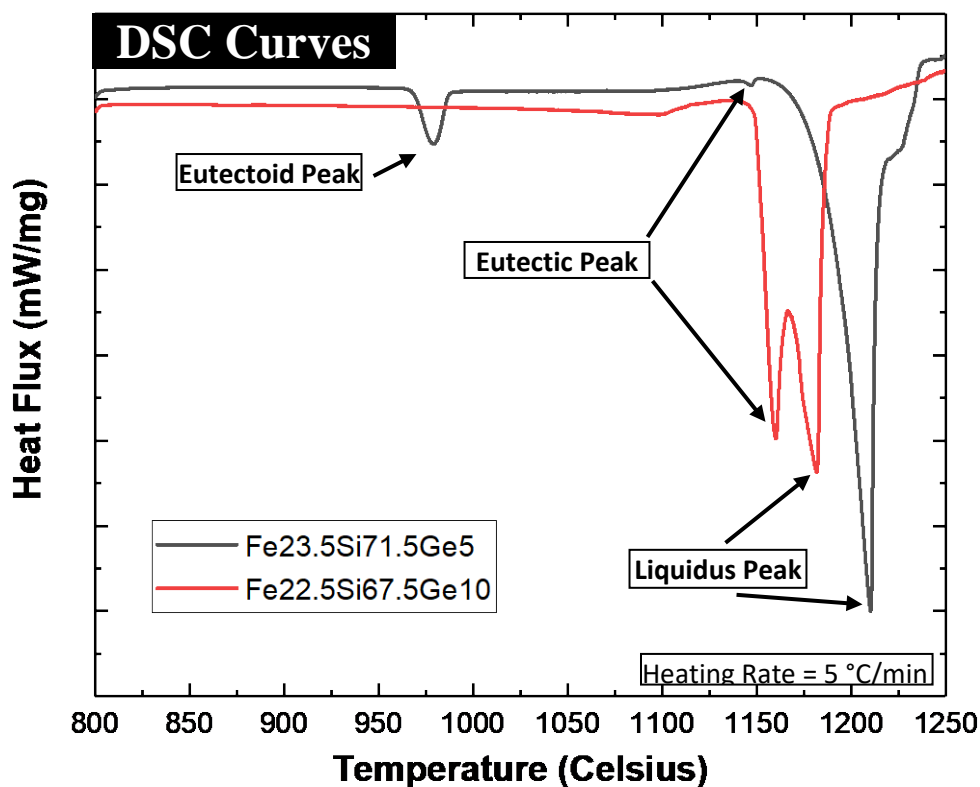


Figure 6.2: DSC curves of samples, Fe_{22.5}Si_{67.5}Ge₁₀ (Red) and Fe_{23.5}Si_{71.5}Ge₅ (Black) which are the compositions with the largest and smallest change in enthalpy due to $L \Leftrightarrow \alpha\text{-FeSi}_2 + \varepsilon\text{-FeSi} + \text{Si}_{1-x}$ eutectic solidification, respectively.

eutectoid and eutectic isotherms, and the liquidus temperature. The eutectoid and eutectic isotherm temperatures are determined by the onset of their corresponding peaks, which is the temperature at which the phase transformation begins. Peak onset was determined by the intersection of the extended baseline and maximum peak slope. The peak position of the highest temperature peak is considered to be the liquidus, where the sample is fully molten. Data obtained from DSC curves can be found in Table 6.3. Error bars were calculated by the average value taken from DSC curves of three successive thermal cycles. The eutectic isotherm occurred at 1147.5 ± 2.6 °C and was consistent for all compositions. Ge has clearly lowered the eutectic isotherm temperature from the 1210.1 ± 0.2 °C isotherm measured for the hypoeutectic Fe₂₇Si₇₃ sample. A small peak corresponding to the eutectoid isotherm was present in most compositions. Despite going through the same thermal treatment, the peak corresponding to the eutectoid decomposition is missing in a few compositions and it is not clear why eutectoid formation isn't occurring. This suppression could arise from the inherent sluggish nature of the eutectoid decomposition, despite the long

Table 6.3: Compiled DSC data for all compositions.

Sample	Enthalpy Change	Eutectoid Temp.	Eutectic Temp.	Liquidus Temp.
Fe₂₇Si₇₃	-	938.7 ± 0.0	1210.1 ± 0.2	1237.5 ± 0.7
Fe₂₈Si₆₈Ge₄	21.2 ± 2.0	971.3 ± 1.0	1143.1 ± 0.4	1198 ± 0.6
Fe₂₂Si_{66.5}Ge_{11.5}	50.4 ± 1.5	978.4 ± 0.4	1148.1 ± 0.5	1188.2 ± 0.4
Fe₂₆Si₅₉Ge₁₅	90.5 ± 3.7	977.5 ± 0.7	1149.3 ± 0.4	1178 ± 0.3
Fe₁₅Si₇₀Ge₁₅	37.4 ± 2.1	974.9 ± 0.8	1146.6 ± 0.3	1179.9 ± 0.9
Fe₁₅Si₆₅Ge₂₀	49.3 ± 2.5	965.4 ± 1.3	1147.4 ± 0.3	1171.8 ± 0.5
Fe₂₀Si₆₅Ge₁₅	56.0 ± 1.2	977.5 ± 0.7	1145.9 ± 0.14	1182.3 ± 0.6
Fe₃₂Si₆₃Ge₅	24.0 ± 0.4	978.7 ± 0.2	1148.9 ± 0.7	1194.2 ± 0.2
Fe₃₁Si₅₉Ge₁₀	48.1 ± 0.6	-	1149.8 ± 0.3	1182.9 ± 0.9
Fe₂₀Si₆₀Ge₂₀	113.6 ± 4.6	-	1150.1 ± 0.1	1174.8 ± 0.4
Fe_{23.5}Si_{71.5}Ge₅	0.6 ± 0.3	968.4 ± 0.2	1141.7 ± 0.9	1209.4 ± 0.8
Fe₂₇Si₆₃Ge₁₀	50.8 ± 1.7	-	1149.7 ± 0.1	1187.2 ± 0.2
Fe_{22.5}Si_{67.5}Ge₁₀	110.3 ± 4.9	-	1149.9 ± 0.1	1181.8 ± 0.1
Aveage Fe-Si-Ge	-	974.1 ± 4.8	1147.5 ± 2.6	-

isothermal age at an optimized decomposition temperature. Whereas the eutectic isotherm shifts to lower temperatures with Ge addition, the eutectoid isotherm temperature increases significantly from 938.7 °C to 974.1 ± 4.8 °C. Some of the liquidus peaks have anomalous, high-temperature shoulders. The cause is not clear, and could be caused by a discontinuity in thermal contact caused by the molten boule attaching itself to the wall of the Al₂O₃ cups. The shoulders do not appear to be caused by an additional phase transformation and do not change the interpretation.

6.3.2 Liquidus Surface and Microstructure of As-Cast Alloys

The liquidus surface, as shown in Figure 6.3, was determined through DSC measurements and extrapolation of known liquidus temperatures from binary phase diagrams for Fe-Si [4], Fe-Ge [4], and Si-Ge [102] alloys. The ternary contour maps extend past our measured compositions to show general trends; however, these regions were *not* experimentally determined.

In the Fe-Si binary phase diagram, the α phase congruently solidifies and has two peritectic $\alpha + L$ shoulders which occur over a narrow temperature but broad compositional range, see Chapter 1.2.2. The path of the two shallow eutectic valleys ($\alpha + DC$ and $\alpha + \epsilon$) on either side of the congruent α dome merge at a relatively small concentration of Ge, and form a cotectic ($\alpha + \epsilon$) line whose bounds are proposed in Figure 6.3.b. SEM micrographs of as-cast microstructures of compositions on either side of these lines corroborate the singular presence of proeutectic ϵ (Figure 6.4.a) or DC (Figure 6.4.b). The two microstructures shown here, along with the Fe₂₈Si₆₈Ge₄ and other ternary compositions, have a ternary eutectic morphology ($L \rightarrow \alpha + \epsilon + DC$). Ignoring the proeutectic phases, the $\alpha + DC$ lamellae clearly have grown in a coupled manner along with cooperatively grown $\epsilon + DC$ at the lamellar exterior. The $\epsilon + DC$ do not penetrate deep into the lamellae. This is due to compositional changes ($\epsilon + DC$ colonies growth

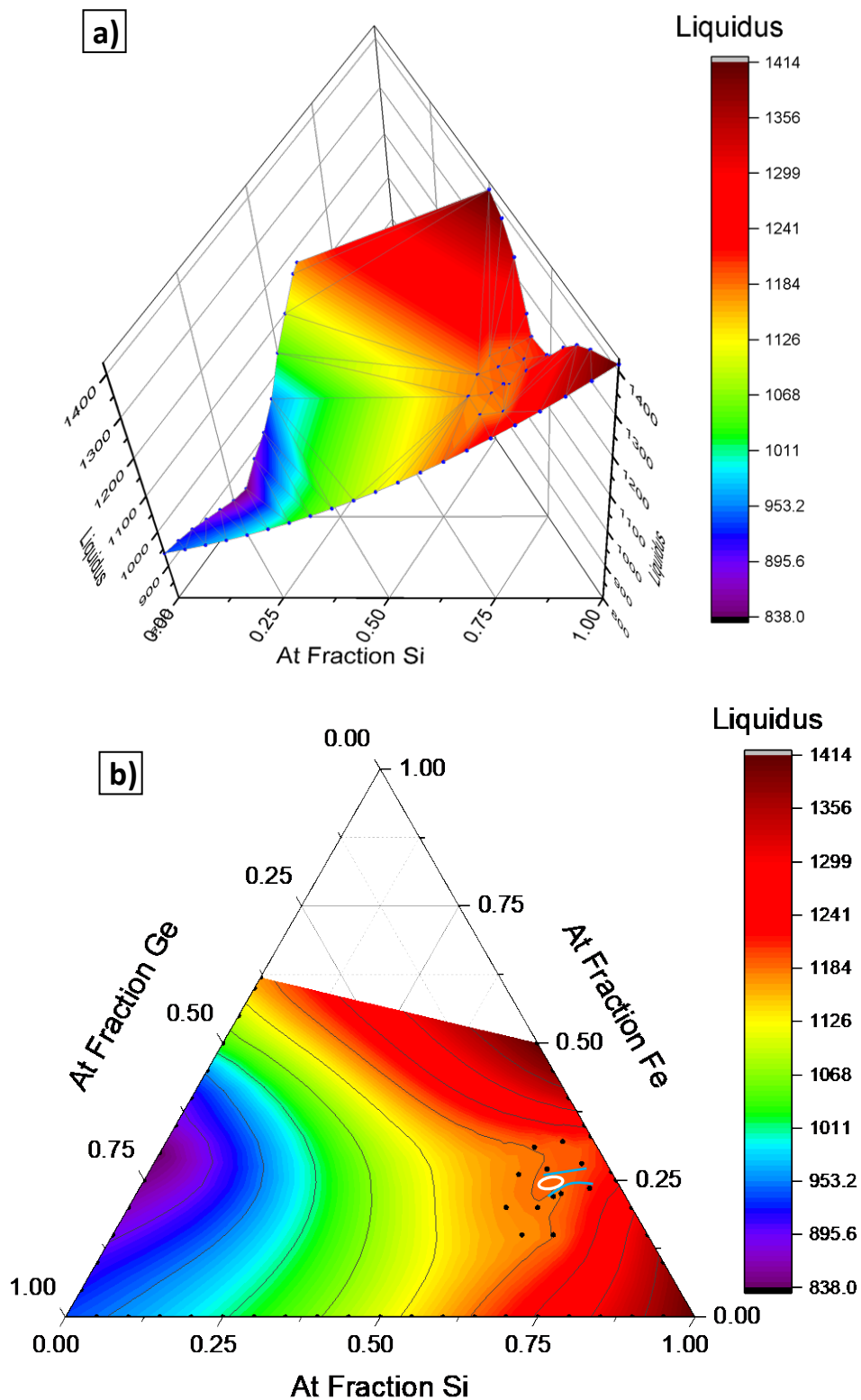


Figure 6.3: a) 3D and b) 2D ternary surface plots of liquidus temperatures. Data points were taken from experimental measurements and Fe-Si, Si-Ge, and Fe-Ge binary phase diagrams. The blue curves bound the location of the $\epsilon + DC$ cotectic line, above the upper line proeutectic ϵ forms and proeutectic DC forms below the lower line. The white oval indicates our estimate for the ternary eutectic point.

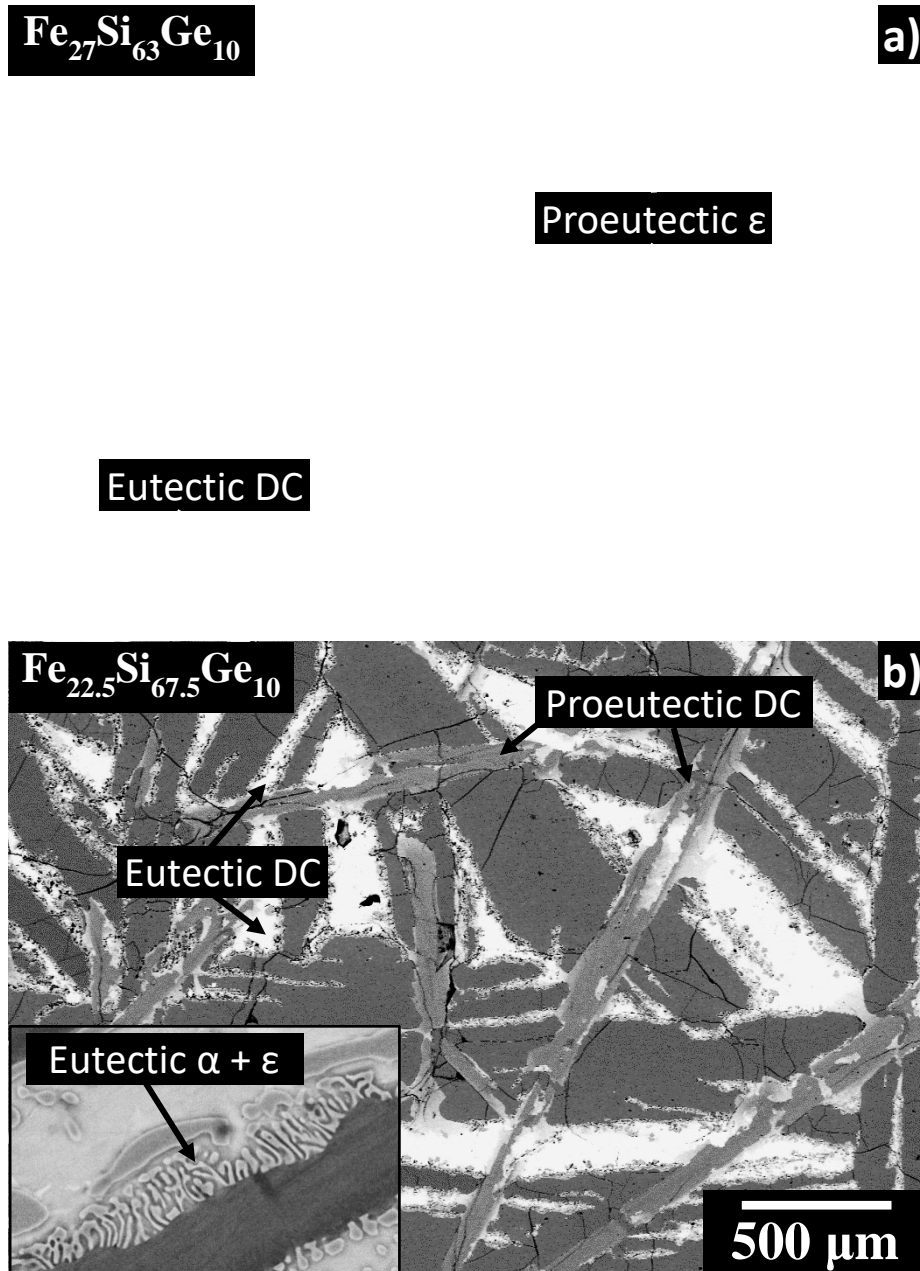


Figure 6.4: SEM micrographs of as-cast microstructures of a) $\text{Fe}_{27}\text{Si}_{63}\text{Ge}_{10}$ showing the proeutectic ϵ and b) $\text{Fe}_{22.5}\text{Si}_{67.5}\text{Ge}_{10}$ showing the presence of proeutectic DC. Inset shows the eutectic $\alpha + \epsilon$ microstructure found at the edge of the eutectic DC lamellae. The cross sections were taken from the top of each boule.

ejects Ge into DC lamella until composition becomes unfavorable for coupled growth) and low ϵ volume fraction; we estimate the composition of the ternary eutectic point to be within the white oval, for reasons we will discuss in the following section. The liquidus in this region appears

analogous to the flat region in the Fe-Si binary phase diagram; such broad and narrow features make resolving liquidus surface features nontrivial.

6.3.3 Tammann Triangle

The Tammann triangle method [62][60] was used to estimate the ternary eutectic composition. The magnitude of the change in enthalpy (area of the ternary eutectic solidification peak) relates to the volume of the melt undergoing eutectic solidification; the closer the composition is to the ternary eutectic point the larger volume and the change of enthalpy [62]. By examining the change in enthalpy for several compositions, it is possible to extrapolate the composition that results in the highest change. Figure 6.5.a shows a ternary surface plot of the Tammann triangle. The change of entropy grows larger as more Ge is added to the system, as Ge content increases the volume of proeutectic decreases as the liquidus approaches the ternary eutectic isotherm, as shown in Figure 6.5.b. One sample, $\text{Fe}_{22.5}\text{Si}_{67.5}\text{Ge}_{10}$, has an unexpected increase in the change of enthalpy, Figure 6.5.a, which suggests that a larger volume of eutectic solidified than the data points around it. The same composition has a drop in liquidus temperature and lies near our bounds for the cotectic line, which runs into the ternary eutectic point. This composition was analyzed three consecutive times with identical results with identical conditions as the rest of the DSC scans, and is not believed to be caused by instrumental error. We estimate the ternary eutectic point to be within the bounds of the white oval, which is centered at $\text{Fe}_{25}\text{Si}_{65}\text{Ge}_{10}$. However, due to the low resolution of compositions, it is not possible to obtain a more accurate location.

6.3.4 Conclusion

In this chapter, we mapped key phase transformations and regions of the Si-rich Fe-Si-Ge ternary phase system. Three-phase regions at 1000 °C and 900 °C were experimentally characterized, and

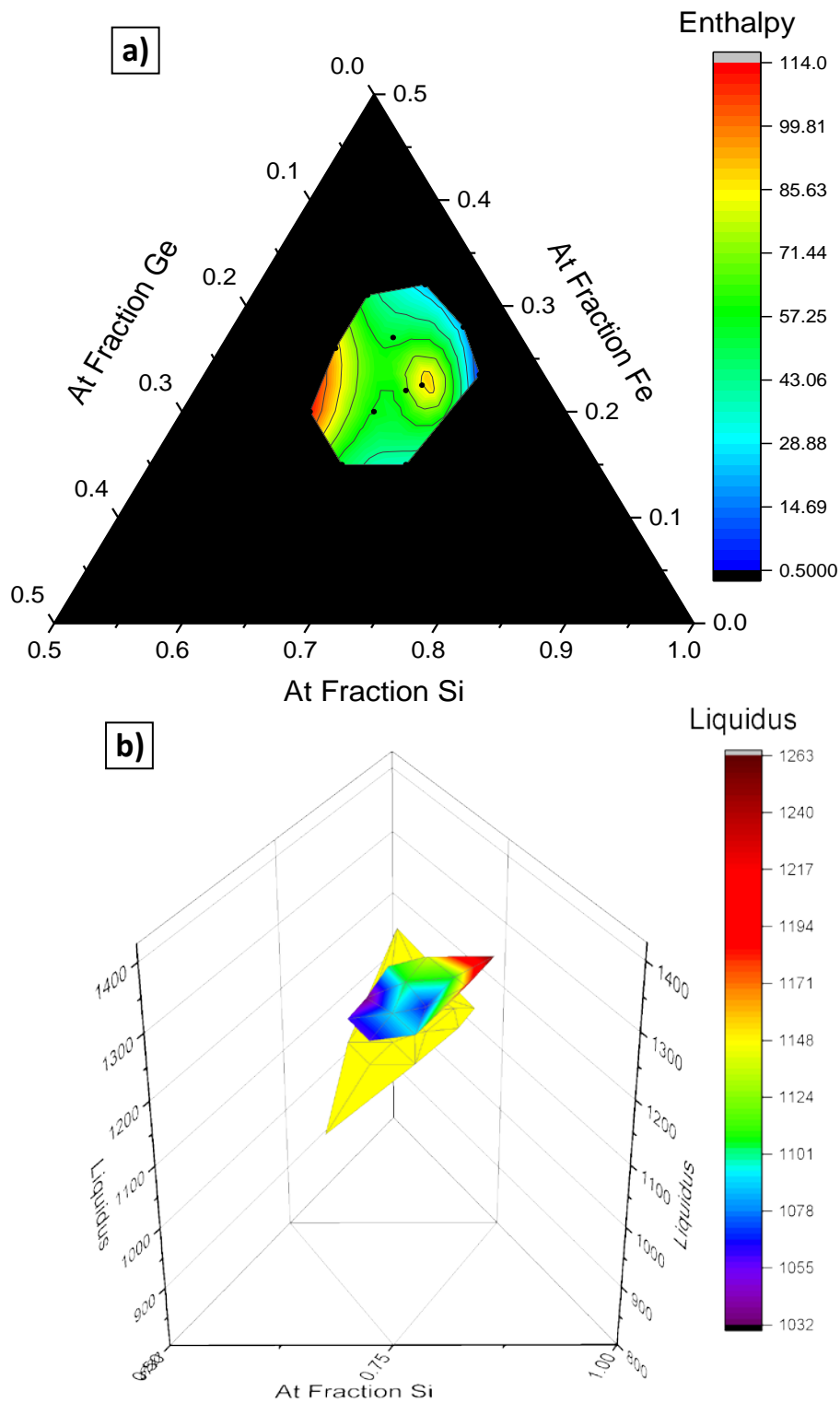


Figure 6.5: a) Truncated ternary surface diagram of the Tammann triangle, the color gradient relates to the change in enthalpy. b) 3D diagram depicting the measured liquidus surface (ranging from red to purple) as it slopes towards lower temperatures in respect to the eutectic isotherm (yellow plane).

were found to have invariant DC compositions of 32.3 ± 0.6 at% and 42.5 ± 0.5 at% Ge respectively. The latter represents the upper Ge concentration limit of the DC phase in the $\beta + DC$ two-phase region, implying that larger Ge contents cannot be obtained via close-to-equilibrium methods. The intermetallic phases only incorporated small amounts of Ge; Rietveld analysis of these phases show that lattice parameters are not affected by the entrained Ge, and are all within error of known and measured binary Fe-Si values. Ge is also shown to depress the $L \Leftrightarrow \alpha\text{-FeSi}_2 + \varepsilon\text{-FeSi} + \text{Si}_{1-x}\text{Ge}_x$ eutectic isotherm temperature from 1210.1 ± 0.2 °C to 1147.5 ± 2.6 °C and heighten the eutectoid isotherm temperature from 938.7 °C to 974.1 ± 4.8 °C. The bounds for the location of the $\varepsilon + DC$ cotectic line has been found through SEM micrographs. The exact location of $L \Leftrightarrow \alpha\text{-FeSi}_2 + \varepsilon\text{-FeSi} + \text{Si}_{1-x}\text{Ge}_x$ ternary eutectic point was not found, however evidence suggests that the cotectic line could be near $\text{Fe}_{22.5}\text{Si}_{167.5}\text{Ge}_{10}$.

7 Conclusion

7.1 Summary

This dissertation discusses the hierarchical structuring of Fe-Si based alloys for the improvement of thermoelectric efficiency. Meso-scale to atomic-scale structuring was achieved via controlled eutectoid + eutectic process conditions that were optimized to enhance thermal scattering. We have shown that fine nano-scale/meso-scale structuring (eutectoid interweaved between eutectic lamellae) improved thermal scattering as we had hypothesized; however, it was the atomic-scale (Ge concentration of $\text{Si}_{1-x}\text{Ge}_x$ nanowires) that had the greatest impact on thermal conductivity. This dissertation had two main emphases, characterize the effects of processing on microstructure and relate the microstructure to thermal properties. If the thermoelectric figure of merit is to be improved, then it will require absolute control over microstructure.

From the binary Fe-Si alloy system, we characterized the eutectoid microstructure and phase transformation mechanisms. The nucleation of $\beta + \text{DC}$ colonies at high undercoolings (567°C) is energetically unfavorable and requires cracks, DC lamellae, or Cu impurities to facilitate nucleation in a reasonable time-frame; this temperature was found to create a fine nanocomposite of DC nanowires in a $\beta\text{-FeSi}_2$ matrix. Two processing extremes were chosen to produce samples with thermal conductivities where β/DC heterointerfaces dominate (567°C , fine nanowires with 11.0 interfaces/ μm) and bulk phases dominate (910°C , coarse equiaxed particles with 0.3 interfaces/ μm). As we will discuss later, this nanostructuring reduced thermal conductivity by a factor of 2. The 567°C aging temperature produced fine eutectoid lamella with ~ 11.0 interfaces/ μm regardless of the initial composition of α .

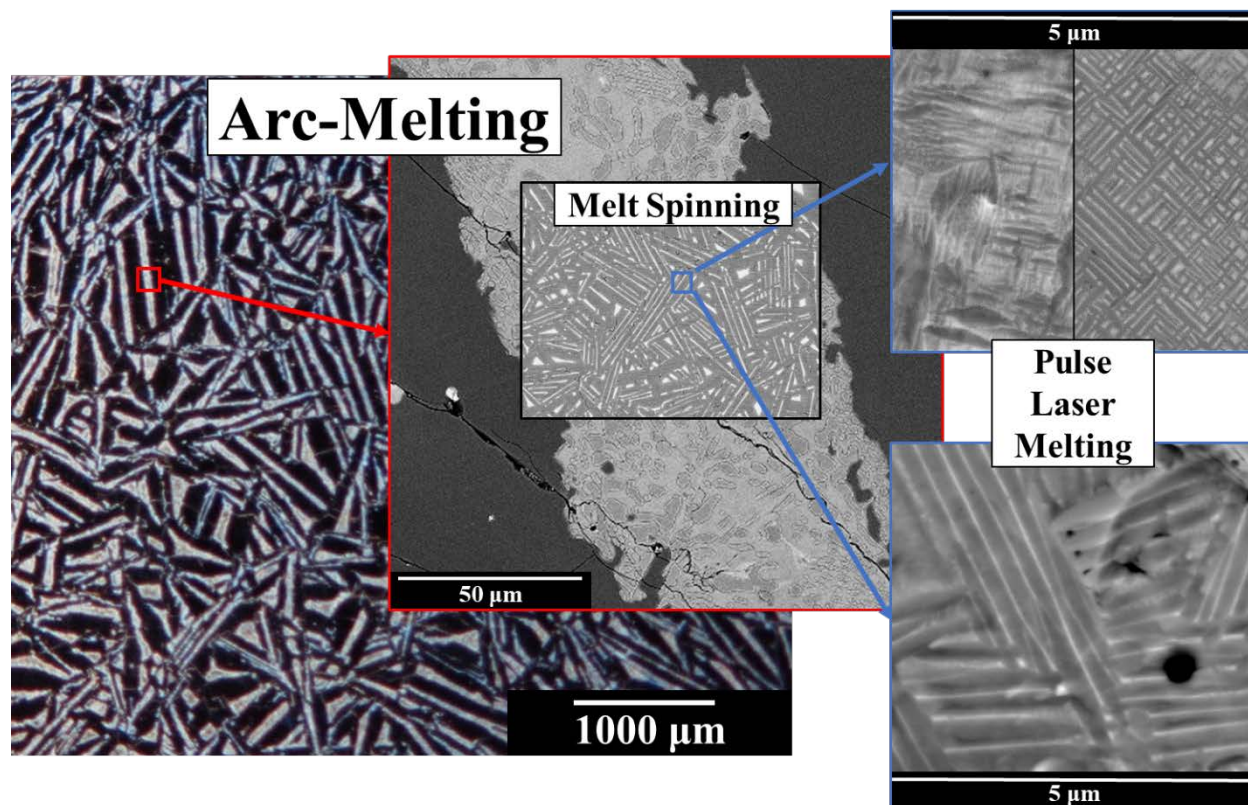


Figure 7.1: Micrographs depicting lengthscales of eutectic lamellae made by arc-melting, melt-spinning, and pulse laser melting techniques. The scale bars for the illuminated areas and the inlays are consistent.

The ternary $\text{Fe}_{28}\text{Si}_{68}\text{Ge}_4$ alloy was utilized for meso-scale structuring. The solidification rate effectively controlled meso-scale features such as α grain size, which in turn affects the aged $\beta + \text{DC}$ colony size, and DC lamellar lengthscales (Figure 7.1). Increasing the rate from 10^2 °C/s (arc-melting) to 10^6 °C/s (melt-spinning), reduced the interlamellar spacing by two orders of magnitude from 131 to 1.5 μm and the aged $\beta + \text{DC}$ colony size from 16 μm to 800 nm. Nanostructured eutectic lamellae and β/β interfaces were found to be insignificant contributors to thermal scattering; however, a consequence of eutectic and eutectoid engineering is a Group IV supersaturated α phase, from $\text{Fe}_{24.6}\text{Si}_{73.8}\text{Ge}_{1.6}$ (arc-melt) to $\text{Fe}_{24.8}\text{Si}_{72.2}\text{Ge}_{3.0}$ (melt-spin), and is far more advantageous for thermal scattering. The composition of the eutectoid nanowires is inherently dependent upon the amount of entrained Group VI elements in the α phase. Exploratory work into pulse laser

melting found that a solidification rate of $10^9 - 10^{12} \text{ }^\circ\text{C/s}$ was capable of producing supersaturated α with compositions of $\text{Fe}_{28}\text{Si}_{68}\text{Ge}_4$, $\text{Fe}_{22.5}\text{Si}_{67.5}\text{Ge}_{10}$, and $\text{Fe}_{23.5}\text{Si}_{71.5}\text{Ge}_5$. If these supersaturated α compositions could be aged (at $567 \text{ }^\circ\text{C}$) and characterized, then our theoretical model predicts the resulting microstructure could have a thermal conductivity as low as $\sim 2 \text{ W/mK}$. This would be an order of magnitude decrease in thermal conductivity and could profoundly increase zT . Ultra-fine lamellar regions were also identified from the PLM process with interlamellar spacing of 175 nm , and could potentially be as promising as the supersaturated α material. However, due to processing challenges the PLM materials were not able to be characterized beyond SEM.

As previously stated, nanostructuring of the eutectoid decomposition had resulted in a 50x increase in heterointerface density vis-à-vis highly coarsened particles in the Fe-Si alloy. This increase also had a concomitant 2x reduction in thermal conductivity, from 22.8 to 12.1 W/mK . Matthiessen's rule for a thermal circuit was used to attribute individual thermal conductivity contributions to the

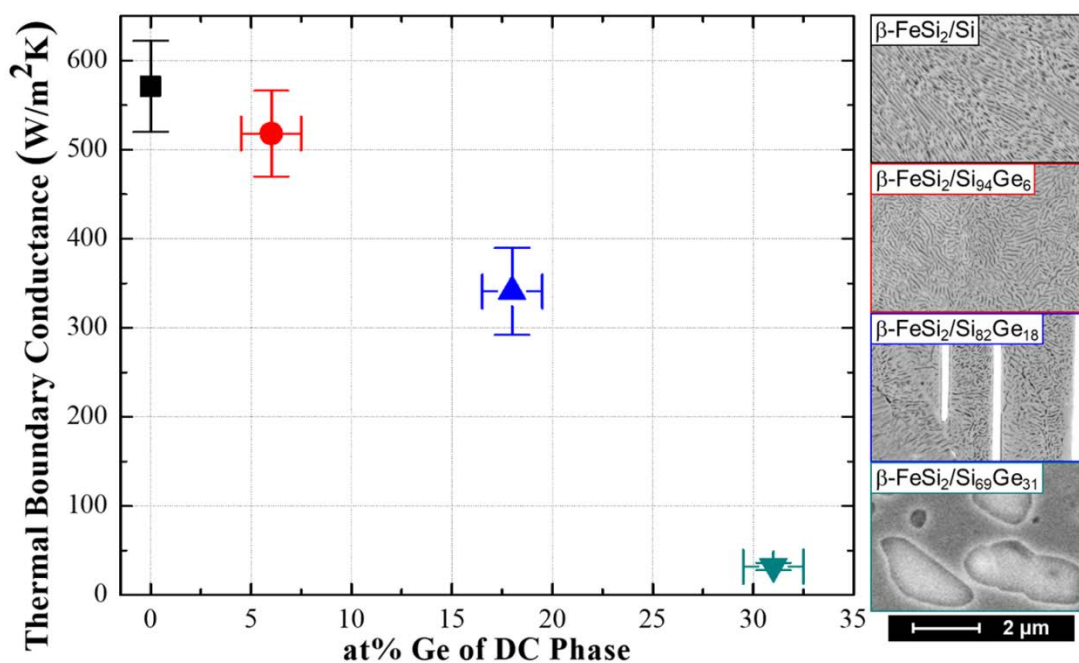


Figure 7.2: Plot showing the decrease in TBC as a function of at% Ge. The data points are color coded to the micrographs and corresponding $\beta/\text{Si}_{1-x}\text{Ge}_x$ interface.

heterointerface. The β/Si_{100} interface is clearly a poor scatterer of phonons. We found that through different eutectic/eutectoid processing routes in the Fe-Si-Ge alloy (Figure 7.2), we were able to vary the Ge concentration of DC inclusions. Not only does alloy scattering caused by Ge impurities benefit bulk thermal conductivity, but by examining a range of DC compositions it was discovered that thermal boundary conductance is also highly susceptible to composition. By producing $\sim\text{Si}_{70}\text{Ge}_{30}$ nanoinclusions in a β matrix, we were able to significantly drop thermal boundary conductance from 571 to 49 MW/m²K vis-à-vis the pure Si sample. It was also discovered that TBC is the more significant contributor of thermal conductivity. As coarsened, high TBC particles had a thermal conductivity (8.9 W/mK), which is comparable to the meso-scale/nano-scale structured sample (8.3 W/mK). A hierarchical eutectic/eutectoid microstructure did not provide any obvious benefits for thermal scattering (beyond atomic-scale structuring), as fine Ge-rich nanoinclusions are more significant scatterers of phonons.

The various compositions and heat treatments performed over the course of this dissertation yielded valuable data for the construction of a ternary phase diagram; Three-phase regions were identified at 1000 °C and 900 °C, $\alpha + \varepsilon + \text{DC}$ and $\beta + \varepsilon + \text{DC}$ respectively. The isothermal sections from these two temperatures, along with all data points are combined in Figure 7.3, and the temperatures at which ε exists at equilibrium is color coded: 1) above and below the eutectoid isotherm in the red region, 2) above the eutectoid isotherm in the purple region, and 3) does not exist at any temperature in the blue region. The max DC equilibrium composition of the heterointerface was identified as $\beta/\text{Si}_{56.5}\text{Ge}_{43.5}$. This composition cannot be achieved by arc-melting, as the melt needs to quickly solidify through the eutectoid isotherm to avoid ε nucleation. Nonequilibrium techniques such as melt-spinning and powder processing are capable of avoiding

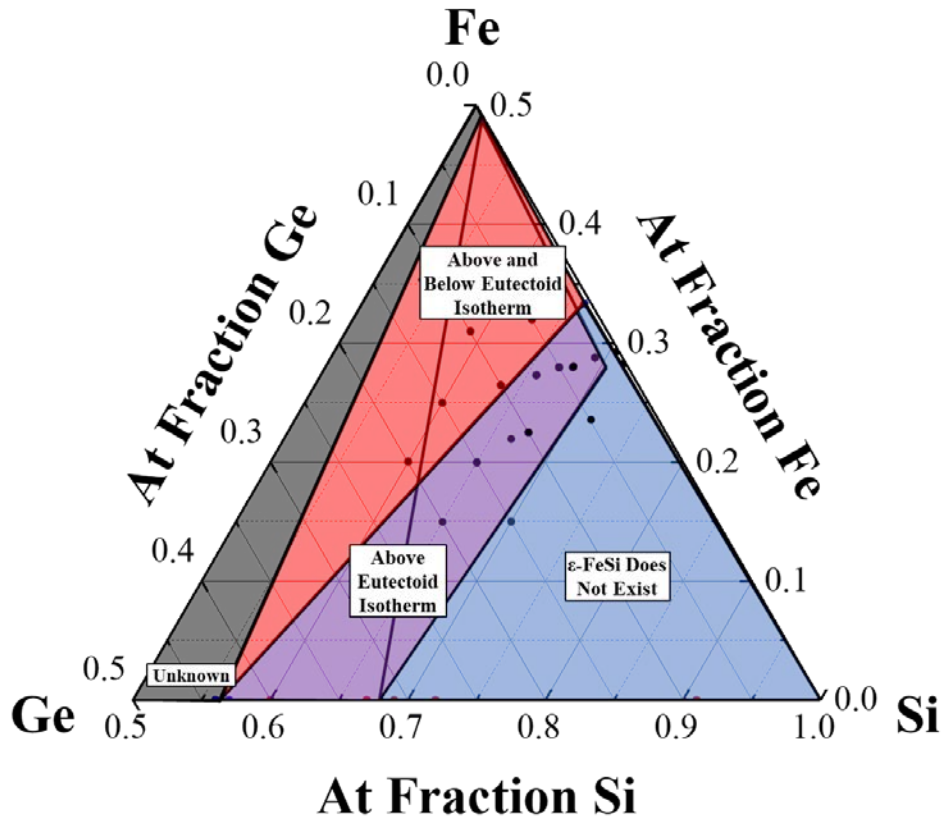


Figure 7.3: Combination of 900 and 1000 °C isothermal sections. ϵ is not stable at equilibrium in the blue region, only stable above the eutectoid isotherm in the purple region, and is stable above and to an unknown temperature below the eutectoid isotherm.

ϵ nucleation at high temperatures and required to produce to produce a two-phase $\alpha + \text{DC}$ microstructure in the purple region of Figure 7.3

7.2 Future Work

Although funding for this project has ended, we have not yet fully explored the design space afforded us by the Fe-Si based alloys or by nonequilibrium solidification:

- Develop processing techniques for PLM, preferably with a different type of high-powered laser, to produce bulk samples with PLM microstructures. A more systematic approach to experimentation would better illuminate how PLM conditions engender microstructures.

- Explore κ_l and TBC for sample compositions with $\beta/\text{Si}_{56.5}\text{Ge}_{43.5}$ interfaces, which is the highest equilibrium Ge concentration allowed for this system. Volume fractions could be varied to further tailor thermoelectric properties.
- Obtain all thermoelectric properties from a hierarchically optimized PLM sample.
- Investigate electrical boundary conductance as a function of Ge concentration.
- Investigate the effects of bandgap engineering on $S^2\sigma$ by varying $\text{Si}_{1-x}\text{Ge}_x$ nanowire composition and substitute other isoelectronic elements for bandgap and valence band alignment.
- Alloying of isoelectronic Fe group elements. Os makes a semiconducting, isostructural β - OsSi_2 [125] and could potentially increase the bandgap and further enhance phonon scattering. Ru might not have isostructural phase [126][127] but it is a heavy element and has good solid solubility in Fe. However, there are a few major issues in using these materials: they are both expensive, toxic, have melting temperatures well over 2000 °C, and could be difficult and dangerous to arc-melt.
- The nonequilibrium processing via PLM provides a means of creating supersaturated matrices that would be otherwise impossible. For instance, isoelectronic/isostructural substitution of Sn into the SiGe alloy [128]. Sn has low solid solubility in the disilicide and DC phases. If a nonequilibrium technique like PLM were able to supersaturate Sn solute into the α matrix, it could then be directed into DC nanowires upon aging. However, it is not clear how competing, low solubility elements would arrange themselves during a eutectoid decomposition.

References

- [1] L.D. Zhao, S. Hao, S.H. Lo, C.I. Wu, X. Zhou, Y. Lee, H. Li, K. Biswas, T.P. Hogan, C. Uher, C. Wolverton, V.P. Dravid, M.G. Kanatzidis, High thermoelectric performance via hierarchical compositionally alloyed nanostructures, *J. Am. Chem. Soc.* 135 (2013) 7364–7370. doi:10.1021/ja403134b.
- [2] C.B. Vining, An inconvenient truth about thermoelectrics, *Nat. Mater.* 8 (2009) 83–85. doi:10.1038/nmat2361.
- [3] Z.G. Chen, G. Hana, L. Yanga, L. Cheng, J. Zou, Nanostructured thermoelectric materials: Current research and future challenge, *Prog. Nat. Sci. Mater. Int.* 22 (2012) 535–549. doi:10.1016/j.pnsc.2012.11.011.
- [4] T.B. Massalski, *Binary Alloy Phase Diagrams*, 2nd ed., ASM International, Materials Park, Ohio, 1990.
- [5] A. Kundu, N. Mingo, D.A. Broido, D.A. Stewart, Role of light and heavy embedded nanoparticles on the thermal conductivity of SiGe alloys, *Phys. Rev. B - Condens. Matter Mater. Phys.* 84 (2011) 125426-1-125426–5. doi:10.1103/PhysRevB.84.125426.
- [6] F.L.B.M. Redzuan, I. Mikio, T. Masatoshi, Synthesis of Co-doped β -FeSi₂/Si composites through eutectoid decomposition and its thermoelectric properties, *J. Mater. Sci.* 53 (2018) 7683–7690. doi:10.1007/s10853-018-2066-1.
- [7] M. Mohebbali, Y. Liu, L. Tayebi, J.S. Krasinski, D. Vashaee, Thermoelectric figure of merit of bulk FeSi₂-Si_{0.8}Ge_{0.2} nanocomposite and a comparison with β -FeSi₂, *Renew. Energy.* 74 (2015) 940–947. doi:10.1016/j.renene.2014.08.059.
- [8] P.E. Hopkins, Thermal Transport across Solid Interfaces with Nanoscale Imperfections: Effects of Roughness, Disorder, Dislocations, and Bonding on Thermal Boundary Conductance, *Thermal Transport across Solid Interfaces with Nanoscale Imperfections: Effects of Roughness*, *ISRN Mech. Eng.* 2013 (2013) 1–19. doi:10.1155/2013/682586.
- [9] LLNL Energy Flow Charts, Lawrence Livermore Natl. Lab. (2015). <https://flowcharts.llnl.gov/> (accessed January 29, 2016).
- [10] G.D. Mahan, J. Sofo, The best thermoelectric, *Proc. Natl. Acad. Sci. USA.* 93 (1996) 7436–7439.
- [11] G.J. Snyder, E.S. Toberer, Complex thermoelectric materials, *Nat. Mater.* 7 (2008) 105–114. doi:10.1038/nmat2090.
- [12] G. Tan, F. Shi, S. Hao, L.-D. Zhao, H. Chi, X. Zhang, C. Uher, C. Wolverton, V.P. Dravid, M.G. Kanatzidis, Non-equilibrium processing leads to record high thermoelectric figure of merit in PbTe–SrTe, *Nat. Commun.* 7 (2016) 1–9. doi:10.1038/nprot.2016.089.
- [13] G.J. Snyder, E.S. Toberer, Complex thermoelectric materials., *Nat. Mater.* 7 (2008) 105–114. doi:10.1038/nmat2090.
- [14] Z.H. Dughaish, Lead telluride as a thermoelectric material for thermoelectric power

- generation, *Phys. B Condens. Matter.* 322 (2002) 205–223. doi:10.1016/S0921-4526(02)01187-0.
- [15] J.P. Heremans, C.M. Thrush, D.T. Morelli, Thermopower enhancement in lead telluride nanostructures, *Phys. Rev. B - Condens. Matter Mater. Phys.* 70 (2004) 1–5. doi:10.1103/PhysRevB.70.115334.
- [16] X.B. Zhao, X.H. Ji, Y.H. Zhang, T.J. Zhu, J.P. Tu, X.B. Zhang, Bismuth telluride nanotubes and the effects on the thermoelectric properties of nanotube-containing nanocomposites, *Appl. Phys. Lett.* 86 (2005) 1–3. doi:10.1063/1.1863440.
- [17] B. Poudel, Q. Hao, Y. Ma, Y. Lan, A. Minnich, B. Yu, X. Yan, D. Wang, A. Muto, D. Vashaee, X. Chen, J. Liu, Dresselhaus, G. Chen, Z. Ren, High-Thermoelectric Performance of Nanostructured Bismuth Antimony Telluride Bulk Alloys, *Science* (80-.). 320 (2008) 634–638. doi:10.1126/science.1155140.
- [18] D.L. Medlin, G.J. Snyder, Interfaces in bulk thermoelectric materials, *Curr. Opin. Colloid Interface Sci.* 14 (2009) 226–235. doi:10.1016/j.cocis.2009.05.001.
- [19] M. Zebarjadi, K. Esfarjani, A. Shakouri, J. Bahk, Z. Bian, M. Zebarjadi, K. Esfarjani, A. Shakouri, J. Bahk, Z. Bian, Effect of nanoparticle scattering on thermoelectric power factor, *Appl. Phys. Lett.* 94 (2009) 1–3. doi:10.1063/1.3132057.
- [20] M. Zebarjadi, K. Esfarjani, Z. Bian, A. Shakouri, Low-Temperature Thermoelectric Power Factor Enhancement by Controlling Nanoparticle Size Distribution, *Nano Lett.* 11 (2011) 225–230. doi:10.1021/nl103581z.
- [21] J. Bahk, Z. Bian, M. Zebarjadi, P. Santhanam, R. Ram, A. Shakouri, J. Bahk, Z. Bian, M. Zebarjadi, P. Santhanam, R. Ram, Thermoelectric power factor enhancement by ionized nanoparticle scattering Thermoelectric power factor enhancement by ionized nanoparticle scattering, *Appl. Phys. Lett.* 99 (2011) 1–3. doi:10.1063/1.3625950.
- [22] M. Fanciulli, G. Weyer, H. Von Känel, N. Onda, Conversion electron Mössbauer spectroscopy study of iron silicide films grown by MBE, *Thin Solid Films.* 275 (1996) 8–11. doi:10.1088/0031-8949/1994/T54/003.
- [23] T.D. Hunt, K.J. Reeson, K.P. Homewood, S.W. Teon, R.M. Gwilliam, B.J. Sealy, Optical properties and phase transformations in α and β iron disilicide layers, *Nucl. Instruments Methods Phys. Res. Sect. B Beam Interact. with Mater. Atoms.* 84 (1994) 168–171. doi:10.1016/0168-583X(94)95747-9.
- [24] J. Tani, H. Kido, Hall Effect and Thermoelectric Properties of FeSi_x , *Jpn. J. Appl. Phys.* 39 (2000) 1054–1057. doi:10.1143/JJAP.39.1054.
- [25] I. Yamauchi, T. Nagase, I. Ohnaka, Eutectoid decomposition in Fe_2Si_5 based alloys with a small amount of 10(Pd, Pt) and 11(Cu, Ag, Au) group elements, *J. Mater. Sci.* 37 (2002) 1429–1435. doi:10.1023/A:1014545302508.
- [26] J. van Ek, P. Sterne, P. Turchi, Fe, Ru, and Os disilicides: Electronic structure of ordered compounds, *Phys. Rev. B.* 54 (1996) 7897–7908. doi:10.1103/PhysRevB.54.7897.
- [27] A. Heinrich, H. Griessmann, G. Behr, K. Ivanenko, J. Schumann, H. Vinzelberg,

- Thermoelectric properties of β -FeSi₂ single crystals and polycrystalline β -FeSi_{2+x} thin films, *Thin Solid Films*. 381 (2001) 287–295. doi:10.1016/S0040-6090(00)01758-2.
- [28] A.I. Al-Sharif, M. Abu-Jafar, A. Qteish, Structural and electronic structure properties of FeSi: The driving force behind the stability of the B20 phase, *J. Phys. Condens. Matter*. 13 (2001) 2807–2815. doi:10.1088/0953-8984/13/12/305.
- [29] S. Kiatgamolchai, S. Nilpairach, J. Wanichsampan, A. Thueploy, The effects of elements with different melting points on ϵ -FeSi size in FeSi₂ alloy, *J. Alloys Compd.* 666 (2016) 237–242. doi:10.1016/j.jallcom.2016.01.068.
- [30] J.M. Tomczak, K. Haule, G. Kotliar, Thermopower of the correlated narrow gap semiconductor FeSi and comparison to RuSi, 2013. doi:10.1007/978-94-007-4984-9_4.
- [31] T. Fromherz, G. Bauer, Energy gaps and band structure of SiGe and their temperature dependence, in: E. Kasper (Ed.), *Prop. Strained Relaxed Silicon Ger.*, INSPEC, London, United Kingdom, 1994: pp. 87–93.
- [32] T.E. Whall, E.H.C. Parker, Silicon-germanium heterostructures - advanced materials and devices for silicon technology, *J. Mater. Sci. Mater. Electron.* 6 (1995) 249–264. doi:10.1007/BF00125880.
- [33] D.A. Porter, K.E. Easterling, Alloy Solidification, in: *Phase Transform. Met. Alloy.*, 2nd ed., Chapman & Hall, London, United Kingdom, 1997: pp. 222–229.
- [34] W.A. Soffa, 8 – Diffusional Phase Transformations in the Solid State, 2014. doi:10.1016/B978-0-444-53770-6.00008-3.
- [35] J. Baker, J. Cahn, Solute trapping by rapid solidification, *Acta Metall.* 17 (1969) 575–578. doi:10.1016/0001-6160(69)90116-3.
- [36] C.B. Vining, Thermoelectric Properties of Silicides, in: R. D.M. (Ed.), *CRC Handb. Thermoelectr.*, CRC Press, Boca Raton, 1995. doi:10.1201/9781420049718.
- [37] J. Tani, H. Kiso, Thermoelectric Properties of β -Fe_{1-x}Co_xSi₂ Semiconductors, *Jpn. J. Appl. Phys.* 40 (2001) 3236–3239. doi:10.1143/JJAP.40.3236.
- [38] M. Ito, H. Nagai, E. Oda, S. Katsuyama, K. Majima, Effects of P doping on the thermoelectric properties of ??-FeSi₂, *J. Appl. Phys.* 91 (2002) 2138–2142. doi:10.1063/1.1436302.
- [39] T. Tsunoda, M. Mukaida, Y. Imai, Thermoelectric properties of Ru- or Ge-doped β -FeSi₂ films prepared by electron beam deposition, *Thin Solid Films*. 381 (2001) 296–302. doi:10.1016/S0040-6090(00)01759-4.
- [40] X. Qu, S. Lü, J. Hu, Q. Meng, Microstructure and thermoelectric properties of β -FeSi₂ ceramics fabricated by hot-pressing and spark plasma sintering, *J. Alloys Compd.* 509 (2011) 10217–10221. doi:10.1016/j.jallcom.2011.08.070.
- [41] I. Yamauchi, A. Suganuma, T. Okamoto, I. Ohnaka, Effects of Cu addition on the β -phase formation rate in Fe₂Si₅ thermoelectric materials, *J. Mater. Sci.* 32 (1997) 4603–4611. doi:10.1023/A:1004323930521.

- [42] T. Jun-ichi, H. Kido, Electrical Properties of Cr-Doped β -FeSi₂, *Jpn. J. Appl. Phys.* 38 (1999) 2717–2720.
- [43] U. Ail, S. Gorsse, S. Perumal, M. Prakasam, A. Umarji, S. Vives, P. Bellanger, R. Decourt, Thermal conductivity of β -FeSi₂ Si endogenous composites formed by the eutectoid decomposition of α -Fe₂Si₅, *J Mater Sci.* (2015) 6713–6718. doi:10.1007/s10853-015-9225-4.
- [44] T. Nagase, I. Yamauchi, I. Ohnaka, Eutectoid decomposition in rapidly solidified α -Fe₂Si₅-based thermoelectric alloys, *J. Alloys Compd.* 316 (2001) 212–219. doi:10.1016/S0925-8388(00)01453-5.
- [45] M. Abudakka, A. Nozariasbmarz, L. Tayebi, J.S. Krasinski, D. Vashaee, Development of Inexpensive SiGe–FeSi₂ Thermoelectric Nanocomposites, *Energy Harvest. Syst.* 2 (2015) 47–53.
- [46] A. Nozariasbmarz, Z. Zamanipour, P. Norouzzadeh, J.S. Krasinski, D. Vashaee, Enhanced thermoelectric performance in a metal/semiconductor nanocomposite of iron silicide/silicon germanium, *RSC Adv.* 6 (2016) 49643–49650. doi:10.1039/c6ra01947a.
- [47] H.Y. Chen, X.B. Zhao, E. Mueller, A. Mrotzek, Y.F. Lu, Microstructures and thermoelectric properties of Fe_{0.92}Mn_{0.08}Si_x alloys prepared by rapid solidification and hot pressing, *J. Appl. Phys.* 94 (2003) 6621–6626. doi:10.1063/1.1622773.
- [48] A. Bag, C. Mukherjee, S. Mallik, C.K. Maiti, Low Frequency Noise in Polycrystalline p- β -FeSi₂/Ge Heterojunction Solar Cells, 20th IEEE Int. Symp. Phys. Fail. Anal. Of Integrated Circuits. (2013) 377–380.
- [49] K. Noda, Y. Terai, Y. Fujiwara, Growth condition dependence of Ge-doped β -FeSi₂ epitaxial film by molecular beam epitaxy, *J. Cryst. Growth.* 378 (2013) 376–380. doi:10.1016/j.jcrysgro.2012.11.010.
- [50] H. Chen, P. Han, X.D. Huang, L.Q. Hu, Y. Shi, Y.D. Zheng, Semiconducting Ge–Si–Fe alloy grown on Si(100) substrate by reactive deposition epitaxy, *Appl. Phys. Lett.* 69 (1996) 1912. doi:10.1063/1.117619.
- [51] V. Raghavan, Fe-Ge-Si (Iron-Germanium-Silicon), *J. Phase Equilibria.* 23 (2002) 443–444.
- [52] G. Chen, *Nanoscale Energy Transport and Conversion: A Parallel Treatment of Electrons, Molecules, Phonons, and Photons*, Oxford University, New York, 2005.
- [53] N. Mingo, D. Hauser, N.P. Kobayashi, M. Plissonnier, A. Shakouri, Nanoparticle-in-alloy approach to efficient thermoelectrics: Silicides in SiGe, *Nano Lett.* 9 (2009) 711–715. doi:10.1021/nl8031982.
- [54] C. Dames, G. Chen, Theoretical phonon thermal conductivity of Si/Ge superlattice nanowires, *J. Appl. Phys.* 95 (2004) 682–693. doi:10.1063/1.1631734.
- [55] D. V. Papavassiliou, K. Bui, H. Nguyen, Thermal Boundary Resistance Effects in Carbon Nanotube Composite, in: N. Silvestre (Ed.), *Adv. Comput. Nanomechanics*, Wiley, Chichester, United Kingdom, 2015: p. 284.

- [56] H.J.T. Ellingham, Reducibility of oxides and sulfides in metallurgical processes, *J.Soc.Chem. Ind.* 63 (1944) 125.
http://web.mit.edu/2.813/www/readings/Ellingham_diagrams.pdf.
- [57] S.A. Speakman, X-ray Diffraction Shared Experimental Facility, MIT Cent. Mater. Sci. Eng. (n.d.).
- [58] L.B. McCusker, R.B. Von Dreele, D.E. Cox, D. Louër, P. Scardi, Rietveld refinement guidelines, *J. Appl. Crystallogr.* 32 (1999) 36–50. doi:10.1107/S0021889898009856.
- [59] P.W. Trimby, Orientation mapping of nanostructured materials using transmission Kikuchi diffraction in the scanning electron microscope, *Ultramicroscopy.* 120 (2012) 16–24. doi:10.1016/j.ultramic.2012.06.004.
- [60] G.G. Chernik, A Differential Scanning Calorimetry Study of a Binary System, *J. Colloid Interface Sci.* 141 (1991) 400–408. doi:[https://doi.org/10.1016/0021-9797\(91\)90336-7](https://doi.org/10.1016/0021-9797(91)90336-7).
- [61] J. Shawe, R. Riesen, J. Widmann, M. Schubnell, Interpreting DSC curves Part 1: Dynamic measurements, *UserCom.* (2000) 1–28.
- [62] L. Rycerz, Practical remarks concerning phase diagrams determination on the basis of differential scanning calorimetry measurements, *J. Therm. Anal. Calorim.* 113 (2013) 231–238. doi:10.1007/s10973-013-3097-0.
- [63] D.G. Cahill, Analysis of heat flow in layered structures for time-domain thermoreflectance, *Rev. Sci. Instrum.* 75 (2004) 5119–5122. doi:10.1063/1.1819431.
- [64] A.J. Schmidt, X. Chen, G. Chen, Pulse accumulation, radial heat conduction, and anisotropic thermal conductivity in pump-probe transient thermoreflectance, *Rev. Sci. Instrum.* 79 (2008) 114902–(1–9). doi:10.1063/1.3006335.
- [65] P.E. Hopkins, J.R. Serrano, L.M. Phinney, S.P. Kearney, T.W. Grasser, C.T. Harris, Criteria for Cross-Plane Dominated Thermal Transport in Multilayer Thin Film Systems During Modulated Laser Heating, *J. Heat Transfer.* 132 (2010) 081302–(1–10). doi:10.1115/1.4000993.
- [66] S. Alam, T. Nagai, Y. Matsui, Heat capacity study of β -FeSi₂ single crystals, *Phys. Lett. A.* 353 (2006) 516–518. doi:10.1016/j.physleta.2006.03.041.
- [67] W.E. Forsythe, Specific Heat of Various Solids, in: *Smithson. Phys. Tables*, 9th ed., The Smithsonian Institution, Washington DC, 1954: pp. 155–158.
- [68] I. Yamauchi, T. Nagase, I. Ohnaka, Temperature dependence of β -phase transformation in Cu added Fe₂Si₅ thermoelectric material, *J. Alloys Compd.* 292 (1999) 181–190. doi:10.1016/S0925-8388(99)00155-3.
- [69] D.E. Soffa, W.A., Laughlin, Diffusional Phase Transformations in the Solid State, in: D.E. Laughlin, K. Hono (Eds.), *Phys. Metall.*, 5th ed., 2014: pp. 851–1020. doi:10.1016/B978-0-444-53770-6.00008-3.
- [70] G. Sharma, R. V. Ramanujan, G.P. Tiwari, Instability mechanisms in lamellar microstructures, *Acta Mater.* 48 (2000) 875–889. doi:10.1016/S1359-6454(99)00378-X.

- [71] E. Werner, The spheroidization of thin plates, *Acta Metall.* 37 (1989) 2047–2053. doi:10.1016/0001-6160(89)90090-4.
- [72] M. Hillert, Diffusion controlled growth of lamellar eutectics and eutectoids in binary and ternary systems, *Acta Metall.* 19 (1971) 769–778. doi:10.1016/0001-6160(71)90133-7.
- [73] W.A. Tiller, Applicability of minimum rate of entropy production to the solidification of lamellar eutectics, *J. Appl. Phys.* 34 (1963) 3615–3617. doi:10.1063/1.1729267.
- [74] K. Nakajima, M. Apel, I. Steinbach, The role of carbon diffusion in ferrite on the kinetics of cooperative growth of pearlite: A multi-phase field study, *Acta Mater.* 54 (2006) 3665–3672. doi:10.1016/j.actamat.2006.03.050.
- [75] K. Ankit, A. Choudhury, C. Qin, S. Schulz, M. McDaniel, B. Nestler, Theoretical and numerical study of lamellar eutectoid growth influenced by volume diffusion, *Acta Mater.* 61 (2013) 4245–4253. <http://dx.doi.org/10.1016/j.actamat.2013.03.050>.
- [76] D. Turnbull, H.N. Treafits, Kinetics of precipitation of tin from lead-tin solid solutions, *Acta Metall.* 3 (1955) 43–54. doi:10.1016/0001-6160(55)90011-0.
- [77] J.W. Cahn, The kinetics of cellular segregation reactions, *Acta Metall.* 7 (1959) 18–28. doi:10.1016/0001-6160(59)90164-6.
- [78] J.M. Shapiro, J.S. Kirkaldy, Theory of Decomposition of Eutectoids Assuming Local Equilibrium and Phase Boundary Diffusion, *Acta Metall.* 16 (1968) 579–585. doi:10.1016/0001-6160(68)90132-6.
- [79] F.M. d’Heurle, P. Gas, Kinetics of formation of silicides: A review, *J. Mater. Res.* 1 (1986) 205–221. doi:10.1557/JMR.1986.0205.
- [80] Y. Wada, S. Nishimatsu, Grain Growth Mechanism of Heavily Phosphorus-Implanted Polycrystalline Silicon, *J. Electrochem. Soc.* 125 (1978) 1499–1504. doi:10.1149/1.2131703.
- [81] V.F. Zackay, H.I. Aaronson, eds., *Decomposition of Austenite by Diffusional Processes*, Interscience Publishers, New York, 1962.
- [82] M. Hillert, The Formation of Pearlite, in: J. Agren, Y. Brechet, C. Hutchinson, J. Philibert, G. Purdy (Eds.), *Thermodyn. Phase Transform. Sel. Work. Mats Hillert*, 1st ed., EDP Sciences, Les Ulis, 2006: pp. 179–231.
- [83] H.I. Aaronson, M. Enomoto, J.K. Lee, Pearlite Reaction, in: *Mech. Diffus. Phase Transform. Alloy.*, 1st ed., CRC Press, Boca Raton, 2010: pp. 575–599.
- [84] H.J. Lee, G. Spanos, G.J. Shiflet, H.I. Aaronson, Mechanisms of the bainite (non-lamellar eutectoid) reaction and a fundamental distinction between the bainite and pearlite (lamellar eutectoid) reactions, *Acta Metall.* 36 (1988) 1129–1140. doi:10.1016/0001-6160(88)90166-6.
- [85] Z. Wang, N. Mingo, Diameter dependence of SiGe nanowire thermal conductivity, *Appl. Phys. Lett.* 97 (2010) 24–26. doi:10.1063/1.3486171.
- [86] D. Li, Y. Wu, P. Kim, L. Shi, P. Yang, A. Majumdar, Thermal conductivity of individual

- silicon nanowires, *Appl. Phys. Lett.* 83 (2003) 2934–2936. doi:10.1063/1.1616981.
- [87] R. Cheaito, J.C. Duda, T.E. Beechem, K. Hattar, J.F. Ihlefeld, D.L. Medlin, M.A. Rodriguez, M.J. Champion, E.S. Piekos, P.E. Hopkins, Experimental investigation of size effects on the thermal conductivity of silicon-germanium alloy thin films, *Phys. Rev. Lett.* 109 (2012) 1–5. doi:10.1103/PhysRevLett.109.195901.
- [88] Z. Aksamija, I. Knezevic, Thermal conductivity of $\text{Si}_{1-x}\text{Ge}_x/\text{Si}_{1-y}\text{Ge}_y$ superlattices: Competition between interfacial and internal scattering, *Phys. Rev. B - Condens. Matter Mater. Phys.* 88 (2013) 155318. doi:10.1103/PhysRevB.88.155318.
- [89] B.M. Foley, H.J. Brown-shaklee, J.C. Duda, R. Cheaito, B.J. Gibbons, D. Medlin, F. Jon, P.E. Hopkins, B.J. Gibbons, D. Medlin, J.F. Ihlefeld, P.E. Hopkins, Thermal conductivity of nano-grained SrTiO_3 thin films, 231908 (2012) 1–4. doi:10.1063/1.4769448.
- [90] B.F. Donovan, B.M. Foley, J.F. Ihlefeld, J.-P. Maria, P.E. Hopkins, Spectral phonon scattering effects on the thermal conductivity of nano-grained barium titanate, *Appl. Phys. Lett.* 105 (2014) 082907. doi:10.1063/1.4893920.
- [91] B. Abeles, Lattice thermal conductivity of disordered semiconductor alloys at high temperatures, *Phys. Rev.* 131 (1963) 1906–1911. doi:10.1103/PhysRev.131.1906.
- [92] A.M. Marconnet, K.E. Goodson, From the Casimir Limit to Phononic Crystals : 20 Years of Phonon Transport Studies Using Silicon-on-Insulator Technology, *J. Heat Transfer.* 135 (2013) 1–10. doi:10.1115/1.4023577.
- [93] A.J.H. Mcgaughey, E.S. Landry, D.P. Sellan, C.H. Amon, A.J.H. Mcgaughey, E.S. Landry, D.P. Sellan, C.H. Amon, Size-dependent model for thin film and nanowire thermal conductivity, *Appl. Phys. Lett.* 99 (2011) 1–3. doi:10.1063/1.3644163.
- [94] E.T. Swartz, R.O. Pohl, Thermal boundary resistance, *Rev. Mod. Phys.* 61 (1989) 605–668. doi:10.1103/RevModPhys.61.605.
- [95] C. Monachon, L. Weber, C. Dames, Thermal Boundary Conductance :A Materials Science Perspective, *Annu. Rev. Mater. Res.* 46 (2016) 433–463. doi:10.1146/annurev-matsci-070115-031719.
- [96] N. Ye, J.P. Feser, S. Sadasivam, T.S. Fisher, T. Wang, C. Ni, A. Janotti, Thermal transport across metal silicide-silicon interfaces: An experimental comparison between epitaxial and nonepitaxial interfaces, *Phys. Rev. B.* 95 (2017) 1–9. doi:10.1103/PhysRevB.95.085430.
- [97] A. Giri, S.W. King, W.A. Lanford, A.B. Mei, D. Merrill, L. Li, R. Oviedo, J. Richards, D.H. Olson, J.L. Braun, J.T. Gaskins, F. Deangelis, A. Henry, P.E. Hopkins, Interfacial Defect Vibrations Enhance Thermal Transport in Amorphous Multilayers with Ultrahigh Thermal Boundary Conductance, *Adv. Mater.* 1804097 (2018) 1–6. doi:10.1002/adma.201804097.
- [98] M.N. Croker, R.S. Fidler, R.W. Smith, The Characterization of Eutectic Structures, *Proc. Roy. Soc. Lond. A.* 335 (1973) 15–37.
- [99] F. Kurz, Solidification Microstructure: Eutectic and Peritectic, in: *Fundam. Solidif., Third*

- Edit, Aedermansdorf, Switzerland, 1992: p. 94.
- [100] D.M. Stefanescu, Chapter 10: Solidification of Two-Phase Alloys - Micro-Scale Solidification, in: *Sci. Eng. Cast. Solidif.*, Third Edit, Springer, 2015: pp. 197–232.
- [101] H. Meco, R.E. Napolitano, Non-Equilibrium Solute Partitioning and Microstructure Formation in Rapidly Solidified Al-Sm Alloys, *Mater. Sci. Forum.* 539–543 (2007) 2810–2815. doi:10.4028/www.scientific.net/MSF.539-543.2810.
- [102] H. Herzog, Crystal structure, lattice parameters and liquidus-solidus curve of the SiGe system, in: E. Kasper (Ed.), *Prop. Strained Relaxed Silicon Ger.*, INSPEC, London, United Kingdom, 1995: pp. 49–52.
- [103] S.-M. Lee, D.G. Cahill, R. Venkatasubramanian, Thermal conductivity of Si–Ge superlattices, *Appl. Phys. Lett.* 70 (1997) 2957–2959. doi:10.1063/1.118755.
- [104] R. Braunstein, A.R. Moore, F. Herman, Intrinsic optical absorption in germanium-silicon alloys, *Phys. Rev.* 109 (1958) 695–710. doi:10.1103/PhysRev.109.695.
- [105] W.A. Jensen, N. Liu, E. Rosker, B.F. Donovan, B. Foley, P.E. Hopkins, J.A. Floro, Eutectoid transformations in Fe-Si Alloys for thermoelectric applications, *J. Alloys Compd.* 721 (2017) 705–711. doi:10.1016/j.jallcom.2017.06.023.
- [106] J.P. Freedman, X. Yu, R.F. Davis, A.J. Gellman, J.A. Malen, Thermal interface conductance across metal alloy – dielectric interfaces, 035309 (2016) 1–7. doi:10.1103/PhysRevB.93.035309.
- [107] A. Majumdar, P. Reddy, Role of electron-phonon coupling in thermal conductance of metal-nonmetal interfaces, *Appl. Phys. Lett.* 84 (2004) 4768–4770. doi:10.1063/1.1758301.
- [108] K.T. Regner, L.C. Wei, J.A. Malen, Interpretation of thermoreflectance measurements with a two-temperature model including non-surface heat deposition, *J. Appl. Phys.* 118 (2015) 235191. doi:10.1063/1.4937995.
- [109] D.G. Cahill, R.B. Wilson, Anisotropic failure of Fourier theory in time-domain thermoreflectance experiments, *Nat. Commun.* 5 (2014) 1–11. doi:10.1038/ncomms6075.
- [110] R.B. Wilson, J.P. Feser, G.T. Hohensee, D.G. Cahill, Two-channel model for nonequilibrium thermal transport in pump-probe experiments, *Phys. Rev. B - Condens. Matter Mater. Phys.* 88 (2013) 1–11. doi:10.1103/PhysRevB.88.144305.
- [111] M. V. Shugaev, C. Wu, O. Armbruster, A. Naghilou, N. Brouwer, D.S. Ivanov, T.J.-Y. Derrien, N.M. Bulgakova, W. Kautek, B. Rethfeld, L. V. Zhigilei, Fundamentals of ultrafast laser–material interaction, *MRS Bull.* 41 (2016) 960–968. doi:10.1557/mrs.2016.274.
- [112] S. Mahanty, Gouthama, Surface modification of Al–Si alloy by excimer laser pulse processing, *Mater. Chem. Phys.* 173 (2016) 192–199. doi:10.1016/j.matchemphys.2016.02.001.
- [113] D.E. Aspnes, A.A. Studna, Dielectric functions and optical parameters of Si, Ge, GaP,

- GaAs, GaSb, InP, InAs, and InSb from 1.5 to 6.0 eV, *Phys. Rev. B.* 27 (1983) 985–1008. doi:10.1103/PhysRevB.27.985.
- [114] R.K. Singh, J. Narayan, A Novel Method for Simulating Laser-Solid Interactions in Semiconductors and Layered Structures, *Mater. Sci. Eng. B.* 3 (1989) 217–230.
- [115] J.P. Kruth, L. Froyen, J. Van Vaerenbergh, P. Mercelis, M. Rombouts, B. Lauwers, Selective laser melting of iron-based powder, *J. Mater. Process. Technol.* 149 (2004) 616–622. doi:10.1016/j.jmatprotec.2003.11.051.
- [116] S.I. Dolgaev, A. V Simakin, V. V Voronov, G.A. Shafeev, F. Bozon-verduraz, Nanoparticles produced by laser ablation of solids in liquid environment, *Appl. Surf. Sci.* 186 (2002) 546–551. doi:https://doi.org/10.1016/S0169-4332(01)00634-1.
- [117] G.W. Yang, Laser ablation in liquids : Applications in the synthesis of nanocrystals, *Prog. Mater. Sci.* 52 (2007) 648–698. doi:10.1016/j.pmatsci.2006.10.016.
- [118] Periodic Table, WolframResearch. (2017). <http://periodictable.com/>.
- [119] D.. Eaglesham, M. Cerullo, Dislocation-Free Stranski-Krastanow Growth of Ge on Si(100), *Phys. Rev. Lett.* 64 (1990) 1943–1946. doi:10.1103/PhysRevLett.64.1943.
- [120] W.A. Jensen, N. Liu, B.F. Donovan, J.A. Tomko, P.E. Hopkins, J.A. Floro, Synthesis and thermal transport of eco-friendly Fe-Si-Ge alloys with eutectic/eutectoid microstructure, *Mater. Chem. Phys.* 207 (2017) 67–75. doi:10.1016/j.matchemphys.2017.12.038.
- [121] N. Liu, W.A. Jensen, M. Zebarjadi, J.A. Floro, Tunable β -FeSi₂ – Si_{1-y}Ge_y nanocomposites by a novel React/Transform Spark Plasma Sintering approach for thermoelectric applications, *Mater. Today Phys.* 4 (2018) 19–27. doi:10.1016/j.mtphys.2018.02.004.
- [122] T. Sadoh, Y. Murakami, A. Kenjo, T. Enokida, T. Yoshitake, Strain in β -FeSi₂ modulated by Ge segregation in solid-phase growth of [a-Si/a-FeSiGe]_n stacked structure, *Appl. Surf. Sci.* 237 (2004) 146–149. doi:10.1016/j.apsusc.2004.06.059.
- [123] T. Sadoh, M. Owatari, Y. Murakami, a. Kenjo, T. Yoshitake, M. Itakura, T. Enokida, M. Miyao, Formation of SiGe/??-FeSi₂ superstructures from amorphous Si/FeSiGe layers, *Thin Solid Films.* 461 (2004) 77–80. doi:10.1016/j.tsf.2004.02.068.
- [124] T. Sadoh, M. Owatari, Y. Murakami, A. Kenjo, T. Yoshitake, M. Itakura, T. Enokida, M. Miyao, Formation of SiGe/ β -FeSi₂ superstructures from amorphous Si/FeSiGe layers, *Thin Solid Films.* 461 (2004) 77–80. doi:10.1016/j.tsf.2004.02.068.
- [125] Y. Gao, H.W. Liu, Y. Lin, G. Shao, Fabrication and characterization of novel Fe(Os)Si₂ semiconductor, *Phys. Procedia.* 11 (2011) 75–78. doi:10.1016/j.phpro.2011.01.016.
- [126] V.L. Shaposhnikov, A.B. Filonov, A. V. Krivosheeva, L.I. Ivanenko, V.E. Borisenko, Structural , electronic and optical properties of a new binary phase – ruthenium disilicide, *Phys. Status Solidi.* 242 (2005) 2864–2871. doi:10.1002/pssb.200440108.
- [127] V.L. Shaposhnikov, Electronic properties of isostructural ruthenium and osmium silicides and germanides, *Phys. Rev. B.* 60 (1999) 16494–16498. doi:10.1103/PhysRevB.60.16494.

- [128] S. Wirths, D. Buca, S. Mantl, Si-Ge-Sn alloys: From growth to applications, *Prog. Cryst. Growth Charact. Mater.* 62 (2016) 1–39. doi:10.1016/j.pcrysgrow.2015.11.001.

Appendix 1: Procedures for Mounting a Melt-Spun Ribbon in Epoxy

Mounting ribbons in epoxy is a nontrivial process, and cannot be done with the same methods as the bulk material. A few of the challenges to overcome are: 1) the ribbons are extremely brittle and should only be handled with vacuum tweezers, 2) the epoxy is denser than the Fe-Si-Ge ribbons, so they will “float away” if not properly secured, and 3) the Buehler brand disposable molds do not have flat bottoms, and cause the polished surface normal to be too far unaligned from the growth direction to accurately observe eutectic structures. The following methods produce viable samples and were found through trial and error.

Mounting Procedures

1. 1” diameter cylinder mold (Buehler), which can be used in standardized holders for SEM, EBSD, plasma cleaners, etc.
 - a. First score the bottom-inside of the plastic mold, otherwise the superglue will not stick to the plastic.
 - b. Use Crystalbond to fix a ribbon to a broken shard of a Si wafer (diameter < 1”). Make sure that the ribbon concavity is facing up, press the ribbon flat, and cool the wafer so that the Crystalbond hardens. The ribbon might break when flattened, but this is acceptable as it increases the polishable surface area.
 - b. With the ribbon facing up, superglue the bottom of the Si shard to the bottom-inside of the mold. This creates a flat surface for future polishing.
 - i. Sandwiching the ribbon between the plastic and the Si shard does not create a secure epoxy base. The only thing holding the ribbon to the mount is the Crystalbond and it will not survive the polishing process.

- c. Fill the mold with correctly measured epoxy with Ni conducting filler. Let the mold set overnight.
 - d. Now, we need to polish through the Si wafer to the ribbon. Start with 800 grit paper until the Si wafer starts to “disappear”, then polish with 1200 grit until scratches appear on the ribbon.
 - e. Polish with fine alumina (0.3 μm) and diamond suspensions (0.05 nm) as described in Appendix 3.
2. The second method is simpler and produces a smaller epoxy mount.
- a. From a solid strip of staples, break off a large section. Then break off another section that is just small enough to fit tightly inside the first when rotated 90°. This makes a tight square mold made by still connected staple sections.
 - b. Superglue the ribbons to the bottom and fill with conducting epoxy.
 - c. Polish with 800 grit paper until the ribbon is revealed. Then follow the polishing procedure in Appendix 3.
 - d. The other side of the mount will not be flat, and should be ground away using 360 grit paper. Make sure to polish everything flat.

Appendix 2: Procedure for Rietveld Refinement

The procedure for Rietveld is as follows.

1. The first step is to take high-resolution XRD data. For the PANalytical X'pert Pro, we found that there were insignificant differences in lattice parameters and volume fractions from 2 - 12 hours long scans at the smallest step size ($0.008^\circ 2\theta$). The Empyrean is an inherently better machine and is capable of obtaining pristine spectrums, far better than what was possible with the X'pert, in a quarter of the time. It should be noted that Rietveld

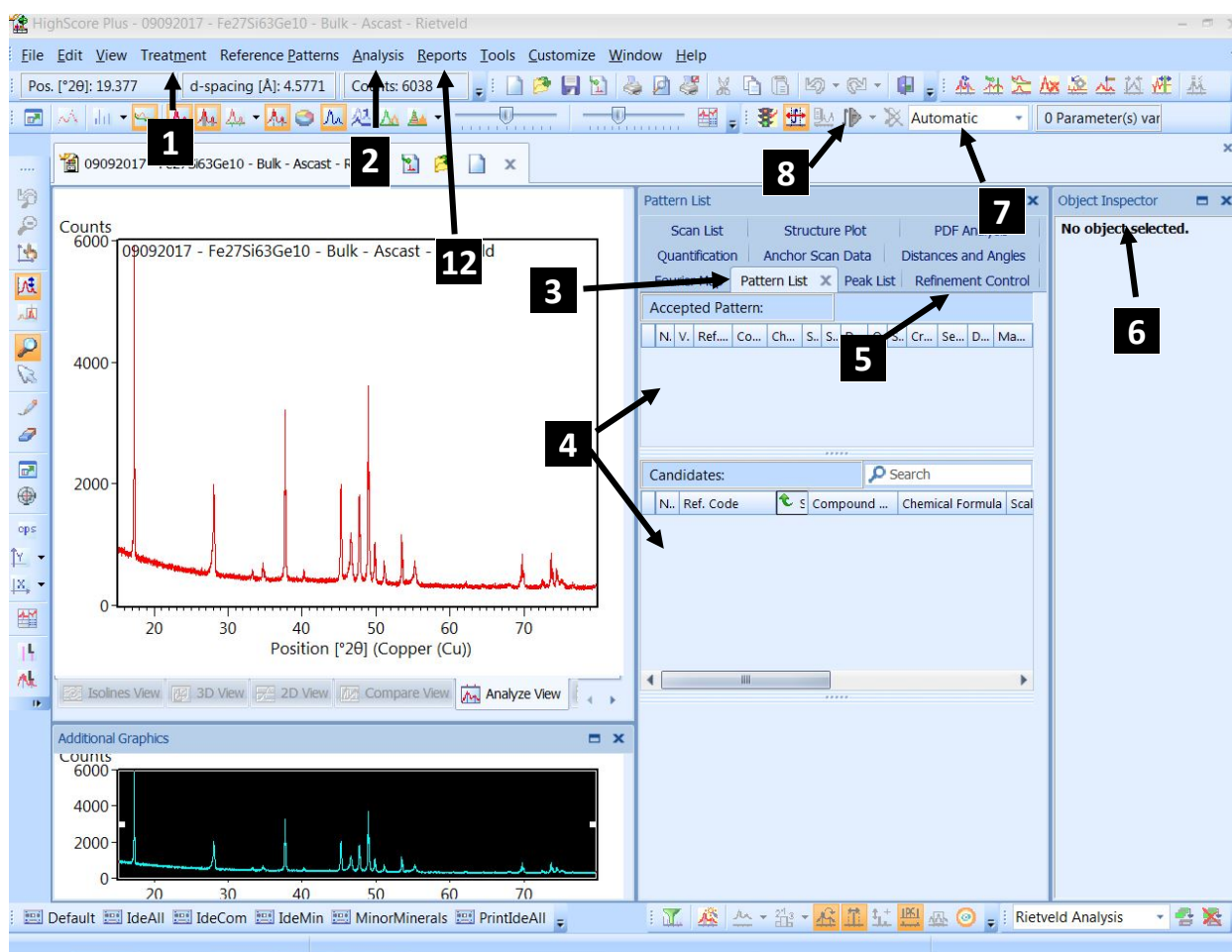


Figure A2.1: The HighScore Plus program, with important tabs and windows marked for reference.

refinement data was taken on the inferior machine, but should have no impact on our values or interpretation.

- a. Perform a high-resolution scan by using the lowest step size and high scan step times. Several peaks for each phase are required, so a broad scan across $15 - 100^\circ$ 2θ is ideal.
 - b. The program is not intuitive, so Figures A2.1 and Figure A2.2 are labeled with numbers that correspond to major windows and tabs in the following steps.
2. The .XDML file is the proprietary file extension from PANalytical and can be loaded into their proprietary software “HighScore Plus”.
- a. First identify the background, which is found under the “Treatment” tab (1) and is called “Determine Background”.
 1. On the new popup window click the “Manual” tab, click the “Use cubic spline Interpolation”. This fits the base points with a cubic spline.
 2. Add and Move base points until the dark green interpolation line is in the middle of the background noise and accurately fits the entire baseline. Accept the background, but **DO NOT “SUBTRACT”**. Subtracting the background causes subtle shifts in peak positions.
 - b. Next identify peak positions, which is found under the “Treatment” tab (1) and called “Search Peaks”.
 1. Change the “Minimum significance” value so that all clearly defined peaks are marked, and that random noise is not erroneously marked as peaks. Then click “Accept”.

- c. Under the “Analysis” tab (2), expand “Search and Match”, and click “Execute Search and Match”
 1. Click “Edit” under the “Restrictions”, which will open up a periodic table. Click Fe, Si, and Ge until they fall under the colored category of “Possible elements” and the other elements are under “None of”. The program will now only search for crystal structures that have any combination of Fe, Si, and Ge.
 2. Click on the “Quality” tab, and make sure “Skip patterns without structure data” is selected. The returned PDF4’s will automatically have structural data so creating your own from Wyckoff numbers is not required.
 3. Click the “Close” button. On the “Search and Match” window, click “Search”.
 4. When the search is complete, the “OK” button must be pressed, or you will not be able to interact with the rest of the program.
 5. Under the “Pattern Search” tab and window (3), HighScore will give you back hundreds of possible matches from the PDF4 database, this is organized according to a score. This value indicates how well it matches the measured spectrum, but does not mean that it is the best choice. **DO NOT BLINDLY ACCEPT HIGHSCORE PLUS!**
 6. Drag phases from “Candidates” to the “Accepted Patterns” window (4) until all the peaks are accounted for.

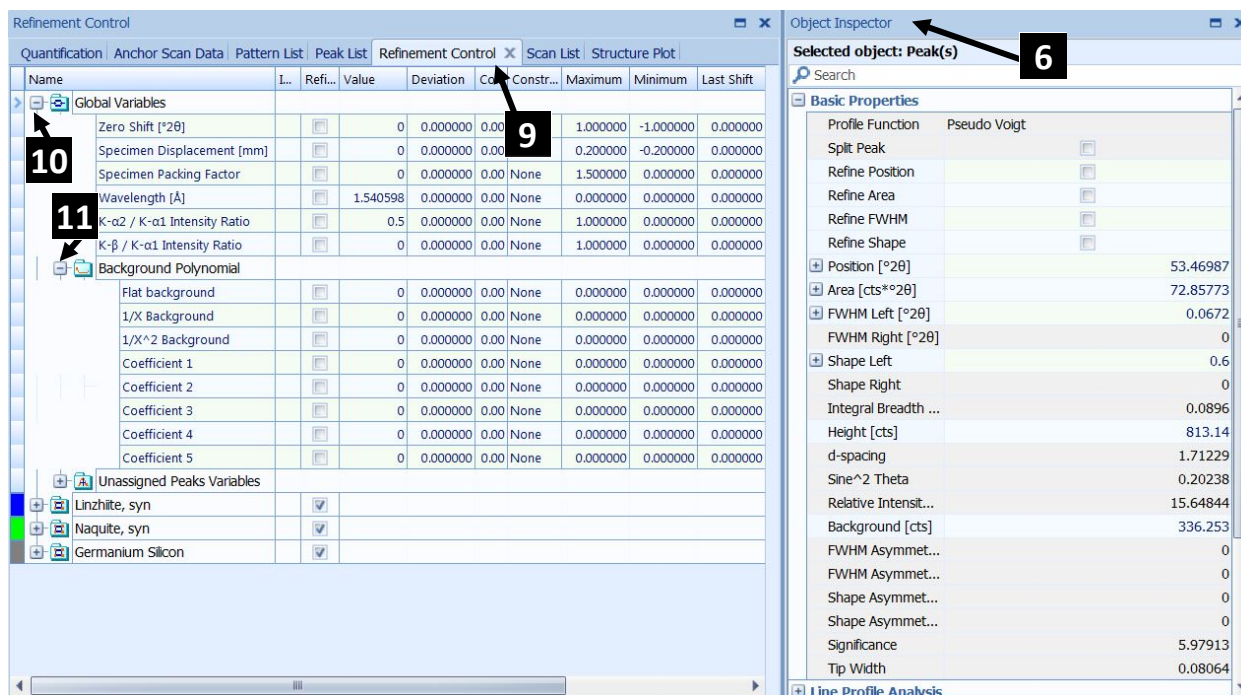


Figure A2.2: Expanded “Refinement Control” and “Object Inspector” windows.

7. Select all the phases, right mouse click, and select “Convert Pattern to Phase”.
8. Save your file as a .HPF in case there is an issue with the refinement.
 - d. Now click on the “Refinement Control” tab in the center window (5) and expand the “Object Inspector” window (6).
 - e. In the top tabs, turn “Automatic” to “Manual” (7).
 - f. If desired, the HKL or 2θ of each peak can be labeled at this point.
3. Step one of refinement, remove the background. There are two ways that this can be done, and are described by an online powerpoint procedure made by MIT [57]. I prefer their manual fit as this method produces better results and. For the sake of explanation, whenever a parameter is selected, click the refine button (8), and from here on it will be assumed that refining occurs after every step.

- a. First right mouse click and anywhere in the “Refinement Control” window (9), expand “Refine All” and select “Scale Factors”. This will scale the theoretical peaks, which now appear on the plot as a blue fit line as opposed to the red measured data.
 - b. Expand the “Global Variables” tab (10), then expand the “Background Polynomial” tab (11). And select the “Flat background” button.
 - c. Click “1/X Background”.
 - d. Then “Coefficient 1”.
 - e. Then “Coefficient 2”.
 - f. Manually check that the background fit (black line) is within the noise. If it is, move on to the next step, if it isn't this means the background of your data is bad, possibly due to poor mounting and the data should be scanned again.
4. Back in the “Refinement Control” window (9), under the “Global Variables” tab (10), click the “Specimen Displacement [mm]” button. This accounts for any vertical offset from sample in the holder, and is very powerful. Powder Si standards were purposefully offset and this function aligned it the peaks perfectly. How this is achieved mathematically is not known. Try to properly align your samples anyway.
 5. Next comes the refinement steps which are accessed by right clicking over the “Refinement Control” window (9) and expanding the “Refine All” tab. Remember to refine (8) after each parameter is selected and check the theoretical fit on the plot and also the goodness of fit (GOF). To find the GOF, click on the “Global Variables” tab (10) and it is located on the “Object Investigator” windows (6).

- a. “Scale Factors” again, this determines the amplitude of the peaks. Peak amplitudes are not necessarily the same over multiple scans, but that is not important.
- b. “Cells”, this uses the structural data to recreate the spectrum and vary lattice parameters to fit the data. If an alloy that follows Vegard’s law is analyzed, it is possible to manually change the lattice parameters (to your predicted values) by expanding that phase’s tab and changing the values under “Unit Cell”. This is dangerous so keep an eye on the fit line.
- c. “U’s”, “W’s”, and “V’s” are Cagliotti parameters and are used to fit the full-width half-max. Refine after each selection.
- d. “Pref. Orientation Parameter”, if the sample is powdered or has fine grains, texture should not be an issue. Click this button anyway as it fits the intensity well. However, if one peak is significantly smaller or larger than the other and is not being properly fitted, click on the problematic phase, go to the “Object Inspector” window (6), and go the “Preferred Orientation” section and manually adjust the problematic hkl orientations. If it is over fitted, decrease the “Parameter (March/Dollase)” value, if it is under-fitted increase it.
- e. “Asymmetry Parameters”, this accounts for asymmetry in the peak. Occasionally this will mess up one side of the peak fitting. Keep an eye on it.
- f. Peak shape 1, changes an unknown parameter to change peak shape. This usually makes the fit better.
- g. Peak Shape 2, not sure what the difference is from peak shape 1, usually doesn’t do anything.

Appendix 3: Mirror-Shine Polish Procedures

1. This is a standard mirror-shine polishing procedure. After each polishing cycle, rinse the sample surface, air dry, and observe under an optical microscope. If all scratches are parallel move down to the next grit, otherwise do the same grit over. Do each step for ~ 2 min. Always rotate the sample 90° from the last polish. If large scratches are still visible after going down a grit size, go back to the prior grit and polish again. The Fe-Si-Ge alloys are hard, but do not need any more pressure than the weight of your hand. Each polishing step is roughly an order of magnitude decrease in particles diameter.
 - a. When using the grinding paper, have the wheel rotate at 200 RPM with water constantly flowing over the surface. Before the 2 minutes are over, **DO NOT LOOK AT THE SAMPLE AND THEN CONTINUE POLISHING.** The pressure of your hand on the sample will be different and will cause a new, angled polish surface to appear. It is very noticeable.
 - i. Use 360 grit on the polishing wheel to remove any macroscopic inconsistencies.
 - ii. Then, if the sample surface was already relatively smooth, polish with 800 grit paper.
 - iii. Then 1200 grit paper.
 - b. For the suspension polish, do not run water over the cloth while polishing, and spray new suspension on the cloth occasionally. Turn the speed down to 80 RPM
 - i. Run water over the cloth to dampen it, run your finger across the surface to dislodge coarse particles and to feel for anything that will cause scratches, dry at 1000 RPM.

- ii. Polish with 0.3 μm Alumina powder, make a thick slurry and use liberally.
Every 45 sec or so add more slurry to the cloth.
 - 1. Alumina sticks to the sample surface, so turn on the water and run the sample against the cloth for one minute, with periodic rinses.
 - iii. If scratches are not, or barely noticeable, move one to 0.05 diamond spray.
Similarly spray more suspension onto the cloth every ~ 45 sec. Clean the surface.
- c. To obtain a deformationless surface for EBSD:
- i. Ion polishing is *not* recommended on aged samples, as the Ar ions preferentially etch the high interface density and roughens the surface.
 - ii. Vibratory polish has been shown to work.
 - 1. Fill the basin with 0.05 μm colloidal Si, and tune the frequency so that the sample makes ~ 10 complete rotations per minute. Allow the sample to polish for 2 hours. Clean the sample surface by rubbing it against a clean polishing cloth under running water for several minutes.

Appendix 4: Preliminary TEM

Preliminary TEM Microscopy was performed on an SPS disk made from $\text{Fe}_{21.4}\text{Si}_{71.5}\text{Ge}_5\text{Co}_{2.1}$ that was aged at 680 C for 10 hours. A disk of ~ 1 mm thickness was made by using the department's vibratory disk punch. The disk was then mechanically thinned with 1200 grit paper to ~ 200 μm , and then dimpled using 0.3 μm diamond spray. The disk was then ion milled for ~ 3 hours with

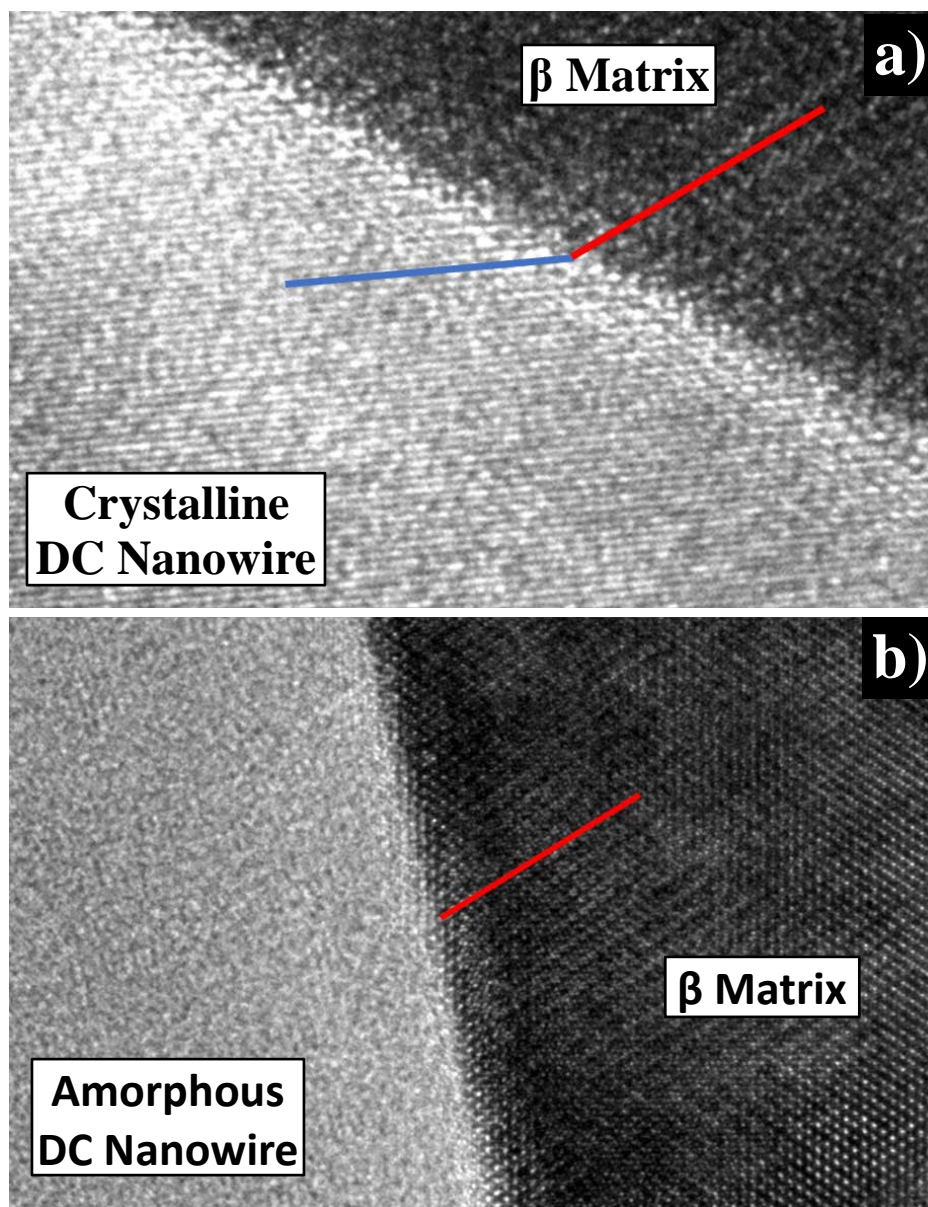


Figure A4.1: TEM images with an unknown scale bar, showing the sharp interface between the β matrix and a) the crystalline DC nanowire and b) the amorphous DC nanowire. The colored lines are oriented along atom rows.

guns at 10° (top) and 5° (bottom). After a hole pierced the sample, the angles were reduced to 5° and 2° respectively, and the sample was milled for another hour. The stage was cooled with liquid nitrogen to suppress beam-induced phase transformations.

The following images do not have scale bars, but regardless there is still some important information to be gleaned. TKD-EBSD (Chapter 3) observed the grain orientation of the DC nanowires and β matrix. While the β matrix had an excellent signal, the DC was for the most part illegible. These TEM images suggest that the issue is not caused by instrument limitation. In Figure A4.1.a atomic planes (red and blue lines) are clearly seen on either side of the sharp interface

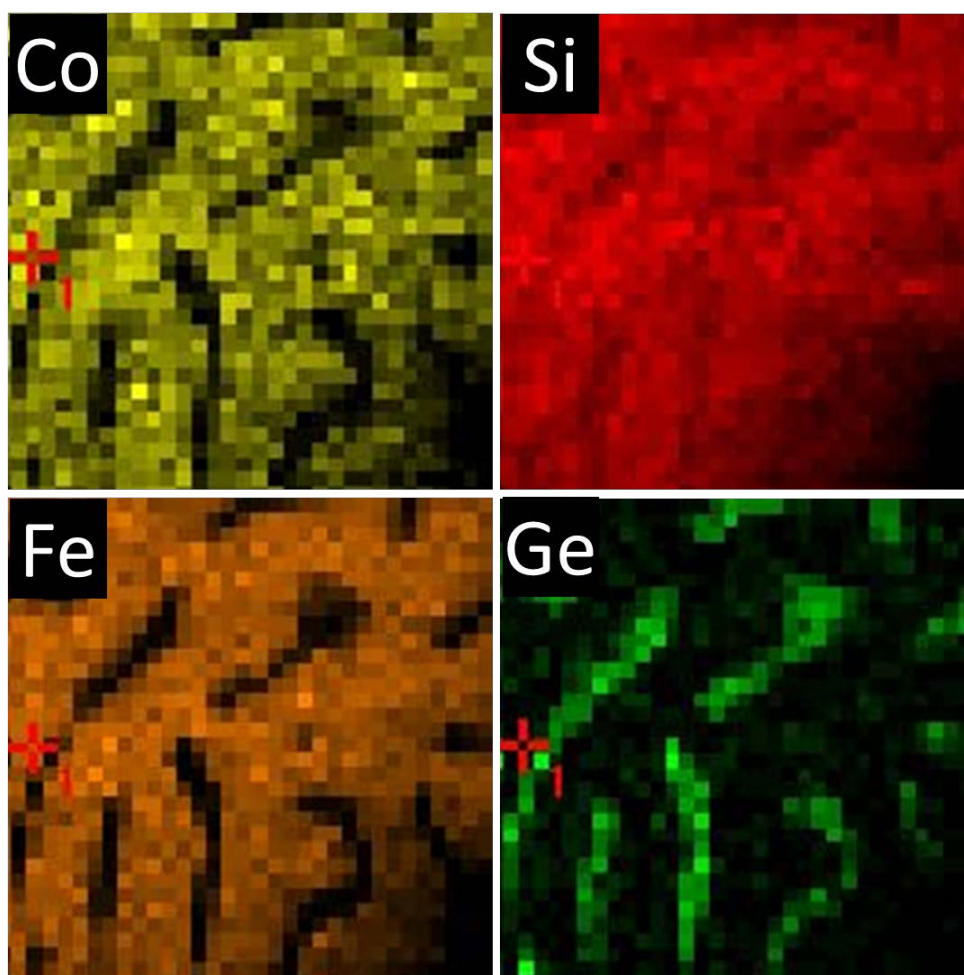


Figure A4.2: TEM-EDS map depicting the disposition of constituent elements. Ge disposition is mostly inside the nanowires, because it was ejected during the eutectoid phase transformation. It should also be noted that Co substitutes Fe sites in the β matrix.

between β matrix (dark phase) and DC nanowires (light phase). However, in Figure A4.1.b no such order can be found in the DC nanowire, and suggests that the phase has been amorphized during the ion mill process. A TEM-EDS map (Figure A.4.2) was taken and corroborates what we found in TKD-EDS, that the β matrix is mostly free of Ge as it has segregated into the nanowires. Co doping also shows that it stays within the β matrix.

Appendix 5: Callaway-Debye Model and Size Effect

To explain the decrease in thermal conductivity that occurred beyond bulk and alloy scattering, we used thermal boundary conductance to treat each interface as an additional phonon scattering location. Another way at looking at the decrease in κ is due to a “size effect”, which occurs when phonon mean free paths are longer than the width of a nanowire. Using the Callaway-Debye model, we calculated the thermal conductivities with our measured nanowire sizes and compositions. The following equations and their values were taken from Wang and Mingo [85] and the mathematical model was reproduced in MATLAB. The thermal conductivity is described by

$$\kappa = \frac{k_B^4 T^3}{2\pi^2 v_b \hbar^3} \int_0^{\frac{\hbar\omega_c}{k_B T}} \tau(T, y) y^4 \frac{e^y}{(e^y - 1)^2} dy \quad A5-1$$

where, k_B is the Boltzmann’s constant, \hbar is the reduced Plank’s constant, T is the Temperature, ω_c is the frequency cutoff, and v_b is the speed of sound through the solid material, and τ is the scattering rate. By using Matthiessen’s equation, τ can be split into its constituent scattering rates: Umklapp, alloy, and boundary scattering. The following equations are all used to determine the scattering rate,

$$\frac{1}{\tau} = \frac{1}{\tau_{Umklapp}} + \frac{1}{\tau_{Alloy}} + \frac{1}{\tau_{Boundary}} \quad A5-2$$

$$\frac{1}{\tau_{Umklapp}} = (1 - x) \frac{1}{\tau_{U, Si}} + x \frac{1}{\tau_{U, Ge}} \quad A5-3$$

$$\frac{1}{\tau_{U, Si}} = B_{Si} \omega^2 T e^{\frac{C_{Si}}{T}} \quad A5-4$$

$$\frac{1}{\tau_{U, Ge}} = B_{Ge} \omega^2 T e^{\frac{C_{Ge}}{T}} \quad A5-5$$

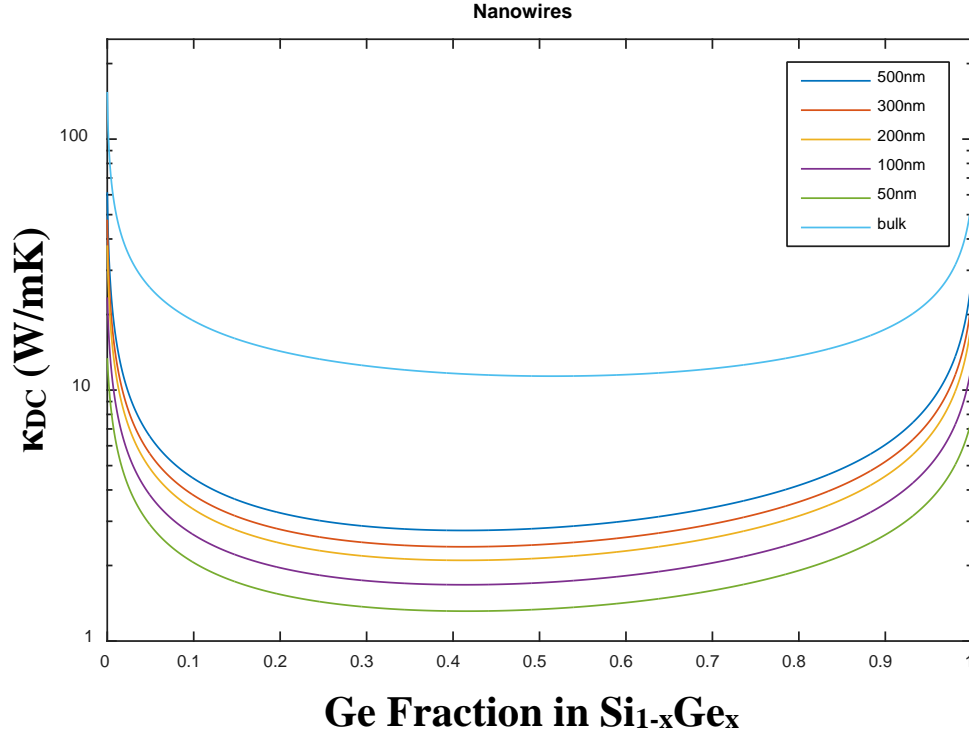


Figure A5.1: Plot using the Callaway-Debye model to show the effects on Ge fraction and lengthscale of SiGe nanowires on thermal conductivity.

$$\frac{1}{\tau_{Alloy}} = x(1-x)A\omega^4 \quad \text{A5-6}$$

$$\frac{1}{\tau_{Boundary}} = \frac{v_b}{D} \quad \text{A5-7}$$

where x is the atomic fraction of Ge, $\frac{1}{\tau_{U,Si/Ge}}$ are the individual Umklapp scattering rates of pure Si or Ge and are weighted by atomic fraction in Equation A5.3; A , B , and C are parameters that are adjusted to fit experimental data, and D is the nanowire diameter. By plugging these Equations A5.2 - A5.7 into Equation A5-1 and using MATLAB to solve the integral and plot κ as a function of Ge with several D values, we obtained Figure A5.1. This figure shows both the effects of alloy scattering on thermal conductivity, and also the dependence of nanowire width on κ . Plugging in the newly calculated κ_{DC} values into

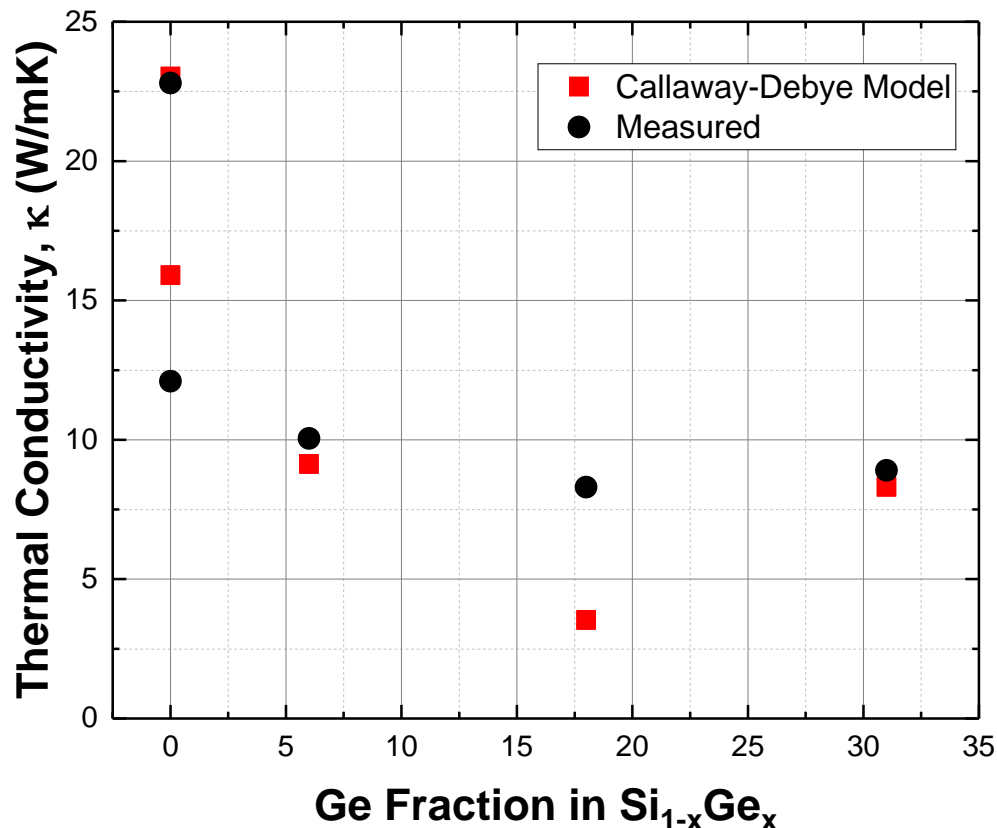


Figure A5.2: Comparison of thermal conductivities predicted by the Callaway-Debye model and measurements taken via TDTR.

$$\frac{1}{\kappa_T} = \frac{f_\beta}{\kappa_\beta} + \frac{f_{DC}}{\kappa_{DC}} \quad \text{A5.8}$$

where f_β and f_{DC} are the volume fractions and κ_β is thermal conductivity of β calculated in Chapter 3. From Figure A5.2, we can see that the model approximates our measured thermal conductivities reasonably well. This shows that, even though size effect and thermal boundary conduction take a different approach to model the heat transfer of nanostructured materials, both can reasonable model the system. For reasons that are not understood, the nanostructured Binary $\text{Fe}_{28.4}\text{Si}_{71.6} + 567$ °C/56 hr sample and rapid-cool + 567 °C/56 hr sample are under and overestimated respectively. It is currently unclear what features could be causing these discrepancies and would require more in-depth modeling and experimentation, which goes beyond the scope of this project.

Appendix 6: 2D to 3D Interface Density – Geometric Correction Factor

A6.1 Nanowires to Lamellae

The interface density was calculated by the linear intercepts method, as described in Chapter 2.2.2.3. This method approximates the 2D interface density; however, our materials consists of three-dimensional inclusions (nanowires and lamellae). To account for this discrepancy, we estimated a geometric correction factor, by creating a simple model to calculate the interface density of nanowires and lamellae in 2D and 3D, Figure A6.1. In 2D, both lamella and nanowire are identical; difference in interface density do not appear until the nano inclusions are expanded into the third dimension. When the inclusion thickness (t) and width (w) are similar, we call it a nanowire; when $t \gg w$ we call it a lamella. By finding the ratio of surface area to volume for 3D,

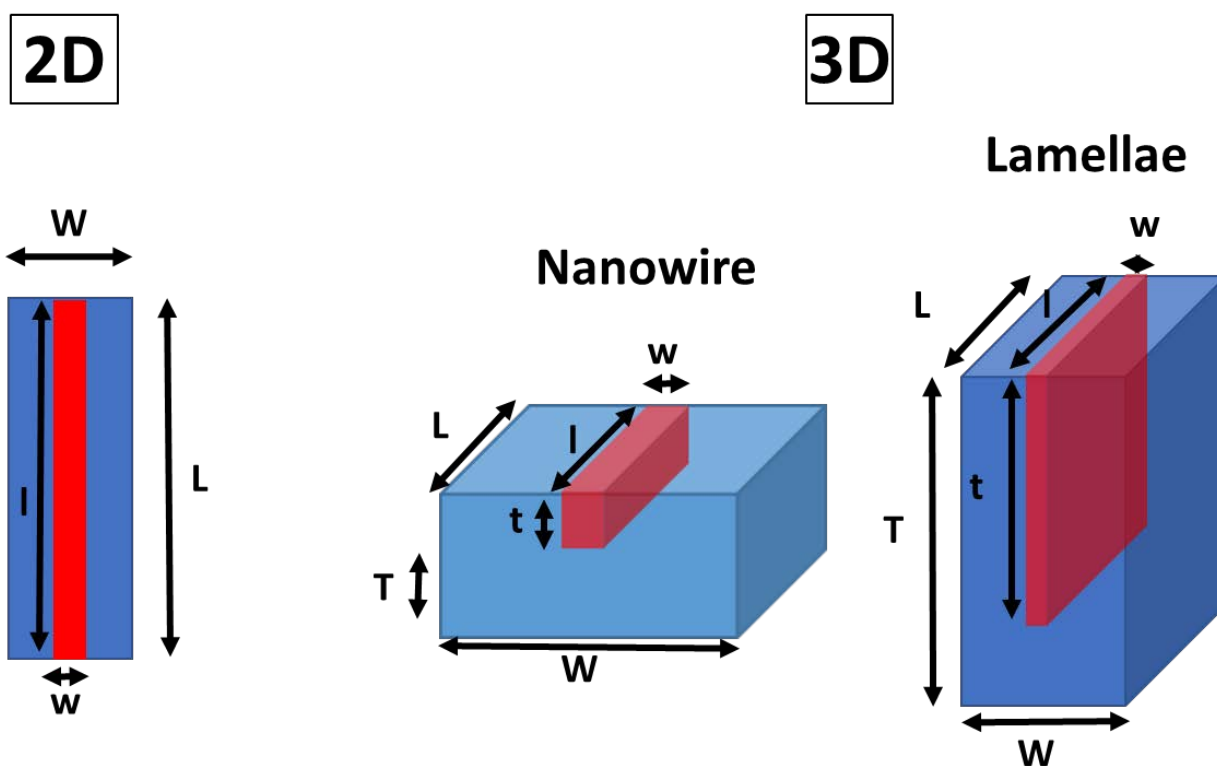


Figure A6.1: Simplified model to determine a) the perimeter to area ratio of a 2D system and b) the surface area to volume ratio for a 3D system. The dimensions of the Si inclusions and the β matrix are labeled.

or perimeter to area for 2D, systems, we can estimate a geometric correction factor to convert our measured values to the 3D value. In 2D space the Si inclusion and the β -FeSi₂ matrix are both rectangles, and the interface density is simply,

$$\rho_{int} = \frac{\text{Perimeter}}{\text{Total Area}} = \frac{2(lw)}{LW} \quad \text{A6-1}$$

where l and L are the lengths of the DC inclusion and matrix, and w and W are the widths of the DC inclusion and matrix, respectively.

In 3D space, the inclusion and matrix are now boxes, and the interface density is now the ratio of the surface area to the total volume,

$$\rho_{int} = \frac{\text{Surface Area}}{\text{Total Volume}} = \frac{2lw+2wt+2tl}{LWT} \quad \text{A6-2}$$

T denotes the inclusion thickness and T the thickness of the β matrix. It is important that the volume fraction stays constant, regardless of the size of the inclusion and matrix, so to achieve this W and T are both functions of volume fraction of DC (f_{DC}), or area fraction. This value was constant at our measured value of 0.86 for nanostructured Fe_{28.4}Si_{17.6}. The following equations were used to vary the dimensions according to f_{DC} .

$$f_{Si} = \frac{V_{DC}}{V_{\beta} + V_{DC}} \quad \text{A6-3}$$

$$W = \frac{lw}{f_{DC}L} \quad \text{A6-4}$$

$$T = \frac{lwt}{f_{DC}LW} \quad \text{A6-5}$$

where V is the volume of the nanoconstituent. Equations A6-1 and A6-2, with the adjusted matrix dimensions (Equations A6-3 – A6.5) were plotted as a function of t . Figure A6.2 shows the 2D and 3D interface densities for our model. We can see that the 2D model closely approximates the 3D interface density of lamellae; this makes sense as the integration over a uniform 3D volume is approximated by the 2D area, granted that each two-dimensional slice is identical to the 2D area. However, when t approaches w (nanowire), we see a dramatic increase of interface density. The geometric correction factor is simply $x = \frac{\rho_{3D}}{\rho_{2D}}$ and was found that $x = 2$ for nanowires. There are also two asymptotes in this plot, which corresponds to the $\frac{Surface\ Area}{Volume}$ ratio of the inclusion, one

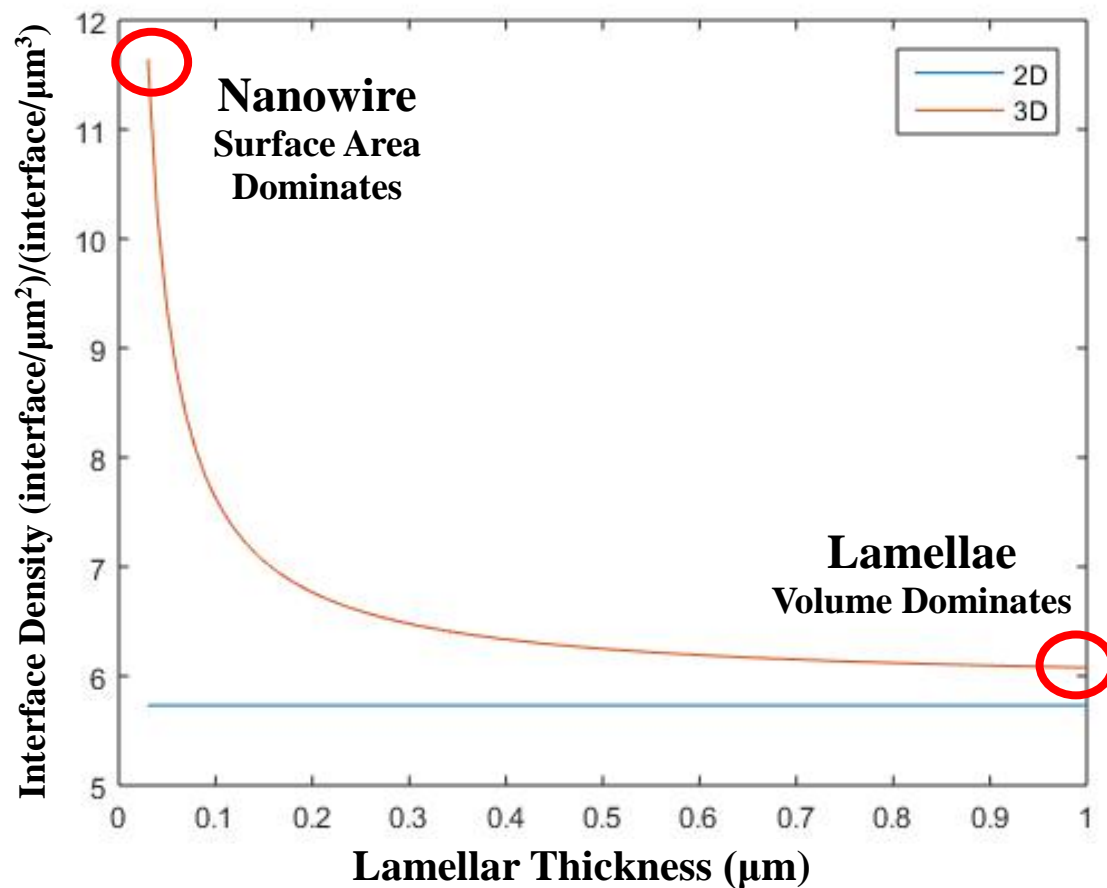


Figure A6.2: Plot of 2D and 3D models showing the change in interface density as a function of inclusion thickness, ranging from large (lamellae) to small (nanowire). The geometric correction factor at $0.03\ \mu\text{m}$ is 2.

where the surface area dominates (nanowire) and the other where the volume dominates (lamella). Interestingly, what is being shown in Figure A6.2 is the reason why we want to nanostructure materials; smaller particles have a more interfacial area per volume, and interface scattering effects become prevalent.

A.6.2 Spheroids

Most of our processing parameters produced fine nanowires (Chapters 3 and 4), but we also investigated coarsened samples where the nanowires had decomposed into spheroids. A similar model was created substituting equations (volume, area, surface area, etc.) for rectangles for those of spheres. The previous equations were then modified to find the area, circumference and volume of a circle or sphere:

$$W = \frac{\pi r^2}{f_{DC}L} \quad \text{A6-6}$$

$$T = \frac{\frac{4}{3}\pi r^3}{f_{DC}*L*W} \quad \text{A6-7}$$

where r is the spheroid radius and the variable. This changes the interface density equations to:

$$\rho_{int} = \frac{\text{Circumference}}{\text{Total Area}} = \frac{2\pi r}{LW} \quad \text{A6-8}$$

for 2D and

$$\rho_{int} = \frac{\text{Surface Area}}{\text{Total Volume}} = \frac{4\pi r^2}{LWT} \quad \text{A6-9}$$

for 3D. Figure A6.3 shows the 2D to 3D interface density plot. We found that for spheroids the geometric correction factor $x = 1.5$.

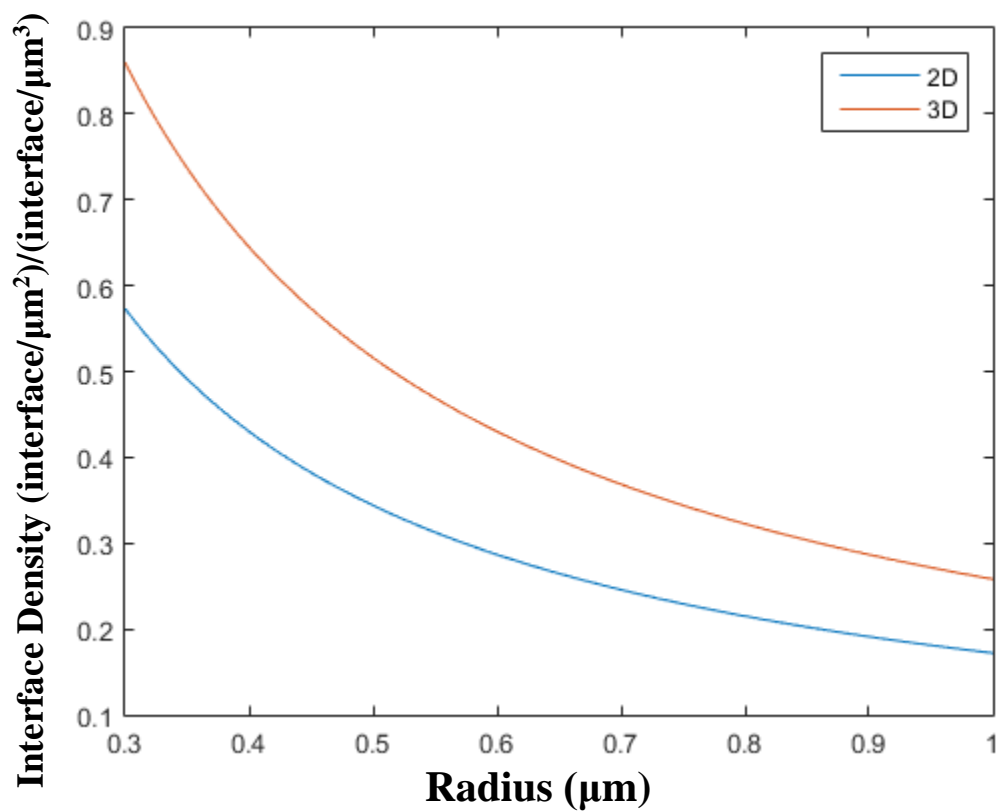


Figure A6.3: Plot of 2D and 3D models showing the change in interface density as a function of spheroid radius. The geometric correction factor is consistently 1.5.

Appendix 7: Models for Predicting Thermal Conductivity

From our experiments in Chapter 4, it is clear that TBC and interface density are the most significant contributors to thermal conductivity. A simple theoretical model utilizing Matthiessen's rule was created to better illuminate how $h_{k,\beta/DC}$ and ρ_{int} interact to influence bulk thermal conductivity. For our simple model, we estimated the ρ_{int} as a function of volume fraction (f). In order to do this, we made a number of assumptions: 1) the nanowire dimensions were constant, 2) the interlamellar spacing and thus the matrix dimensions are changing to facilitate a constant f , 3) nanowires are rectangular, and 4) the finest spacing occurs when $f = 0.5$. So now we can calculate f by the equation,

$$f_{DC} = \frac{2r^2L}{(\lambda+r)^2L} \quad A7-1$$

where r is the width/thickness of the nanowire, L is the length of the matrix, and $(\lambda + r)$ is the interlamellar spacing dependent width (and thickness) of the matrix. Solving Equation A7-1 for λ gives,

$$\lambda = \left(\sqrt{\frac{2\pi}{f_{DC}}} - 1 \right) r \quad A7-2$$

which means that the interlamellar spacing is now dependent on a variable f .

The interface density is simply the ratio of the surface area of the nanowire ($S_{A,DC}$) divided by the volume of the matrix (V_m),

$$V_m = (\lambda + r)^2L \quad A7-3$$

$$S_{A,DC} = 2rr + 2rL + 2rL \quad A7-4$$

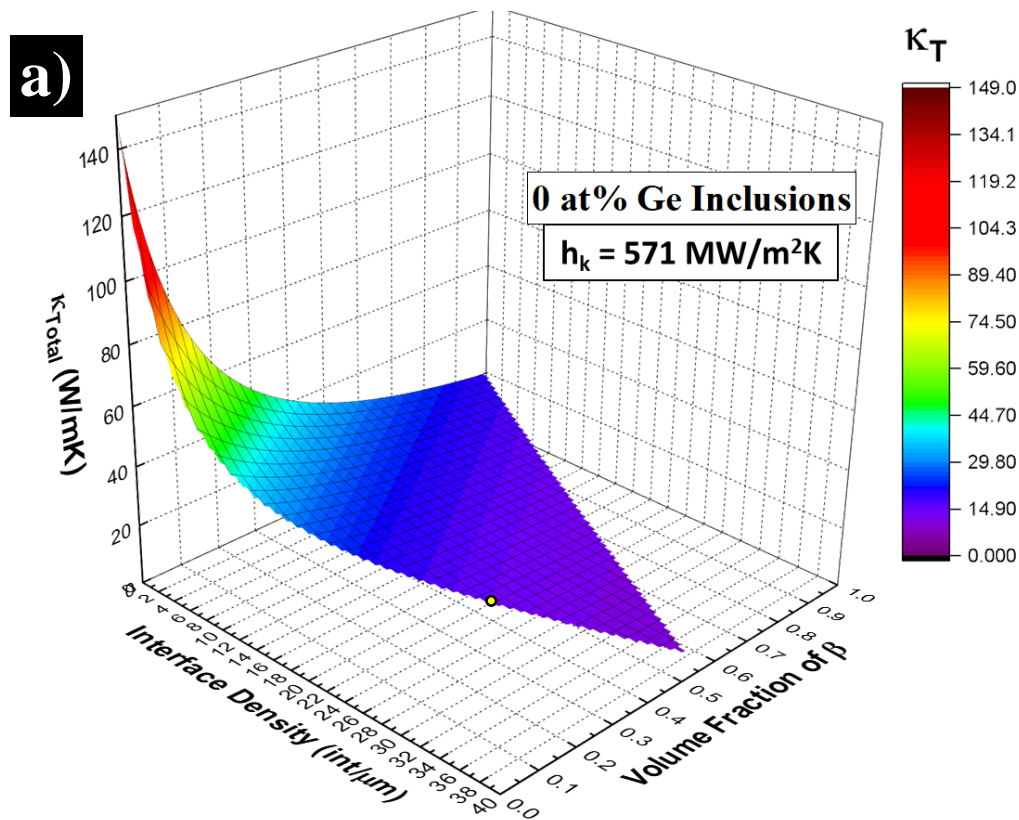
$$\rho_{\beta/DC} = \frac{S_{A,DC}}{V_m} \quad A7-5$$

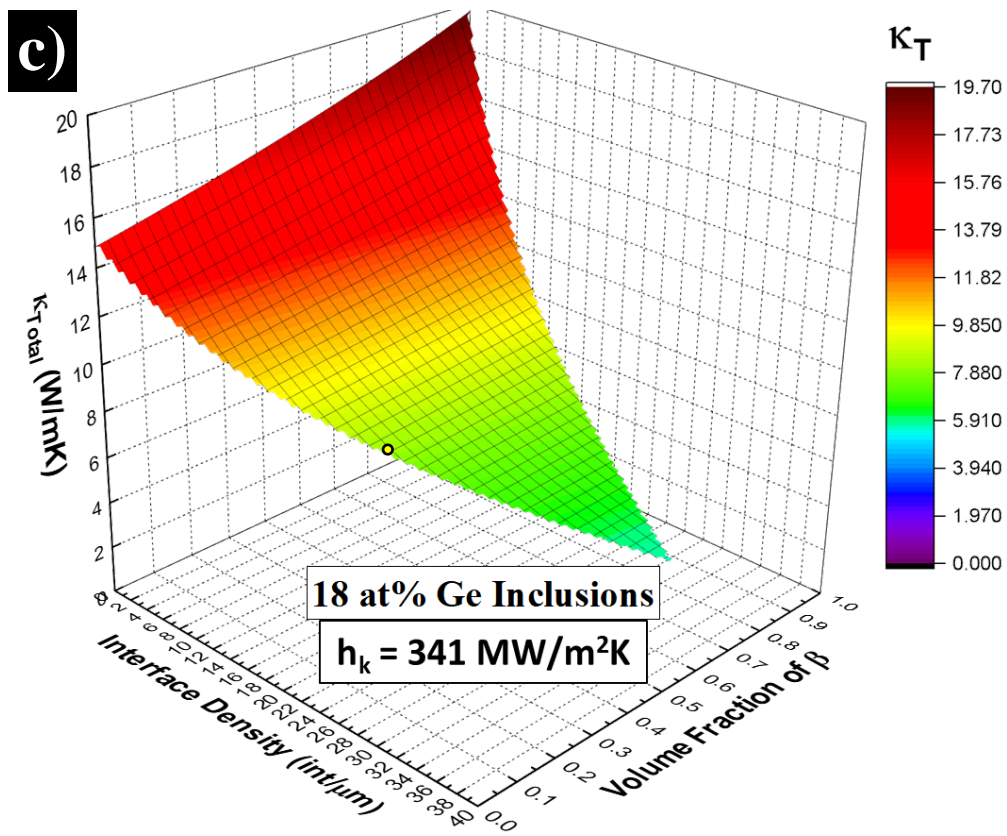
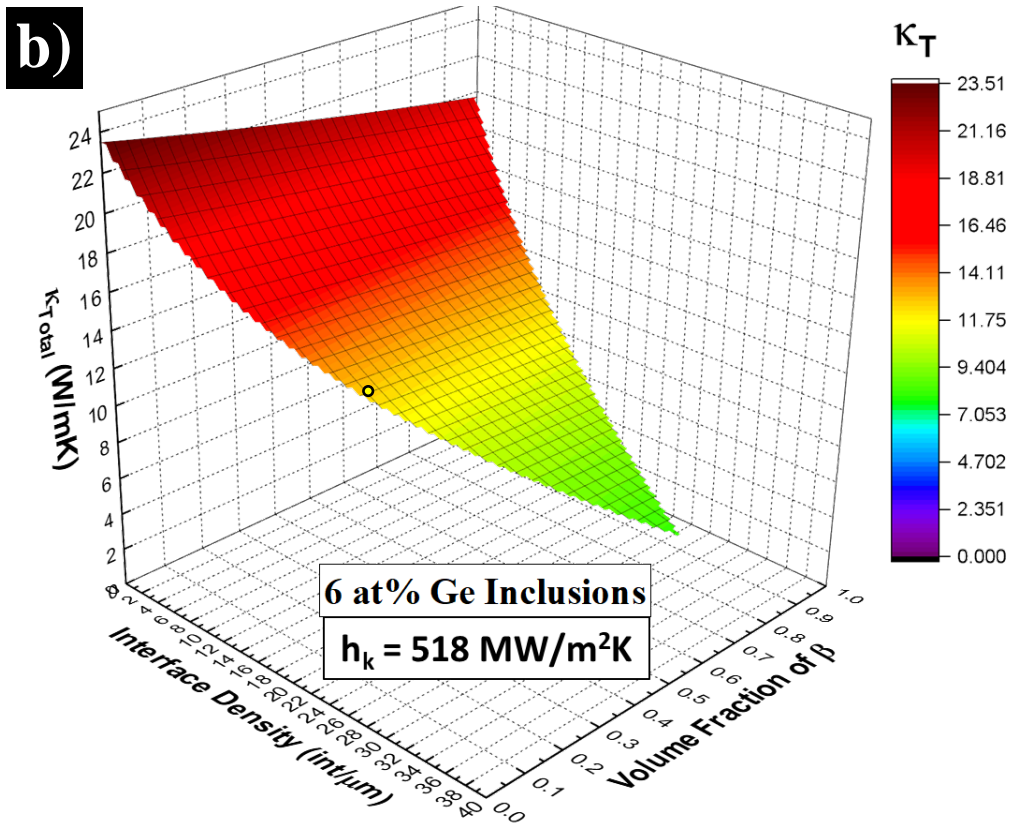
and now the interface density is also dependent upon volume fraction. Now for a given f there is ρ_{int} . By plugging Equations A7.2, A7.3, and A7.4 into Equation A7.5 we can estimate the interface density as a function of volume fraction.

To solve Matthiesen's equation,

$$\frac{1}{\kappa_T} = \frac{f_\beta}{\kappa_\beta} + \frac{f_{DC}}{\kappa_{DC}} + \frac{\rho_{\beta/DC}}{h_{k,\beta/DC}} \quad A7-6$$

the values were taken from Table 4.3, as all the pertinent information for the inclusion compositions 0, 6, 18, and 31 at % Ge have already been calculated. We can plot the thermal conductivity, for a given inclusion composition, as a function of interface density and volume fraction. These plots are contained within Figure A7.1.





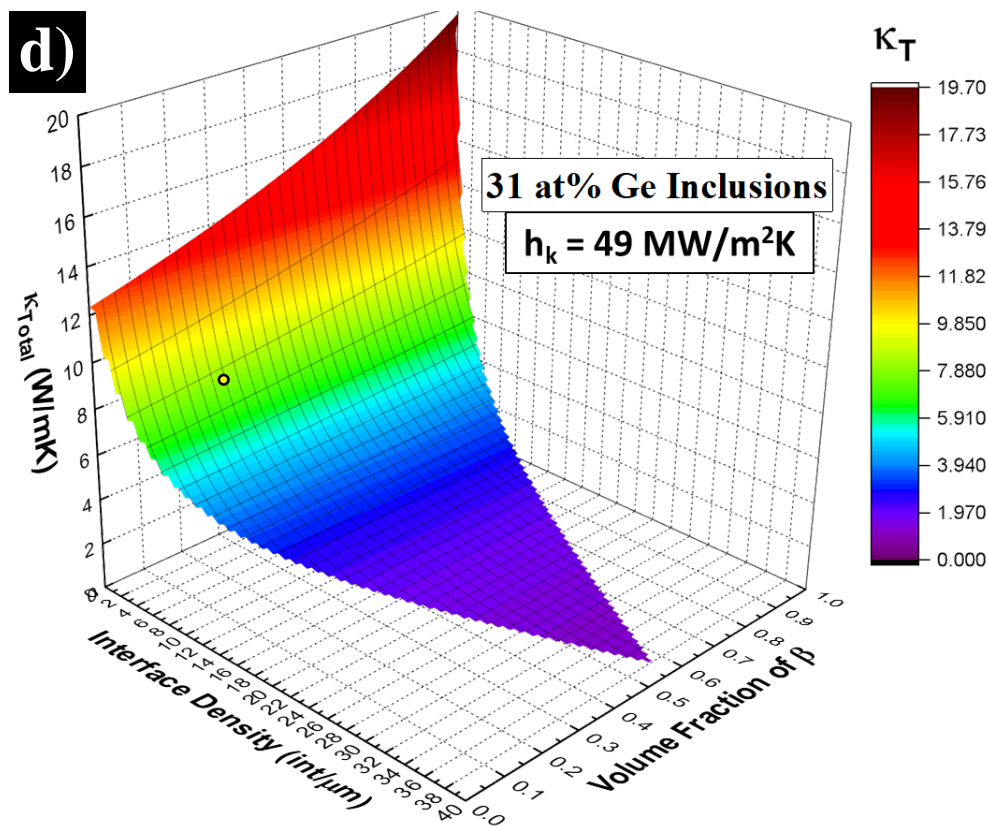


Figure A7.1: Surface plots using Matthiessen's equations to determine the theoretical κ_t as a function of interface density and volume fraction. κ_{DC} and h_k were obtained from a given at% Ge inclusion: a) 0 at% Ge, b) 6 at% Ge, c) 18 at% Ge, and d) 31 at% Ge. The yellow dots designate the interface density of ~ 22 int/ μm , and this falls around our measured thermal conductivity values.

The Figures A7.1a-c imply that doubling ρ_{int} from ~ 22 int/ μm (obtained when aged at 567°C) to ~ 40 int/ μm could decrease current κ by $1 - 3$ W/mK. This might be at a point of diminishing return for reducing lengthscales, as producing finer nanowires from solid-state techniques becomes more difficult. However, in our Figure A7.1.d sample we have not nanostructured the DC inclusions and there is a possible reduction to ~ 2 W/mK if we could obtain ~ 22 int/ μm . The TBC is the most significant contributor to thermal scattering and should be prioritized before ρ_{int} .

It should be noted that some of our measured interface density do not fall within the plotted values, and the yellow dots are moved to the nearest point on the plot surface. However, these plots show

that when interfaces dominate, the bulk volume fractions (and their bulk thermal conductivity values) are no longer significant. Taking this into account, our interface density (ignoring f) approximates our measured κ_T for all the graphs, and are shown as yellow dots on the plots. This model ignores phonon wavelengths and wavelength dependent scattering and it is possible that these graphs are not accurate at high interface densities. Regardless this simple theoretical model approximates our measured data and we considered it an accurate illustration of microstructural contributions to thermal conductivity.

Appendix 8: Attempts at Liquid Pulse Laser Ablation

The motivation for these experiments was to circumvent issues caused by PLM, such as shallow melt depth and surface cracking, by first melting powders and then sintering them into a dense SPS disk. As long as homogenization occurred before ablation, then any damage to the ablated nanoparticle surface is trivial. We attempted to achieve this via liquid pulse laser ablation of SPS disks and powders [116][117]. LPLA, like in the previously discussed PLM, uses a high-power laser to melt a sample surface. In PLM, the laser-induced plasma plume is ejected into the chamber where it can deposit on another surface or possibly form nanoparticles. A small amount of material is lost to plasma, but this is acceptable for bulk materials. In LPLA (Figure A8.1), the plasma

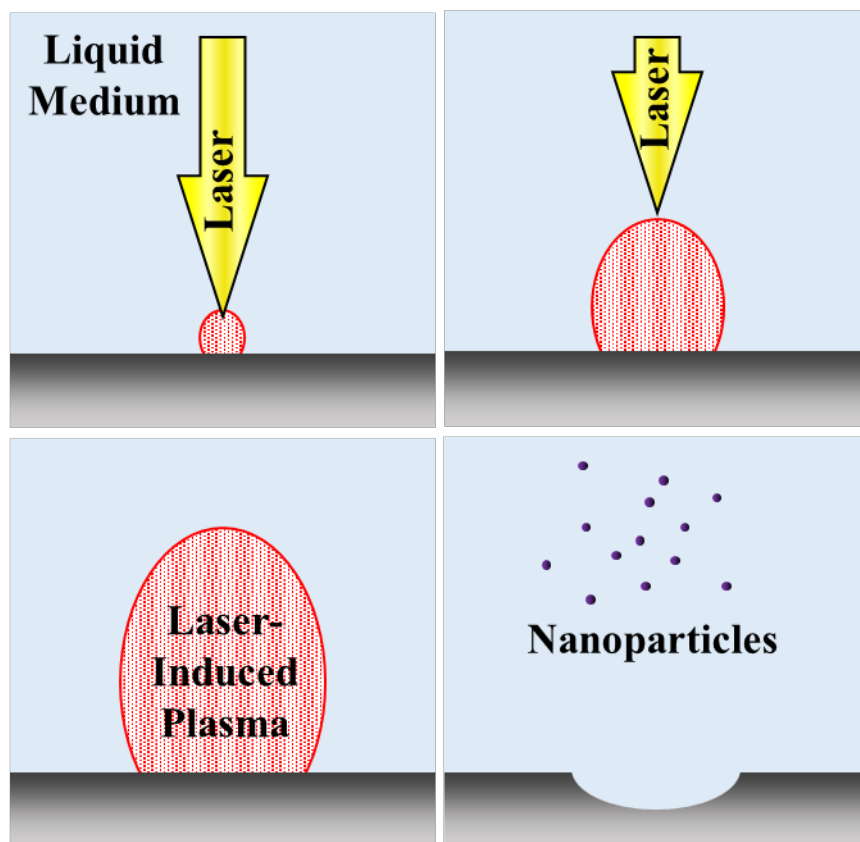


Figure A8.1: Simplified diagram depicting the liquid pulse laser ablation process. First the incident laser pulse heats the sample surface, and creates a plasma plume. The liquid medium constrains the growth of the plume which then coalesces into nanoparticles.

plume is constrained by the liquid medium which coerces the formation of ablated nanoparticles. We sought to collect these nanoparticles for sintering in the hope that this would produce a bulk material with PLM-like microstructure. These LPLA experiments were performed with the excimer laser from Chapter 5 with the following parameters: 5g of material (either in SPS or powder form) immersed in 40 mL of ethanol, laser-pulsed at 10 Hz for 30 min at 2.5 J/cm² fluence, and rastered so that two full passes were made across the sample diameter. The process is shockingly violent, as each pulse would cause the sample to shift, bubbles to nucleate on the sample surface, and even splash ethanol out of the beaker (a fused quartz plate kept the solution from spilling over).

A8.1 LPLA of SPS Disks

The first experiments explored LPLA of SPS disks made from hand-powdered Fe₂₈Si₆₈Ge₄ ribbons. Both DI water and ethanol were tested as the immersion liquid; but DI water resulted in 6% at O at the sample surface (as detected by SEM-EDS) so ethanol was used for all subsequent experiments. The disks and powders were aged at 567 °C for 56 hours (complete decomposition) before LPLA, so that melted material could be easily identifiable as α -FeSi₂ in XRD or SEM characterization.

A large laser-pulse count on a polished SPS disk caused the surface to bead up (Figure A8.2.a). From SEM characterization we confirmed that ablation was occurring and observed ablated nanoparticles that settled on the SPS disk. These particles are not found on a previous pulse laser ablation experiment conducted in an Ar atmosphere, Figure A8.2.b; the lack of particles on the surface show that without the constraint of the liquid medium the plasma plume and any resultant nanoparticles are lost. The beads are not fully melted; a polished cross-section revealed that the bead interior was not affected by the laser, but the exterior (~ 500 nm melt zone) does indicate

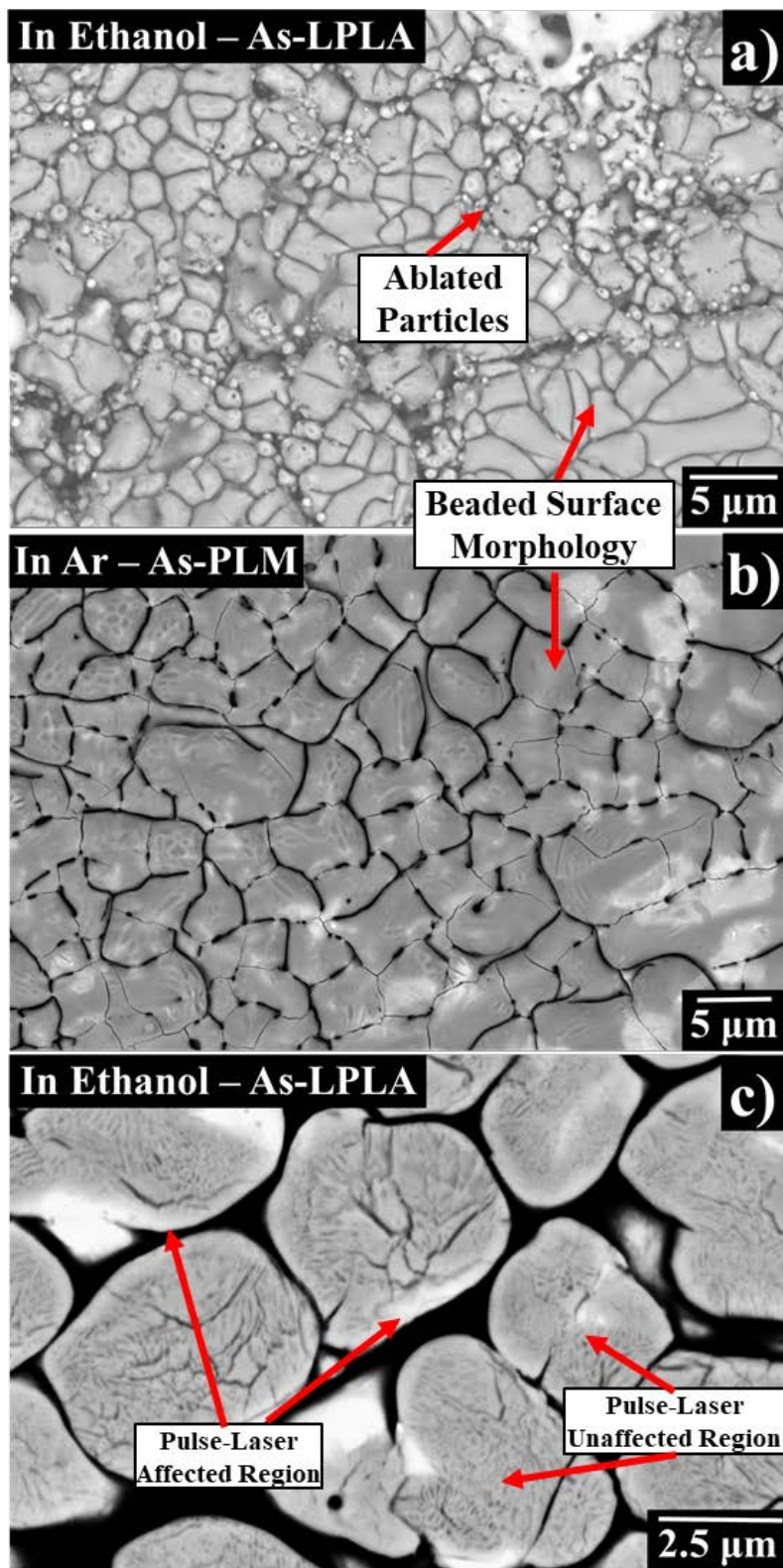


Figure A8.2: SEM micrographs of ablated SPS disks, over-processing caused the surface to bead up. PLA was performed in a) ethanol immersion and b) Ar atmosphere. c) A cross-section of the beads reveals that only the outside layer was affected.

melting as the eutectoid lamellae were solutionized. A double-sided piece of tape was used to collect the ablated material, after evaporation, in the beaker and on the sample surface. Despite having observed ablated particles in SEM, XRD analysis did not detect an α signal as the melt volume was too low.

It should be mentioned that Figure A8.2 suggests that these beads are not compositionally homogenized. Large amounts of SiGe persist on the surface and within the beads. The produced nanoparticles from SPS disks (from hand-powdered $\text{Fe}_{28}\text{Si}_{68}\text{Ge}_4$ ribbons) do not have the supersaturated α phase that we desire; however, high-energy ball milling is capable of producing particles sizes of ~ 200 nm and SPS could make an ultra-fine material for facile homogenization.

A8.2 LPLA of Powder

After it was discovered that LPLA did create a low volume of ablated nanoparticles, the next step was to increase the LPLA melt volume. Instead of having using an incident surface, of which only ~ 500 nm could be melted, it was hypothesized that powder could provide a larger surface area for the incident laser and could be stirred so that fresh powders could be ablated. 5g of powder was made from $\text{Fe}_{28}\text{Si}_{68}\text{Ge}_4$ ribbons via mortar and pestle and sieved to a particle diameter below 40 μm . The powder was mixed with ~ 40 mL of ethanol and the solution and was allowed to settle. The micrograph, Figure A8.3.a, shows the typical powder morphology before ablation; it is characterized by its jagged edges and eutectic/eutectoid microstructures.

We immediately ran into a challenge caused by the powder mixing into suspension. The force of the incident beam was such that the unconstrained powder was mix with the liquid medium, and each pulse would further stir the suspension. The laser was initially focused on the settled powder, but the mixed suspension obscured the beam such that it did not focus and the resultant fluence

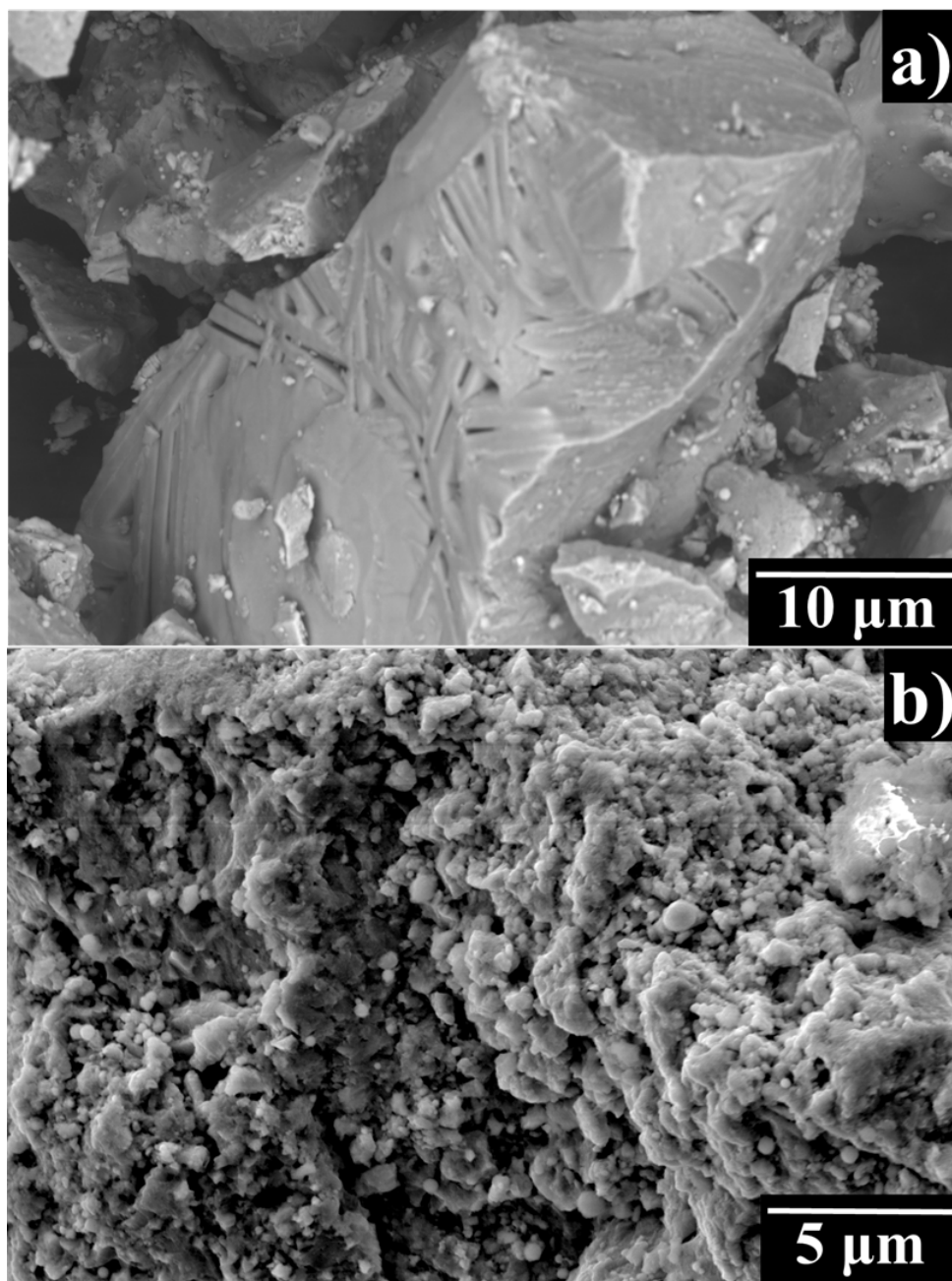


Figure A8.3: Micrographs showing a) pre-PLA powder particle with rough edges and b) a powder particle covered in ablated nanoparticles.

was too low for melting. Focusing the laser at the top of the ethanol disturbed the liquid medium too much and caused it to splash over the beaker, even with the fused quartz plate in place. No melted powder was observed from these experiments.

It became clear that powder particles needed to be constrained to the focal length. This eliminates the possibility of a suspension forming and stirring, but a significant portion of surface layer powder could still be ablated. A 2 mm thick plate of fused quartz was placed over the powder, and constrained it to the focal length and highest fluence. After LPLA and evaporation, a piece of double-sided tape was used to collect the surface layer powder. In SEM, several powder particles were found covered in clusters of nanoparticles; this morphology is similar to what was observed in the literature for LPLA of Si [116], and is caused by the plasma plume and subsequent nanoparticles coalescing on the close-proximity powder particles. Unfortunately, XRD was not able to detect the ablated nanoparticles: the α signal was overwhelmed by the large volume fraction of untransformed β .

These experiments suggest that LPLA, at least with the excimer laser, is not suitable to produce a detectable amount of ablated material. As mention in Chapter 5, the excimer laser is not the optimal tool for laser processing of Fe-Si based alloys and better results could be achieved with alternate laser equipment with longer pulse times.